

2022

The Fate And Transport Of Nitrogen In Subterranean Estuaries

Stephanie J. Wilson

William & Mary - Virginia Institute of Marine Science, sjw100@francis.edu

Follow this and additional works at: <https://scholarworks.wm.edu/etd>



Part of the [Marine Biology Commons](#), and the [Oceanography Commons](#)

Recommended Citation

Wilson, Stephanie J., "The Fate And Transport Of Nitrogen In Subterranean Estuaries" (2022).
Dissertations, Theses, and Masters Projects. William & Mary. Paper 1673281650.
<https://dx.doi.org/10.25773/v5-18sm-k126>

This Dissertation is brought to you for free and open access by the Theses, Dissertations, & Master Projects at W&M ScholarWorks. It has been accepted for inclusion in Dissertations, Theses, and Masters Projects by an authorized administrator of W&M ScholarWorks. For more information, please contact scholarworks@wm.edu.

The Fate and Transport of Nitrogen in Subterranean Estuaries

A Dissertation

Presented to

The Faculty of the School of Marine Science

The College of William & Mary

In Partial Fulfillment

of the Requirements for the Degree of

Doctor of Philosophy

by

Stephanie J. Wilson

May 2022

APPROVAL PAGE

This dissertation is submitted in partial fulfillment of
the requirements for the degree of
Doctor of Philosophy

Stephanie J. Wilson

Approved by the Committee, May 2020

Bongkeun Song, Ph.D.
Committee Chair / Advisor

Iris C. Anderson, Ph.D.
Co-Advisor

Elizabeth Canuel, Ph.D.

Craig Tobias, Ph.D.
University of Connecticut, Dept. of Marine Science
Groton, CT, USA

Bess Ward, Ph.D.
Princeton University
Princeton, NJ, USA

This dissertation is dedicated to my parents. Thank you for instilling in me the value of hard work and encouraging me to be curious about the world. Without your unending support, this would not have been possible.

TABLE OF CONTENTS

Acknowledgements.....	vii
List of Tables	viii
List of Figures.....	x
Abstract.....	xvii
Chapter 1. Introduction.....	2
1.1 References.....	8
1.2 Figures.....	11
Chapter 2. Temporal and spatial variations in subterranean estuary geochemical gradients and nutrient cycling rates: impacts on groundwater nutrient export to estuaries.....	12
2.1. Abstract.....	12
2.2. Introduction.....	13
2.3. Methods.....	16
2.3.1. Study site description.....	16
2.3.2. Experimental design.....	16
2.3.3. Seasonal porewater geochemical monitoring.....	17
2.3.4. Spatial and tidal porewater geochemical monitoring.....	18
2.3.5. Potential N removal rate incubations.....	18
2.3.6. Darcy discharge calculations.....	19
2.3.7. Potential discharge of nutrients in SGD to the overlying water.....	20
2.3.8. Statistical analyses.....	21
2.4. Results.....	22
2.4.1. Seasonal Variation in STE porewater geochemical gradients.....	22
2.4.2. Spatial and tidal variation in STE porewater geochemical profiles.....	23
2.4.3. Seasonal potential N removal rates.....	24
2.4.4. Darcy discharge calculations.....	24
2.4.5. SGD nutrient flux calculations.....	24
2.5. Discussion.....	25
2.5.1. Spatial and temporal variability in STE geochemical profiles.....	25
2.5.2. Potential N removal rates.....	27
2.5.3. Groundwater discharge.....	28
2.5.4. Potential nutrient fluxes.....	29
2.6. References.....	34
2.7. Tables.....	38
2.8. Figures.....	41
2.9. Appendix A.....	48
2.10. Appendix B.....	60
Chapter 3. Geochemical Drivers Impacting Nitrifying Communities in Sandy Sediments.....	61
3.1. Abstract.....	61
3.2. Introduction.....	62
3.3. Results.....	64
3.3.1. Porewater & sediment geochemical parameters.....	64

3.3.2. Microbial community composition.....	65
3.3.3. <i>amoA</i> gene abundances.....	66
3.3.4. Geochemical features related to <i>amoA</i> abundances.....	67
3.4. Discussion.....	67
3.4.1. Geochemical gradients along with depth in the GP-STE	68
3.4.2. Stratification of microbial and nitrifying communities of the GP-STE....	68
3.4.3. Comparison of AOA and AOB abundances in the GP-STE.....	70
3.4.4. Geochemical features related to <i>amoA</i> gene abundances in the GP-STE..	71
3.5. Conclusions.....	72
3.6. Experimental Procedures	73
3.6.1. Sampling site and sample collection	73
3.6.2. Molecular analyses: Metabarcoding analysis of 16S rRNA genes.....	74
3.6.3. Molecular analyses: <i>amoA</i> gene qPCR assays.....	75
3.6.4. Statistical analyses.....	76
3.7. References.....	77
3.8. Tables.....	80
3.9. Figures.....	81
3.10. Appendix C.....	86
3.11. Appendix D.....	90
Chapter 4. Nitrification in a subterranean estuary: an <i>ex situ</i> and <i>in situ</i> method	
comparison determines nitrate is available for discharge.....	91
4.1. Abstract.....	91
4.2. Introduction.....	92
4.3. Methods.....	95
4.3.1. Study Site Description and Experimental Set up.....	95
4.3.2. Conservative Mixing Models.....	96
4.3.3. <i>In situ</i> experiment with $^{15}\text{NH}_4^+$ tracer injection.....	98
4.3.4. <i>Ex situ</i> sediment slurry incubations with $^{15}\text{NH}_4^+$ tracer addition.....	100
4.4. Results.....	100
4.4.1. Nitrification rates estimated by conservative mixing models	102
4.4.2. Nitrification rates measured by an <i>in situ</i> $^{15}\text{NH}_4^+$ tracer injection	
experiment.....	103
4.4.3. Nitrification rates measured in <i>ex situ</i> sediment slurry incubations with added	
$^{15}\text{NH}_4^+$ tracer.....	104
4.5. Discussion.....	105
4.5.1. Mixing model calculations.....	105
4.5.2. <i>In situ</i> tracer experiment.....	106
4.5.3. <i>Ex situ</i> sediment slurry incubation experiments.....	108
4.5.4. Comparing nitrification rate measurement with different methods.....	110
4.5.5. Implications for N in STEs.....	112
4.6. References.....	113
4.7. Tables.....	116
4.8. Figures.....	117
4.9. Appendix E	125
4.10. Appendix F.....	126

Chapter 5. Subterranean estuaries modify groundwater nutrient fluxes to the global ocean	127
5.1. Abstract	127
5.2. Main	128
5.2.1. Global distribution of nutrients in subterranean estuaries	129
5.2.2. Nutrient transformations within subterranean estuaries.....	132
5.2.3. Nutrient fluxes to the global ocean.....	133
5.2.4. Implications.....	135
5.2.5. Limitations.....	136
5.3. Methods.....	138
5.3.1. Data compilation.....	138
5.3.2. Statistical Analyses.....	139
5.3.3. Subterranean estuary transformations	140
5.3.4. Calculating SGD endmembers and nutrient fluxes to the global ocean....	141
5.4. References.....	144
5.5. Figures.....	148
5.6. Appendix G.....	152
5.7. Appendix H.....	169
Chapter 6. Conclusions.....	170

ACKNOWLEDGEMENTS

First I would like to thank my advisors, Drs. Bongkeun Song and Iris Anderson for being amazing scientific mentors throughout my graduate career. From hot summer days sampling at the Gloucester Point Beach, to presentations in Puerto Rico, you have been always supported me and continuously challenged me to become a better scientist. BK, thank you for pushing me to be creative, supporting my curiosity, and taking me around the world to study the marine environment. I hope I have officially “hatched”. Iris, thank you for challenging me to be skeptical and meticulous in my work, for serving as a role model for women in science, and for constantly advocating for me. Lastly, thank you both for your support beyond academia; I am truly grateful to have you in my life.

I would like to thank my committee members Dr. Elizabeth Canuel and Dr. Bess Ward for their help and support throughout my time at VIMS. I would like to give a special thank you to my committee member Dr. Craig Tobias who took me on as an adopted advisee. Thank you for your insight, for challenging me to think bigger, and for allowing me to work in your lab throughout the years.

I would like to acknowledge Dr. Isaac Santos, who served as my mentor and host while I visited the University of Gothenburg. I also want to thank Amy Moody and Dr. Tristan McKenzie, who were integral to my meta-analysis work, along with the many co-authors who supplied data and/or expertise.

During my time at VIMS, I have had the pleasure of working with many incredible members of the faculty, staff, administration, and student body. I would like to acknowledge the extensive support provided by Hunter Walker, Michele Cochran, and Renia Prassie who I worked closely with at VIMS. I would also like to thank the entire VIMS community for making this a truly great place to work.

I especially would like to thank my Song and Anderson lab mates, past and present, Miguel Semedo, Ann Arfken, Ken Czaplá, Samantha Fortin, Brianna Stanley, Abby Golder, Michelle Woods, Derek Detweiler, and our adopted lab mate Brian Kim for years of support, advice, and friendship. As well as a special thank you to my adopted lab mates at UConn and in Gothenburg: Peter Ruffino, Clare Schlink, Sydney Twarz, Cloudy Majtenyi Hill, Gloria Rooibos, and Alex Cabral.

Finally I would also like to thank my friends and family for their endless support. Thank you for always listening and encouraging me to push forward even when things were hard. I would truly not be here without you. Thank you to Dad, Dina, Banks, G-ma, Joe, Mom, and Bill, as well as, Michelle & Cody, Cristin, Colleen, and Amy.

LIST OF TABLES

CHAPTER 2

Table 1. Potential N removal rates measured seasonally in sediment slurries using the IPT method (Song and Tobias, 2011) in $\text{mmoles N m}^{-2} \text{ day}^{-1}$ and the associated standard deviation..38

Table 2. Average horizontal, vertical, and total groundwater (GW) discharge \pm standard error for each month sampled. Average of all measurements = $34.1 \pm 8.4 \text{ L m}^{-2} \text{ day}^{-1}$38

Table 3. Nutrient fluxes via SGD for each season reported in $\text{mmol m}^{-2} \text{ d}^{-1} \pm$ standard error and the N:P ratio of discharge. Deep endmember represents the flux estimated using DIN and PO₄²⁻ concentrations at the 300 cm depth in the STE. The shallow endmember fluxes represent those estimated using concentrations at the 50 cm depth. The anoxic zone and total DNF fluxes were calculated using the N removal two scenarios described in section 2.3.7.....39

Table 4. Comparison of SGD nutrient fluxes from different sites. DIN = dissolved inorganic nitrogen, DIP = dissolved inorganic phosphorus..... 40

Appendix A

Table S1. ANOVA Results; statistically significant p-values are shown in bold.....48

Table S2. P-values from Pearson Correlation significance test ($\alpha > 0.05$)..... 49

Table S3. Comparison of DIN inputs to the lower portion of York River Estuary in $10^6 \text{ mmol N day}^{-1}$ for an area of 33,146,225 m^2 , area includes Gloucester Point to Mouth of York River. Submarine groundwater discharge (SGD) fluxes are those calculated in this study, ^A Advective river fluxes were calculated using the York River Water Quality Model published by Lake & Brush (2015), and ^B Seasonal benthic fluxes were measured by Woods et al. (in prep) in the lower York River. SGD as % of Advective represents the magnitude of SGD derived nutrient flux/ Diffusive river nutrient flux x 100..... 49

Table S4. Discharge ANOVA Results; statistically significant p-values are shown in bold.....50

CHAPTER 3

Table 1. Three most parsimonious models as determined by the delta Akaike information criterion corrected (dAICc), variance explained (R^2), and model weights (Wt) for AOA and AOB abundances based on *amoA* gene quantification. H is the hypothesis number, Model includes the dependent variable ($\log(\text{amoA copy numbers g}^{-1})$) and explanatory variables (NUTs = porewater and extractable DIN, pH, Sal = salinity, and DO)..... 80

CHAPTER 4

Table 1. STE mixing model calculations of production of NO_3^- and consumption of NH_4^+ in the top 100 cm of the STE in each season sampled.116

Table 2. Background geochemical parameters at injection sites (50 cm injection wells) prior to in situ tracer experiment.....116

Table 3. Benchtop sediment slurry incubation rates (\pm Standard error) determined by $^{15}\text{N-NO}_x$ production overtime in incubation samples. Average potential nitrification rate (of all measurements) was 62.44 ± 7.23116

Appendix E

Table S1. STE mixing model calculations of production of NO_3^- and consumption of NH_4^+ in the top 50 cm of the STE in each season sampled.....125

CHAPTER 5

Appendix G

Table S1. STE Behavior with respect to NO_3^- , NH_4^+ , DON, and DIP shown as the percentage of sites exhibiting that behavior and the total number of sites assessed for each analyte.....152

Table S2. Fluxes of DON, DIN, and DIP resulting from various endmember and SGD flux assumptions in Tmoles yr^{-1} (\pm standard error).....153

LIST OF FIGURES

CHAPTER 1

Figure 1. Conceptual diagram exhibiting the flow of fresh, terrestrial groundwater meeting and mixing with saline groundwater and recirculated seawater in the subterranean estuary (STE). The mixture of fresh and saline water that forms in the STE is then released to the ocean as submarine groundwater discharge (SGD)..... 11

CHAPTER 2

Figure 1. Conceptual diagram of biogeochemical cycling in the subterranean estuary and discharge of dissolved inorganic nitrogen (DIN) and dissolved inorganic phosphorus (DIP) in submarine groundwater discharge (SGD) to coastal waters..... 41

Figure 2. Study site map: (A) Gloucester Point region of YRE, study site (GP-STE, star) 37.248884 N, 76.505324 W; (Arc GIS online); (B) GP-STE Sampling Scheme: All piezometers (circles) were constructed at the mid-tide line (MTL) of the GP-Beach. Piezometers shown were sampled once at low tide to determine spatial variability (0-120 cm). Piezometers were sampled across seasons (filled circles, depths: 0-300 cm) and over two tidal cycles (filled circles, depths: 0-120 cm). Three pressure transducer wells were placed at the mid-tide line (MTL) at three depths (100, 70, and 50cm); one well was placed at the low-tide line (LTL) at 100cm.....42

Figure 3. Seasonal GP-STE porewater depth profiles. (A) Salinity, (B) DO (mg/L), (C) Nitrate (μM), (D) Ammonium (μM), (E) Phosphate (μM), (F) Sulfide (μM), (G) DIC (mM), (H) DOC (μM)..... 43

Figure 4. Spatial variability at the mid-tide line across the beach face: (A) Salinity, (B) DO (mg/L), (C) Nitrate (μM), (D) Ammonium (μM), (E) Phosphorus (μM), (F) DIC (mM). Points represent means and error bars represent one standard error in each direction..... 44

Figure 5. Tidal variability at the mid-tide line over a tidal cycle (spring tide; sampled at high, mid, and low tide) in the spring (black) and summer (grey) of 2020: (A) Salinity, (B) DO (mg/L), (C) Nitrate (μM), (D) Ammonium (μM), (E) Phosphorus (μM), (F) DIC (mM). Points represent means and error bars represent one standard error in each direction..... 45

Figure 6. Comparison of advective (black), benthic flux (grey), SGD deep endmember flux (dark blue), and SGD shallow endmember flux (blue), SGD anoxic denitrification scenario flux (light blue), and SGD total denitrification scenario flux (periwinkle) of DIN in the lower YRE. A) shows all calculated fluxes and panel B) shows all fluxes except the advective flux. Error bars represent one standard error in each direction..... 46

Figure 7. Comparison of advective (black), benthic flux (grey), SGD deep endmember flux (dark blue), and SGD shallow endmember flux (blue) of PO_4^{2-} in the lower YRE. A) shows all calculated fluxes and panel B) shows all fluxes except the advective flux. Error bars represent one standard error in each direction.....47

Appendix A

Figure S1. Seasonal GP-STE porewater depth profiles of porewater nitrite (NO_2^-) concentrations (μM); all concentrations $< 1.7 \mu\text{M}$ 51

Figure S2. Tidal variability at the mid-tide line over a tidal cycle (spring tide; sampled at high, mid, and low tide) in the spring 2020: salinity, dissolved oxygen (mg/L), nitrate (μM), ammonium (μM), dissolved inorganic phosphorus (μM), DIC (mM)..... 52

Figure S3. Tidal variability at the mid-tide line over a tidal cycle (spring tide; sampled at high, mid, and low tide) in the summer 2020: salinity, dissolved oxygen (mg/L), nitrate (μM), ammonium (μM), dissolved inorganic phosphorus (μM), DIC (mM) 53

Figure S4. Spatial variability at the mid-tide line across the beach face: salinity, dissolved oxygen (mg/L), nitrate (μM), ammonium (μM), dissolved inorganic phosphorus (μM), and DIC (mM)..... 54

Figure S5. Pearson correlation analysis of STE porewater geochemical analytes. The Pearson correlation coefficient is indicated by the number in each dot, the size of the dot indicates the strength of the correlation, color indicates the direction of the correlation (red = negative, blue = positive), squares with circles were correlations with a p-value < 0.05 , but those without circles indicate non-significant (p-value > 0.05) correlations..... 55

Figure S6. Total groundwater discharge for each season sampled in 2019 (black) and tidal data for the same month from VECOS at the Gloucester Point monitoring station (grey)..... 56

Figure S7. Total groundwater discharge for each season sampled in 2020 (black) and tidal data for the same month from VECOS at the Gloucester Point monitoring station (grey)..... 57

Figure S8. York River box boundaries, Gloucester Point Beach STE is located at the border of boxes 7 and 8. SGD, Benthic, and Advective fluxes were extrapolated to the total area in box 8 (47.88 km^2)..... 58

Figure S9: A) Submarine groundwater discharge (SGD) seepage zone defined (not to scale) in the lower portion of the YRE (Box 8 according to Lake and Brush 2015). B) Conceptual diagram of seepage zone broken into sections with distance from the shoreline where the first 10m from the shoreline was defined as the zone exhibiting discharge as measured at the GP-STE, the next 10m represents the zone with half the discharge measured at the GP-STE, and the next 20m out from the shoreline is assumed to exhibit one-fourth the discharge measured at the shoreline of

the GP-STE. This approach of sectioning the seepage zone allows for a simple model of exponential decay of SGD moving away from the shoreline.....59

Figure S10. Box and whisker plots of seasonal discharge (A), DIN fluxes calculated using the shallow (50 cm) endmember (B), and PO4²⁻ fluxes calculated using the shallow (50 cm) endmember (C). An Asterix indicates statistical significance from other seasons (ANOVA, p-value < 0.05).....59

CHAPTER 3

Fig. 1. GP-STE geochemical depth profiles as averages of seasonal measurements. A) Dissolved oxygen (DO, mg/L), salinity, and DIC (mM). B) pH, C) Nitrate (μM), nitrite (μM), and ammonium (μM). D) Extractable nitrate (μM), extractable nitrite (μM), and extractable ammonium (μM). Error bars indicate one standard error in each direction)..... 81

Fig. 2. Principal Coordinate Analysis (PCoA) showing microbial community structure merged across seasons at each STE sediment depth (indicated by color). Depth is labeled with the top depth of the respective core section depth, for example 0 indicates core section 0-10 cm. Sample dissimilarity was calculated using the Bray-Curtis dissimilarity index and a multivariate permutational analysis of variance (PERMANOVA) was used to analyze amplicon sequence variant (ASV) dissimilarity with depth (p-value < 0.001) and season (p-value >0.05)..... 82

Fig. 3. Sediment community composition (Family level) at each depth and season sampled at the GP-STE. Depth is labeled with the top of the respective core section depth, where 0 indicates the 0-10 cm section of the core..... 83

Fig. 4. A) AOA, B) AOB, and C) NOB community composition shown as average relative abundance (number of specific ASVs/total number of sample 16S ASVs x 100%) at the family level averaged across seasons sampled at each depth interval in the GP-STE. Depth is labeled by the top of the respective core section depth, where 0 indicates the top of core section 0-10 cm..84

Fig. 5. Abundance of archaeal (black) and bacterial (grey) *amoA* genes (copies g sediment⁻¹) at each sediment depth averaged across seasons sampled at the GP-STE where 0 indicates core section 0-10 cm; error bars represent one standard deviation in each direction..... 85

Appendix C

Fig. S1. 16S metabarcoding analysis presenting the sediment community composition (Phylum level) for each season at each depth sampled at the GP-STE..... 86

Fig. S2. A canonical analysis of principal coordinates (CAP) plot of sediments community structure in the GP-STE by season (shape) and depth (color). Sample dissimilarity was calculated using the Bray-Curtis dissimilarity index. A multivariate permutational ANOVA (PERMANOVA) was used to analyze ASV dissimilarity with depth (p = 0.001) and season (p > 0.05)..... 86

Fig. S3. Comparison of AOA (A) and AOB (B) abundances in each season determined by qPCR of *amoA* genes. An ANOVA indicated that the numbers of AOA and AOB did not vary significantly with season..... 87

Fig. S4. Comparison of relative abundance of AOA (A) and AOB (B) communities (both *Gammaproteobacterial* and *Betaproteobacteria*) as determined by 16S sequencing. An ANOVA indicated that the relative abundance of AOA and AOB did not vary significantly with season..... 88

Fig. S5. A) Comparison of AOA abundance as determined by 16S sequencing and qPCR, $R^2=0.86$. B) Comparison of *Betaproteobacterial* AOB abundance as determined by 16S sequencing and qPCR (B), $R^2=0.52$ 89

Fig. S6. A: AOA) Archaeal *amoA* copies compared to porewater pH; line signifies a linear model: $AOA\ amoA \sim pH$, $R^2 = 0.22$ (p-value < 0.001). B: AOB) Bacterial *amoA* copies compared to porewater pH; line signifies a linear model: $AOB\ amoA \sim pH$, $R^2 = 0.36$ (p-value < 0.001)..... 89

CHAPTER 4

Figure 1. Conceptual diagram depicting observed data compared to conservative mixing lines calculated using endmembers from groundwater and overlying water.....117

Figure 2. Conceptual diagram of in situ experiment showing tracer plume introduction to the injection well and potential oxidation of the tracer ($^{15}NH_4^+$) within the STE subsurface to $^{15}NO_2^-$ and $^{15}NO_3^-$ by nitrification.....117

Figure 3. A) Porewater NO_3^- concentrations (μM) in all seasons with porewater depth (cm), B) Porewater NH_4^+ concentrations (μM) in all seasons with porewater depth (cm). C) Porewater NO_3^- concentrations (μM) versus porewater salinity, with conservative mixing line (gray) for reference, D) Porewater NH_4^+ concentrations (μM) in all seasons versus porewater STE salinity, with the conservative mixing line (gray) for reference.....118

Figure 4. Analytes (μM) vs. salinity used to calculate production or consumption via mixing models for each season A) Spring 2018, Nitrate, B) Spring 2018, Ammonium, C) Summer 2018, Nitrate, D) Summer 2018, Ammonium, E) Fall 2018, Nitrate, F) Fall 2018, Ammonium, G) Winter 2019, Nitrate, H) Winter 2019, Ammonium. Points represent individual observed data points and lines indicate conservative mixing lines resulting from groundwater and surface water endmembers.....119

Figure 5. Groundwater NO_x^- concentrations (μM) over time after injection in the *in situ* tracer injections #1 (A) and #2 (B) and NH_4^+ concentrations (μM) in injections #1 (C) and #2 (D); well ID is indicated by point shape.....120

Figure 6. SF₆ concentrations (pM) in groundwater samples over time after the *in situ* tracer injections #1 (A) and #2 (B); sample well DI is indicated by point shape.....121

Figure 7. Enrichment of ¹⁵NO_x, shown in delta notation, in groundwater samples after the *in situ* tracer injections #1 (A) and #2 (B); sample well ID indicated by point shape.....121

Figure 8. Nitrified N concentrations (μM; ¹⁵NO_x⁻ corrected for dilution of ¹⁵NH₄⁺ tracer) in groundwater samples after the *in situ* tracer injections #1 (A) and #2 (B). Where sampling well is indicated by shape.....122

Figure 9. NH₄⁺ concentrations (μM) overtime in sediment slurry incubations. Each point represents the mean of triplicate samples and the error bars represent one standard error in each direction.....122

Figure 10. A) NO_x concentrations (μM) overtime and B) ¹⁵NO_x (nmoles) overtime in sediment slurry incubations for each core depth section (indicated by point shape). Each point represents the mean of triplicate cores samples and error bars represent one standard error in each direction.....123

Figure 11. Potential nitrification rates in sediment slurry incubations versus the ambient porewater ammonium concentration (μM) at the associated depth (p-value = 0.014).....123

Figure 12. Comparison of average nitrification rates (μmoles N m⁻² d⁻¹) as determined by the *in situ* tracer experiment (average of both injection sites), sediment slurry incubation (averaged over all depth sections), and conservative mixing models of ammonium loss and nitrate production (sum of mass lost from 0-50 cm; averaged across seasons). Error bars represent one standard error in each direction. An analysis of variance (ANOVA) revealed a significant fixed effect of measurement method on nitrification rates for the GP-STE (p-value = 0.006), a post-hoc Tukey test indicated that the *in situ* tracer experiment was statistically different from the sediment slurry and conservative mixing estimation based on ammonium loss, but not nitrate production. The sediment slurry and conservative mixing estimations (both ammonium and nitrate) were not statistically different from one another.....124

CHAPTER 5

Figure 1. Map indicating sample site locations (n=216), including local-scale sample size (count, indicated by dot size). Histograms showing concentrations of b) DIN (n=5,660), c) DON (n=1,890), and d) DIP (n=4,569) on a log scale. Scatter plots of e) DIN, f) DON, and g) DIP concentrations (μM) with sample salinity. The full dataset is available (submitted to Pangaea) and data can be viewed using the Shiny Interactive Map.....148

Figure 2. Ternary plots of N speciation in groundwater samples by site lithology and salinity, indicated by color, in a) Mixed, b) Muddy, c) Rocky, and d) Sandy sites. DIN (μM): DIP (μM) ratios for e) Mixed, f) Muddy, g) Rocky, and h) Sandy sites with the Redfield Ratio (16:1) line shown in black.....149

Figure 3. Conceptual diagrams of a) conservative, b) productive, c) consumptive, and d) undefined behavior in subterranean estuaries. Examples of each classification with respect to NO_3^- (μM) and PO_4^{2-} (μM) in subterranean estuaries from the meta-dataset including e) Calanques of Marseille-Cassis, f) Kasitna Bay, g) Waquiot Bay, and h) Killary as well as i) Rarotonga, j) Monterey Bay (Seabright), k) Gloucester Point, and j) Kona Coast.....150

Figure 4. Bar plots comparing fluxes via total SGD and rivers (Seitzinger *et al.*, 2005; Seitzinger *et al.*, 2010; Harrison *et al.*, 2005) of a) DIN, b) DON, and c) DIP to the global ocean.....151

Appendix G

Figure S1. Global maps showing site averaged a) DIP, b) DIN, and c) DON concentrations in $\mu\text{mol L}^{-1}$ where color indicates concentration.....154

Figure S2. Spatial heterogeneity of global groundwater samples where dot color corresponds to continent a) for b) DIN, c) DON, and d) DIP. No clear spatial trends were determined. Dark grey points are indicative of data from islands.....155

Figure S3. Random forest analysis output: feature importance (%) to groundwater nutrient concentrations of DIN (a), DON (b) and DIP (c).....156

Figure S4. Histogram of untransformed groundwater nutrient concentrations, which clearly shows the log normal distribution of a) DIN, b) DON, and c) DIP concentrations.....157

Figure S5. Violin plots showing the distribution of log transformed nutrient concentrations of DIN, DON, and DIP across different factors: Site Type (A-C), Ocean Basin (D-F), and salinity (G-I).....158

Figure S6. Violin plots showing the distribution of log transformed nutrient concentrations of DIN, DON, and DIP across site specific Ecological Coastal Unit (ECU) Classifications (A-C) and Dürr Type Classifications (D-F).....159

Figure S7. Violin plots showing the distribution of log transformed nutrient concentrations of a) DIN, b) DON, and c) DIP for each Koeppen Geiger Climate classification.....160

Figure S8. Comparison of log transformed, site averaged groundwater DIN, DON, and DIP concentrations compared to average rainfall (a-c), average evaporation (d-f), and average baseflow (g-i). No statistically significant relationships were identified between site climatological estimates and groundwater nutrient concentrations.....161

Figure S9. Comparison of log transformed, site averaged groundwater DIN, DON, and DIP concentrations compared to site average annual SGD (Q , $\text{km}^3 \text{ yr}^{-1}$) (a-c), average annual fresh SGD (F-SGD, $\text{m}^2 \text{ yr}^{-1}$) (d-f), and average annual coastal groundwater discharge (cgd, $\text{m}^2 \text{ yr}^{-1}$) (g-i). No statistically significant relationships were identified between site specific discharge estimates and groundwater nutrient concentrations.....162

Figure S10. Comparison of log transformed, site averaged groundwater DIN, DON, and DIP concentrations compared to land cover data within a 1 km radius of each site. % of bare land cover (a-c), % built up land cover (d-f), % tree coverage (g-i), % shrub cover (j-l) % crop cover (m-o), and total N application (p-r) (Luijendijk et al., 2020; Potter et al., 2011). Each relationship was assessed with linear regression, plots with significant relationships (p-value < 0.05) include the linear regression line (blue) on the plot.....163

Figure S11. Comparison of log transformed, site averaged groundwater NO₃⁻ and NH₄⁺ concentrations compared to site specific annual average rainfall (a-b), average evaporation (c-d), and average baseflow (e-f). No statistically significant relationships were identified between climatological estimates and groundwater nutrient concentrations.....164

Figure S12. Comparison of log transformed, site averaged groundwater NO₃⁻ and NH₄⁺ concentrations compared to site average annual SGD (Q, km³ yr⁻¹) (a-c), average annual fresh SGD (F-SGD, m² yr⁻¹) (d-f), and average annual coastal groundwater discharge (cgd, m² yr⁻¹) (g-i). No statistically significant relationships were identified between site specific discharge estimates and groundwater nutrient concentrations.....165

Figure S13. Comparison of log transformed, site averaged groundwater NO₃⁻ and NH₄⁺ concentrations compared to land cover data within a 1 km radius of each site. % of bare land cover (a-c), % built up land cover (d-f), % tree coverage (g-i), % shrub cover (j-l) % crop cover (m-o), and total N application (p-r) (Luijendijk et al., 2020; Potter et al., 2011). Each relationship was assessed with linear regression, plots with significant relationships (p-value < 0.05) include the linear regression line (blue) on the plot.....166

Figure S14. Ternary plot showing groundwater N composition binned by sample salinity (color); no clear trends identified.....167

Figure S15. Ternary plot showing N composition when binned by site type (color); no clear trends identified.....167

Figure S16. Ternary plot showing N composition binned by sample depth (color); no clear trends identified.....168

ABSTRACT

The subterranean estuary (STE) is a subsurface ecosystem where fresh groundwater mixes with intruding, recirculated seawater at the coastline. Despite being present globally, STEs and their potential impacts as hotspots for biogeochemical processing, or as a source of nutrients to coastal systems, are not well understood. STEs have been recognized as highly reactive zones for biogeochemical reactions, which influence the fate and transport of nutrients, organic matter, and trace metals discharged to the coastal ocean. Biogeochemical processing of nitrogen (N) in STEs influences N in submarine groundwater discharge (SGD) including its availability for use by primary producers and cascading eutrophication. The overarching goal of this dissertation was to assess N cycling in STEs and to evaluate how these processes may impact exchanges of N with adjacent marine environments. In chapter two, seasonal, tidal, and spatial variation in geochemical gradients as well as N cycling rates were examined to determine their influence on nutrient fluxes in SGD in the Gloucester Point beach STE (GP-STE). Geochemical gradients varied significantly across seasons, but not over tidal and spatial scales, driving seasonal variance in STE nutrient concentrations and fluxes. The nitrate, ammonium, and dissolved oxygen gradients in the GP-STE suggested nitrification was a major biogeochemical process determining the fate of groundwater derived N. The GP-STE was identified as a source of N and phosphorus (P) to the overlying York River estuary in all seasons, but denitrification reduced N export. In chapter three, the microbial community of the sandy GP beach along with the composition and abundance of nitrifiers was examined with depth in four seasons. The microbial community varied significantly with depth, but not with season. Nitrifiers were present in the top one meter of the beach indicating the genetic potential for nitrification in the system, but their abundances decreased with depth. Multivariate analysis indicated that porewater nutrient concentrations, pH, and dissolved oxygen were major drivers of subsurface nitrifier abundance. In chapter four, STE nitrification rates were measured using conservative mixing models, an *in situ* tracer experiment, and *ex situ* sediment slurry incubations. All three methods indicated nitrification is occurring in the GP-STE; however, the *in situ* tracer experiment revealed variation in nitrification rates over space and time that was not captured by the mixing model calculations or slurry incubations. These data suggest that, due to heterogeneity in the subsurface environment, *in situ* experiments may be the best approach for estimating STE process rates. Chapter five used a global meta-dataset to examine the groundwater nutrient pool, determine STE behavior with regards to nutrients, and assess the impact STE processing has on groundwater fluxes to the global ocean. The composition and concentrations of the groundwater nutrients were influenced by sample salinity, latitude, land use, and site type. DON represented >30% of the groundwater N pool. STEs, at the global scale, produced DIN and DIP, but reduced DON concentrations in groundwater nutrients, resulting in higher DIN and DIP fluxes, but lower DON fluxes in fresh SGD to the global ocean. Total SGD fluxes of DIN and DON were estimated to be higher than riverine fluxes to the ocean, but DIP fluxes from total SGD were half the riverine input. Overall, this dissertation reveals the importance of STE biogeochemical processes on exchanges of nutrients along the land-ocean continuum from groundwater to the coastal ocean.

The Fate and Transport of Nitrogen in Subterranean Estuaries

Chapter 1. Introduction

Nitrogen (N) is a limiting nutrient in many marine systems, including coastal estuaries (Nixon, 1995). Increased nutrient loading to estuarine and coastal ecosystems, adjacent to which 40% of the human population resides, can cause eutrophication, harmful algal blooms, and oxygen depleted dead zones (Nixon, 1995; Howarth, 2008). There are several sources of N to coastal zones including watersheds, rivers, surface water runoff, and groundwater; however, of these sources groundwater is the most poorly constrained (Leote *et al.*, 2008; Moore, 2009). The impact of groundwater derived N on coastal waters will depend on its concentration and speciation, which determine its fate in the environment.

At the coastline, meteoric groundwater is advected upward and mixes with intruding seawater in subterranean estuaries (STEs, Figure 1) (Moore, 1999). A portion of the mixed fresh groundwater and saline, recirculated seawater formed in STEs, flows to the coastal ocean as submarine groundwater discharge (SGD) (Slomp and Cappellen, 2004; Boehm *et al.*, 2006; Burnett *et al.*, 2006; Hays and Ullman, 2007; Beck *et al.*, 2016). STEs form in a variety of coastal environments around the world including sandy shorelines, mangrove dominated ecosystems, coral reefs, and lava tubes (Moore, 1999, 2009; Burnett *et al.*, 2006; Mulligan and Charette, 2006; Santos *et al.*, 2015). Despite their global presence, the role of STEs in coastal biogeochemical processing and as a source of nutrients to coastal systems is not well defined.

Nutrient budgets for coastal zones often overlook SGD, a considerable oversight as SGD nutrient fluxes are estimated to be the same order of magnitude as global riverine nutrient fluxes (Cho *et al.*, 2018). SGD nutrient fluxes often exceed riverine fluxes at the local scale (Santos *et al.*, 2021); however, our current understanding of groundwater discharge and its effects on

coastal zones are based on limited data. This is of particular concern for coastal regions already stressed by nutrient pollution, such as the tributaries of the Chesapeake Bay. Substantial discharge of N, estimated to be anywhere between 92 to 260 mmol of N per m of shoreline⁻¹ d⁻¹, may be released in SGD to tributaries of the Chesapeake Bay (Reay *et al.*, 1992; Beck *et al.*, 2016). In order to fully understand biogeochemical cycling and manage nutrient pollution along the terrestrial-aquatic transition zone, groundwater derived inputs must be accounted for (Santos *et al.*, 2021).

STEs have been recognized as highly reactive zones, which influence the fate and transport of nutrients, organic matter, and trace metals discharged in SGD to the coastal ocean (Moore, 1999, 2009; Testa *et al.*, 2002; Santos *et al.*, 2009; Beck *et al.*, 2010, 2016; Charette, 2015). STEs are also highly variable, as they are subject to a variety of abiotic factors including precipitation and recharge, waves and tidal pumping, shifts in hydraulic gradients, and hydraulic conductivity which vary over timescales from hours to decades (Robinson *et al.*, 2018). These factors are important to STE geochemistry, mixing, and the flow of SGD to the ocean.

Steep geochemical gradients are characteristic of STEs and result from the mixing of two distinct water bodies: fresh groundwater and recirculated seawater (Moore, 1999; Beck *et al.*, 2010). Seawater entering the STE is often oxic, sulfate rich, and can provide labile organic matter. In contrast, groundwater consists of meteoric waters that are often anoxic with high levels of dissolved inorganic nitrogen (DIN) from anthropogenic and natural sources. Groundwater is typically low in organic matter that can be recalcitrant and comprised partially of humic substances (O'Connor *et al.*, 2015). DIN concentrations can be up to five times higher in groundwater than in surface waters (Valiela *et al.*, 1990; Slomp and Cappellen, 2004; Beck *et al.*, 2010; Beusen, A. H. W.; Slomp, C. P.; Bouwman, 2013). Biogeochemical processing and

potential removal of N in STEs influences N concentration and speciation in SGD, which determines its availability for use by primary producers and effects eutrophication in estuaries or coastal waters.

DIN may be produced within STEs by remineralization of organic matter (Harrison, 1978; Nixon, 1981; Caffrey, 2019). Within sediment porewater, organic matter supplied from overlying seawater may be decomposed, releasing ammonium (NH_4^+). In the oxic portion of the STE, this will occur via aerobic respiration. In the anoxic portion of the STE, nitrate (NO_3^-), sulfate, iron, manganese, or carbon dioxide may serve as terminal electron acceptors for anaerobic respiration. In the oxic zone of the STE, ammonium (NH_4^+) can be oxidized to NO_3^- , whereas, in anoxic sediment NH_4^+ may accumulate (Caffrey, 2019). N released by remineralization will be subject to N processing or removal within the STE prior to discharge to the overlying water.

Gradients of salinity and dissolved oxygen (DO) will influence the processing of N in STEs. In the oxic zone, nitrification oxidizes NH_4^+ to NO_3^- . Nitrification is mediated by ammonia oxidizing archaea (AOAs), ammonia oxidizing bacteria (AOBs), nitrite oxidizing bacteria (NOB) and complete ammonia oxidizers (comammox) (Kessel *et al.*, 2015). AOAs and AOBs complete the first step of nitrification, which oxidizes NH_3 to nitrite (NO_2^-) (Slater and Capone, 2003). Both AOAs and AOBs have been observed in STEs (Santoro *et al.*, 2008; Wu *et al.*, 2021), and shifts in nitrifier community structure were related to salinity (Santoro *et al.*, 2008). NO_2^- is then oxidized to NO_3^- by nitrite oxidizing bacteria (NOB). Comammox bacteria have the ability to oxidize NH_3 to NO_3^- , mediating both steps of nitrification (Daims *et al.*, 2015; Kessel *et al.*, 2015). Nitrification is an important step in the N cycle, as it changes the form and, therefore, the availability of N to microorganisms. It may also impact the mobility of subsurface

N as NH_4^+ binds more strongly to sediments than NO_3^- (Weston *et al.*, 2010). Nitrification can also be coupled to denitrification, providing NO_3^- to microbial N removal processes at the oxic-anoxic interface for N removal as dinitrogen gas (N_2) (Jenkins and Kemp, 1984).

Within anoxic sediments DIN may be removed via denitrification or anaerobic ammonium oxidation (anammox) and released as N_2 (Herbert, 1999; Brandes *et al.*, 2007; Plummer *et al.*, 2015). Denitrification is the stepwise reduction of NO_3^- to N_2 gas mediated by denitrifying microbes. It is an important N removal pathway within some STE sediments, reducing the groundwater derived DIN load (Addy *et al.*, 2002). Anammox is the anaerobic oxidation of ammonium (NH_4^+) coupled to the reduction of nitrite (NO_2^-) to produce N_2 . The anammox process is mediated by a unique group of slow-growing microbes in the order *Brocadiales*, which are ubiquitously found in both marine and freshwater environments (Trimmer and Nicholls, 2009; Lisa *et al.*, 2014; Oshiki *et al.*, 2016). Anammox bacteria have been identified in STE sediments containing ladderane lipids, which are specific to this group (Sáenz *et al.* 2012), and via high-throughput sequencing (Wu *et al.*, 2021), indicating that anammox bacteria may also aid in groundwater DIN removal in STEs. Anammox has been identified as an important process in groundwater systems (Smith *et al.* 2015). While denitrification and anammox remove fixed N from STE sediments, dissimilatory nitrate reduction to ammonium (DNRA) reduces NO_3^- to NH_4^+ , thereby retaining N in the sediments (Giblin *et al.*, 2013).

Despite recognition of the complex biogeochemical cycling that can occur in STEs, process rates are not widely constrained, and ecological implications are not clear. When estimating nutrient export in SGD, many studies overlook the processing and removal of nutrients in STEs, which determines the effects of SGD on coastal water quality. In the face of

widespread coastal eutrophication, it is essential to account for groundwater as a source of limiting nutrients and to determine how nutrient cycling in STEs may modify inputs along the land-ocean continuum. The overarching goal of this dissertation is to examine biogeochemical cycling and transport of nutrients, specifically N, in STEs. I hypothesize that groundwater is a significant source of N to the coastal ocean and that STEs determine groundwater N concentrations and speciation in SGD. This dissertation consists of four research chapters with the following specific objectives:

Chapter 2: Temporal and spatial variations in subterranean estuary geochemical gradients and nutrient cycling rates: impacts on groundwater nutrient export to estuaries

- Assess variation in geochemical gradients, N cycling rates, and nutrient export over seasonal, spatial, and tidal scales.

Chapter 3: Geochemical factors impacting nitrifying communities in sandy sediments

- Examine STE microbial community structure, and more specifically the nitrifying community, with respect to STE geochemical gradients.

Chapter 4: Nitrification in a subterranean estuary: an ex situ and in situ method comparison determines nitrate is available for discharge

- Measure nitrification in STE sediments and compare three measurement methodologies including conservative mixing models informed by *in situ* geochemical measurements of nitrate and ammonium along the STE salinity gradient, an *in situ* tracer experiment with a ^{15}N -ammonium injection, and *ex situ* sediment slurry incubations amended with ^{15}N -labeled ammonium.

Chapter 5: Subterranean estuaries modify fresh and saline submarine groundwater fluxes to the global ocean

- Characterize groundwater nutrient concentration and speciation with salinity, site lithology, and land-use in a meta-dataset including 216 sites from around the world, determine the role STEs play in biogeochemical cycling at the land-ocean interface with conservative mixing model analysis, and calculate nutrient export via submarine groundwater discharge to the global ocean.

1.1. References

- Addy, K., Kellogg, D.Q., Gold, A.J., Groffman, P.M., Ferendo, G., and Sawyer, C. (2002) In Situ Push–Pull Method to Determine Ground Water Denitrification in Riparian Zones. *J Environ Qual* **31**: 1017–1024.
- Beck, A.J., Cochran, J.K., and Sañudo-Wilhelmy, S.A. (2010) The distribution and speciation of dissolved trace metals in a shallow subterranean estuary. *Mar Chem* **121**: 145–146.
- Beck, A.J., Kellum, A.A., Luek, J.L., and Cochran, M.A. (2016) Chemical Flux Associated with Spatially and Temporally Variable Submarine Groundwater Discharge , and Chemical Modification in the Subterranean Estuary at Gloucester Point , VA (USA). *Estuaries and Coasts* **39**: 1–12.
- Beusen, A. H. W. ; Slomp, C. P.; Bouwman, A.F. (2013) Global land – ocean linkage : direct inputs of nitrogen to coastal waters via submarine groundwater discharge. *Environ Res Lett* **8**.
- Boehm, A.B., Paytan, A., Shellenbarger, G.G., and Davis, K.A. (2006) Composition and flux of groundwater from a California beach aquifer: Implications for nutrient supply to the surf zone. *Cont Shelf Res* **26**: 269–282.
- Brandes, J.A., Devol, A.H., and Deutsch, C. (2007) New Developments in the Marine Nitrogen Cycle. *Chem Rev* 577–589.
- Burnett, W.C., Aggarwal, P.K., Aureli, A., Bokuniewicz, H., Cable, J.E., Charette, M.A., et al. (2006) Quantifying submarine groundwater discharge in the coastal zone via multiple methods. *Sci Total Environ* **367**: 498–543.
- Caffrey, J.M. (2019) Spatial and Seasonal Patterns in Sediment Nitrogen Remineralization and Ammonium Concentrations in San Francisco Bay , California. *Estuaries* **18**: 219–233.
- Charette, M.A. (2015) Nitrogen Biogeochemistry of Submarine Groundwater Discharge.
- Cho, H.M., Kim, G., Kwon, E.Y., Moosdorf, N., Garcia-Orellana, J., and Santos, I.R. (2018) Radium tracing nutrient inputs through submarine groundwater discharge in the global ocean. *Sci Rep* **8**: 1–7.
- Daims, H., Lebedeva, E. V., Pjevac, P., Han, P., Herbold, C., Albertsen, M., et al. (2015) Complete nitrification by *Nitrospira* bacteria. *Nature* **528**: 504–509.
- Giblin, A.E., Tobias, C.R., Song, B., Weston, N., and Banta, G.T. (2013) The Importance of Dissimilatory Nitrate Reduction to Ammonium (DNRA) in the Nitrogen Cycle of Coastal Ecosystems. *Oceanography*.
- Harrison, W.G. (1978) Experimental measurement of nitrogen remineralization in coastal waters. *Limnol Oceanogr*.
- Hays, R. and Ullman, W.J. (2007) Dissolved Nutrient Fluxes through a Sandy Estuarine Beachface (Cape Henlopen , Delaware , U.S.A.): Contributions from Fresh Groundwater Discharge , Seawater Recycling , and Diagenesis. *Estuaries and Coasts* **30**: 710–724.
- Herbert, R.A. (1999) Nitrogen cycling in coastal marine ecosystems. *FEMS Microbiol Rev* 563–590.
- Howarth, R.W. (2008) Coastal nitrogen pollution: A review of sources and trends globally and regionally. *Harmful Algae* **8**: 14–20.
- Jenkins, M.C. and Kemp, W.M. (1984) The coupling of nitrification and denitrification in two estuarine sediments. *Limnol Oceanogr* **29**: 609–619.
- Kessel, M.A.H.J. Van, Speth, D.R., Albertsen, M., Nielsen, P.H., Camp, H.J.M.O. Den, Kartal, B., et al. (2015) Complete nitrification by a single microorganism. *Nature* **528**: 555–559.

- Leote, C., Iba, Æ.J.S., and Rocha, C. (2008) Submarine Groundwater Discharge as a nitrogen source to the Ria Formosa studied with seepage meters. *Biogeochemistry* **88**: 185–194.
- Lisa, J.A., Song, B., Tobias, C.R., and Duernberger, K.A. (2014) Impacts of freshwater flushing on anammox community structure and activities in the New River Estuary, USA. *Aquat Microb Ecol* **72**: 17–31.
- Moore, W.S. (2009) The Effect of Submarine Groundwater Discharge on the Ocean. *Ann Rev Mar Sci* **2**: 59–88.
- Moore, W.S. (1999) The subterranean estuary: A reaction zone of ground water and sea water. *Mar Chem* **65**: 111–125.
- Mulligan, A.E. and Charette, M.A. (2006) Intercomparison of submarine groundwater discharge estimates from a sandy unconfined aquifer. *J Hydrol* **327**: 411–425.
- Nixon, S.W. (1995) Coastal marine eutrophication: A definition, social causes, and future concerns. *Ophelia* **41**: 199–219.
- Nixon, S.W. (1981) Remineralization and Nutrient Cyclign in Coastal Marine Ecosystems. *Estuaries Nutr.*
- O'Connor, A.E., Luek, J.L., Mcintosh, H., and Beck, A.J. (2015) Geochemistry of redox-sensitive trace elements in a shallow subterranean estuary. *Mar Chem* **172**: 70–81.
- Oshiki, M., Satoh, H., and Okabe, S. (2016) Ecology and physiology of anaerobic ammonium oxidizing bacteria. *Environ Microbiol.*
- Plummer, P., Tobias, C., and Cady, D. (2015) Nitrogen reduction pathways in estuarine sediments: Influences of organic carbon and sulfide. *J Geophys Res Biogeosciences* **120**.
- Reay, W.G., Gallagher, D.L., and Simmons Jr., G.M. (1992) Groundwater discharge and its impact on surface water quality in a Chesapeake Bay inlet. *JAWRA J Am Water Resour Assoc* **28**: 1121–1134.
- Robinson, C.E., Xin, P., Santos, I.R., Charette, M.A., Li, L., and Barry, D.A. (2018) Groundwater dynamics in subterranean estuaries of coastal unconfined aquifers : Controls on submarine groundwater discharge and chemical inputs to the ocean. *Adv Water Resour* **115**: 315–331.
- Sáenz, J.P., Hopmans, E.C., Rogers, D., Henderson, P.B., Charette, M.A., Schouten, S., et al. (2012) Distribution of anaerobic ammonia-oxidizing bacteria in a subterranean estuary. *Mar Chem* **136–137**: 7–13.
- Santoro, A.E., Francis, C.A., De Sieyes, N.R., and Boehm, A.B. (2008) Shifts in the relative abundance of ammonia-oxidizing bacteria and archaea across physicochemical gradients in a subterranean estuary. *Environ Microbiol* **10**: 1068–1079.
- Santos, I.R., Burnett, W.C., Chanton, J., Mwashote, B., Suryaputra, A., Dittmar, T., et al. (2015) Nutrient in a Gulf of Mexico subterranean and groundwater- estuary biogeochemistry derived fluxes to the coastal ocean. *Limnol Oceanogr* **53**: 705–718.
- Santos, I.R., Burnett, W.C., Dittmar, T., Suryaputra, I.G.N.A., and Chanton, J. (2009) Tidal pumping drives nutrient and dissolved organic matter dynamics in a Gulf of Mexico subterranean estuary. *Geochim Cosmochim Acta* **73**: 1325–1339.
- Santos, I.R., Chen, X., Lecher, A., Sawyer, A., Moosdorf, N., Rondellas, V., et al. (2021) Submarine groundwater discharge impacts on coastal nutrient biogeochemistry. *Nat Rev Earth Environ* 108–119.
- Slater, J.M. and Capone, D.G. (2003) Denitrification in aquifer soil and nearshore marine sediments influenced by groundwater nitrate. *Deep Sea Res Part B Oceanogr Lit Rev* **34**: 1041.

- Slomp, C.P. and Cappellen, P. Van (2004) Nutrient inputs to the coastal ocean through submarine groundwater discharge : controls and potential impact. *J Hydrol* **295**: 64–86.
- Smith, R.L., Böhlke, J.K., Song, B., and Tobias, C.R. (2015) Role of Anaerobic Ammonium Oxidation (Anammox) in Nitrogen Removal from a Freshwater Aquifer. *Environ Sci Technol* **49**: 12169–12177.
- Testa, J.M., Charette, M.A., Sholkovitz, E.R., Allen, M.C., Rago, A., and Herbold, C.W. (2002) Dissolved iron cycling in the subterranean estuary of a coastal bay: Waquoit Bay, Massachusetts. *Biol Bull* **203**: 255–256.
- Trimmer, M. and Nicholls, J.C. (2009) Production of nitrogen gas via anammox and denitrification in intact sediment cores along a continental shelf to slope transect in the North Atlantic. *Limnol Oceanogr* **54**: 577–589.
- Valiela, I., Costa, J., Foreman, K., Teal, J.M., Howes, B., and Aubrey, D. (1990) Transport of groundwater-borne nutrients from watersheds and their effects on coastal waters. *Biogeochemistry* **10**: 177–197.
- Weston, N.B., Giblin, A.E., Banta, G.T., Hopkinson, C.S., and Tucker, J. (2010) The Effects of Varying Salinity on Ammonium Exchange in Estuarine Sediments of the Parker River, Massachusetts. *Estuaries and Coasts* **33**: 985–1003.
- Wu, J., Hong, Y., Wilson, S.J., and Song, B. (2021) Microbial nitrogen loss by coupled nitrification to denitrification and anammox in a permeable subterranean estuary at Gloucester Point , Virginia. *Mar Pollut Bull* **168**:

1.2. Figures

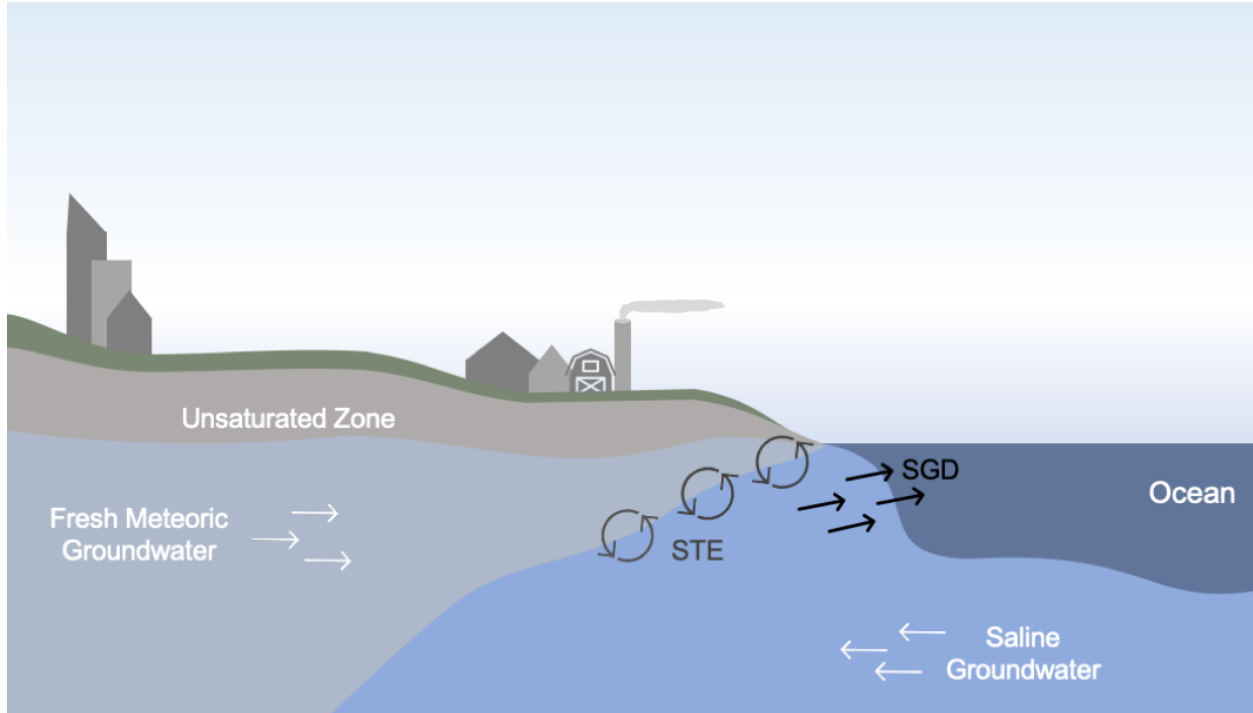


Figure 1. Conceptual diagram exhibiting the flow of fresh, terrestrial groundwater meeting and mixing with saline groundwater and recirculated seawater in the subterranean estuary (STE). The mixture of fresh and saline water that forms in the STE is then released to the ocean as submarine groundwater discharge (SGD).

Chapter 2. Temporal and Spatial Variations in Subterranean Estuary Geochemical Gradients and Nutrient Cycling Rates: Impacts on Groundwater Nutrient Export to Estuaries

2.1. Abstract

Subterranean estuaries (STEs) form at the land-sea boundary where groundwater and seawater mix. These biogeochemically reactive zones influence groundwater-borne nutrient concentrations and speciation prior to export via submarine groundwater discharge (SGD). We examined a STE located along the York River Estuary (YRE), VA to determine if SGD delivers dissolved inorganic nitrogen (DIN) and phosphorus (DIP) to the overlying York River. We assessed variations in STE geochemical profiles with depth across locations, times and tidal stages, estimated N removal along the STE flow path, measured hydraulic gradients to estimate SGD, and calculated potential nutrient fluxes to the YRE. Salinity, dissolved oxygen (DO), DIN, and DIP varied with depth and season ($p < 0.05$), but not location or tidal stage. Ammonium dominated DIN deep in the STE. Moving toward the sediment surface, ammonium concentrations decreased as nitrate and DO concentrations increased, suggesting nitrification. Potential sediment N removal rates were $< 8 \text{ mmol N m}^{-2} \text{ d}^{-1}$. The total groundwater discharge rate was $34.1 \pm 8.4 \text{ L m}^{-2} \text{ d}^{-1}$; discharge followed tidal and seasonal patterns. SGD fluxes estimated with the 50 cm endmember ranged from 0.32 to 16.00 $\text{mmol m}^{-2} \text{ d}^{-1}$ and from 0.02 to 0.15 $\text{mmol m}^{-2} \text{ d}^{-1}$ for DIN and DIP, respectively. However, microbial N removal in the STE showed the potential to attenuate 3-100% of the DIN export. SGD fluxes were on the same order of magnitude as benthic fluxes, but accounted for $< 10\%$ of the nutrients delivered by net tidal advection in the YRE. Our results indicate the importance of accounting for biogeochemical

transformations in STEs when estimating SGD fluxes and their role in coastal eutrophication and biogeochemistry.

2.2. Introduction

Subterranean estuaries (STEs) form at the coastline where groundwater and seawater mix forming steep geochemical gradients (Moore, 1999). STEs, which are recognized as highly reactive zones for biogeochemical processing, influence the fate and transport of nutrients, organic matter, and trace metals discharged to the coastal ocean via groundwater (Moore, 1999, 2009; Santos *et al.*, 2009, 2021). Seawater entering the STE is sulfate rich, typically oxic, and can provide labile dissolved organic matter (Slomp and Cappellen, 2004). In contrast, groundwater is generally anoxic, accumulates high levels of dissolved inorganic nitrogen (DIN) and phosphorus (DIP) from anthropogenic and natural sources along its flow path, and typically has recalcitrant organic matter and high concentrations of dissolved inorganic carbon (DIC) (Valiela *et al.*, 1990; Slomp and Cappellen, 2004; Santos *et al.*, 2021). DIN concentrations in groundwater can be up to five times higher than concentrations in surface waters (Valiela *et al.*, 1990; Slomp and Cappellen, 2004).

Nitrogen (N) and phosphorus (P) are both limiting nutrients in marine systems and most mid-Atlantic coastal estuaries are N limited (Nixon, 1995). There are several sources of N to coastal zones including drainage from the surrounding watersheds, rivers, surface water runoff, anthropogenic sources, and submarine groundwater discharge (SGD); however, of these sources SGD is the most poorly constrained (Leote *et al.*, 2008; Moore, 2009). SGD is a mixture of groundwater and recirculated seawater that is released from STEs to overlying water (Slomp and Cappellen, 2004; Boehm *et al.*, 2006; Burnett *et al.*, 2006). Nutrient budgets for coastal zones

often overlook SGD (Santos *et al.*, 2021), which may be a considerable oversight as Cho *et al.* (2018) estimated that SGD discharges 2.3 ± 0.6 Tmol DIN yr⁻¹ and 0.06 ± 0.02 Tmol DIP yr⁻¹ to the global ocean, a flux on the same order of magnitude as that from rivers globally. SGD derived nutrients have also been shown to support primary production in a variety of coastal systems including oceanic islands (Kim *et al.*, 2011), coastal embayments (Zhang *et al.*, 2020), lagoons (Andrisoa *et al.*, 2019), and estuaries (Guo *et al.*, 2020). This is of particular concern for coastal regions already at risk for nutrient pollution and although measurements of groundwater nutrient inputs are becoming more common, they often remain unaccounted for in regional nutrient budgets (Lake and Brush, 2015; Santos *et al.* 2021).

Microbial processes in STEs influence the concentration and speciation of N in SGD, which may support potential phytoplankton blooms and further microbial N cycling upon discharge to receiving waters (Figure 1). It is common, with a few exceptions (Kroeger and Charette, 2012), to ignore biogeochemical transformations that may attenuate or alter the species of N associated with SGD. Fluxes are commonly calculated as the product of the endmember concentration and a water flux with no attenuation along the flow path, which could cause overestimations of nutrient export via SGD. Transformations that change speciation are equally important as they have implications for N mobility in the subsurface, the fate of N after discharge, and influence the assemblage of primary producers present in overlying water.

Processes including nitrification, denitrification, anaerobic ammonium oxidation (anammox), dissimilatory nitrate reduction to ammonia (DNRA), mineralization, and microbial N assimilation all influence the groundwater N pool. When oxygen is available, nitrification oxidizes ammonium (NH₄⁺) to nitrate (NO₃⁻). Nitrification acts as a gateway to N removal processes such as denitrification and anammox (Brandes *et al.* 2007; Herbert 1999).

Denitrification is the enzymatically mediated stepwise reduction of NO_3^- to NO_2^- , NO , N_2O , and finally to N_2 gas. In anoxic STEs, denitrification may remove accumulated DIN in groundwater (Tobias *et al.*, 2001; Addy *et al.*, 2002). Anammox is the anaerobic oxidation of ammonium (NH_4^+) coupled to the reduction of nitrite (NO_2^-) to produce N_2 . This process has been observed in both marine and freshwater environments (Lisa *et al.* 2014; Oshiki *et al.* 2016; Nicholls and Trimmer 2009) and is important to N removal in some groundwater systems (Sáenz *et al.*, 2012; Smith *et al.*, 2015). DIP cycling in STEs is usually dominated by abiotic processes; such as sorption to iron or manganese oxides (Charette and Sholkovitz 2002; Spiteri *et al.* 2008; Spiteri *et al.* 2008) or co-precipitation with calcium carbonate (Cable *et al.* 2002). Sorption and precipitation immobilize DIP within the sediment, limiting its release in SGD, and increasing the N:P ratio of SGD. This was shown in a recent review of 239 SGD studies that reported DIN:DIP ratios were higher than Redfield (16:1) in 75% of the included observations (Santos *et al.*, 2021).

In the face of widespread coastal eutrophication, it is important to constrain the fluxes of N and P in coastal zones. The potential for discharge of nutrients in SGD will vary over space and time as temperature, groundwater discharge, nutrient concentrations, and cycling rates vary. Determining how nutrient cycling in STEs may modify inputs of N along the land-ocean continuum will further our understanding of coastal nutrient cycling. This is especially important to the Chesapeake Bay and its tributaries, where it has been hypothesized that excess nutrient inputs contribute to the formation of annual hypoxic zones and harmful algal blooms (HABs) (Anderson *et al.* 2002; Mulholland *et al.* 2009; Reay 2009). Nutrient inputs to the Chesapeake Bay from river tributaries, runoff, and meteoric groundwater have been estimated, but SGD inputs remain unconstrained. Meteoric groundwater estimates only include the freshwater portion of groundwater that flows into the bay, whereas SGD is a mixture of recirculated

seawater and meteoric water formed in STEs. SGD has the potential to be a far larger source of nutrients than meteoric groundwater due to advection of porewater with high concentrations of DIN and DIP (Santos *et al.*, 2021). The goal of this study was to examine the effects of variations in STE geochemistry and microbial N processing rates on potential nutrient discharge to the YRE, a tributary of the Chesapeake Bay, and to determine the importance of SGD derived nutrients when compared to other sources. We hypothesized that the STE is a significant source of nutrients to the overlying water compared to down river and benthic fluxes. The specific objectives were to 1) characterize geochemical gradients in the STE with depth across location and time to determine the scales over which SGD should be quantified, 2) to measure potential N removal rates to assess the importance of microbial attenuation along the groundwater flowpath, and 3) to calculate potential fluxes to the overlying water and compare them to other sources of nutrients in the lower YRE.

2.3. Methods

2.3.1. Study site description

The Gloucester Point STE (GP-STE) is located near the mouth of the YRE in Virginia, USA (37.248884 N, 76.505324 W) (Figure 2A). The YRE, a microtidal and partially mixed tributary of the Chesapeake Bay, is roughly 52 km long from West Point (the confluence of the Pamunkey and Mattaponi rivers, YRE tributaries) to its mouth at Goodwin Island (Reay, 2009). Land use surrounding the YRE is primarily forested (61%), but is suburban adjacent to our study site (Reay, 2009). The Gloucester Point beach is a sandy sediment beach with a tidal range of ~0.8 m; it stretches about 20-30 m across and has constructed jetties at each end. A detailed site description of the GP-STE can be found in Beck *et al.* (2016).

2.3.2. Experimental design

A network of dedicated piezometers (Charette *et al.*, 2006) consisting of 2 cm screens (AMS Gas Vapor Tip) attached to FEP tubing (VersilOn, Saint-Gobain), was constructed at the Gloucester Point beach with depths ranging from 0-300 cm along the mid-tide line. Porewater and sediment were sampled to assess variability across location and time (Figure 2B). To examine seasonal variation in geochemical gradients and N process rates, STE porewater and sediment vibracores were collected in spring 2018, summer 2018, fall 2018, and winter 2019. To assess the variation throughout tidal cycles, porewater was sampled during two spring tides in the spring and summer of 2020 at three tidal stages (low, mid, and high). Spatial variability in geochemical gradients was examined in three profiles (0-120 cm), each three meters apart, which were sampled once at low tide in spring 2020.

2.3.3. Seasonal porewater geochemical monitoring

Porewater samples were collected at low tide during each season (spring, summer, fall, winter) from piezometers placed at depths from 0-300 cm. Masterflex C-Flex L/S Precision Pump tubing (Cole-Palmer) was attached to piezometer tubing and porewater slowly pumped from the ground with an Alexis V3.0 peristaltic pump (Proactive Environmental Products). Salinity, pH, and temperature were measured in a flow-through cell on a YSI sonde (600XL); during sample collection the flow-through cell was placed before the pump to reduce introduction of oxygen by pumping. Dissolved oxygen (DO) was measured with either a YSI (600XL) or a HACH (HQ40d meter with LDO101 Luminescent/Optical DO sensor). Samples for nutrient analyses were filtered with a 0.45 μM disposable groundwater filter capsule (Millipore Sigma) immediately placed on ice, transported to the lab and frozen until analysis. Porewater analyses included: DIN, DIC, PO_4^{2-} , dissolved organic carbon (DOC), and sulfide (H_2S). DIN (NO_3^- , NO_2^- , and NH_4^+) and PO_4^{2-} concentrations were determined on a Lachat autoanalyzer (Lachat Instruments, Lachat

QuikChem FIA+ 8000). DIC samples were collected unfiltered in 12 mL exetainer vials (Labco) containing 1.2 μL of saturated HgCl_2 solution and analyzed within 30 days of collection with an Apollo AS-C3 analyzer with a LiCor 7000 infrared CO_2 analyzer. DOC samples were filtered into pre-combusted (500 $^\circ\text{C}$ for 5hr) scintillation vials, stored frozen, and analyzed on a Shimadzu TOC-Vcsn analyzer. Sulfide samples were collected, filtered with 0.45 μM Puradisc membrane syringe filters (GE Healthcare Life Sciences), into 0.1 M Zinc acetate preventing exposure to air. In the lab sulfide samples were quantified spectrophotometrically (Shimadzu UV-1800) as described by Hines et al. (1989).

2.3.4. Spatial and tidal porewater geochemical monitoring

To assess spatial variability, three porewater profiles were collected from six depths (0, 20, 50, 70, 100, and 120 cm) during low tide. Tidal variability samples were collected from one porewater profile (6 depths: 0, 20, 50, 70, 100, and 120 cm) at the mid-tide line, sampled at three tidal stages, during two tidal cycles (May and June 2020). Salinity, temperature, DO, DIN, PO_4^{2-} , and DIC were collected and analyzed as previously described.

2.3.5. Potential N removal rate incubations

A vibracore was used to collect sediment from the STE at the mid-tide line adjacent to the dedicated piezometers. Cores were collected during seasonal sampling efforts (spring, summer, fall, winter) resulting in four cores, each 110 cm in length. Cores were sectioned at 10 cm intervals and sections were homogenized. Approximately 1 g of the composited sediment from each 10 cm section was used in sediment slurry incubation experiments to measure denitrification and anammox rates. Samples were incubated for 6, 12, or 24 hours in sealed, helium flushed 12 mL exetainer vials (Labco). Denitrification rate incubations were amended with 100 nmoles $^{15}\text{NO}_3^-$ (99 atm%, Cambridge Isotope Laboratories, Inc.), and $^{29,30}\text{N}_2$ products

were measured using a gas bench isotope ratio mass spectrometer (IRMS, Delta V Plus, Thermo Fisher Scientific, Waltham, MA). To measure potential anammox rates, 500 nmoles of $^{15}\text{NH}_4^+$ (99 atm%, Cambridge Isotope Laboratories, Inc.) and 100 nmoles $^{14}\text{NO}_2^-$ were added to the sediment slurries; the production of $^{29}\text{N}_2$ was measured by IRMS. N_2 production rates were calculated using the methods described by Song and Tobias (2011). All incubations were conducted in duplicate.

2.3.6. Darcy discharge calculations

Three pressure transducer wells were constructed out of PVC with 10 cm of slotted PVC centered at 50, 70 and 100 cm depths along the mid-tide line and one at 100 cm depth along the low tide line (Figure 2B). An additional pressure transducer was installed to measure barometric pressure in a dry well above the dune line. Pressure measurements were recorded every fifteen minutes; well water level was calibrated with manual measurements at logger deployment and collection. Darcy discharge was calculated using equation (1) shown below:

$$q = -K_{h,v} \frac{dh}{dx,z} \quad (\text{Equation 1})$$

Where q is the specific groundwater discharge, $K_{h,v}$ is the hydraulic conductivity (horizontal or vertical), h is the hydraulic head determined by pressure transducer data, and (dx) is horizontal distance between two wells positioned normal to the shoreline and (dz) is the vertical distance between two wells at different depths at the same location. Hydraulic conductivity (K_h) of GP-STE sediment was $K_h = 0.0001$ cm/s, measured with repeated slug tests ($n=2$) in the 50 cm well, which aligns with the value reported by Reay (2009) and used by Beck et al. (2016) at this site. This hydraulic conductivity also falls within the range of values reported for medium to coarse grained sand (Domenico and Schwartz 1990). The vertical hydraulic conductivity was assumed to be $0.1 \times K_h$ ($K_v = 0.00001$ cm/s) to account for sediment anisotropy (Tobias et al. 2001).

Horizontal discharge was calculated using the hydraulic head differences between pressure transducers at 100 cm depth in the wells at the mid-tide and the low-tide lines. Vertical discharge was calculated using hydraulic head differences between the 100, 70, and 50 cm pressure transducer wells at the mid-tide line. For each measurement within a sampled month, the discharge in each direction was calculated (equation 1). The total groundwater discharge was assumed to be the sum of the horizontal and vertical discharge (Tobias et al. 2001). Discharge rates were calculated from head measurements made at 15-minute intervals and were averaged for each month sampled resulting in an average total discharge for spring, summer, and fall of 2018, winter of 2019, and spring and summer of 2020. Discharge was compared to tidal height fluctuations collected by the Virginia Estuarine and Coastal Observing System (VECOS) from the Gloucester Point (GP) Continuous Monitoring station.

2.3.7. Potential discharge of nutrients in SGD to the overlying water

Potential fluxes of DIN ($\text{NO}_3^- + \text{NO}_2^- + \text{NH}_4^+$), and PO_4^{2-} in SGD to the overlying water were calculated using the SGD rate determined by equation 1 and the STE endmember nutrient concentration. Calculations were performed as described by Beck et al. (2016) using equation 2:

$$F = C_{gw} * Y \quad (\text{Equation 2})$$

where F is the nutrient flux to the overlying water, C_{gw} is the endmember concentration determined each season, and Y is the average total SGD rate for the sampled month.

Two endmember concentrations (C_{gw}) were used to determine potential fluxes from the GP-STE including a deep, fresh groundwater endmember (300cm), a shallow groundwater endmember (50cm). The deep endmember represents the DIN and PO_4^{2-} concentrations in low salinity (salinity < 5) groundwater that, if transported non-conservatively, would be exported to the overlying York River. The shallow endmember concentration (50 cm) represents the top of

the STE mixing zone, which represents the salinity of SGD collected in seepage meters at this site by Beck et al. (2016). Beck et al. (2016) and Kroeger et al. (2007), another study conducted along another tributary of the Chesapeake Bay, used 50 cm as their SGD endmember, assuming the concentrations at this depth to be representative of the concentration of solutes in SGD, which have already undergone biogeochemical transformations.

To account for N removal via denitrification in the GP-STE prior to discharge, two N removal scenarios were considered. The first scenario assumes denitrification only occurred in the anoxic zone of the STE; depths where $DO < 5$ mg/L (Anoxic DNF). The second scenario accounts for total potential N removal throughout the STE profile; observed potential N removal rates observed in both the oxic and anoxic zones, to account for denitrification that may be occurring in microsites or small anoxic patches throughout the STE profile (Total DNF). These scenarios were applied to the shallow endmember concentration as a percent reduction, which was derived from the potential rate measurements in sediment slurry incubation experiments (Section 2.3.5.).

2.3.8. Statistical analyses

We assessed the effect of season, tidal stage, site, and depth on porewater geochemical parameters (salinity, dissolved oxygen, NO_3^- , NH_4^+ , DIP, and DIC concentrations) using multiple analysis of variance (ANOVA). The ANOVA included fixed effects of season (spring, summer, fall, and winter), tidal stage (low tide, mid tide, high tide), location across the beach (profile A, B, and C), and depth. A post-hoc Tukey multiple comparisons of means was used to determine how geochemical parameters varied across these scales with 95% confidence intervals. The same statistical methodology was used to assess the fixed effect of season and month of total groundwater discharge as well as the effect of season on STE sediment denitrification and

anammox rates. Pearson correlation was used to assess relationships between geochemical analytes in the STE. All statistical analyses were conducted in R (version 3.2.2. Copyright 2015 The R Foundation for Statistical Computing) and the significance level for all statistical tests was $\alpha = 0.05$.

2.4. Results

2.4.1. Seasonal variation in STE porewater geochemical profiles

Porewater salinity varied with season and depth (p -value < 0.05 , Table S1); in all seasons, salinity decreased with depth (Figure 3A). Overlying water (0 cm, York River water) salinity ranged from 9.69 to 18.68 across all seasons; the lowest salinity in overlying water coincided with the highest precipitation in the area during summer 2018. Salinity across seasons ranged from 8.97 to 18.79 at the 50 cm well and 2.51 to 2.75 at the deepest (300 cm) well.

Porewater DO concentrations varied with season and depth (p -value < 0.05 , Table S1). Porewater DO concentrations ranged from 0.00 to 13.18 mg/L in the STE and decreased with depth in all seasons (Figure 3B). The highest DO concentrations were observed in the top 0-50 cm of the STE, followed by a decrease from 50 to 100 cm; below 100 cm porewater concentrations were consistently $< 5 \text{ mg L}^{-1}$.

Concentrations of NH_4^+ varied with depth (p -value < 0.05) in the STE, but not with season. From 0 to 100 cm, NH_4^+ concentrations were always $< 20 \text{ } \mu\text{M}$, but increased with depth below 100 cm (Figure 3D). Concentrations of NO_3^- ranged from 25 to 70 μM at depths from 40 to 100 cm; whereas below 110 concentrations were $< 5 \text{ } \mu\text{M}$ (Figure 3C). Season and depth both had a significant effect on porewater NO_3^- concentrations (p -value < 0.05 , Table S1). NO_2^- concentrations in the STE were always lower than 1.7 μM in all depths and seasons (Figure S1).

Porewater PO_4^{2-} and DIC concentrations increased with depth in all seasons (Figure 3E and 3G). PO_4^{2-} concentrations ranged from 0.16 to 15.76 μM and DIC concentrations ranged from 2 to 6 mM. Both season and depth had significant effects (p -value < 0.05) on PO_4^{2-} and DIC. H_2S concentrations increased with depth in every season (Figure 3F), varying from 0 to 3500 μM . DOC concentrations in STE porewater ranged from 250 to 1500 μM (Figure 3H). There was a consistent pattern observed in each season sampled; elevated DOC concentrations ($> 400 \mu\text{M}$) were observed from roughly 80 to 250 cm.

2.4.2. Spatial and tidal variation in STE porewater geochemical profiles

Spatial variability of porewater geochemical characteristics was evaluated by sampling three profiles along the mid-tide line of the beach (Figure 4). Profiles of salinity, DO, DIN, PO_4^{2-} , and DIC all showed similar trends to those observed during seasonal sampling and variations observed with site across the beach face were not statistically different (p -value > 0.05 , Table S1). Porewater geochemical variation was also examined throughout two tidal stages for salinity, DO, DIN, DIP, and DIC; profiles exhibited similar patterns as those observed during seasonal and spatial surveys (Figure 5). All analytes had similar concentrations and patterns with depth across tidal stages (p -value > 0.05 , Table S1).

All porewater samples (seasonal, spatial, and tidal) were combined to assess correlations between geochemical analytes (Figure S5, Table S2). There was a negative correlation between porewater salinity and NH_4^+ (p -value < 0.05) and a positive correlation between salinity and NO_3^- (p -value < 0.05). NH_4^+ and NO_3^- concentrations exhibited a negative correlation (p -value < 0.05). Porewater salinity had a positive correlation with DO; correlation coefficient = 0.78 (p -value < 0.05), but was negatively correlated with PO_4^{2-} and DIC; (p -value < 0.05). Porewater

DIC and DIP had a strong positive correlation (Pearson coefficient = 0.93, p-value < 0.05). DIC also had a positive correlation with porewater NH_4^+ concentrations (p-value < 0.05).

2.4.3. Seasonal potential N removal rates

In all seasons and depths sampled, potential anammox rates were $<0.05 \text{ mmol N m}^{-2} \text{ day}^{-1}$ and denitrification rates ranged from 0 to $2.48 \text{ mmol N m}^{-2} \text{ day}^{-1}$ (Table 1). The highest rates of denitrification were observed in fall 2018; lowest rates were observed in spring 2018 (Table S1, p-value > 0.05). In all seasons the highest rates of denitrification were observed in surficial sediment (0-50 cm).

2.4.4. Darcy discharge calculations

Horizontal discharge averaged for each of the sampled months ranged from 14.1 to $22.4 \text{ L m}^{-2} \text{ day}^{-1}$ and the average vertical discharge ranged from -3.8 to $62.5 \text{ L m}^{-2} \text{ day}^{-1}$ (Table 2). Negative vertical discharge rates were observed periodically in winter 2019 and spring 2020, this is consistent with a change in the direction of the vertical hydraulic gradient, indicative of recharge. The average total groundwater discharge ranged from 19.0 to $81.5 \text{ L m}^{-2} \text{ day}^{-1}$; highest discharge rates were observed during summer and the lowest in winter (Table 2, p-value < 0.05). The magnitude of the vertical and horizontal gradients and, therefore, total groundwater discharge fluctuated with season and tide; lower discharge rates were observed at high tide and the highest discharge was observed in Summer (Figures S6 and S7).

2.4.5. SGD nutrient flux calculations

Calculated fluxes of DIN and PO_4^{2-} from the GP-STE to overlying water are shown in Table 3. The SGD DIN fluxes calculated using the deep, groundwater endmember ranged from 3.45 ± 0.02 to $16.00 \pm 0.07 \text{ mmol m}^{-2} \text{ day}^{-1}$. PO_4^{2-} fluxes estimated with the deep endmember ranged from 0.28 ± 0.002 and $1.28 \pm 0.006 \text{ mmol m}^{-2} \text{ day}^{-1}$. The shallow endmember (50 cm) fluxes of

DIN ranged from 0.32 ± 0.001 to 3.36 ± 0.015 mmol m⁻² day⁻¹. The lowest and highest DIN fluxes were observed in spring and summer respectively (Table S3, p-value < 0.05). The groundwater PO₄²⁻ flux calculated with the shallow endmember (50 cm) ranged from 0.01 ± 0.0001 (spring) to 0.15 ± 0.0007 (summer) mmol m⁻² day⁻¹.

To account for potential N removal, the reduction of DIN by denitrification, as measured in sediment slurry incubations, was incorporated into flux estimations. Accounting for maximum N removal only in the anoxic zone, SGD DIN fluxes become 0.28 - 3.09 mmol m⁻² day⁻¹, reducing shallow endmember DIN fluxes 3-81%. Using the total N removal observed in both oxic and anoxic zones of the STE, fluxes of DIN become $-5.52 - 1.54$ mmol m⁻² day⁻¹, reducing the shallow endmember DIN fluxes 4 to >100%. These data suggest that the STE acts as a sink for DIN, when accounting for maximum potential N removal throughout the sediment profile, during fall and winter.

2.5. Discussion

2.5.1. Spatial and temporal variability in STE geochemical profiles

Variations in STE porewater profiles may be driven by location, sampling depth, season, and tidal stage. This variation is important in determining which C and N cycling processes are occurring in STEs and at what rates. In the GP-STE, although season and depth had significant effects on porewater salinity, DO, DIN, PO₄²⁻, and DIC, location and tidal stage did not have significant effects (Table S1). Steep geochemical gradients are common in STEs; thus, we expected to observe changes in geochemical analytes with depth. Tidal pumping has been reported as a major driver of variability in other STEs (Robinson *et al.*, 2018); however, this does not seem to be the case in the GP-STE where stability in geochemical profiles was observed across varying stages of tidal amplitude in this study and previous work (Beck *et al.* 2016).

Porewater salinity and DO profiles observed were as expected when oxic seawater mixes with advected anoxic groundwater. Our observations align with previous measurements of salinity, DO, and nutrient profiles at this site (O'Connor *et al.*, 2015; Beck *et al.*, 2016), but porewater DO penetrated deeper than has been observed in other coastal sediments (Cai and Sayles, 1996). The observed DO profile could result from wave action from passing ships in the nearby channel, and the high permeability of the sandy sediment in the lower YRE.

Groundwater supplies high concentrations of NH_4^+ (~200 μM) to the GP-STE, likely due to remineralization of organic matter during transport to the coast. Schutte *et al.* (2018) reported similar NH_4^+ concentrations with depth on Sapelo Island, GA, USA, but other east coast sites such as Waquoit Bay, MA, USA observe NO_3^- rich groundwater (Talbot *et al.*, 2003; Spiteri, Caroline P Slomp, *et al.*, 2008). As groundwater moves along its flow path and reaches the STE mixing zone, NH_4^+ concentrations decrease, coinciding with increasing NO_3^- and DO concentrations. The STE profiles and the negative correlation observed between NH_4^+ and NO_3^- concentrations suggest that the loss of NH_4^+ and production of NO_3^- is the result of nitrification. Nitrification in the surficial sediments is typical in sandy STEs (Santos *et al.*, 2021) and deep oxygen penetration has been proposed as a driver of nitrification of groundwater derived NH_4^+ in sandy systems (Schutte *et al.*, 2017); our data suggest a similar dynamic.

The profiles of PO_4^{2-} , DIC, NH_4^+ , and H_2S were typical of the GP-STE and concentrations increased with depth as previously observed (O'Connor *et al.*, 2018; Wu *et al.*, 2021). The deepest groundwater samples were enriched with PO_4^{2-} , DIC and NH_4^+ . Porewater PO_4^{2-} , DIC, and NH_4^+ were negatively correlated with salinity (Figure S5) and DIC was positively correlated with PO_4^{2-} and NH_4^+ (Figure S5), suggesting these analytes are products of remineralization. H_2S also increased with depth; deep oxygen penetration in the STE likely

drives less energetically favorable redox reactions, such as sulfate reduction, deeper into the sediments.

2.5.2. Potential N removal rates

Denitrification was the dominant microbial N removal pathway in the GP-STE; anammox rates were ubiquitously low. The observed denitrification rates were similar to those observed by Jiao *et al.* (2018) in a sandy STE in Daya Bay, China using a similar slurry incubation method, but were lower than N removal rates in some other coastal sediments (Cornwell *et al.*, 1999; Hall *et al.*, 2005). GP-STE sediments have only ~0.26% organic content (determined by combustion of dried sediment, unpublished data), which could limit denitrification rates in the STE. The organic matter that is available may also be recalcitrant; O'Connor *et al.* (2015) observed that $43 \pm 18\%$ of the total GP-STE DOC pool was comprised of humic material, indicative of low lability. Low concentrations of oxidized DIN, which is required for anammox and denitrification, in the anoxic zone of the GP-STE would also limit N removal *in-situ*. The NO_3^- profile (Figure 3C) showed no NO_3^- below 100 cm where the anoxic zone begins and NH_4^+ concentrations begin to increase.

Most calculations of SGD nutrient fluxes do not account for transformations or removal along the flow path (Charette and Buesseler, 2004; Beck *et al.*, 2016; Correa *et al.*, 2020). Our slurry incubations were performed under anoxic conditions with excess NO_3^- and, therefore, do not account for *in-situ* oxygen and substrate concentrations. However, our incubations provide potential rates under optimal conditions for these processes. Potential rates are typically considered over-estimations, but can be useful to calculate a potential “maximum” N that could be removed in the STE. Since denitrification is an anoxic process and increased oxygen availability decreases denitrification rates (Bonin and Raymond, 1990; Seitzinger *et al.*, 2006), it is likely that STE N removal would occur mainly at depths that exhibit low oxygen or anoxic

conditions. If we assume that the denitrification would not occur above 60cm, where > 5 mg/L DO is observed (Oh and Silverstein, 1999), the maximum N removal in the top 1 m^3 would be $\sim 1,507 \mu\text{moles N m}^2 \text{ day}^{-1}$. This is approximately 20% of the available NO_3^- pool in the top 1 m^3 of the STE ($\sim 7,439 \mu\text{moles N}$). The majority of the N pool, therefore, would be available for discharge to the overlying water. However, the highest potential rates of denitrification and anammox at this site were observed in surficial sediments. The surficial STE sediments are oxic, which may inhibit denitrification, but the oxic region is closer to labile organic matter provided by overlying water and it is possible that N removal is occurring in anoxic microsites or patches (Arango *et al.*, 2007). The maximum N removal in both oxic and anoxic zones of the sediment profile, would attenuate the entirety of the STE DIN pool in fall and winter result in a $\sim 80\%$ DIN pool reduction in summer and spring. The true rate of N removal in the STE is likely somewhere between this 20-100% removal. A ^{15}N labeled *in situ* tracer experiment conducted at the GP-STE indicated denitrification in surficial sediments (50 cm) of less than $0.075 \text{ mmoles N m}^{-2} \text{ d}^{-1}$ suggesting that denitrification in the oxic zone is not a major contribution *in situ* (Wilson *et al.*, in prep). However, N removal rates observed at our site have the potential to partially or fully attenuate DIN prior to discharge and it is important to incorporate this reduction into flux calculations to not overestimate DIN export via SGD.

2.5.3. Groundwater discharge

Tidal variation observed in hydraulic gradients at the GP-STE was in contrast with our geochemical profiles suggesting minimal change throughout tidal cycles during our variability study (Figures S1, S2, and Table S1). STEs are dynamic systems that, in addition to tidal and seasonal impacts, may also be influenced by landward and seaward forces (Slomp and Van Cappellen 2004). Factors such as rainfall and wave action are likely to affect groundwater flow

in the GP-STE. The flow of groundwater will, in turn, impact STE geochemistry and nutrient cycling rates, and thus STE variability.

We observed groundwater discharge to the overlying York River in all seasons. The calculated discharge rates are of the same order of magnitude as those previously estimated for the GP-STE by Beck et al 2016 (3.9 to 6.2 cm day⁻¹; i.e. 39 to 62 L m⁻² day⁻¹). Horizontal hydraulic gradients were observed consistently at the YRE STE, indicating that water was moving outward from land, but vertical hydraulic gradients varied with season. Negative vertical gradients, indicating recharge and potential movement of the seepage face, were observed periodically in winter 2019 and spring 2020. These negative vertical gradients could result from lower rainfall during the winter months leading to lower groundwater flow. Higher tidal heights observed in winter may also increase the pressure from the overlying water, decreasing groundwater flow; the reversal of hydraulic gradients in the subsurface contributes to typically high variability in STE profiles (Moore, 1999). Changes in the direction of the hydraulic gradient may also indicate a shift in the location of the discharge zone along the beach face. The period of highest groundwater discharge, Summer 2018, was also a period of high rainfall in the area suggesting that the magnitude of discharge may be dominantly controlled by seasonal watershed hydrology rather than shorter-term tidal drivers.

2.5.4. Potential nutrient fluxes

Fluxes from groundwater were calculated in several ways including using a deep endmember, assuming conservative transport of nutrients, a shallow endmember (50 cm), to represent STE mixing zone concentrations, and two scenarios that account for potential microbial N removal prior to discharge (Table 3). The deep endmember fluxes were the largest potential fluxes for DIN and PO₄²⁻ as the deep groundwater is enriched with inorganic nutrients. Using a

groundwater endmember and assuming conservative transport has traditionally been the approach for groundwater fluxes studies; however, this approach may overestimate nutrient fluxes as it does not account for microbial processing in the STE. The shallow endmember (50 cm), represents the nutrient concentrations at the top of the STE mixing zone, likely these concentrations represent nutrient concentrations post-processing, but there is still potential for N removal as SGD is discharged. Accounting for potential denitrification in the STE reduced DIN fluxes, which reinforces the importance of accounting for biogeochemical cycling along the groundwater flow path.

DIN and PO_4^{2-} fluxes were of the same order of magnitude as those previously calculated for the GP-STE and the Elizabeth River, another tributary of the Chesapeake Bay (Charette and Buesseler, 2004; Beck *et al.*, 2016). Reay and Simmons (1992) reported higher DIN discharge from groundwater to the Chesapeake Bay (~ 260 mmol DIN m shoreline⁻¹ day⁻¹, assuming a shoreline of 1.86×10^7 m); however, they used only seepage meters to determine groundwater discharge, which can induce flow under certain conditions (Rosenberry *et al.* 2008). When compared to SGD fluxes in other coastal systems, our estimates for the GP-STE site fall within the range of those previously reported (Table 4).

SGD commonly has higher N:P ratios than Redfield, as was reported in a recent review by Santos *et al.* (2021). In some cases the N:P ratio of SGD is >50 (Santos *et al.*, 2021), which far exceeds the stoichiometry found in the two tributaries draining into the YRE; the Pamunkey (average DIN:DIP ratio = 13.24 ± 1.60) and the Mattaponi (average DIN:DIP ratio = 15.58 ± 1.58) (CBNERR-VA VIMS, 2021). It has been hypothesized that the high N:P ratios found in SGD may cause systems to become P rather than N limited (Santos *et al.*, 2021). The average inorganic DIN:DIP ratio of the YRE itself is 39.9 ± 11.74 and fluctuates seasonally; exhibiting N

limitation in the summer and fall and P limitation in winter (Sin *et al.*, 1999; Killberg-Thoreson *et al.*, 2013; Stanley, 2021). Despite reported N limitation in the summer, the lower YRE still has annual algal blooms, which could be supported by high N:P ratio groundwater discharged during the Summer. When high SGD rates are coupled to the high porewater DIN concentrations that we observed in summer, fluxes of DIN from SGD to the lower YRE would be higher, coincident with annual summer HAB events (Reay, 2009). Our data suggest that the DIN:DIP ratio of groundwater, calculated using the shallow endmember, varies with season. The summer and winter SGD exhibited DIN:DIP ratios exceeding Redfield ratio, whereas in spring 2018 and fall 2019 SGD N:P ratios were closer to Redfield. It is important to account for SGD as a source of DIN:DIP water that differs from other nutrient sources, as this will influence biogeochemistry and may stimulate primary production in the overlying water.

Along with SGD, estuaries receive N and P from their tributaries, from watershed runoff, and from benthic fluxes that release nutrients to the water column. In order to compare sources within the YRE, advective and benthic fluxes of DIN and DIP from previous work were extrapolated to the lower York River for comparison to SGD fluxes. The advective DIN and DIP fluxes, which represent nutrient loading flowing downstream, were outputs of a water quality model developed by Lake and Brush (2015) for the YRE. The model separates the YRE into several boxes and the advective flux used here represented the nutrients flowing in YRE surface water from Box 7 to Box 8 (Lake and Brush 2015); this flux was extrapolated to the entire area of the lower YRE (Box 8, 47.88 km², Figure S8). The benthic fluxes of DIN and DIP were determined experimentally by Woods *et al.* (in prep) with whole core incubations conducted seasonally in 2019 and 2020. The benthic fluxes measured in the lower portion of the YRE, were extrapolated to the same area of the lower YRE (Box 8, 47.88 km²). The SGD fluxes determined

in this study were extrapolated to a seepage zone on either side of the lower YRE. The seepage zone was defined as 40m on either side of the river. This was based on seepage meter measurements by Beck et al. (2016) and includes discharge rates exponentially decreasing with distance from the shoreline. The area of seepage zone was determined as the boundary of Box 8 from Lake and Brush (2015) with a 40 m buffer split into three zones 0-10 m, 10-20 m, and 20-40 m (Figure S9) and calculated in ArcGIS. SGD DIN and PO_4^{2-} discharge rates were extrapolated to the area of the seepage zone for comparison to the benthic and advective sources (Figure 6 & 7, Table S3).

The advective fluxes was the largest source of inorganic nutrients to the lower YRE in all seasons, this flux was an order of magnitude higher than both benthic and SGD fluxes (Figure 6 & 7). Our data, therefore, suggest that riverine transport downstream in the lower YRE is the dominant source of inorganic nutrients to this system. It is possible that a portion of these nutrients transported in YRE surface water are the result of SGD upstream, as groundwater discharge has been observed along the length of the river (Luek and Beck, 2014). The highest estimate of potential SGD fluxes, calculated using the deep endmember approach, was roughly 4-11% and 1-4% of the tidal advective DIN and PO_4^{2-} fluxes, respectively. Benthic fluxes represented net uptake of N in spring, fall, and winter in the YRE, which may be the result of benthic microalgae. This uptake may attenuate SGD derived nutrients as SGD flows through surficial sediments and, when combined with microbial N removal in the STE, SGD derived nutrients may be completely attenuated prior to discharge in spring, fall, and winter. In the summertime, DIN was released from the benthos and SGD derived DIN was not completely attenuated by STE N removal, so SGD serves as additional source of DIN during the summer months. DIP benthic fluxes were negligible with no discernable uptake or release of P suggesting

little or no uptake of SGD derived PO_4^{2-} by the benthos. This extrapolation exemplifies the magnitude of SGD fluxes in this coastal system, but applies widely to other systems (Table 4), where SGD may also be a source of inorganic nutrients. There is likely temporal and spatial variability in the rate of groundwater discharge along the entire YRE, but our observations indicate that the GP-STE is a net source of nutrients to the overlying water in summer despite N removal and uptake.

STEs act as biogeochemical reactors for groundwater and surface water and are important transition zones along the land-ocean continuum. Our data reveal how biogeochemical cycling in STEs can significantly influence SGD nutrient loading. At this site, groundwater delivers high concentrations of dissolved inorganic nutrients to the STE where they may be transformed or attenuated, by both biotic and abiotic processes such as nitrification, denitrification and sorption to sediments, prior to discharge to the overlying water. In the lower portion of the YRE, during the fall, and winter, nitrification and subsequent denitrification in the STE may protect the YRE from high nutrient groundwater discharge. Despite the maximum potential N removal by denitrification in the STE, SGD was a source of nutrients to the YRE in spring and summer. SGD has been reported as an appreciable source of nutrients to some estuaries and coasts, which may cause eutrophication and formation of HABs (Santos *et al.*, 2021). In the lower YRE, SGD appears to be a small source as compared to riverine transport especially after accounting for N removal in the STE. As groundwater nutrient fluxes are further constrained, reactions in STEs altering SGD export should be considered to better estimate groundwater nutrient loading. This will determine whether groundwater should be included in future water quality models and when investigating drivers of coastal zone primary production and biogeochemistry.

2.6. References

- Addy, K., Kellogg, D.Q., Gold, A.J., Groffman, P.M., Ferendo, G., and Sawyer, C. (2002) In Situ Push–Pull Method to Determine Ground Water Denitrification in Riparian Zones. *J Environ Qual* **31**: 1017–1024.
- Anderson, D.M., Glibert, P.M., and Burkholder, J.M. (2002) Harmful algal blooms and eutrophication: Nutrient sources, composition, and consequences. *Estuaries* **25**: 704–726.
- Andrisoa, A., Stieglitz, T.C., Rodellas, V., and Raimbault, P. (2019) Primary production in coastal lagoons supported by groundwater discharge and porewater fluxes inferred from nitrogen and carbon isotope signatures. *Mar Chem* **210**: 48–60.
- Arango, C., Tank, J.L., Schaller, J.L., Royer, T. V, Bernot, M.J., and David, M.B. (2007) Benthic organic carbon influences denitrification in streams with high nitrate concentration. *Freshw Biol* **52**: 1210–1222.
- Beck, A.J., Kellum, A.A., Luek, J.L., and Cochran, M.A. (2016) Chemical Flux Associated with Spatially and Temporally Variable Submarine Groundwater Discharge , and Chemical Modification in the Subterranean Estuary at Gloucester Point , VA (USA). *Estuaries and Coasts* **39**: 1–12.
- Boehm, A.B., Paytan, A., Shellenbarger, G.G., and Davis, K.A. (2006) Composition and flux of groundwater from a California beach aquifer: Implications for nutrient supply to the surf zone. *Cont Shelf Res* **26**: 269–282.
- Bonin, P. and Raymond, N. (1990) Effects of oxygen on denitrification in marine sediments. *Hydrobiologia* **207**: 115–122.
- Brandes, J.A., Devol, A.H., and Deutsch, C. (2007) New Developments in the Marine Nitrogen Cycle. *Chem Rev* **577**–589.
- Burnett, W.C., Aggarwal, P.K., Aureli, A., Bokuniewicz, H., Cable, J.E., Charette, M.A., et al. (2006) Quantifying submarine groundwater discharge in the coastal zone via multiple methods. *Sci Total Environ* **367**: 498–543.
- Cable, J.E., Corbett, D.R., and Walsh, Maud, M. (2002) Phosphate uptake in coastal limestone aquifers: a fresh look at wastewater management. *Limnol Oceanogr Bull* **11**: 29–32.
- Cai, W.J. and Sayles, F.L. (1996) Oxygen penetration depths and fluxes in marine sediments. *Mar Chem* **52**: 123–131.
- Charette, M.A., Allen, M.C., and Sites, F. (2006) Precision Ground Water Sampling in Coastal Aquifers Using a Direct-Push , Shielded-Screen Well-Point System Materials and Procedures. *Groundw Monit Remediat* **87**–93.
- Charette, M.A. and Buesseler, K.O. (2004) Submarine groundwater discharge of nutrients and copper to an urban subestuary of Chesapeake Bay (Elizabeth River). **49**: 376–385.
- Charette, M.A. and Sholkovitz, E.R. (2002) Oxidative precipitation of groundwater-derived ferrous iron in the subterranean estuary of a coastal bay. *Geophys Res Lett* **29**: 85-1-85–4.
- Chesapeake Bay National Estuarine Research Reserve in Virginia, Virginia Institute of Marine Science (CBNERR-VA VIMS), 2021. Virginia Estuarine and Coastal Observing System (VECOS).
- Cornwell, J.C., Kemp, W.M., and Kana, T.M. (1999) Denitrification in coastal ecosystems: Methods, environmental controls, and ecosystem level controls, a review. *Aquat Ecol* **33**: 41–54.
- Correa, R.E., Tait, D.R., Sanders, C.J., Conrad, S.R., Harrison, D., Tucker, J.P., et al. (2020) Submarine groundwater discharge and associated nutrient and carbon inputs into Sydney

- Harbour (Australia). *J Hydrol* **580**:
- Guo, X., Xu, B., Burnett, W.C., Wei, Q., Nan, H., Zhao, S., et al. (2020) Does submarine groundwater discharge contribute to summer hypoxia in the Changjiang (Yangtze) River Estuary? *Sci Total Environ* **719**: 137450.
- Hall, W., Isla, R., Service, N.P., Park, A.N., Box, P.O., Harbor, B., et al. (2005) Denitrification Capacity in a Subterranean Estuary below a Rhode Island Fringing Salt Marsh. *Estuaries* **28**: 896–908.
- Herbert, R.A. (1999) Nitrogen cycling in coastal marine ecosystems. *FEMS Microbiol Rev* 563–590.
- Killberg-Thoreson, L., Sipler, R.E., and Bronk, D.A. (2013) Anthropogenic Nutrient Sources Supplied to a Chesapeake Bay Tributary Support Algal Growth: A Bioassay and High-Resolution Mass Spectrometry Approach. *Estuaries and Coasts* **36**: 966–980.
- Kim, G., Kim, J.S., and Hwang, D.W. (2011) Submarine groundwater discharge from oceanic islands standing in oligotrophic oceans: Implications for global biological production and organic carbon fluxes. *Limnol Oceanogr* **56**: 673–682.
- Kroeger, K.D. and Charette, M.A. (2012) Nitrogen biogeochemistry of submarine groundwater discharge. *Limnol Oceanogr* **53**: 1025–1039.
- Kroeger, K.D., Swarzenski, P.W., Crusius, J., Bratton, J.F., and Charette, M.A. (2007) Submarine Ground-Water Discharge: Nutrient Loading and Nitrogen Transformations. *US Geol Surv Fact Sheet 2006-3110* 4.
- Leote, C., Iba, Æ.J.S., and Rocha, C. (2008) Submarine Groundwater Discharge as a nitrogen source to the Ria Formosa studied with seepage meters. *Biogeochemistry* **88**: 185–194.
- Lisa, J.A., Song, B., Tobias, C.R., and Duernberger, K.A. (2014) Impacts of freshwater flushing on anammox community structure and activities in the New River Estuary, USA. *Aquat Microb Ecol* **72**: 17–31.
- Luek, J.L. and Beck, A.J. (2014) Radium budget of the York River estuary (VA , USA) dominated by submarine groundwater discharge with a seasonally variable groundwater end-member. *Mar Chem* **165**: 55–65.
- Moore, W.S. (2009) The Effect of Submarine Groundwater Discharge on the Ocean. *Ann Rev Mar Sci* **2**: 59–88.
- Moore, W.S. (1999) The subterranean estuary: A reaction zone of ground water and sea water. *Mar Chem* **65**: 111–125.
- Mulholland, M.R., Morse, R.E., Boneillo, G.E., Bernhardt, P.W., Filippino, K.C., Procise, L.A., et al. (2009) Understanding Causes and Impacts of the Dinoflagellate , *Cochlodinium polykrikoides* , Blooms in the Chesapeake Bay. *Estuaries and Coasts* 734–747.
- Nicholls, J.C. and Trimmer, M. (2009) Widespread occurrence of the anammox reaction in estuarine sediments. *Aquat Microb Ecol* **55**: 105–113.
- Nixon, S.W. (1995) Coastal marine eutrophication: A definition, social causes, and future concerns. *Ophelia* **41**: 199–219.
- O'Connor, A.E., Krask, J.L., Canuel, E.A., and Beck, A.J. (2018) Seasonality of major redox constituents in a shallow subterranean estuary. *Geochim Cosmochim Acta* **224**: 344–361.
- O'Connor, A.E., Luek, J.L., Mcintosh, H., and Beck, A.J. (2015) Geochemistry of redox-sensitive trace elements in a shallow subterranean estuary. *Mar Chem* **172**: 70–81.
- Oh, J. and Silverstein, J. (1999) Oxygen inhibition of activated sludge denitrification. *Water Res* **33**: 1925–1937.
- Oshiki, M., Satoh, H., and Okabe, S. (2016) Ecology and physiology of anaerobic ammonium

- oxidizing bacteria. *Environ Microbiol*.
- Reay, W.G. (2009) Water Quality within the York River Estuary. *J Coast Res* **10057**: 23–39.
- Robinson, C.E., Xin, P., Santos, I.R., Charette, M.A., Li, L., and Barry, D.A. (2018) Groundwater dynamics in subterranean estuaries of coastal unconfined aquifers: Controls on submarine groundwater discharge and chemical inputs to the ocean. *Adv Water Resour* **115**:
- Rosenberry, D.O., Labaugh, J.W., and Hunt, R.J. (2008) Use of Monitoring Wells , Portable Piezometers , and Seepage Meters to Quantify Flow Between Surface Water and Ground Water. *F Tech Estim Water Fluxes Between Surf Water Gr Water* 128.
- Sáenz, J.P., Hopmans, E.C., Rogers, D., Henderson, P.B., Charette, M.A., Schouten, S., et al. (2012) Distribution of anaerobic ammonia-oxidizing bacteria in a subterranean estuary. *Mar Chem* **136–137**: 7–13.
- Santos, I.R., Burnett, W.C., Dittmar, T., Suryaputra, I.G.N.A., and Chanton, J. (2009) Tidal pumping drives nutrient and dissolved organic matter dynamics in a Gulf of Mexico subterranean estuary. *Geochim Cosmochim Acta* **73**: 1325–1339.
- Santos, I.R., Chen, X., Lecher, A., Sawyer, A., Moosdorf, N., Rondellas, V., et al. (2021) Submarine groundwater discharge impacts on coastal nutrient biogeochemistry. *Nat Rev Earth Environ* 108–119.
- Schutte, C.A., Wilson, A.M., Evans, T., Moore, W.S., and Joye, S.B. (2017) Deep oxygen penetration drives nitrification in intertidal beach sands. *Limnol Oceanogr* **63**: 1–16.
- Seitzinger, S., Harrison, J.A., Böhlke, J.K., Bouwman, A.F., Lowrance, R., Peterson, B., et al. (2006) Denitrification across landscapes and waterscapes: A synthesis. *Ecol Appl* **16**: 2064–2090.
- Sin, Y., Wetzel, R.L., and Anderson, I.C. (1999) Spatial and temporal characteristics of nutrient and phytoplankton dynamics in the York River Estuary, Virginia: Analyses of long-term data. *Estuaries* **22**: 260–275.
- Slomp, C.P. and Cappellen, P. Van (2004) Nutrient inputs to the coastal ocean through submarine groundwater discharge : controls and potential impact. *J Hydrol* **295**: 64–86.
- Smith, R.L., Böhlke, J.K., Song, B., and Tobias, C.R. (2015) Role of Anaerobic Ammonium Oxidation (Anammox) in Nitrogen Removal from a Freshwater Aquifer. *Environ Sci Technol* **49**: 12169–12177.
- Song, B. and Tobias, C.R. (2011) Methods in Enzymology: Chapter 3 Molecular and Stable Isotope Methods to Detect and Measure Anaerobic Ammonium Oxidation (ANAMMOX) in Aquatic Ecosystems.
- Spiteri, C., Cappellen, P. Van, and Regnier, P. (2008) Surface complexation effects on phosphate adsorption to ferric iron oxyhydroxides along pH and salinity gradients in estuaries and coastal aquifers. *Geochim Cosmochim Acta* **72**: 3431–3445.
- Spiteri, C., Slomp, Caroline P, Charette, M.A., Tuncay, K., and Meile, C. (2008) Flow and nutrient dynamics in a subterranean estuary (Waquoit Bay , MA , USA): Field data and reactive transport modeling. **72**: 3398–3412.
- Spiteri, C., Slomp, Caroline P., Tuncay, K., and Meile, C. (2008) Modeling biogeochemical processes in subterranean estuaries: Effect of flow dynamics and redox conditions on submarine groundwater discharge of nutrients. *Water Resour Res* **44**: 1–18.
- Stanley, B.C. (2021) Differential Nitrogen Uptake by Aquatic Communities in a Chesapeake Bay Tributary and in the Coastal Alaskan Arctic.
- Talbot, J.M., Kroeger, K.D., Rago, A., Allen, M.C., and Charette, M.A. (2003) Nitrogen flux and

- speciation through the subterranean estuary of Waquoit Bay, Massachusetts. *Biol Bull* **205**: 244–245.
- Tobias, C.R., Macko, S.A., Anderson, I.C., Canuel, E.A., Harvey, J.W., Survey, U.S.G., et al. (2001) Tracking the fate of a high concentration groundwater nitrate plume through a fringing marsh : A combined groundwater tracer and in situ isotope enrichment study. **46**: 1977–1989.
- Valiela, I., Costa, J., Foreman, K., Teal, J.M., Howes, B., and Aubrey, D. (1990) Transport of groundwater-borne nutrients from watersheds and their effects on coastal waters. *Biogeochemistry* **10**: 177–197.
- Wu, J., Hong, Y., Wilson, S.J., and Song, B. (2021) Microbial nitrogen loss by coupled nitrification to denitrification and anammox in a permeable subterranean estuary at Gloucester Point , Virginia. *Mar Pollut Bull* **168**..
- Zhang, Y., Santos, I.R., Li, H., Wang, Q., Xiao, K., Guo, H., and Wang, X. (2020) Submarine groundwater discharge drives coastal water quality and nutrient budgets at small and large scales. *Geochim Cosmochim Acta* **290**: 201–215.

2.7. Tables

Table 1. Potential N removal rates measured seasonally in sediment slurries using the IPT method (Song and Tobias, 2011) in $\text{mmoles N m}^{-2} \text{day}^{-1}$ and the associated standard deviation.

Depth	Spring 2018		Summer 2018		Fall 2018		Winter 2019	
	Anammox Rate ($^{29}\text{N}_2$)	Denitrification Rate ($^{30}\text{N}_2$)	Anammox Rate ($^{29}\text{N}_2$)	Denitrification Rate ($^{30}\text{N}_2$)	Anammox Rate ($^{29}\text{N}_2$)	Denitrification Rate ($^{30}\text{N}_2$)	Anammox Rate ($^{29}\text{N}_2$)	Denitrification Rate ($^{30}\text{N}_2$)
0-10 cm	0.00 ± 0.00	0.00 ± 0.00	0.00 ± 0.00	1.10 ± 0.15	0.00 ± 0.00	2.44 ± 0.18	0.00 ± 0.00	0.56 ± 0.04
10-20 cm	0.00 ± 0.00	0.01 ± 0.01	0.00 ± 0.00	0.00 ± 0.35	0.00 ± 0.00	2.44 ± 0.18	0.00 ± 0.00	0.36 ± 0.03
20-30 cm	0.00 ± 0.00	0.00 ± 0.00	0.00 ± 0.00	0.15 ± 0.01	0.00 ± 0.00	0.87 ± 0.17	0.00 ± 0.00	0.47 ± 0.05
30-40 cm	0.00 ± 0.00	0.00 ± 0.00	0.00 ± 0.00	0.03 ± 0.00	0.00 ± 0.00	0.88 ± 0.16	0.00 ± 0.00	0.29 ± 0.01
40-50 cm	0.00 ± 0.00	0.00 ± 0.00	0.00 ± 0.00	0.02 ± 0.00	0.00 ± 0.00	2.48 ± 0.25	0.00 ± 0.00	0.27 ± 0.03
50-60 cm	0.00 ± 0.00	0.00 ± 0.00	0.00 ± 0.00	0.05 ± 0.03	0.00 ± 0.00	0.84 ± 0.25	0.00 ± 0.00	0.17 ± 0.02
60-70 cm	0.01 ± 0.01	0.07 ± 0.00	0.00 ± 0.00	0.02 ± 0.01	0.00 ± 0.00	0.47 ± 0.16	0.00 ± 0.00	0.03 ± 0.14
70-80 cm	0.00 ± 0.00	0.00 ± 0.00	0.00 ± 0.00	0.17 ± 0.05	0.00 ± 0.00	0.20 ± 0.06	0.00 ± 0.00	0.14 ± 0.03
80-90 cm	0.00 ± 0.00	0.00 ± 0.00	0.00 ± 0.00	0.04 ± 0.01	0.00 ± 0.00	0.11 ± 0.01	0.00 ± 0.00	0.04 ± 0.02
90-100 cm	0.00 ± 0.00	0.01 ± 0.01	0.00 ± 0.00	0.00 ± 0.01	0.00 ± 0.00	1.01 ± 0.10	0.00 ± 0.00	0.00 ± 0.00
100-110 cm	0.00 ± 0.00	0.00 ± 0.00	0.00 ± 0.00	0.01 ± 0.01	0.00 ± 0.00	0.18 ± 0.05	0.00 ± 0.00	0.00 ± 0.00

Table 2. Average horizontal, vertical, and total groundwater (GW) discharge ± standard error for each month sampled. Average of all measurements = $34.1 \pm 8.4 \text{ L m}^{-2} \text{day}^{-1}$.

	Spring		Summer		Fall	Winter
	2018	2020	2018	2020	2018	2019
Horizontal Discharge ($\text{L m}^{-2} \text{day}^{-1}$)	22.4 ± 0.03	20.5 ± 0.04	18.9 ± 0.1	21.8 ± 0.2	14.3 ± 0.2	22.0 ± 0.02
Vertical Discharge ($\text{L m}^{-2} \text{day}^{-1}$)	13.4 ± 0.1	-1.4 ± 0.1	62.2 ± 0.3	0.8 ± 0.3	25.2 ± 0.1	-3.7 ± 0.1
Total GW Discharge ($\text{L m}^{-2} \text{day}^{-1}$)	35.8 ± 0.1	19.1 ± 0.1	81.1 ± 0.4	23.1 ± 0.1	39.3 ± 0.3	18.3 ± 0.1

Table 3. Nutrient fluxes via SGD for each season reported in $\text{mmol m}^{-2} \text{d}^{-1} \pm$ standard error and the N:P ratio of discharge. Deep endmember represents the flux estimated using DIN and PO₄²⁻ concentrations at the 300 cm depth in the STE. The shallow endmember fluxes represent those estimated using concentrations at the 50 cm depth. The anoxic zone and total DNF fluxes were calculated using the N removal two scenarios described in section 2.3.7.

Endmember		Spring	Summer	Fall	Winter
SGD DIN Flux	Deep Endmember	6.64 ± 0.02	16.00 ± 0.07	6.71 ± 0.05	3.45 ± 0.02
	Shallow Endmember	0.32 ± 0.0009	3.36 ± 0.02	1.43 ± 0.01	0.45 ± 0.003
	Anoxic Zone DNF	0.31 ± 0.0008	3.09 ± 0.01	0.27 ± 0.002	0.40 ± 0.003
	Total DNF	0.31 ± 0.0008	1.54 ± 0.007	-5.52 ± 0.03	0.09 ± 0.0005
SGD PO ₄ ²⁻ Flux	Deep Endmember	0.56 ± 0.002	1.28 ± 0.006	0.59 ± 0.004	0.28 ± 0.002
	Shallow Endmember	0.03 ± 0.00008	0.15 ± 0.0007	0.13 ± 0.0009	0.02 ± 0.0001

Table 4. Comparison of SGD nutrient fluxes from different sites. DIN = dissolved inorganic nitrogen, DIP = dissolved inorganic phosphorus.

DIN mmol m ⁻² d ⁻¹	DIP mmol m ⁻² d ⁻¹	Location	Source
1.14 ± 0.45	0.056 ± 0.022	Gloucester Point Beach, VA, USA	<i>This Study</i>
4.5	0.16	Elizabeth River, VA, USA	Charette et al., 2004
24-72	n.a.	Nauset March Estuary, MA, USA	Portnoy et al., 1998
0.55	n.a.	Waquoit Bay, MA, USA	Charette et al., 2001
2.2	n.a.	Town Cove, MA, USA	Giblin & Gaines (1990)
0.43	n.a.	Sub-estuaries, MA, USA	Charette et al., 2001; Valiela et al., 1992
0.301	0.00058	Bay side of Florida Keys, FL, USA	Corbett et al., 1999
up to 53	up to 0.41	Southern Chesapeake Bay, VA, USA	Gallagher et al (1996)
1.34	0.012	Tumon Bay, Guam	Matson 1993
0.92	0.037	Inner Kahana Bay, HI, USA	Garrison et al 2003
0.16	0.009	Middle Kahana Bay, HI, USA	Garrison et al., 2003
2.4	0.9	North Inlet, SC, USA	Krest et al., 2000
4.7	0.045	Rozelle Bay, AUS	Correa et al., 2020
1.07	0.05	Tauranga Harbour, NZ	Stewart et al., 2018
1.84	0.0003	Point Judith, RI	Scott 1998; Scott and Moran 2001
4.88	0.007	Potter, RI, USA	Scott 1998; Scott and Moran 2001
3.73	0.006	Green Hill, RI	Scott 1998; Scott and Moran 2001
0.16– 0.49	0.012 – 0.035	Pettaquamscutt, RI, USA	Kelly and Moran 2002
DIN mmol m shoreline ⁻¹ d ⁻¹	DIP mmol m shoreline ⁻¹ d ⁻¹	Location	Source
92	n.a.	Gloucester Point Beach, VA, USA	Beck et al., 2016
260	n.a.	Chesapeake Bay, USA	Reay and Gallagher 1992

2.8. Figures

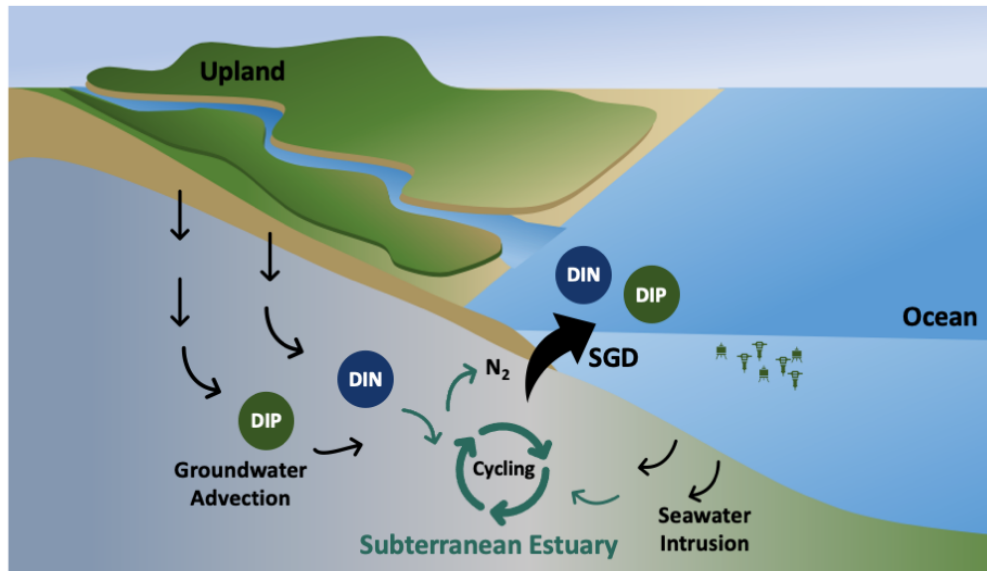


Figure 1. Conceptual diagram of biogeochemical cycling in the subterranean estuary and discharge of dissolved inorganic nitrogen (DIN) and dissolved inorganic phosphorus (DIP) in submarine groundwater discharge (SGD) to coastal waters.

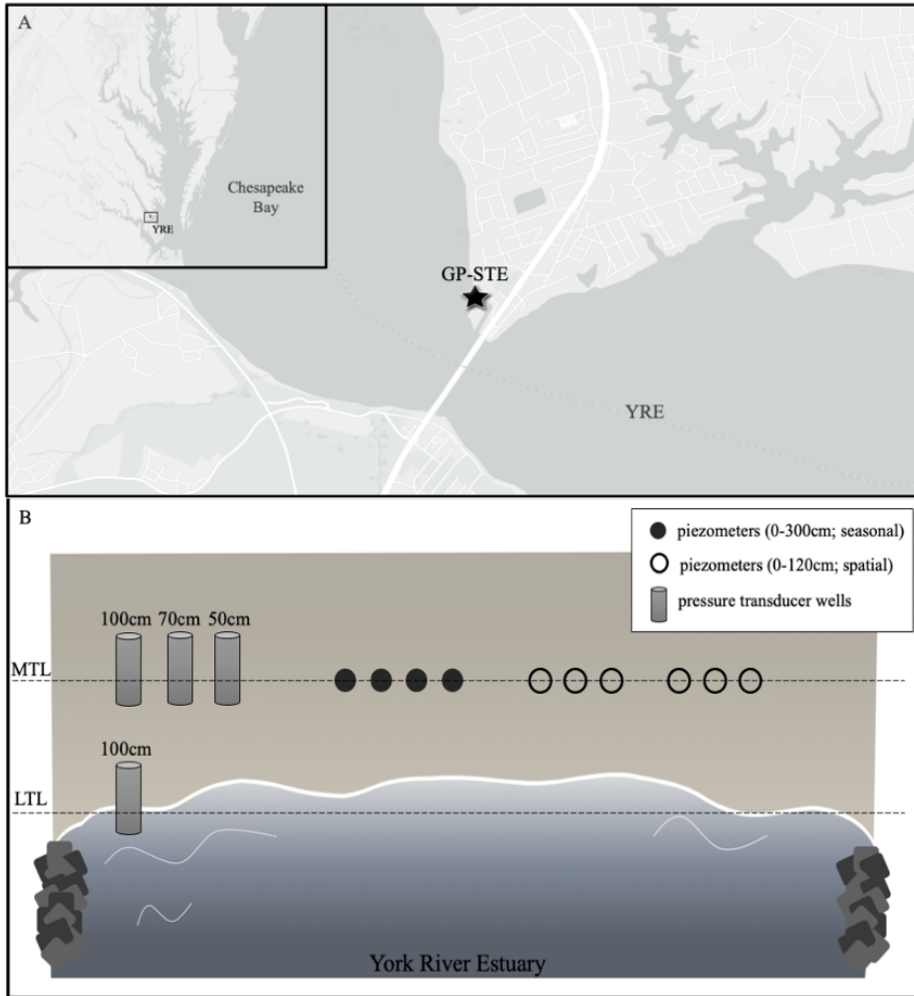


Figure 2. Study site map: (A) Gloucester Point region of YRE, study site (GP-STE, star) 37.248884 N, 76.505324 W; (Arc GIS online); (B) GP-STE Sampling Scheme: All piezometers (circles) were constructed at the mid-tide line (MTL) of the GP-Beach. Piezometers shown were sampled once at low tide to determine spatial variability (0-120 cm). Piezometers were sampled across seasons (filled circles, depths: 0-300 cm) and over two tidal cycles (filled circles, depths: 0-120 cm). Three pressure transducer wells were placed at the mid-tide line (MTL) at three depths (100, 70, and 50cm); one well was placed at the low-tide line (LTL) at 100cm.

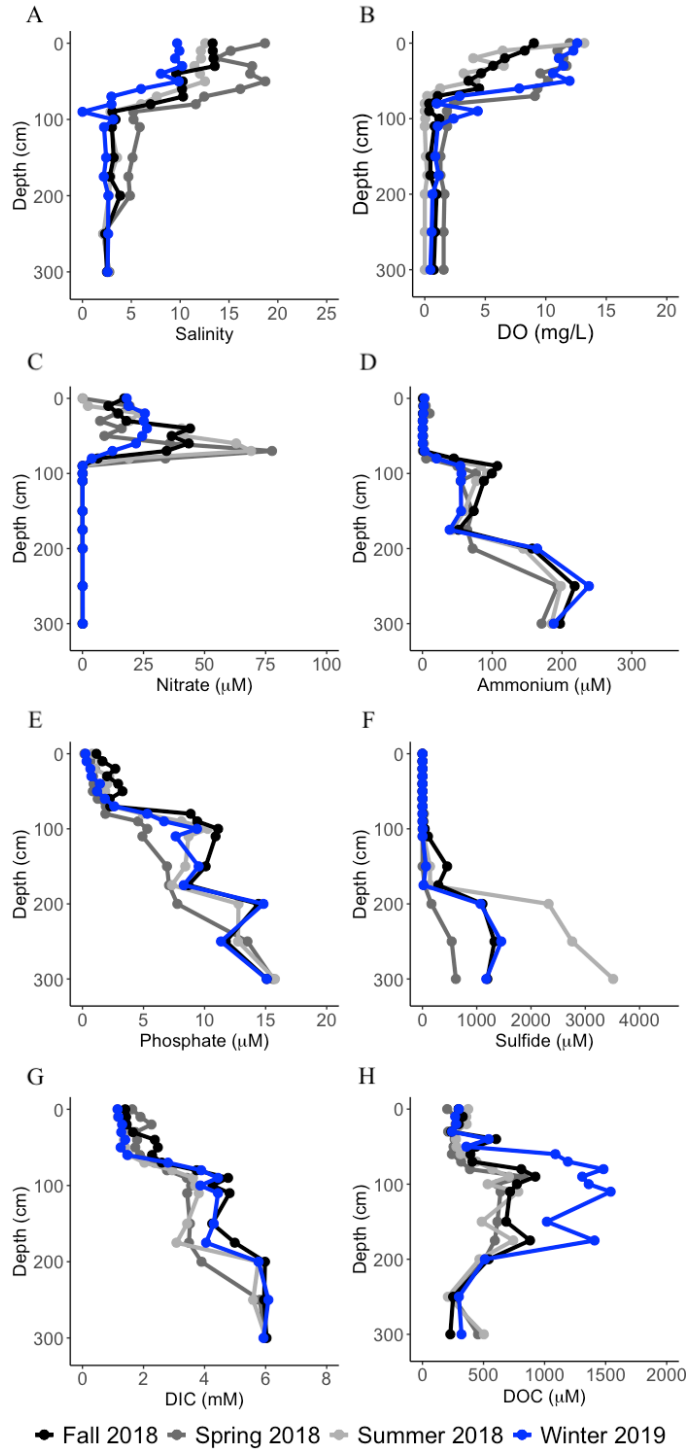


Figure 3. Seasonal GP-STE porewater depth profiles. (A) Salinity, (B) DO (mg/L), (C) Nitrate (μM), (D) Ammonium (μM), (E) Phosphate (μM), (F) Sulfide (μM), (G) DIC (mM), (H) DOC (μM).

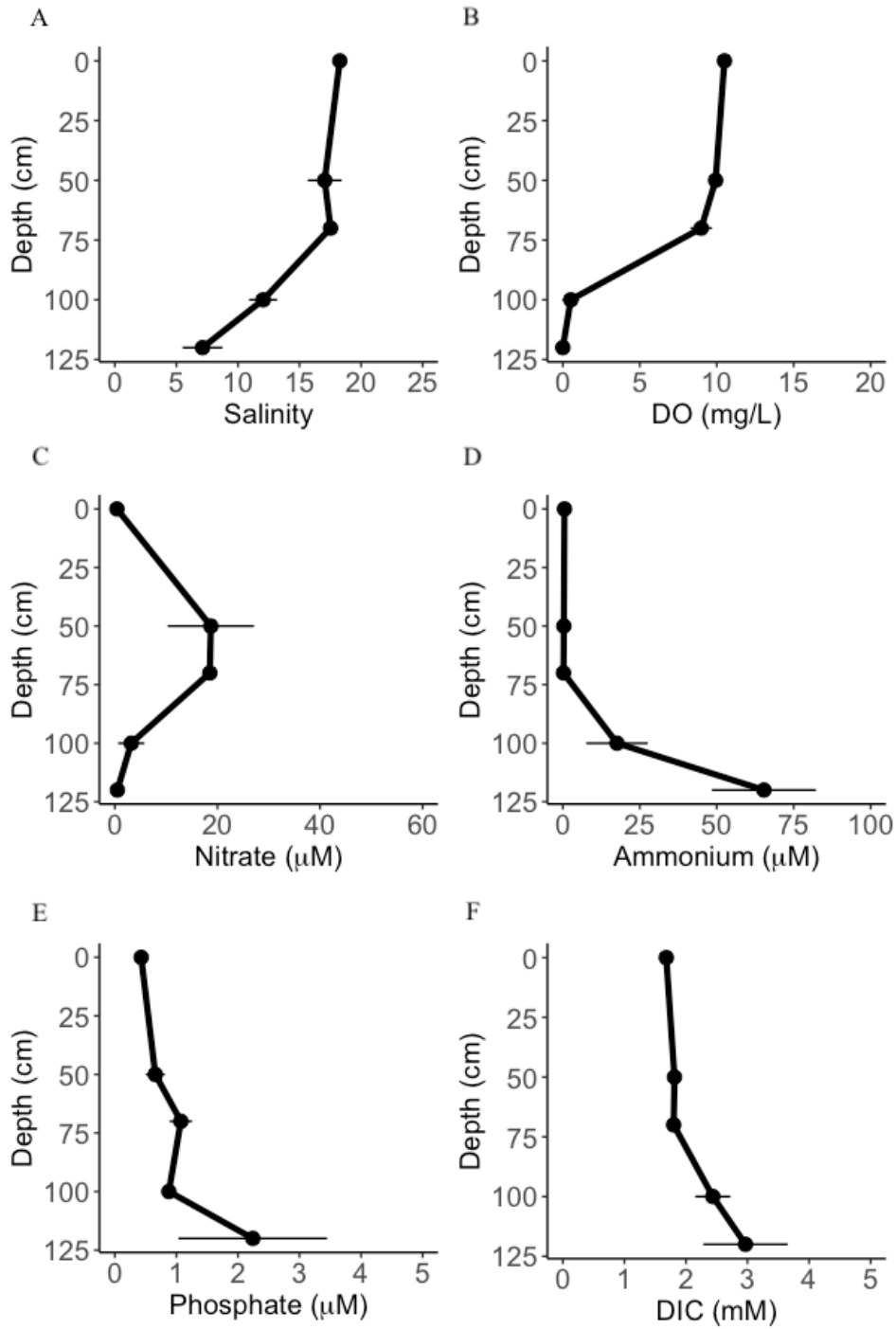


Figure 4. Spatial variability at the mid-tide line across the beach face: (A) Salinity, (B) DO (mg/L), (C) Nitrate (μM), (D) Ammonium (μM), (E) Phosphorus (μM), (F) DIC (mM). Points represent means and error bars represent one standard error in each direction.

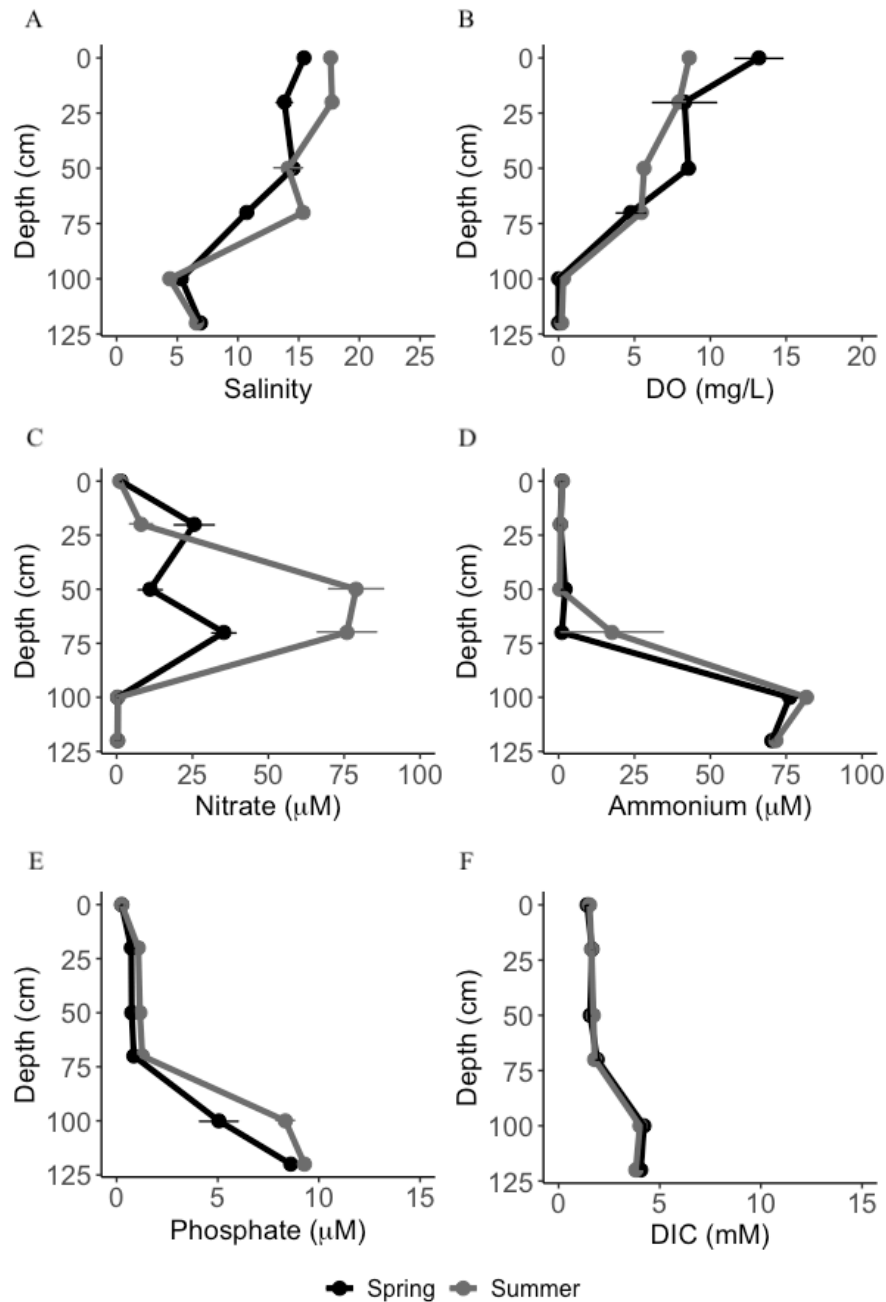


Figure 5. Tidal variability at the mid-tide line over a tidal cycle (spring tide; sampled at high, mid, and low tide) in the spring (black) and summer (grey) of 2020: (A) Salinity, (B) DO (mg/L), (C) Nitrate (μM), (D) Ammonium (μM), (E) Phosphorus (μM), (F) DIC (mM). Points represent means and error bars represent one standard error in each direction.

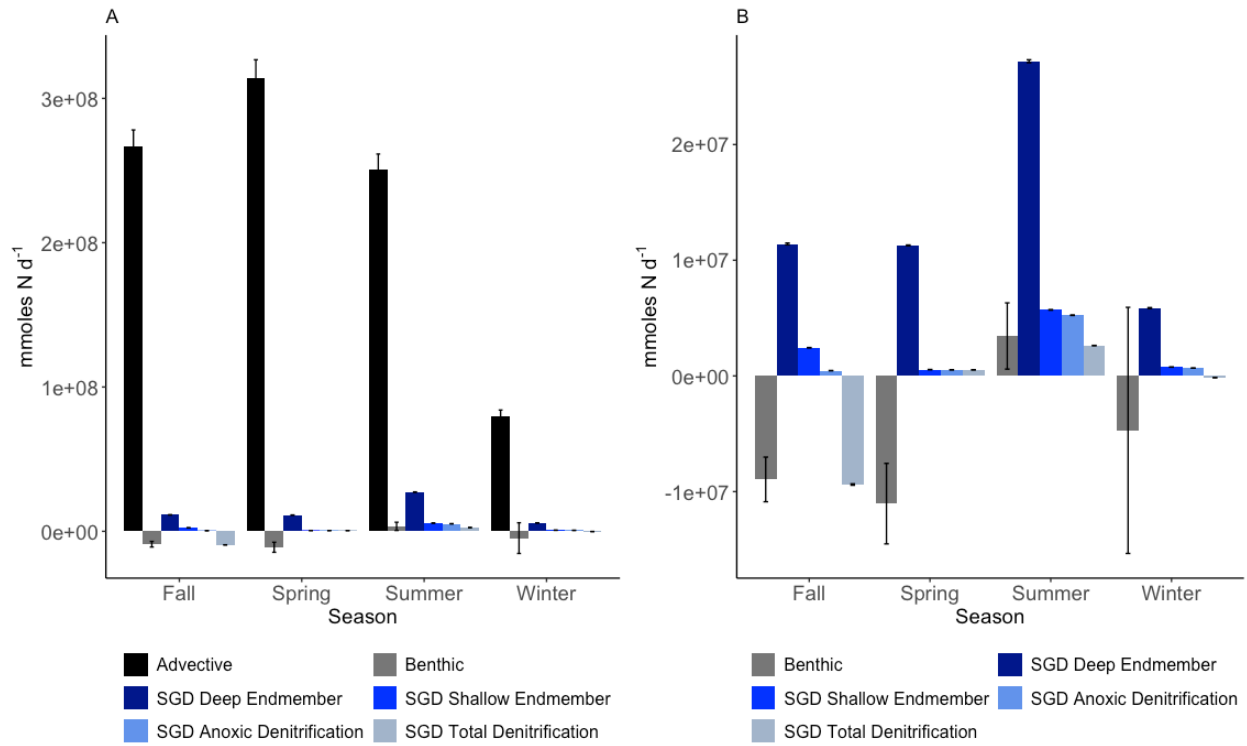


Figure 6. Comparison of advective (black), benthic flux (grey), SGD deep endmember flux (dark blue), and SGD shallow endmember flux (blue), SGD anoxic denitrification scenario flux (light blue), and SGD total denitrification scenario flux (periwinkle) of DIN in the lower YRE. A) shows all calculated fluxes and panel B) shows all fluxes except the advective flux. Error bars represent one standard error in each direction.

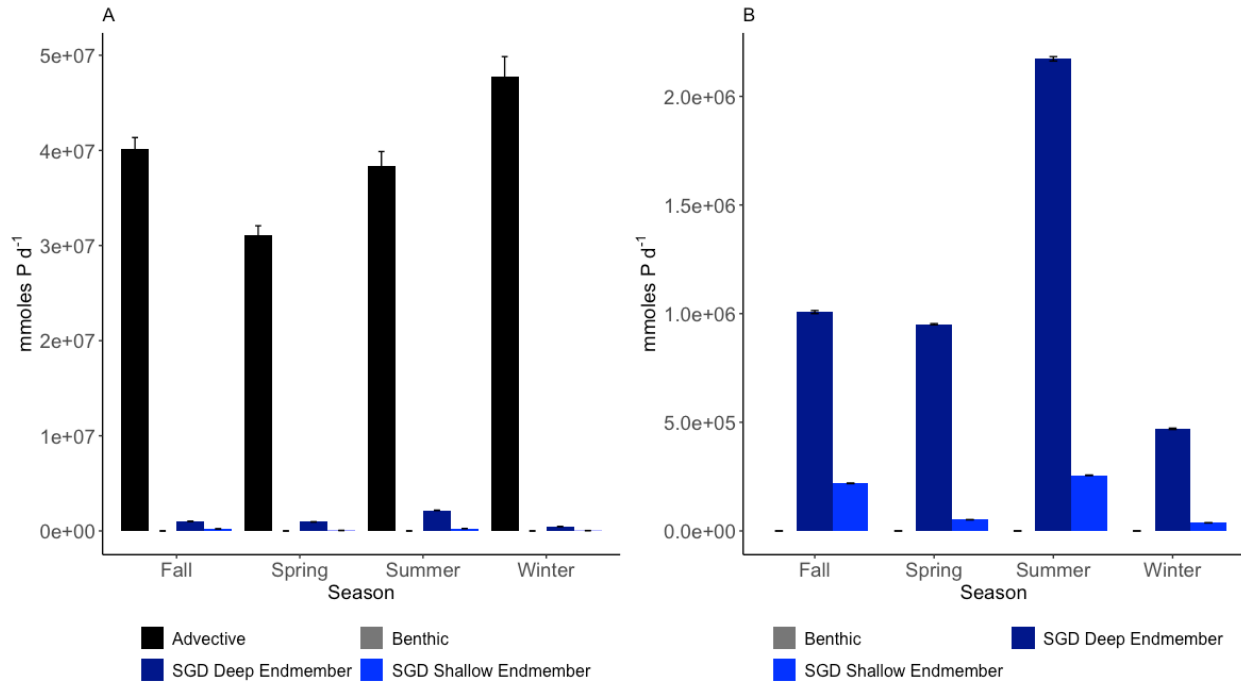


Figure 7. Comparison of advective (black), benthic flux (grey), SGD deep endmember flux (dark blue), and SGD shallow endmember flux (blue) of PO_4^{2-} in the lower YRE. A) shows all calculated fluxes and panel B) shows all fluxes except the advective flux. Error bars represent one standard error in each direction.

2.9. Appendix A

Table S1. ANOVA Results; statistically significant p-values are shown in bold.

Independent Variable	p-value
Salinity ~ Season + Tidal Stage + Site + Depth	
Season	7.83 x 10⁻¹¹
Tidal Stage	0.70
Site	0.12
Depth	< 2.00 x 10⁻¹⁶
DO ~ Season + Tidal Stage + Site + Depth	
Season	0.026
Tidal Stage	0.90
Site	0.95
Depth	1.65 x 10⁻⁸
NO3- ~ Season + Tidal Stage + Site + Depth	
Season	2.98 x 10⁻¹¹
Tidal Stage	0.23
Site	0.23
Depth	< 2.00 x 10⁻¹⁶
NH4+ ~ Season + Tidal Stage + Site + Depth	
Season	0.08
Tidal Stage	0.05
Site	0.70
Depth	< 2.00 x 10⁻¹⁶
DIP ~ Season + Tidal Stage + Site + Depth	
Season	5.28e-06
Tidal Stage	0.101
Site	0.063
Depth	< 2.00 x 10⁻¹⁶
DIC ~ Season + Tidal Stage + Site + Depth	
Season	0.0173
Tidal Stage	0.634
Site	0.3571
Depth	< 2.00 x 10⁻¹⁶
Anammox Rates ~ Season	
Season	0.007
Denitrification Rates ~ Season	
Season	4.0 x 10⁻⁵

Table S2. P-values from Pearson Correlation significance test ($\alpha > 0.05$).

	DO	NO3	NH4	PO4	DIC	DOC	H2S
Sal	7.65×10^{-28}	1.04×10^{-4}	7.52×10^{-23}	9.23×10^{-33}	1.00×10^{-32}	1.61×10^{-17}	7.44×10^{-6}
DO		2.83×10^{-2}	5.13×10^{-16}	5.97×10^{-22}	5.33×10^{-26}	3.44×10^{-12}	5.28×10^{-4}
NO3			5.59×10^{-7}	9.39×10^{-8}	1.90×10^{-7}	1.33×10^{-4}	0.02
NH4				5.10×10^{-50}	2.31×10^{-56}	8.08×10^{-3}	1.95×10^{-20}
PO4					1.50×10^{-57}	1.58×10^{-7}	2.91×10^{-14}
DIC						1.99×10^{-8}	1.74×10^{-13}
DOC							0.33

Table S3. Comparison of DIN inputs to the lower portion of York River Estuary in 10^6 mmol N day⁻¹ for an area of 33,146,225 m², area includes Gloucester Point to Mouth of York River. Submarine groundwater discharge (SGD) fluxes are those calculated in this study, ^A Advective river fluxes were calculated using the York River Water Quality Model published by Lake & Brush (2015), and ^B Seasonal benthic fluxes were measured by Woods et al. (in prep) in the lower York River. SGD as % of Advective represents the magnitude of SGD derived nutrient flux/ Diffusive river nutrient flux x 100.

	Flux	Spring	Summer	Fall	Winter
DIN	Advective	314	251	266	795
	Benthic	11.00	3.45	-8.95	-4.71
	SGD: Deep Endmember	11.30	27.20	11.40	5.87
	SGD: Shallow Endmember	0.55	5.70	2.44	0.76
	SGD: Anoxic Zone DNF	0.53	5.25	0.46	0.68
	SGD: Total DNF	0.53	2.62	-9.40	-1.49
DIP	Advective	31.10	38.40	40.20	47.80
	Benthic	n.d.	n.d.	n.d.	n.d.
	SGD: Deep Endmember	0.95	2.17	1.01	0.47
	SGD: Shallow Endmember	0.005	0.26	0.22	0.004

Table S4. Discharge ANOVA Results; statistically significant p-values are shown in bold.

Independent Variable	p-value
Discharge ~ Season + Month	
Season	< 2 x 10⁻¹⁶
Month	< 2 x 10⁻¹⁶
DIN Flux ~ Season + Month	
Season	< 2 x 10⁻¹⁶
Month	< 2 x 10⁻¹⁶
DIP Flux ~ Season + Month	
Season	< 2 x 10⁻¹⁶
Month	< 2 x 10⁻¹⁶

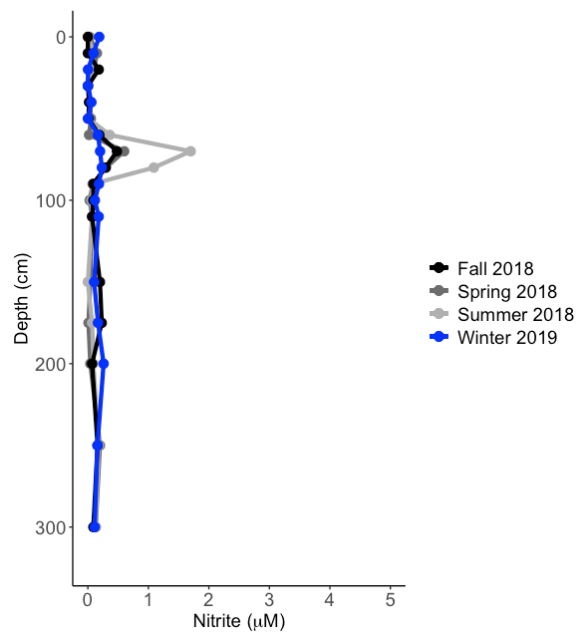


Figure S1. Seasonal GP-STE porewater depth profiles of porewater nitrite (NO₂⁻) concentrations (µM); all concentrations <1.7 µM.

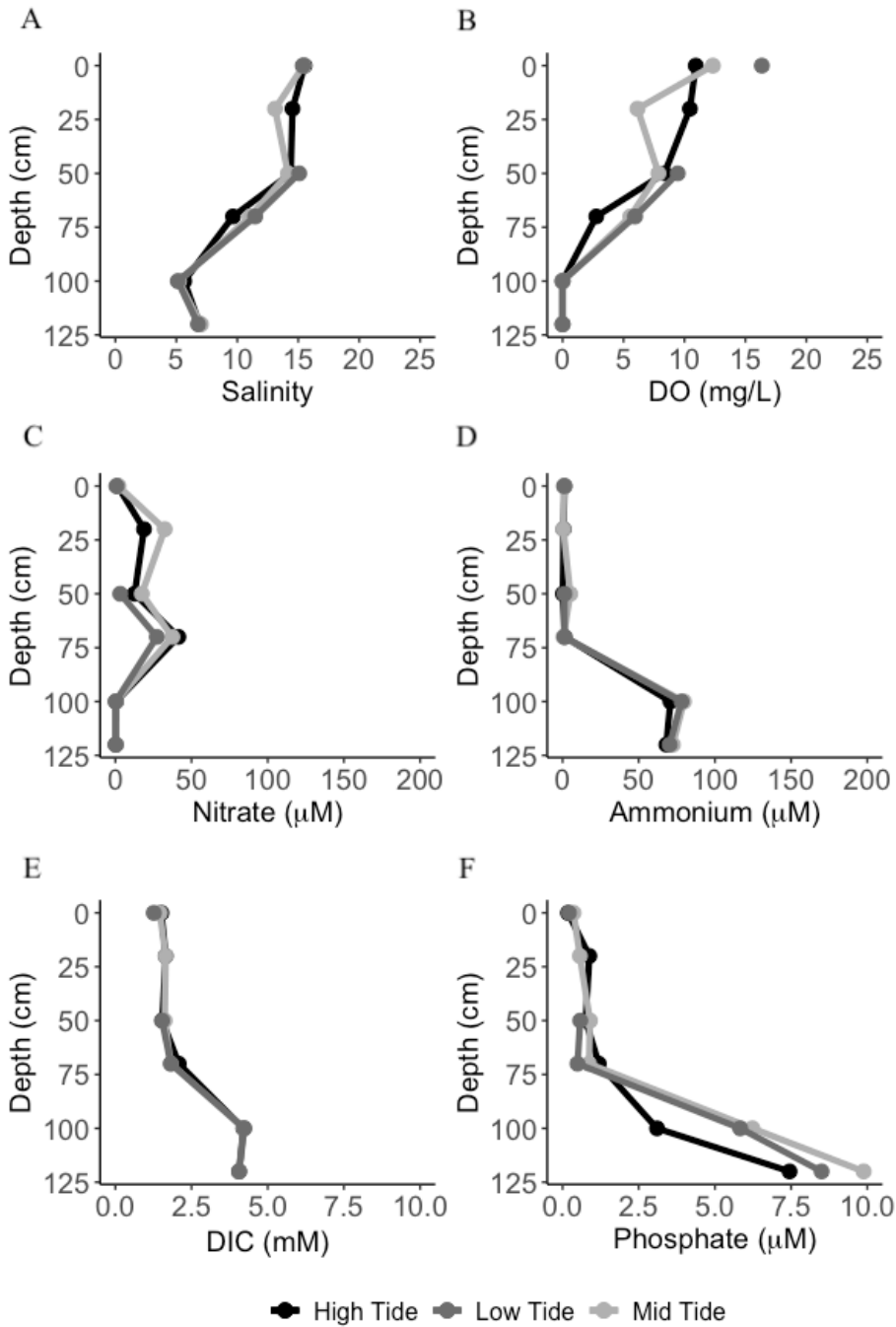


Figure S2. Tidal variability at the mid-tide line over a tidal cycle (spring tide; sampled at high, mid, and low tide) in the spring 2020: salinity, dissolved oxygen (mg/L), nitrate (μM), ammonium (μM), dissolved inorganic phosphorus (μM), DIC (mM).

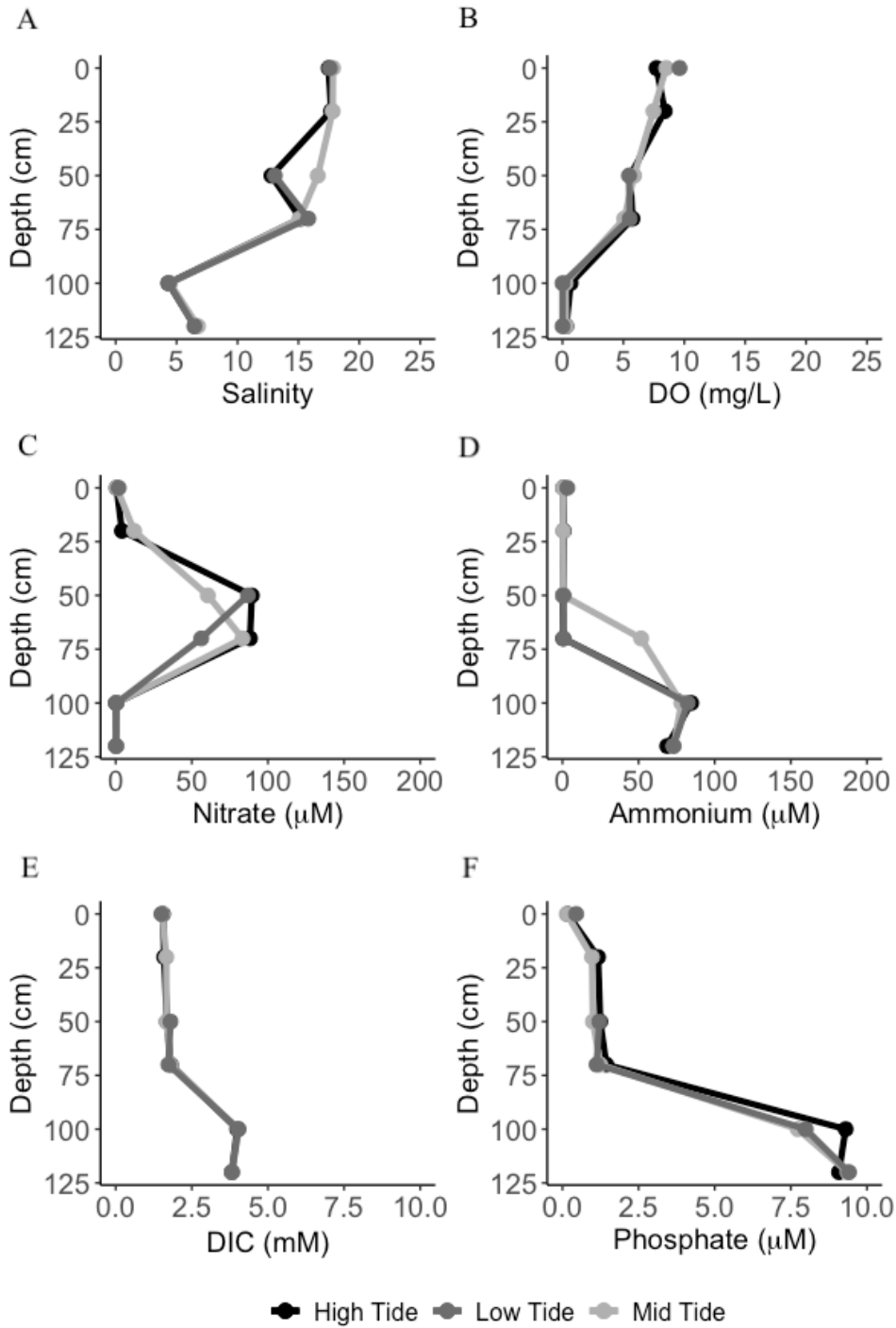


Figure S3. Tidal variability at the mid-tide line over a tidal cycle (spring tide; sampled at high, mid, and low tide) in the summer 2020: salinity, dissolved oxygen (mg/L), nitrate (μM), ammonium (μM), dissolved inorganic phosphorus (μM), DIC (mM).

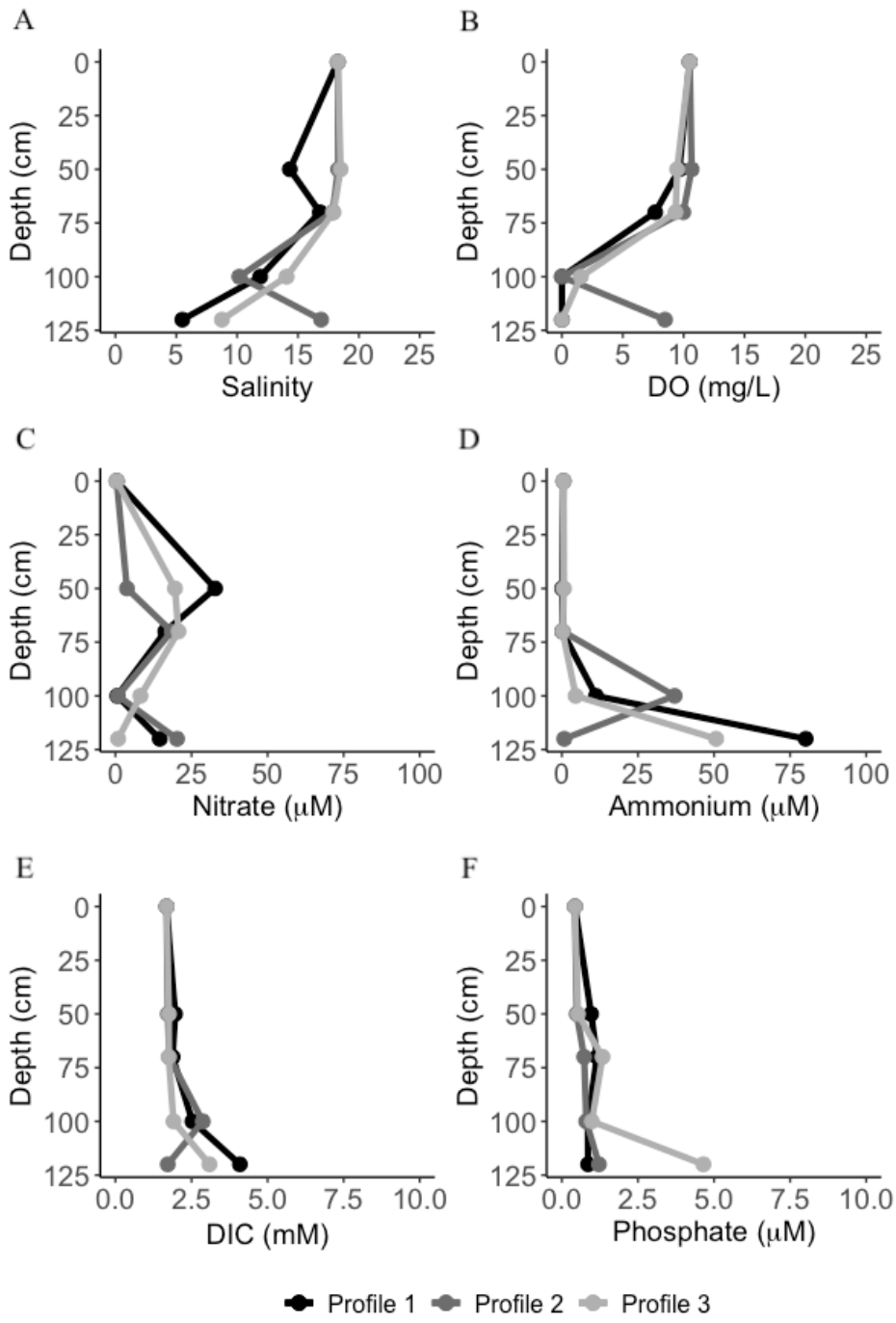


Figure S4. Spatial variability at the mid-tide line across the beach face: salinity, dissolved oxygen (mg/L), nitrate (μM), ammonium (μM), dissolved inorganic phosphorus (μM), and DIC (mM).

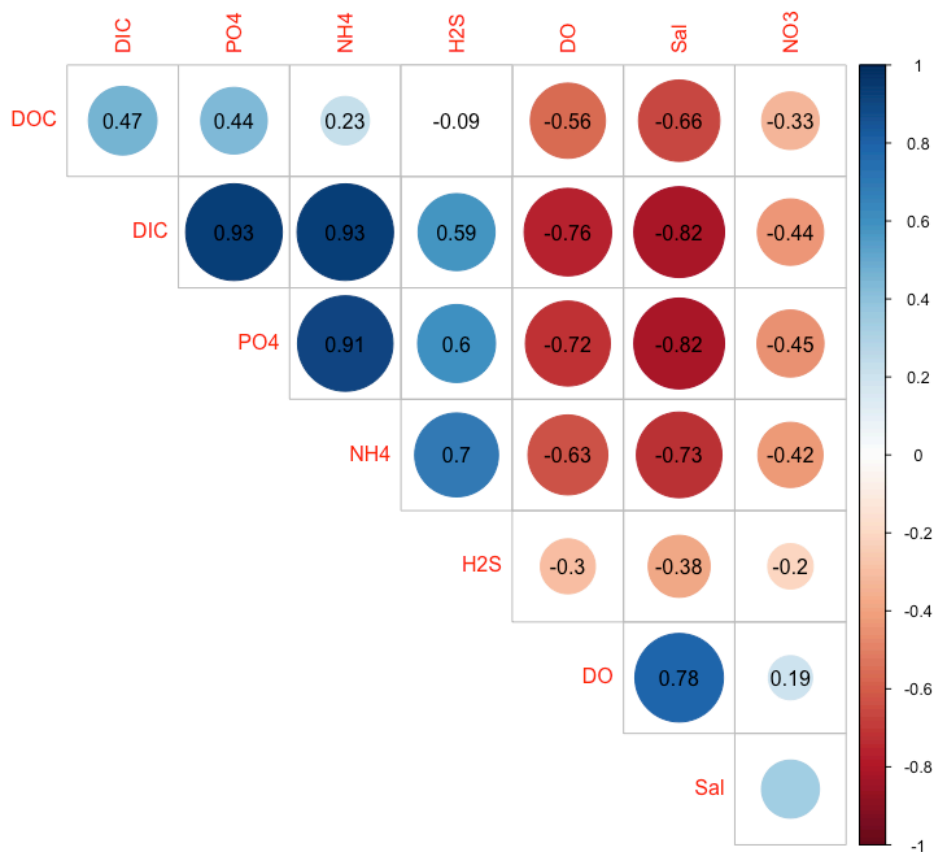


Figure S5. Pearson correlation analysis of STE porewater geochemical analytes. The Pearson correlation coefficient is indicated by the number in each dot, the size of the dot indicates the strength of the correlation, color indicates the direction of the correlation (red = negative, blue = positive), squares with circles were correlations with a p-value < 0.05, but those without circles indicate non-significant (p-value > 0.05) correlations.

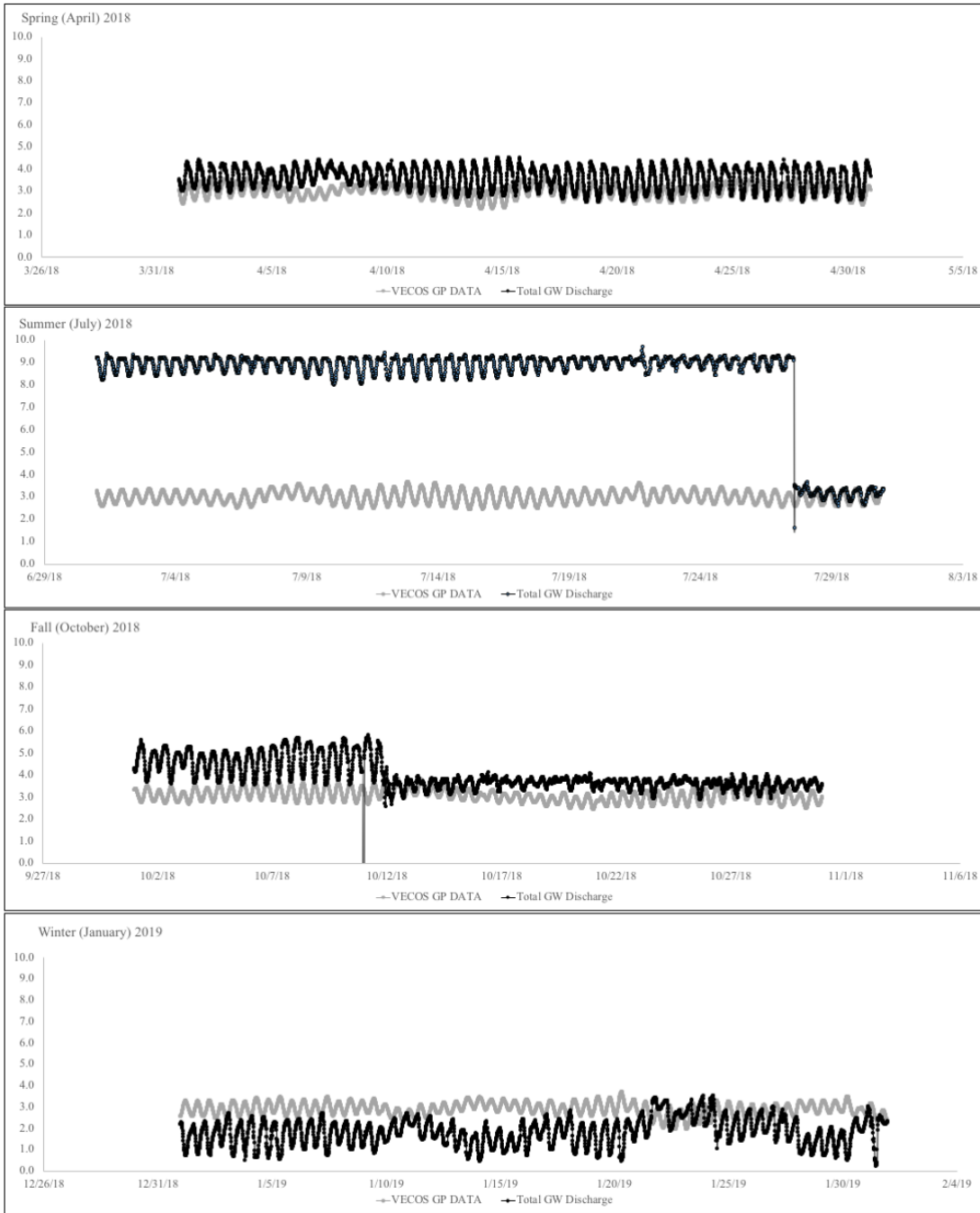


Figure S6. Total groundwater discharge for each season sampled in 2019 (black) and tidal data for the same month from VECOS at the Gloucester Point monitoring station (grey).

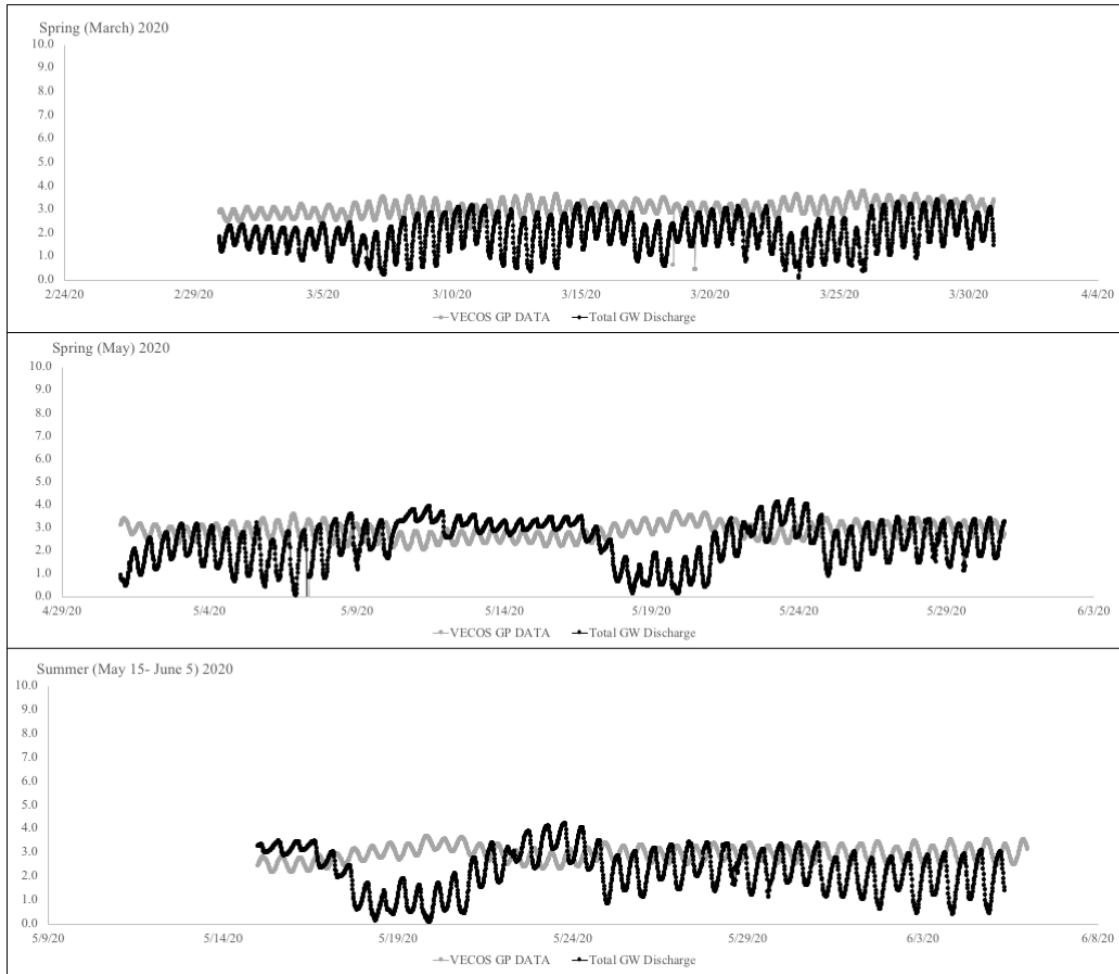


Figure S7. Total groundwater discharge for each season sampled in 2020 (black) and tidal data for the same month from VECOS at the Gloucester Point monitoring station (grey).

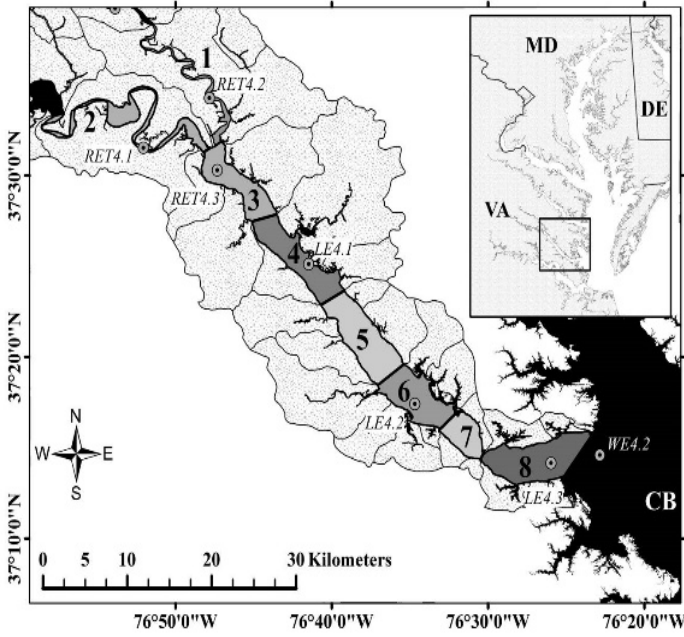


Figure S8. York River box boundaries, Gloucester Point Beach STE is located at the border of boxes 7 and 8. SGD, Benthic, and Advective fluxes were extrapolated to the total area in box 8 (47.88 km²).

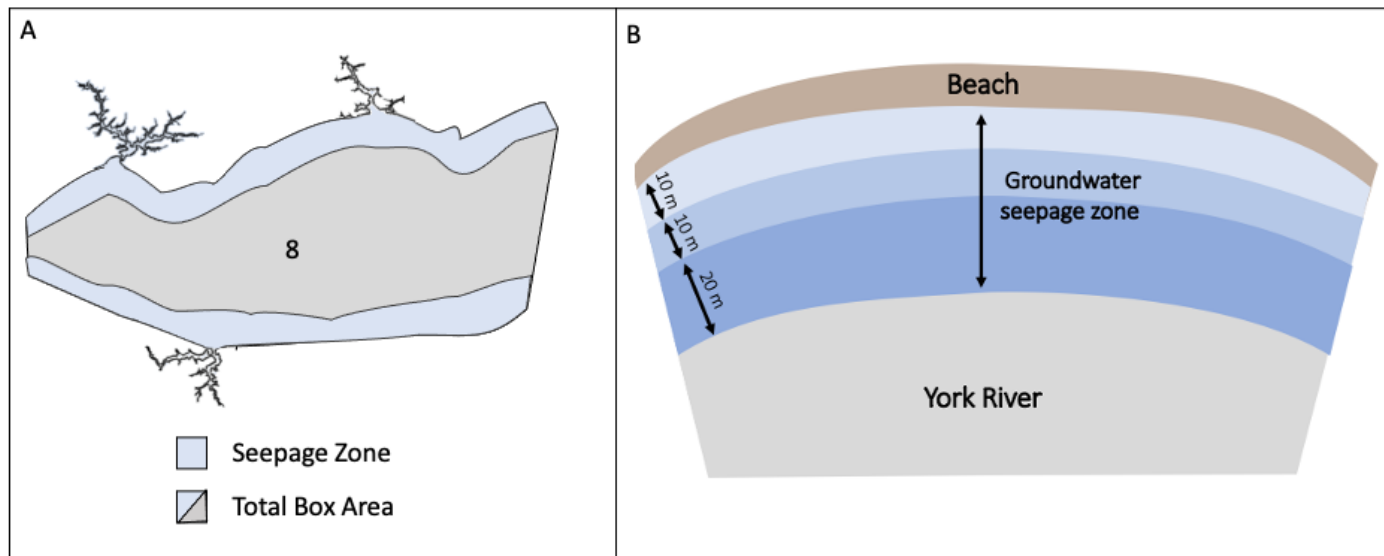


Figure S9: A) Submarine groundwater discharge (SGD) seepage zone defined (not to scale) in the lower portion of the YRE (Box 8 according to Lake and Brush 2015). B) Conceptual diagram of seepage zone broken into sections with distance from the shoreline where the first 10m from the shoreline was defined as the zone exhibiting discharge as measured at the GP-STE, the next 10m represents the zone with half the discharge measured at the GP-STE, and the next 20m out from the shoreline is assumed to exhibit one-fourth the discharge measured at the shoreline of the GP-STE. This approach of sectioning the seepage zone allows for a simple model of exponential decay of SGD moving away from the shoreline.

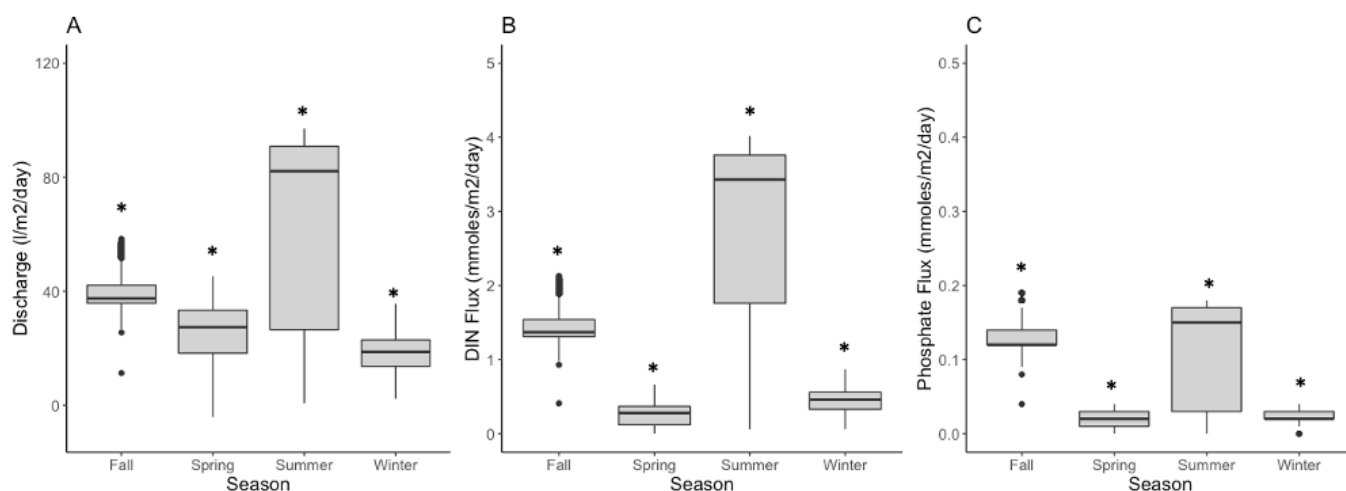


Figure S10. Box and whisker plots of seasonal discharge (A), DIN fluxes calculated using the shallow (50 cm) endmember (B), and PO₄²⁻ fluxes calculated using the shallow (50 cm) endmember (C). An Asterix indicates statistical significance from other seasons (ANOVA, p-value < 0.05).

2.10. Appendix B

All raw data collected in Chapter 2 has been made publicly available via the BCO DMO site, the links to this data are shown below:

Seasonal geochemical profile data:

<https://www.bco-dmo.org/dataset/807664/data>

Spatial and tidal geochemical profile data: BCO DMO submission in progress

Sediment core measurement data: BCO DMO submission in progress

Hydraulic conductivity data: BCO DMO submission in progress

Chapter 3. Geochemical Factors Impacting Nitrifying Communities in Sandy Sediments

3.1. Abstract

Sandy sediment beaches cover 70% of non-ice-covered coastlines and are important ecosystems for nutrient cycling along the land-ocean continuum. Subterranean estuaries (STEs), where groundwater and seawater meet, often form within sandy beaches. STEs are important for biogeochemical cycling of groundwater derived analytes. The STE microbial community facilitates biogeochemical reactions, determining the fate of nutrients, including nitrogen (N), supplied by groundwater. Nitrification influences the fate of N by oxidizing dissolved inorganic nitrogen (DIN), making it available for N removal. We used metabarcoding of 16S rRNA genes and quantitative PCR (qPCR) of *amoA* genes to characterize spatial and temporal variation in STE microbial community structure and nitrifying organisms. We examined nitrifier diversity, distribution, and abundance and how geochemical features influenced their distribution. Sediment microbial communities varied with depth (p-value), and followed geochemical gradients in dissolved oxygen (DO), salinity, pH, DIC, and DIN. Genetic potential for nitrification in the STE was evidenced by taxonomic identification of 16S sequences and qPCR quantification of *amoA* genes. Ammonia oxidizer abundance was best explained by DIN, DO, and pH. Our results suggest that geochemical gradients are closely linked to STE community composition and nitrifier abundance, which are important to determining the fate and transport of groundwater-derived nutrients to coastal waters.

3.2. Introduction

Sandy beaches cover roughly 70% of coastlines without ice (McLachlan and Brown, 2006).

These coastal systems are important habitats that influence and regulate the cycling of nutrients, carbon, and trace metals (Santos *et al.*, 2008; Santoro, 2010; Anschutz *et al.*, 2016; Beck *et al.*, 2017). Within the subsurface of sandy beaches, groundwater flow meets and mixes with intruding seawater in the subterranean estuary (STE; Moore, 1999), an important transition zone along the land-ocean continuum.

The mixing of these two distinct water bodies in STEs is facilitated by the high hydraulic conductivity often observed in sandy, permeable sediments resulting in highly variable systems. Steep geochemical gradients are characteristic of STEs, which often act as biogeochemical hotspots for nutrient, trace metal, and organic matter cycling. Transformations mediated by microbial communities along the STE flow path determine the concentration and speciation of nutrients, such as nitrogen (N), that are discharged to the overlying water by submarine groundwater discharge (SGD) and porewater exchange (Ruiz-González *et al.*, 2021). Despite their role in determining nutrient fluxes, many of the transformations that occur in sandy beaches remain poorly characterized.

Groundwater can accumulate considerable amounts of dissolved inorganic nitrogen (DIN) along its flow path. Reduced DIN in groundwater, such as ammonium (NH_4^+) may be oxidized by nitrification to nitrite (NO_2^-) and then to nitrate (NO_3^-) in the STE. Nitrification is an important process as it makes oxidized forms of DIN available for conversion to di-nitrogen gas (N_2) by the microbial N removal processes: denitrification and anaerobic ammonium oxidation (anammox). In STEs with high groundwater NH_4^+ concentrations, nitrification is required for N removal and subsequently determines DIN concentrations in SGD. Mosier and Francis (2008)

reported that coupled nitrification-denitrification removed up to 50% of the DIN pool in the San Francisco Bay estuary. Erler *et al.* (2014) observed that 80% of observed NH_4^+ in a tropical STE was consumed by nitrification making it available for denitrification. It should also be noted that the product of nitrification, NO_3^- , is more mobile than the reactant, NH_4^+ . Therefore NO_3^- , if not reduced by N removal processes, is more easily discharged than NH_4^+ , and may result in higher DIN concentrations in SGD.

Nitrification occurs in two steps; ammonia oxidation and nitrite oxidation. Ammonia oxidation is the rate limiting step mediated by ammonia oxidizing archaea (AOA) and ammonia oxidizing bacteria (AOB). Ammonia monooxygenase, encoded by *amo* genes, is required for ammonia oxidation, while nitrite oxidation is mediated by nitrite oxidoreductase encoded by *nxr* genes in nitrite oxidizing bacteria (NOB). A recently identified group, complete ammonia oxidizers (comammox), mediate both steps of nitrification (van Kessel *et al.*, 2015; Santoro 2016). The *amoA* gene is often used as a genetic marker for studying nitrification in the environment, including estuaries (Caffrey *et al.*, 2007; Lisa *et al.*, 2015), groundwater (Reed *et al.*, 2010), and STEs (Hong *et al.*, 2019; Santoro *et al.*, 2008). Nitrifier abundance and community composition have been related to salinity (Santoro *et al.*, 2008; Santoro, 2010) and dissolved oxygen (DO) concentrations (Santoro, 2010). Despite these previous studies, it remains unclear what drives shifts in the composition and abundance of nitrifying communities in STEs. Steep geochemical gradients often observed in STEs, and their dynamic nature, provide an ideal system to investigate geochemical factors affecting nitrifier community structures in coastal systems.

The goal of this study was to determine how sediment microbial communities vary with depth and season in a STE, with a focus on nitrifying communities. Four specific study

objectives include 1) to examine sediment microbial community composition along geochemical gradients of a STE, 2) to identify prokaryotic taxa of nitrifying communities (AOA, AOB, NOB, and comammox) in a STE, 3) to quantify AOA and AOB abundance in the STE depth profile, and 4) to determine geochemical features influencing AOA and AOB abundances in a STE.

Sediment microbial communities were examined with depth at the Gloucester Point STE (GP-STE), a well-studied STE at a sandy sediment beach along the York River Estuary, a tributary of the Chesapeake Bay in four seasons (Beck *et al.*, 2016, Hong *et al.*, 2019, Wilson *et al.*, 2021). We used a multi-faceted molecular approach that combined a metabarcoding analysis of 16S rRNA genes to examine microbial community composition and qPCR of *amoA* genes to determine spatial and temporal variation in AOA and AOB abundances, followed by statistical analyses to elucidate important geochemical features influencing resident nitrifying communities.

3.3. Results

3.3.1. Porewater & sediment geochemical parameters

Geochemical gradients in the GP-STE are described in detail by Wilson *et al.* (2022). The GP-STE was generally characterized by three zones; a surficial, oxic zone from 0 to 50 cm, a suboxic transition zone from 60 to 70 cm, and an anoxic zone below 80cm. Salinity, DO, and pH decreased as depth increased. Salinity ranged from 3.21 to 18.68, dissolved oxygen (DO) ranged from 0 to 13.2 mg/L, and pH from 7.8 to 8.1 (Fig. 1A, B). Porewater DIC concentrations increased with depth, ranging from 1.15 to 6.09 mM (Fig. 1A). Porewater NH_4^+ , NO_3^- , and NO_2^- concentrations ranged from 0.25 to 99.56 μM , 0.02 to 77.61 μM , and 0 to 0.5 μM , respectively (Fig. 1C). Porewater NH_4^+ increased with depth, whereas NO_3^- concentrations exhibited a peak between 50-100 cm, the only region where NO_3^- exceeded 10 μM . NO_2^- concentrations remained

constant with depth. Extractable NH_4^+ concentrations increased with sediment depth, whereas extractable NO_3^- and NO_2^- remained constant throughout the profiles (Fig. 1D). Extractable NH_4^+ , NO_3^- , and NO_2^- concentrations ranged from 0.53 to 23.93 μM , 2.51 to 6.60 μM , and 0 to 1.20 μM respectively.

3.3.2. Microbial community composition

16S metabarcoding analysis generated a total of 713,272 reads, with an average of 17,798 reads per sample. As shown in Fig. 2, the beta-diversity of the sediment microbial communities varied significantly with depth (p-value < 0.001), but not with season (p-value > 0.05). The STE sediment communities can be differentiated into sections with depth including oxic sediment communities (0 to 50 cm), suboxic zone communities (60 to 70 cm), and anoxic sediment communities (80-110 cm). Specific parameters explaining microbial community structure included DO, salinity, NH_4^+ , pH, and DIC (Fig. S2).

The 16S sequences, when combined across seasons and depths, were dominated by bacteria, which represented ~80% of the total identified sequences, while archaea accounted for ~20%. The relative abundance of archaea increased with depth, ranging from 2 to 14% at 0 cm and increasing to 30 to 48% at 110 cm. Phyla with the highest relative abundances in the oxic zone of STE sediments included *Acidobacteria*, *Proteobacteria*, *Planctomycetes*, and *Bacteroidetes* (Fig. S1). In the suboxic and anoxic zones, the most abundant phyla included *Acidobacteria*, *Chloroflexi*, and *Planctomycetes* (Fig. S1). At the family level, consistent shifts in community composition were observed with depth in each season (Fig. 3). For example, *Pirellulaceae*, *Nitrosopumilaceae*, and *Methyloligellaceae* are consistently present above 60 cm, whereas, *Acidiferrobacteraceae* and *Syntrophaceae* are observed in samples deeper than 80 cm (Fig. 3).

Nitrifiers, including AOA, AOB, and NOB taxa, were identified from sediment microbial communities (Fig. 4). The relative abundance of AOA sequences ranged from 0.0 – 7.5%, with the majority of AOA present from 0 to 70 cm. Three AOA families were identified, *Caldiarchaeaceae*, *Nitrosopumilaceae*, and *Nitrososphaeraceae* (Fig. 4). The AOA community was heavily dominated by *Nitrosopumilaceae*, representing >99% of the AOA. The relative abundance of AOB in the GP-STE ranged from 1 to 5%, with the highest abundances observed from 30-50 cm (Fig. 4). AOB were split between families *Nitrosomonadaceae* (*Betaproteobacteria*) and *Nitrosococcaceae* (*Gammaproteobacteria*). There was a higher abundance of *Gammaproteobacterial* AOB than *Betaproteobacteria* in the top 80 cm of the GP-STE, but from 90 to 100 cm *Betaproteobacteria* were dominant. Less than 2% of the overall community were identified as NOB, but there were four representative NOB families including: *Nitrospinaceae*, *Nitrospiraceae*, *unclassified Nitrospinota*, and *unclassified Nitrospirota* (Fig. 4). *Nitrospiraceae* was the dominant NOB family (>82% of NOB sequences) and no comammox were observed based on taxonomic classification of 16S sequences.

3.3.3. *amoA* gene abundances

The *amoA* genes in AOA and AOB were detected and quantified with qPCR assays. The *amoA* gene abundances ranged from 4 to 872 and 3 to 606 copies g⁻¹ of sediment for AOA and AOB, respectively. A one-way ANOVA confirmed there was no effect of season on *amoA* abundances (Fig. S3), but the highest numbers of AOA and AOB *amoA* abundances were observed in summer and the lowest abundances in winter (Fig. S3). AOA and AOB abundances both decreased with depth (Fig. 5) and the majority of ammonia oxidizers were present in the top 50 cm. When averaged across sampled seasons, the number of *amoA* genes from AOA exceeds the number of AOB *amoA* genes at depths 0-60 cm (Fig. 5). Below 60 cm the total abundance of

amoA genes at each depth is < 30 copies g^{-1} of sediment. The AOA:AOB ratio ranged from 0.82 to 2.51 observed at 100 cm and 60 cm, respectively.

3.3.4. Geochemical features related to *amoA* abundances

AOA and AOB relative abundances based on 16S sequences were positively correlated to qPCR results of *amoA* genes in AOA and *Betaproteobacterial* AOB (Fig. S5). Therefore, qPCR measurements of AOA and AOB abundances were used as response variables when comparing abundances to STE geochemical features. Hypothesis based combinations of explanatory variables were tested to explain *amoA* abundance. Explanatory variables included in the linear models were geochemical characteristics, including salinity, DO, pH, porewater DIN concentrations, and extractable DIN concentrations. Table 1 shows the top three, most parsimonious models that explained AOA and AOB abundances. The model (H_{1A}) that best explained AOA abundance included porewater NO_3^- , NO_2^- , and NH_4^+ concentrations, extractable NO_3^- and NH_4^+ concentrations, and porewater pH (Table 1). H_{1A} explained 67% of the variation in AOA abundance (p-value = 1.57×10^{-8}), had the lowest delta Akaike information criterion corrected (dAICc) value (0.0), and the highest model weight (0.3). All of the top three models explaining AOA abundance included nutrient concentrations (porewater and extractable) and pH, but the second and third top models also included salinity and DO, respectively. AOB abundance was best explained by the model that included porewater nutrient concentrations, extractable nutrient concentrations, pH, and DO (Table 1, H_{1B}). H_{1B} explained 70% of the variation in AOB abundance (p-value = 2.33×10^{-9}) and was the most parsimonious according to dAICc (0.0) and model weight (0.5) (Table 1). H_{2B} included nutrients (porewater and extractable) and pH, but not DO; whereas H_{3B} included nutrients, pH, and salinity.

3.4. Discussion

3.4.1. Geochemical gradients along with depth in the GP-STE

Salinity and DO decreased with depth, likely reflecting groundwater-seawater mixing in the GP-STE. The elevated concentrations of NH_4^+ and DIC co-occurring with lower pH in the deep, anoxic portion of the GP-STE are likely explained by remineralization of organic matter along the groundwater flow-path. At the suboxic transition zone, NH_4^+ concentrations decreased as DO and NO_3^- concentrations increased (Fig. 1). This could be explained by NH_4^+ transport by groundwater advection that is consumed by nitrifiers producing NO_3^- . The presence of extractable NO_3^- and lack of extractable NH_4^+ in surficial sediment could also result from nitrification. It should be noted that DIN concentrations are lower in the top four sampling depths (0-30cm) than in the deeper porewater, this may be the result of tidal pumping, diluting DIN concentrations and flushing NO_3^- out to overlying water. Spatial and temporal variations in STE geochemical profiles are further described by Wilson *et al* (2022) and similar patterns were observed at this site by Beck *et al* (2016) and Hong *et al* (2019).

3.4.2. Stratification of microbial and nitrifying communities of the GP-STE

To our knowledge, this is the first study to examine sediment microbial community structure with depth across seasons in a STE. Interestingly, the effect of season was minor when compared to changes observed with depth. Shifts in community composition were tightly linked to the observed geochemical gradients of DO, salinity, DIN, and DIC, as the resident microbial community will play a role in, but also be influenced by, the cycling of nutrients and organic matter in the subsurface. Hong *et al.*, (2019) observed similar shifts in community composition with depth at this site and reported that similar geochemical analytes explained microbial community structure.

The families of *Nitrosococcaceae*, *Nitrosomonadaceae*, *Methyloligellaceae* and *Flavobacteriaceae* were only observed in the top 60 to 80 cm of the STE, whereas the families of *Desulfobulbaceae* and *Desulfobacteraceae*, involved in sulfur metabolism, were only present below 70 cm. *Nitrosococcaceae* and *Nitrosomonadaceae* are nitrifying organisms supporting our hypothesis that nitrification is occurring in the surficial, oxic and transition, suboxic zones of the GP-STE. There are few studies that characterize STE microbial community structure; however, a previous study conducted at this site also observed potential for ammonia oxidation and sulfur metabolism within the microbial community (Hong *et al.*, 2019).

The nitrifying communities (AOA, AOB, and NOB) found at the GP-STE site were comprised of marine and freshwater taxa suggesting a consortium derived from both groundwater and overlying seawater water. The AOA were dominated by the family *Nitrosopumilaceae*, a family of marine ammonia oxidizers (Könneke *et al.*, 2005), likely supplied to the GP-STE by the overlying water of York River Estuary. There were also *Nitrososphaeraceae*, a group of soil AOA (Tourna *et al.*, 2011), which may be derived from groundwater or the marsh that lies beyond the dune line of the GP beach. The AOB communities were comprised of two families; *Nitrosomonadaceae*, which have been found in terrestrial, freshwater, and marine ecosystems (Prosser *et al.*, 2014), and *Nitrosococcaceae*, which are a group of marine *Gammaproteobacteria*. *Nitrosococcaceae* and *Nitrosomonadaceae* each represented roughly 50% of the AOB communities in the top 30 cm of the STE, whereas *Nitrosococcaceae* dominated (>60%) the AOB communities from 40 to 80 cm, and from 90 to 100 cm there was a switch to *Nitrosomonadaceae* dominance (>60%). DO concentrations (Geets *et al.*, 2006) and salinity have been related to AOB community composition; however, variation

in AOB community composition in our study did not correlate with the DO profile or porewater salinity.

Nitrospiraceae and *Nitrospinaceae* made up the NOB communities; both families include marine NOB. Marine *Nitrospira* are typically found in natural aquatic ecosystems in the water column or attached to sediments (Daims *et al.*, 2015). Although the relative abundance of these NOB is low, the presence of NOB sequences suggests genetic potential for complete nitrification, producing NO_3^- , in the STE. Previous studies reporting genetic potential for nitrification in STEs have focused solely on AOA and AOB, mediating the first step of nitrification (Hong *et al.*, 2019; Santoro *et al.*, 2008).

Despite decreases in relative abundance with depth, no significant variation in nitrifier community structure with depth was observed; this was surprising as the larger microbial community did vary significantly with depth. Salinity decreases with depth, which has been shown to cause shifts in ammonia oxidizer community composition (Mosier and Francis, 2008; Santoro *et al.*, 2008a; Rogers and Casciotti, 2010), but our data suggest this was not the case at this site.

3.4.3. Comparison of AOA and AOB abundances in the GP-STE

AOA and AOB abundances were consistent with those previously documented at this site (Wu *et al.*, 2021); however, they were lower than those reported for a STE at Huntington Beach, USA (Santoro *et al.*, 2008), and surficial, coastal sediments of the North Sea (Lipsewers *et al.*, 2014). Ammonia oxidizers were present deep (100 cm) in the STE sediment, but the observed abundances decreased with depth (Fig. 5). The majority of AOA and AOB are present in the oxic, surficial zone (0-50 cm), below this the abundances are much lower, suggesting that abundance is consistent with the observed DO and salinity profiles, which also decrease with

depth. The total abundance of nitrifiers determined by 16S sequencing confirms the observation that qPCR-based AOA and AOB abundances decrease with depth. AOA outnumbered AOB abundance at all depths (except 100 cm), opposite to the observations of Santoro *et al.*, (2008) where AOB outnumbered AOA. Higher numbers of AOA in the GP-STE could be indicative of the subsurface environment, which typically have higher numbers of archaea as compared to bacteria with depth (this study, Hong *et al.*, 2019).

3.4.4. Geochemical features related to *amoA* gene abundances in the GP-STE

Our results suggest that geochemical factors including DIN concentrations, pH, DO, and salinity are important explanatory variables of AOA and AOB abundances. Extractable and porewater DIN concentrations were included in all of the most parsimonious models for AOA and AOB; confirming that substrate availability is important to nitrifier abundance (Bouskill *et al.*, 2012; Caffrey *et al.*, 2007). Porewater pH was also an important explanatory variable for AOA and AOB abundances. There was a positive, linear relationship between pH and ammonia oxidizer abundance (Fig. S6); with lower abundance at lower pHs. The availability of NH₃ decreases as pH decreases and, subsequently, ammonia oxidation rates also decrease (Beman *et al.*, 2011; Wannicke *et al.*, 2018). This relationship may have biogeochemical implications as ocean acidification (OA) lowers the pH of marine systems. The unique mixing in STEs of seawater with groundwater, which typically has a lower pH compared to seawater, can give insight to how nitrifying communities may respond to decreases in pH, our data align with previous work suggesting nitrification may be suppressed following lowered pH due to OA (Beman *et al.*, 2011; Wannicke *et al.*, 2018; Pajares and Ramos, 2019).

Interestingly, DO was included in the most parsimonious model (H_{1B}) for AOB, but not AOA (H_{1A}). This could indicate that AOB have a greater sensitivity to DO concentrations than

AOA. Active AOA have been observed in oxygen minimum zones and in cultures with low micromolar levels of DO (Qin *et al.*, 2017) and, therefore, may be more resilient to changes in DO, making substrate availability and pH more important in determining their distribution. Deoxygenation in marine and coastal ecosystems is projected to increase with climate change (Levin and Breitburg, 2015); these conditions could lead to lower nitrification rates, decreased nitrifier abundance, and, potentially, dominance of AOAs over AOBs. Salinity has been shown to effect both AOA and AOB abundances in STEs (Santoro *et al.* 2008) and surface estuaries (Mosier and Francis, 2008). Our results indicate salinity may be significant, but other geochemical factors such as DO, pH, and DIN, may be more important to determining AOA and AOB abundances in the subsurface.

3.5. Conclusions

In this study we examined microbial community structure and, more specifically, the nitrifying community of a sandy sediment STE across depth and seasons. Microbial community structure followed the distinct stratification of observed geochemical gradients with depth. AOA, AOB, and NOB were present, confirming genetic potential for ammonia and nitrite oxidation in the STE. Due to the variable nature of these systems, we were able to conduct a comprehensive examination of genetic potential for ammonia oxidation and the geochemical factors which influence this process. Our data confirmed the importance of substrate availability and DO to ammonia oxidizer abundance. We also found that pH plays a significant role in determining both AOA and AOB abundances, which could have implications for nitrification in the face of OA. This study contributes to our understanding of the microbial dimension of STEs, which has been underrepresented in the literature. In order to fully interpret the impacts of geochemical fluxes

from groundwater in coastal environments, we must better constrain the resident microbial communities and the biogeochemical reactions they support in STEs.

3.6. Experimental Procedures

3.6.1. Sampling site and sample collection

Samples were collected at a STE located at the Gloucester Point Beach (GP-STE: 37.248884°N, 76.505324°W), VA, USA. The beach is a part of the lower York River Estuary (YRE), a microtidal tributary (tidal range ~0.7-0.8 m) of the Chesapeake Bay. This is a sandy sediment beach with a man-made jetty on either side; a detailed site description can be found in Beck *et al.*, (2016).

Porewater and sediment were sampled four times, in April, July, and October of 2018 and January of 2019, referred to here as spring, summer, fall, and winter, respectively. Sediment samples were obtained with a vibracore with resulting cores ranging from 120-260 cm in length; however, only the top 110 cm was used in this study. After transport to the lab, sediment cores were sectioned into 10 cm increments and homogenized. A subsample from each core section was frozen at -80°C for DNA extraction and another subsample was stored at 4°C for sediment characterization and nutrient extraction. To collect extractable nutrients, 1M potassium chloride (KCl) was added to 4g of sediment, shaken for 1 hour before decanting and filtering the extract with a 0.45 µM Whatman Puradisc membrane filter (GE Healthcare Life Sciences). Extracted samples were analyzed for inorganic nutrients NO_3^- , NO_2^- , and NH_4^+ on a Lachat QuikChem 8000 automated ion analyzer (Lachat Instruments, Milwaukee, WI, USA).

Porewater samples were obtained from dedicated piezometers with 2 cm screens (AMS Gas Vapor Tip) attached to Fluorinated Ethylene Propylene (FEP) tubing (VersilOn, Saint-Gobain), positioned at ten centimeter increments from the sediment surface to 120 cm (Charette

et al., 2006). Masterflex C-Flex L/S Precision Pump tubing (Cole-Palmer) was attached to piezometer tubing and porewater was slowly pumped from the ground with an Alexis V3.0 peristaltic pump (Proactive Environmental Products). Porewater was analyzed for salinity, dissolved oxygen (DO), and pH using a flow through YSI (600 XL sonde) or HACH probe (HQ40d meter, Loveland, CO, USA). Nutrient samples were filtered using a 0.45 μM cartridge filter (Millipore Ltd.) and frozen until analysis. Concentrations of porewater NO_3^- , NO_2^- , and NH_4^+ were determined on a Lachat QuikChem 8000 automated ion analyzer (Lachat Instruments, Milwaukee, WI, USA).

3.6.2. Molecular analyses: Metabarcoding analysis of 16S rRNA genes

Sediment DNA was extracted from the homogenized 10 cm vibracore subsections using the PowerSoil PowerLyzer kit (Qiagen) following manufacturer instructions. To maximize DNA yield, two bead tubes were used per sample, both filled with 0.5 grams of sediment, replicate products were combined during the spin filter step. DNA was quantified with a QubitTM fluorometer (Invitrogen) and frozen for later use.

The variable V4 region of the 16S rRNA gene was amplified with a barcoded 515F and 806R primers (Caporaso *et al.*, 2012; Parada *et al.*, 2015) following the Earth Microbiome project protocol. The PCR mixture for 16S amplification consisted of 12.5 μL of 10x GoTaq Master Mix, 1 μL of each primer (10 nM), 6 μL of nuclease free water, and 6 μL of sample DNA (diluted to 0.5 ng/ μL). The PCR cycle began with 3 min at 95°C, followed by 25 cycles of 30 s at 95°C, 1 min at 55°C, and 1 min at 72°C, followed by 5 min at 72°C. Amplification was confirmed and the negative control assessed using 1% agarose gel electrophoresis (target fragment size 354 bp). Samples were sequenced on the MiSeq Platform (Illumina) following the manufacturer's instructions.

Bioinformatic analysis was conducted in R Studio (version 3.2.2. Copyright 2015 The R Foundation for Statistical Computing) using the DADA2 bioinformatic package (Callahan *et al.*, 2016). Primer sequences were trimmed, and raw reads were filtered so that only sequences with quality scores >30 were utilized. Samples were denoised and amplicon sequence variants (ASVs) were identified prior to taxonomic classification with the SILVA v138 taxonomy database (Quast *et al.*, 2013). β -diversity was estimated with the Bray–Curtis dissimilarity calculator in the phyloseq package (McMurdie and Holmes, 2013). Nitrifying organisms were identified by manually searching for specific, known taxonomic groups of AOA, AOB, comammox, and NOB.

3.6.3. Molecular analyses: *amoA* gene qPCR assays

The abundance of *amoA* genes from AOA and AOB was determined by qPCR assays with a QuantStudio 6 Flex (Thermo Scientific) using primer pairs *amoAF* and *amoAR* (Francis *et al.*, 2005) and *amoA1F* and *amoA2R* (Rotthauwe *et al.*, 1997), respectively. It should be noted that the *amoA*-1F and *amoA*-2R primer pair only amplifies β -proteobacteria. Standards consisted of plasmids carrying *amoA* genes, which were prepared through serial dilution and quantified using an Agilent 220 TapeStation System (Agilent Technologies). Archaeal and bacteria *amoA* gene assays were conducted in triplicate on 384 well plates and included negative controls with no DNA template. Each reaction had a total volume of 12 μ L consisting of 1x SYBR green GoTaq qPCR Master Mix (Promega), 0.12 μ L bovine serum albumin (1nM), 1 μ L of each primer (6 μ M), 0.05 μ L CRX dye, 4 μ L sample DNA (diluted to a concentration of 0.5 ng/ μ L) and adjusted to the final volume with nuclease-free water. The qPCR conditions for both AOA and AOB *amoA* gene began with 10 min at 95°C, followed by 45 cycles of 15 s at 95°C, 45 s at 53°C, 30 s at 72°C, and 35 s at 80°C. This was followed by a melting curve to assess qPCR

specificity which included 15 s at 95°C, 1 min at 60°C, 15 s at 95°C, and finally 19 s at 60°C. The efficiency and R² values for the AOA *amoA* standard curve were 70% and 0.99, respectively; the efficiency and R² values for the AOB *amoA* gene standard curve were 98% and 0.99, respectively. The determined quantities of *amoA* were normalized to the number of copies of the *amoA* found in a single AOA (Tourna *et al.*, 2011; Qin *et al.*, 2016) or AOB organism (Norton *et al.*, 2002).

3.6.4. Statistical analyses

All statistical analyses were conducted in R studio (The R Foundation for Statistical Computing, version 3.2.2. Copyright 2015). The β -diversity of the microbial community in the STE was evaluated with a Principal Coordinate analysis (PCoA). A permutational multivariate ANOVA (PERMANOVA) using the Adonis function in the vegan package in R (Oksanen *et al.*, 2019) was used to assess the fixed effects of season and depth on microbial community composition.

A one-way ANOVA was used to assess the effect of season on qPCR *amoA* gene abundances. The *amoA* gene abundances derived from qPCR were then analyzed with multiple linear regression models. Co-linearity was assessed using the VIF function in the car package (Fox *et al.*, 2019) in R. The most parsimonious model was determined by Akaike information criterion (dAICc; Graham *et al.*, 2016), model weights, and variance explained (R²). The delta Akaike information criterion corrected (dAICc) was utilized for model selection to account for limited sample size. All statistical tests were assessed for significance with $\alpha = 0.05$.

3.7. References

- Anschutz, P., Charbonnier, C., Deborde, J., Deirmendjian, L., Poirier, D., Mouret, A., et al. (2016) Terrestrial groundwater and nutrient discharge along the 240-km-long Aquitanian coast. *Mar Chem* **185**: 38–47.
- Beck, A.J., Kellum, A.A., Luek, J.L., and Cochran, M.A. (2016a) Chemical Flux Associated with Spatially and Temporally Variable Submarine Groundwater Discharge , and Chemical Modification in the Subterranean Estuary at Gloucester Point , VA (USA). 1–12.
- Beck, A.J., Kellum, A.A., Luek, J.L., and Cochran, M.A. (2016b) Chemical Flux Associated with Spatially and Temporally Variable Submarine Groundwater Discharge , and Chemical Modification in the Subterranean Estuary at Gloucester Point , VA (USA). *Estuaries and Coasts* **39**: 1–12.
- Beck, M., Reckhardt, A., Amelsberg, J., Bartholomä, A., Brumsack, H.J., Cypionka, H., et al. (2017) The drivers of biogeochemistry in beach ecosystems: A cross-shore transect from the dunes to the low-water line. *Mar Chem* **190**: 35–50.
- Beman, J.M., Chow, C.E., King, A.L., Feng, Y., Fuhrman, J.A., Andersson, A., et al. (2011) Global declines in oceanic nitrification rates as a consequence of ocean acidification. *Proc Natl Acad Sci U S A* **108**: 208–213.
- Bouskill, N.J., Eveillard, D., Chien, D., Jayakumar, A., and Ward, B.B. (2012) Environmental factors determining ammonia-oxidizing organism distribution and diversity in marine environments. *Environ Microbiol* **14**: 714–729.
- Caffrey, J.M., Bano, N., Kalanetra, K., and Hollibaugh, J.T. (2007) Ammonia oxidation and ammonia-oxidizing bacteria and archaea from estuaries with differing histories of hypoxia. *ISME J* **1**: 660–662.
- Callahan, B.J., McMurdie, P.J., Rosen, M.J., Han, A.W., Johnson, A.J.A., and Holmes, S.P. (2016) DADA2: High-resolution sample inference from Illumina amplicon data. *Nat Methods* **13**: 581–583.
- Caporaso, J.G., Lauber, C.L., Walters, W.A., Berg-Lyons, D., Huntley, J., Fierer, N., et al. (2012) Ultra-high-throughput microbial community analysis on the Illumina HiSeq and MiSeq platforms. *ISME J* **6**: 1621–1624.
- Charette, M.A., Allen, M.C., and Sites, F. (2006) Precision Ground Water Sampling in Coastal Aquifers Using a Direct-Push , Shielded-Screen Well-Point System Materials and Procedures. *Groundw Monit Remediat* 87–93.
- Daims, H., Lebedeva, E. V., Pjevac, P., Han, P., Herbold, C., Albertsen, M., et al. (2015) Complete nitrification by Nitrospira bacteria. *Nature* **528**: 504–509.
- Erler, D. V, Santos, I.R., Zhang, Y., Tait, D.R., Befus, K.M., Hidden, A., et al. (2014) Nitrogen transformations within a tropical subterranean estuary. *Mar Chem* **164**: 38–47.
- Fox, J., Weisberg, S., Price, B., Adler, D., Bates, D., Baud-Bovy, G., & Bolker, B. (2019) car: Companion to Applied Regression. R package version 3.0-2.
- Francis, C.A., Roberts, K.J., Beman, J.M., Santoro, A.E., and Oakley, B.B. (2005) Ubiquity and diversity of ammonia-oxidizing archaea in water columns and sediments of the ocean. *Proc Natl Acad Sci U S A* **102**: 14683–14688.
- Geets, J., Boon, N., and Verstraete, W. (2006) Strategies of aerobic ammonia-oxidizing bacteria for coping with nutrient and oxygen fluctuations. *FEMS Microbiol Ecol* **58**: 1–13.
- Graham, E.B., Knelman, J.E., Schindlbacher, A., Siciliano, S., Breulmann, M., Yannarell, A., et al. (2016) Microbes as engines of ecosystem function: When does community structure

- enhance predictions of ecosystem processes? *Front Microbiol* **7**: 1–10.
- Hong, Y., Wu, J., Wilson, S., and Song, B. (2019) Vertical Stratification of Sediment Microbial Communities Along Geochemical Gradients of a Subterranean Estuary Located at the Gloucester Beach of Virginia, United States. *Front Microbiol* 1–11.
- van Kessel, M.A.H.J., Speth, D.R., Albertsen, M., Nielsen, P.H., Op den Camp, H.J.M., Kartal, B., et al. (2015) Complete nitrification by a single microorganism. *Nature* **528**: 555.
- Könneke, M., Bernhard, A.E., de la Torre, J.R., Walker, C.B., Waterbury, J.B., and Stahl, D.A. (2005) Isolation of an autotrophic ammonia-oxidizing marine archaeon. *Nature* **437**: 543–546.
- Levin, L.A. and Breitburg, D.L. (2015) Linking coasts and seas to address ocean deoxygenation. *Nat Clim Chang* **5**: 401–403.
- Lipsewers, Y.A., Bale, N.J., Hopmans, E.C., Schouten, S., Sinnighe Damsté, J.S., and Villanueva, L. (2014) Seasonality and depth distribution of the abundance and activity of ammonia oxidizing microorganisms in marine coastal sediments (North Sea). *Front Microbiol* **5**: 1–12.
- Lisa, J.A., Song, B., Tobias, C.R., and Hines, D.E. (2015) Genetic and biogeochemical investigation of sedimentary nitrogen cycling communities responding to tidal and seasonal dynamics in Cape Fear River Estuary. *Estuar Coast Shelf Sci* **167**: A313–A323.
- McLachlan, A. and Brown, A.C. (2006) *The Ecology of Sandy Shores*, McLachlan, A. and Brown, A.C.B.T.-T.E. of S.S. (Second E. (eds) Burlington: Academic Press.
- McMurdie, P.J. and Holmes, S. (2013) phyloseq: An R Package for Reproducible Interactive Analysis and Graphics of Microbiome Census Data. *PLoS One* **8**: e61217.
- Moore, W.S. (1999) The subterranean estuary: A reaction zone of ground water and sea water. *Mar Chem* **65**: 111–125.
- Mosier, A.C. and Francis, C.A. (2008) Relative Abundance and diversity of ammonia-oxidizing archaea and bacteria in the San Francisco Bay estuary. *Environ Microbiol* **10**: 3002–3016.
- Norton, J.M., Alzerreca, J.J., Suwa, Y., and Klotz, M.G. (2002) Diversity of ammonia monooxygenase operon in autotrophic ammonia-oxidizing bacteria. *Arch Microbiol* **177**: 139–149.
- Oksanen, J., F., Blanchet, G., and Friendly, M. (2019) *Vegan: Community Ecology Package*. R package version 2.5-6.
- Pajares, S. and Ramos, R. (2019) Processes and Microorganisms Involved in the Marine Nitrogen Cycle: Knowledge and Gaps. *Front Mar Sci* **6**.
- Parada, A.E., Needham, D.M., and Fuhrman, J.A. (2015) Every base matters: assessing small subunit rRNA primers for marine microbiomes with mock communities, time series and global field samples. *Environ Microbiol* **18**.
- Prosser, J.I., Head, I.M., and Stein, L.Y. (2014) The Family Nitrosomonadaceae. In *The Prokaryotes: Alphaproteobacteria and Betaproteobacteria*. Rosenberg, E., DeLong, E.F., Lory, S., Stackebrandt, E., and Thompson, F. (eds). Berlin, Heidelberg: Springer Berlin Heidelberg, pp. 901–918.
- Qin, S., Pang, Y., Clough, T., Wrage-Mönnig, N., Hu, C., Zhang, Y., et al. (2017) N₂ production via aerobic pathways may play a significant role in nitrogen cycling in upland soils. *Soil Biol Biochem* **108**: 36–40.
- Qin, W., Martens-Habbena, W., Kobelt, J.N., and Stahl, D.A. (2016) Candidatus Nitrosopumilus. *Bergey's Man Syst Archaea Bact* 1–9.
- Quast, C., Pruesse, E., Yilmaz, P., Gerken, J., Schweer, T., Yarza, P., et al. (2013) The SILVA

- ribosomal RNA gene database project: Improved data processing and web-based tools. *Nucleic Acids Res* **41**: 590–596.
- Reed, D.W., Smith, J.M., Francis, C.A., and Fujita, Y. (2010) Responses of ammonia-oxidizing bacterial and archaeal populations to organic nitrogen amendments in low-nutrient groundwater. *Appl Environ Microbiol* **76**: 2517–2523.
- Rogers, D.R. and Casciotti, K.L. (2010) Abundance and diversity of archaeal ammonia oxidizers in a coastal groundwater system. *Appl Environ Microbiol* **76**: 7938–7948.
- Rothauwe, J.-H., Witzel, K.-P., and Liesack, W. (1997) The Ammonia Monooxygenase Structural Gene *amoA* as a Functional Marker: Molecular Fine-Scale Analysis of Natural Ammonia-Oxidizing Populations. *Appl Environ Microbiol* **63**: 4704–4712.
- Ruiz-González, C., Rodellas, V., and Garcia-Orellana, J. (2021) The microbial dimension of submarine groundwater discharge: current challenges and future directions. *FEMS Microbiol Rev* 1–25.
- Santoro, A.E. (2010) Microbial nitrogen cycling at the saltwater – freshwater interface. *Hydrogeol J* **18**: 187–202.
- Santoro, A.E. (2016) The do-it-all nitrifier. *Science (80-)* **351**: 342–343.
- Santoro, A.E., Francis, C.A., De Sieyes, N.R., and Boehm, A.B. (2008a) Shifts in the relative abundance of ammonia-oxidizing bacteria and archaea across physicochemical gradients in a subterranean estuary. *Environ Microbiol* **10**: 1068–1079.
- Santoro, A.E., Francis, C.A., De Sieyes, N.R., and Boehm, A.B. (2008b) Shifts in the relative abundance of ammonia-oxidizing bacteria and archaea across physicochemical gradients in a subterranean estuary. *Environ Microbiol* **10**: 1068–1079.
- Santos, I.R., Burnett, W.C., Chanton, J., Mwashote, B., Suryaputra, I.G.N.A., and Dittmar, T. (2008) Nutrient biogeochemistry in a Gulf of Mexico subterranean estuary and groundwater- derived fluxes to the coastal ocean. **53**: 705–718.
- Tourna, M., Stieglmeier, M., Spang, A., Könneke, M., Schintlmeister, A., Urich, T., et al. (2011) *Nitrososphaera viennensis*, an ammonia oxidizing archaeon from soil. *Proc Natl Acad Sci U S A* **108**: 8420–8425.
- Wannicke, N., Frey, C., Law, C.S., and Voss, M. (2018) The response of the marine nitrogen cycle to ocean acidification. *Glob Chang Biol* **24**: 5031–5043.
- Wu, J., Hong, Y., Wilson, S.J., and Song, B. (2021) Microbial nitrogen loss by coupled nitrification to denitrification and anammox in a permeable subterranean estuary at Gloucester Point, Virginia. *Mar Pollut Bull* **168**:

3.8. Tables

Table 1. Three most parsimonious models as determined by the delta Akaike information criterion corrected (dAICc), variance explained (R^2), and model weights (Wt) for AOA and AOB abundances based on *amoA* gene quantification. H is the hypothesis number, Model includes the dependent variable ($\log(\text{amoA copy numbers } g^{-1})$) and explanatory variables (NUTs = porewater and extractable DIN, pH, Sal = salinity, and DO).

AOA					AOB				
H	Model	dAICc	R^2	Wt	H	Model	dAICc	R^2	Wt
H _{1A}	AOA ~ NUTs + pH	0.0	0.67	0.3	H _{1B}	AOB ~ NUTs + pH + DO	0.0	0.70	0.5
H _{2A}	AOA ~ NUTs + pH + Sal	0.6	0.68	0.2	H _{2B}	AOB ~ NUTs + pH	0.6	0.70	0.3
H _{3A}	AOA ~ NUTs + pH + DO	0.8	0.67	0.2	H _{3B}	AOB ~ NUTs + pH + Sal	3.4	0.70	0.1

3.9. Figures

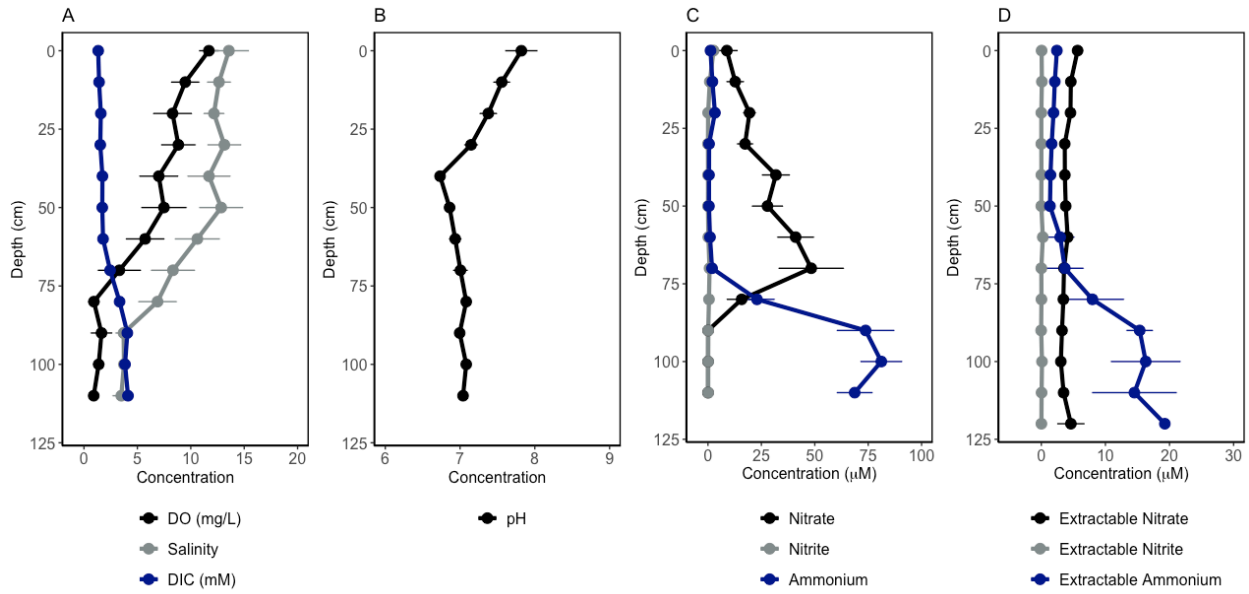


Fig. 1. GP-STE geochemical depth profiles as averages of seasonal measurements. A) Dissolved oxygen (DO, mg/L), salinity, and DIC (mM). B) pH, C) Nitrate (μM), nitrite (μM), and ammonium (μM). D) Extractable nitrate (μM), extractable nitrite (μM), and extractable ammonium (μM). Error bars indicate one standard error in each direction.

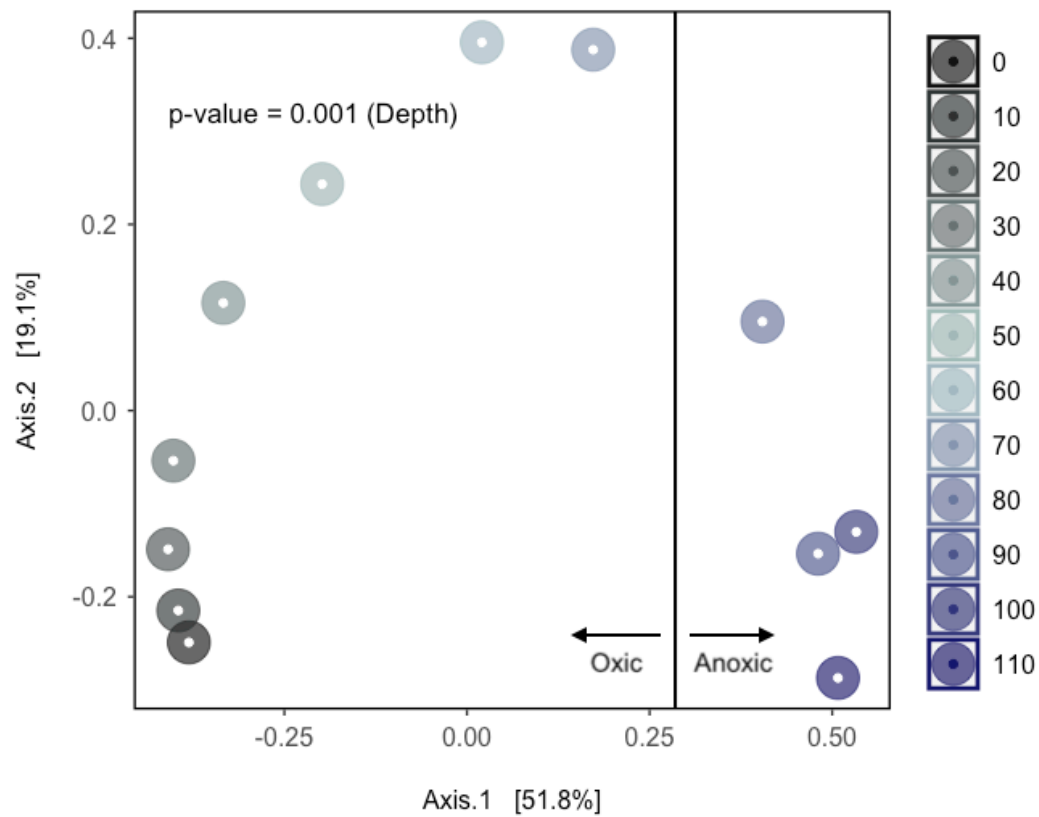


Fig. 2. Principal Coordinate Analysis (PCoA) showing microbial community structure merged across seasons at each STE sediment depth (indicated by color). Depth is labeled with the top depth of the respective core section depth, for example 0 indicates core section 0-10 cm. Sample dissimilarity was calculated using the Bray-Curtis dissimilarity index and a multivariate permutational analysis of variance (PERMANOVA) was used to analyze amplicon sequence variant (ASV) dissimilarity with depth (p -value < 0.001) and season (p -value > 0.05).

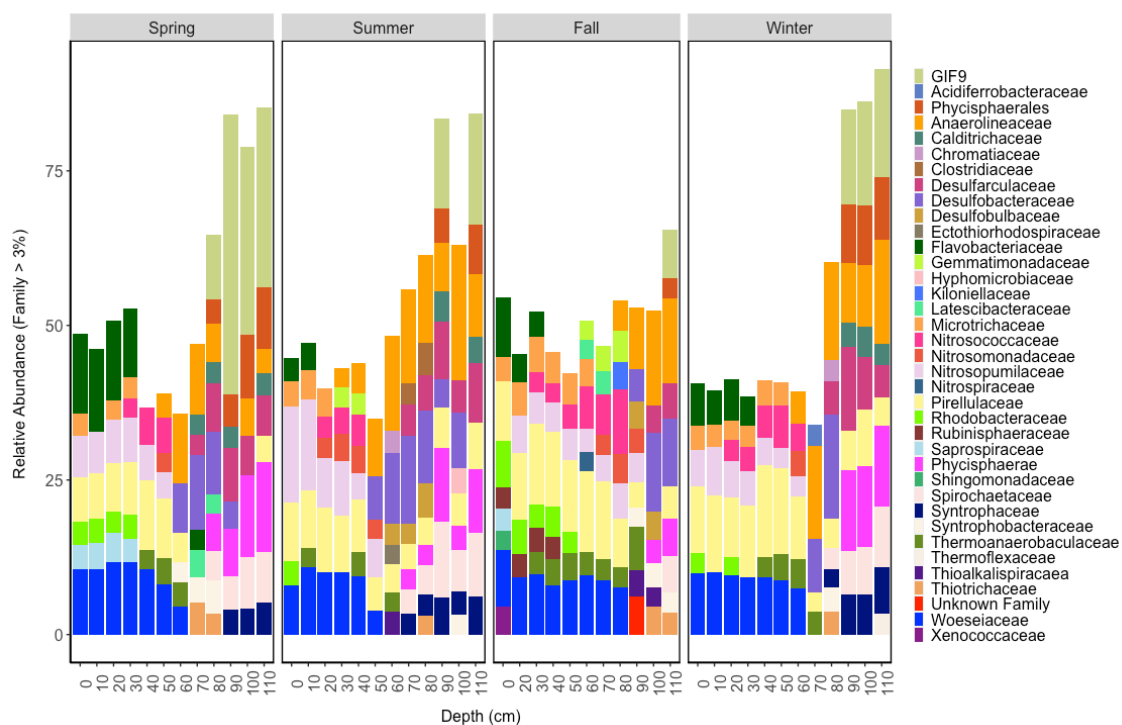


Fig. 3. Sediment community composition (Family level) at each depth and season sampled at the GP-STE. Depth is labeled with the top of the respective core section depth, where 0 indicates the 0-10 cm section of the core.

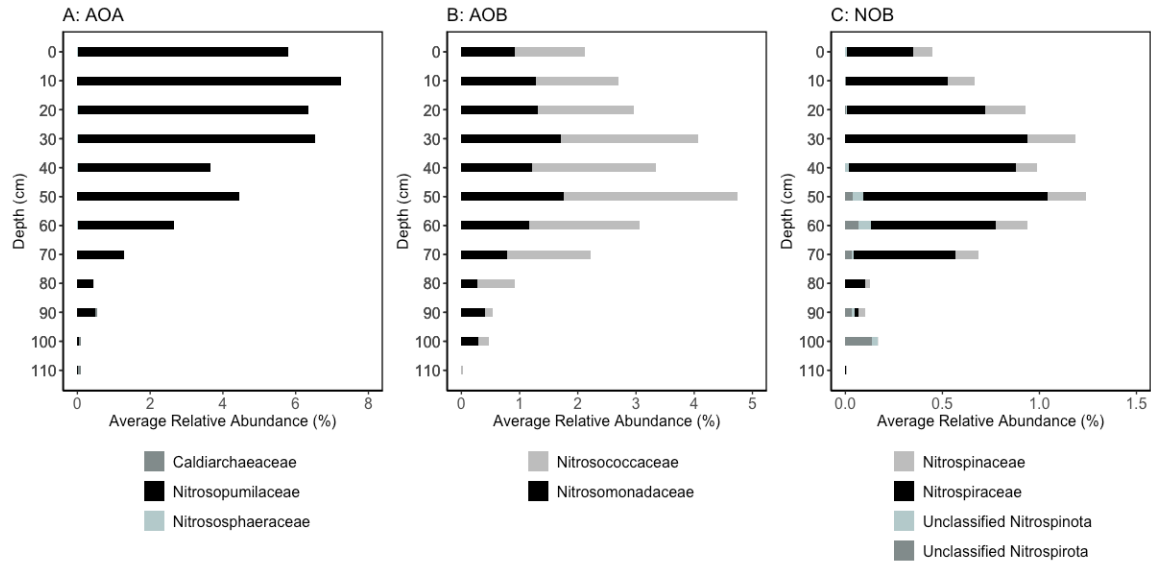


Fig. 4. A) AOA, B) AOB, and C) NOB community composition shown as average relative abundance (number of specific ASVs/total number of sample 16S ASVs x 100%) at the family level averaged across seasons sampled at each depth interval in the GP-STE. Depth is labeled by the top of the respective core section depth, where 0 indicates the top of core section 0-10 cm.

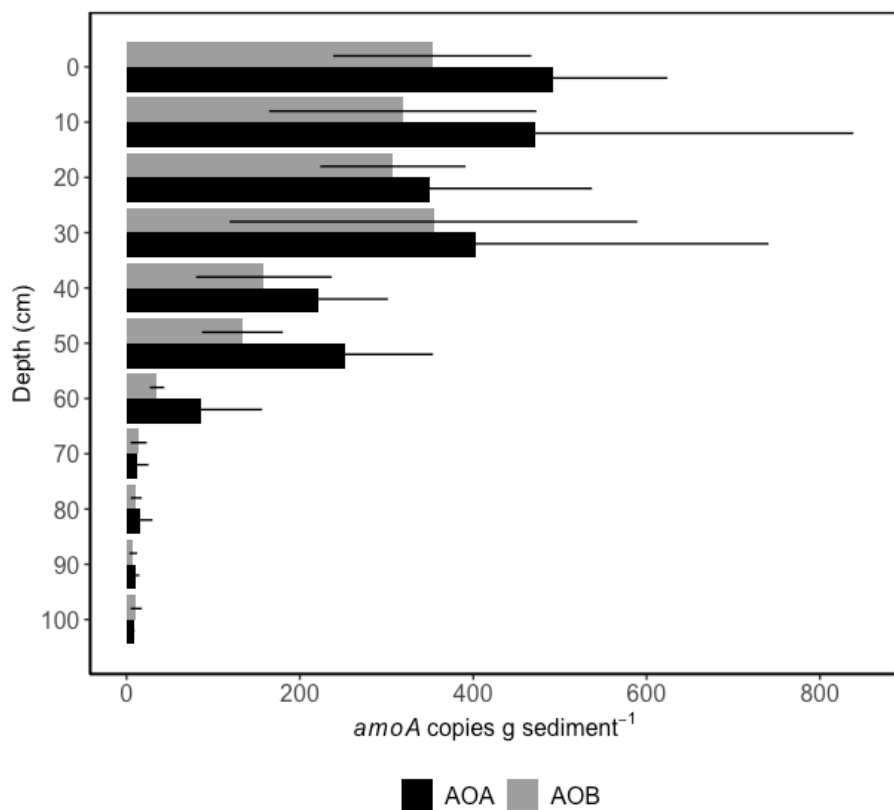


Fig. 5. Abundance of archaeal (black) and bacterial (grey) *amoA* genes (copies g sediment⁻¹) at each sediment depth averaged across seasons sampled at the GP-STE where 0 indicates core section 0-10 cm; error bars represent one standard deviation in each direction.

3.10. Appendix C

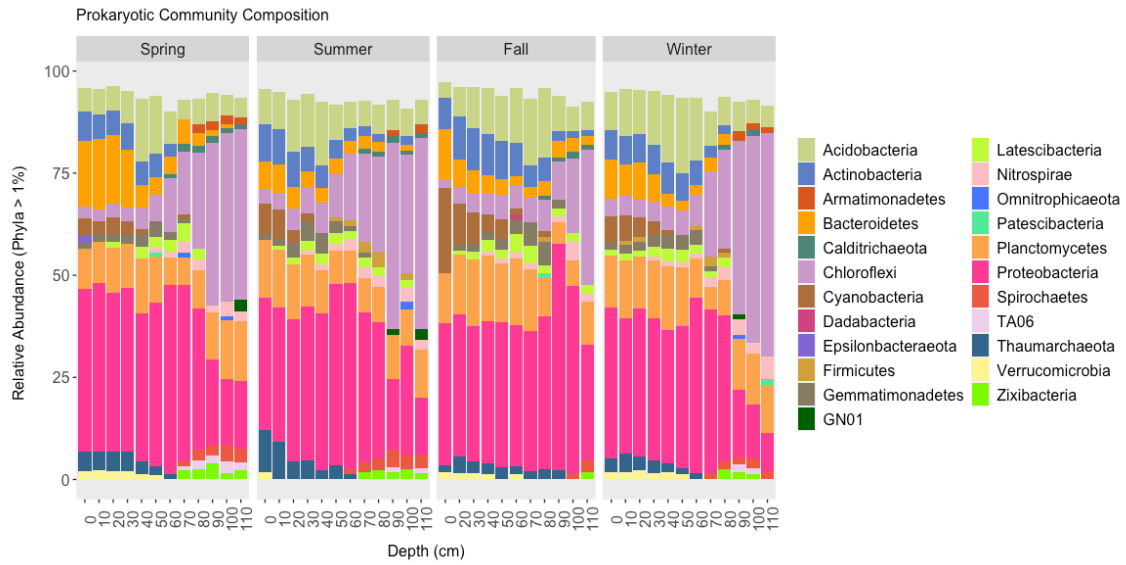


Fig. S1. 16S metabarcoding analysis presenting the sediment community composition (Phylum level) for each season at each depth sampled at the GP-STE.

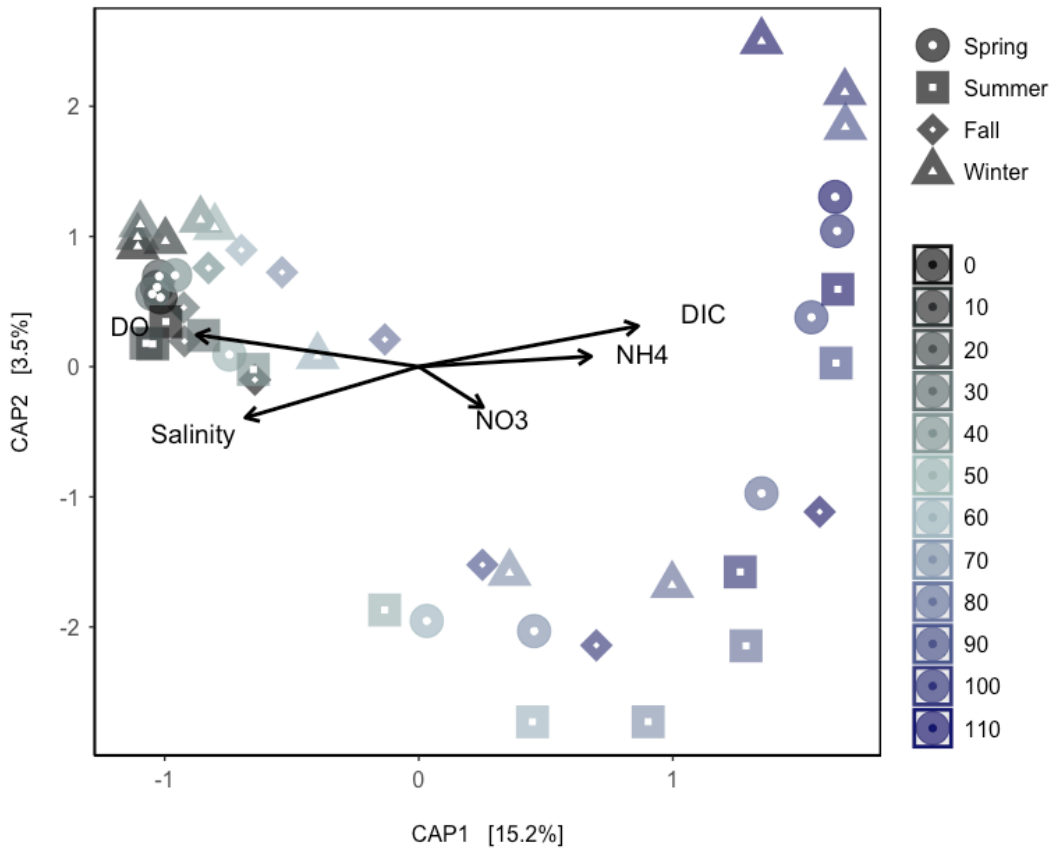


Fig. S2. A canonical analysis of principal coordinates (CAP) plot of sediments community structure in the GP-STE by season (shape) and depth (color). Sample dissimilarity was calculated using the Bray-Curtis dissimilarity index. A multivariate permutational ANOVA (PERMANOVA) was used to analyze ASV dissimilarity with depth ($p = 0.001$) and season ($p > 0.05$).

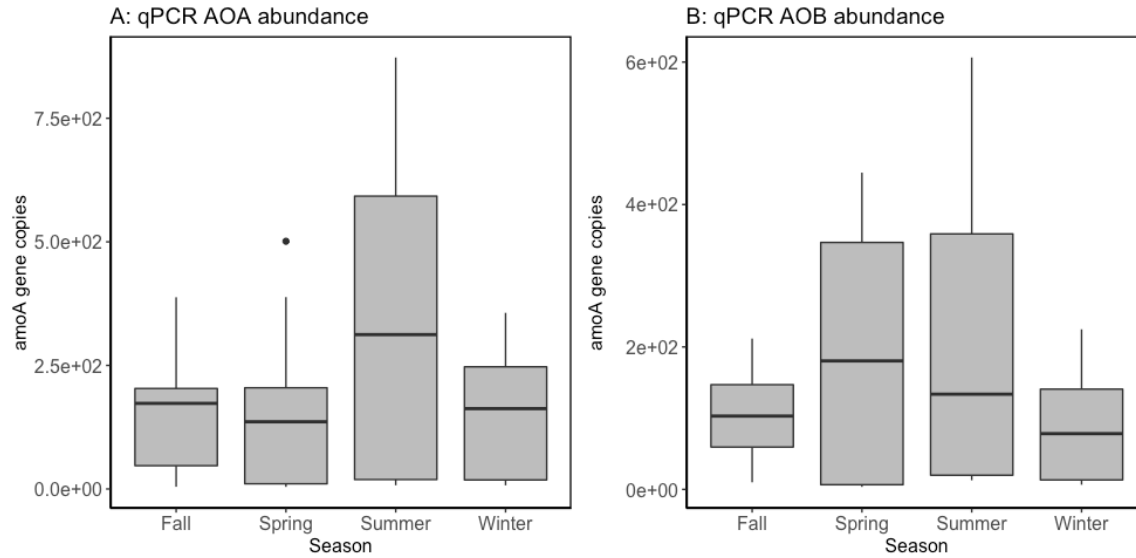


Fig. S3. Comparison of AOA (A) and AOB (B) abundances in each season determined by qPCR of *amoA* genes. An ANOVA indicated that the numbers of AOA and AOB did not vary significantly with season.

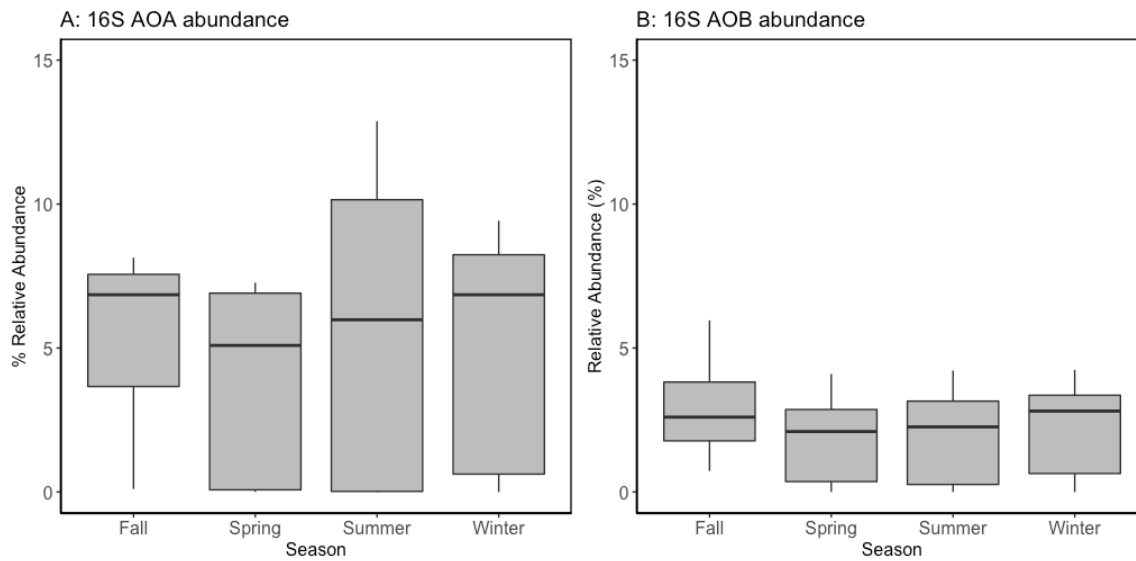


Fig. S4. Comparison of relative abundance of AOA (A) and AOB (B) communities (both *Gammaproteobacterial* and *Betaproteobacteria*) as determined by 16S sequencing. An ANOVA indicated that the relative abundance of AOA and AOB did not vary significantly with season.

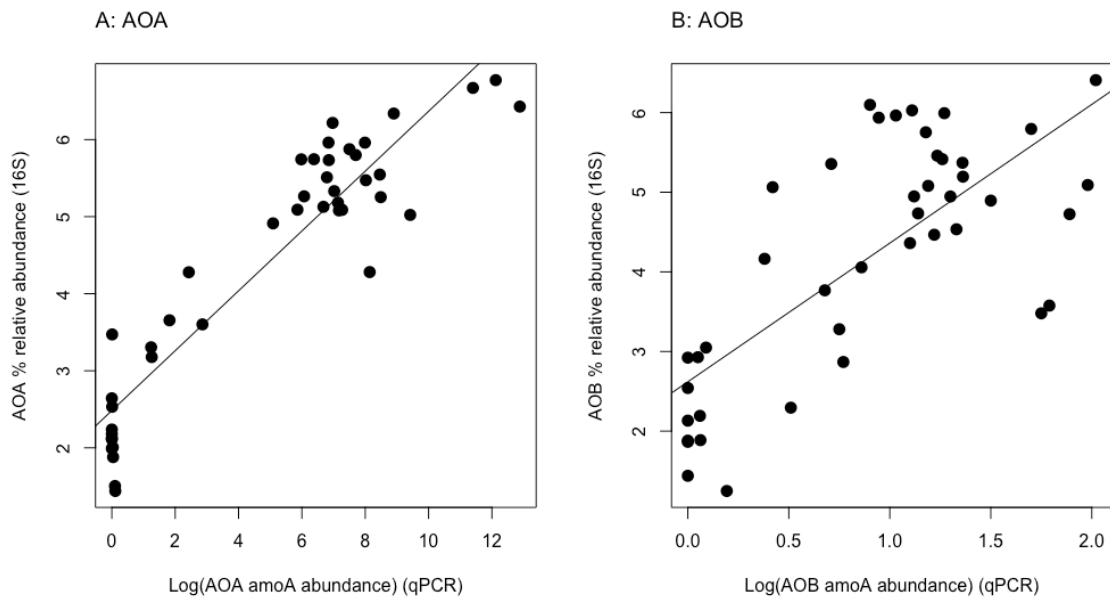


Fig. S5. A) Comparison of AOA abundance as determined by 16S sequencing and qPCR, $R^2=0.86$. B) Comparison of *Betaproteobacterial* AOB abundance as determined by 16S sequencing and qPCR (B), $R^2=0.52$.

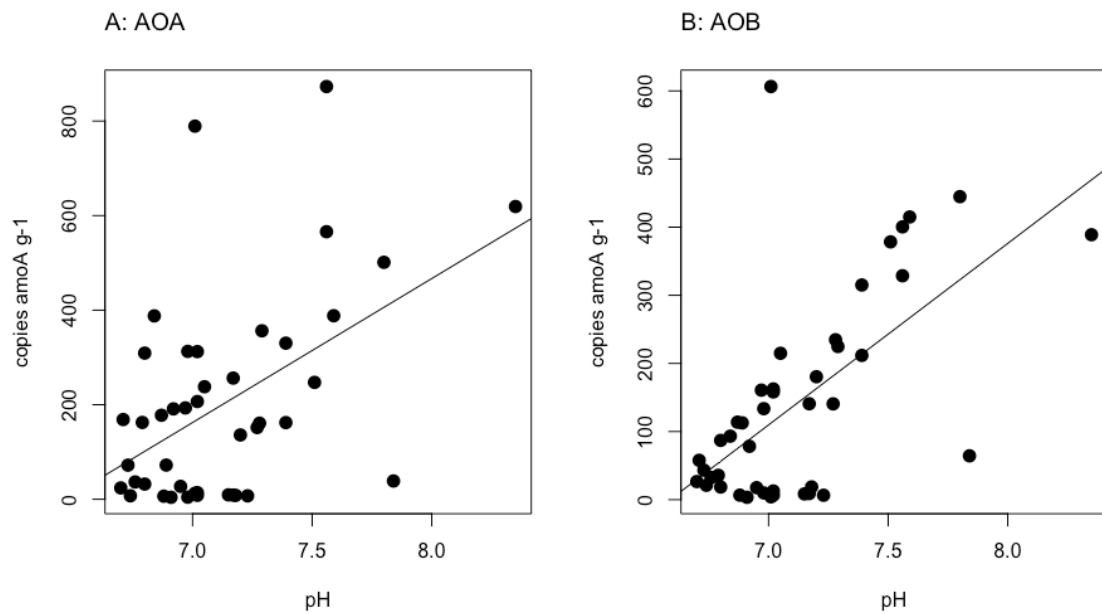


Fig. S6. A: AOA) Archaeal *amoA* copies compared to porewater pH; line signifies a linear model: AOA *amoA* ~ pH, $R^2 = 0.22$ (p -value < 0.001). B: AOB) Bacterial *amoA* copies compared to porewater pH; line signifies a linear model: AOB *amoA* ~ pH, $R^2 = 0.36$ (p -value < 0.001).

3.11. Appendix D

All raw data collected in Chapter 3 has been made publicly available via the BCO DMO site, the links to this data are shown below:

Geochemical profile data:

<https://www.bco-dmo.org/dataset/807664/data>

16S rRNA Sequences:

NCBI with accession number: PRJNA804121

(Submission ID: SUB1104170)

qPCR abundances of AOA and AOB:

BCO-DMO submission in progress

Chapter 4. Nitrification in a subterranean estuary: an *ex situ* and *in situ* method comparison determines nitrate is available for discharge

4.1. Abstract

Subterranean estuaries (STEs) form in the subsurface along the coastline at the interface of groundwater and seawater. STEs are highly reactive zones, supporting a variety of biogeochemical processes including those transforming nitrogen (N). Groundwater can be enriched with dissolved inorganic nitrogen (DIN), and the transformations that occur in the STE determine the fate of that DIN. Nitrification oxidizes ammonium (NH_4^+) to nitrate (NO_3^-) and is a critical process in the N cycle, making DIN available for N removal and influencing DIN mobility in the subsurface. We measured nitrification at the Gloucester Point Beach STE (GP-STE), located in Virginia, USA using both *in situ* and *ex situ* methods including conservative mixing models informed by *in situ* geochemical profiles, an *in situ* experiment with $^{15}\text{NH}_4^+$ tracer injection, and *ex situ* sediment slurry incubations with $^{15}\text{NH}_4^+$ tracer addition. All methods indicated active nitrification, but the *in situ* tracer experiment revealed higher rates than sediment slurry incubations and mixing model estimations (p-value < 0.05). Estimates of nitrification rates in the top 50 cm of the STE ranged from 10.53 to 69.22 $\mu\text{moles N m}^{-2} \text{d}^{-1}$ based on the mixing models; from 94.21 to 225.10 $\mu\text{moles N m}^{-2} \text{d}^{-1}$ in the *in situ* tracer experiment and from 36.57 to 109.02 $\mu\text{moles N m}^{-2} \text{d}^{-1}$ in the sediment slurry incubations. The *in situ* tracer experiment revealed substantially higher nitrification rates and spatial variation that were not captured by the other methods. The geochemical complexity of the STE makes it difficult to replicate *ex situ* and modeled chemical profiles yield net rate estimates, therefore, *in situ* approaches may best quantify transformation rates in the STE. Our data suggest that nitrification in the STE produces

NO₃⁻-enriched groundwater, which may be discharged to overlying water.

4.2. Introduction

As groundwater is transported to the coastal ocean, it passes through the subterranean estuary (STE), a transition zone along the land-ocean continuum where groundwater and seawater meet and mix (Moore, 1999). The mixture of groundwater and recirculated seawater that forms in the STE can then be released to the coastal ocean as submarine groundwater discharge (SGD) (Moore, 1999; Santos *et al.*, 2021). Groundwater may be a source of nitrogen (N) to coastal waters, where N is a limiting nutrient regulating phytoplankton growth (Nixon, 1995; Cho *et al.*, 2018). N accumulates in groundwater along the subsurface flow-path and can be supplied by organic matter remineralization, atmospheric deposition, wastewater or septic leaks, and fertilizer leachate (Cole *et al.*, 1993, 2006; Valiela *et al.*, 1997).

STEs are recognized as important zones where biogeochemical processes influence the concentration and speciation of nutrients, trace metals, and carbon (Santos *et al.*, 2008; Santoro, 2010; Anschutz *et al.*, 2016; Beck *et al.*, 2017). STEs are highly variable and biogeochemically active, the result of shifting hydraulic gradients, tidal pumping, wave set up, and steep geochemical profiles (Slomp and Cappellen, 2004). Biogeochemical cycling within STEs is especially important to groundwater derived N, as it determines the concentration and speciation of N in SGD (Santos *et al.*, 2021; Wilson *et al.*, 2022a). The form of N present in groundwater is central to its fate in the STE and to the overlying water after discharge.

Suboxic and anoxic aquifers are often enriched in ammonium (NH₄⁺) as compared to oxic aquifers that tend to be enriched in nitrate (NO₃⁻) (Smith *et al.*, 2015). Within the subsurface, ammonia oxidation oxidizes NH₄⁺ to nitrite (NO₂⁻), which may then be oxidized by nitrite oxidation to NO₃⁻; collectively referred to here as nitrification. Nitrifying organisms have been

previously observed in STEs (Santoro *et al.*, 2008; Hong *et al.*, 2019; Wilson *et al.*, 2022b) and considering the estimated high export of DIN in SGD (Cho *et al.*, 2016), nitrification is likely an important process in the subsurface N cycle. It is considered a gate-keeping step in the N cycle as it makes reduced N available to microbial N removal processes such as denitrification or anaerobic ammonium oxidation (anammox) (Ward, 2013). This process also influences the mobility of groundwater N as NO_3^- is more mobile than NH_4^+ and may be more likely to be discharged. Nitrification, therefore, is important to determining the form and concentrations of N in STEs.

There are both *ex situ* and *in situ* approaches for estimating nitrification rates in the environment and each method has inherent advantages and disadvantages. Isotope based approaches, such as isotope dilution or tracer methods, have become the standard for *ex situ* incubations. The isotope pool dilution method involves the addition of ^{15}N -labeled NO_3^- to a sediment slurry or core incubation. The added ^{15}N pool is diluted over time by the production of $^{14}\text{NO}_3^-$ as the existing $^{14}\text{NH}_4^+$ pool is oxidized, allowing for calculation of ambient or actual rates of nitrification (Ward, 2011; Jäntti *et al.*, 2012; Lisa *et al.*, 2015). Despite the benefit of not altering substrate concentrations, the isotope pool dilution method has several limitations, including a high minimum detection limit, long incubation times (2-14 days), a limited ability to determine rates in samples with high ambient NO_3^- concentrations, and NO_3^- loss by denitrification before dilution (Enoksson, 1986).

The isotope tracer method involves the addition of ^{15}N -labeled NH_4^+ to track its oxidation to $^{15}\text{NO}_2^-$ and $^{15}\text{NO}_3^-$ (collectively $^{15}\text{NO}_x$) as a measure of nitrification rates (Enoksson, 1986; Jäntti *et al.*, 2012). This method is highly sensitive, but if not aerated properly $^{15}\text{NO}_x$ produced may be denitrified prior to measurement and, because tracer substrate is added, this method is often

considered to estimate potential rates (Enoksson, 1986). To more closely approximate rates in the subsurface, the $^{15}\text{NH}_4^+$ approach has been applied *in situ* in aquifers and groundwater (Böhlke *et al.*, 2006; Smith *et al.*, 2006). During *in situ* tracer experiments, extracted groundwater or porewater is amended with a ^{15}N -labeled substrate (e.g. NH_4^+ for nitrification measurements), and conservative tracers, such as bromide or sulfur hexafluoride (SF_6), then injected into the subsurface creating a tracer plume (Addy *et al.*, 2002; Böhlke *et al.*, 2006; Smith *et al.*, 2006). The plume is sampled over time from the same injection well or from target wells to track movement of tracer from substrate to product pools along undisturbed flow paths to examine transport and fate of the conservative tracer and the ^{15}N -substrate, which can be identified isotopically in N product pools (NO_x , N_2O , N_2 , etc.). This method by-passes any bottle or mesocosm incubation effects as well as collection artefacts since the measurements are made *in situ*; however, these experiments can be high risk as subsurface flow paths are often unpredictable.

Another approach resulting in an *in situ* approximation of net nitrification are conservative mixing curve calculations. In these estimations, salt serves as a conservative tracer to assess non-conservative behavior of NH_4^+ and $^{15}\text{NO}_3^-$. Conservative mixing models were originally developed for, and applied to, surface estuaries (Boyle *et al.*, 1974; Officer and Lynch, 1981), but have since been applied to STEs (Ullman *et al.*, 2003; Santos *et al.*, 2009). Two endmember conservative mixing calculations assume homogeneous mixing of fresh and saline water, that there are only two endmembers in the system, and that these endmembers are constant over space and time. These calculations allow for a simple estimation of net rates and biogeochemical cycling over the timescale of water residence times, but are not a direct measurement.

In contrast to characterization of nitrate removal via denitrification in STEs receiving high nitrate groundwater (Kroeger and Charette, 2012), rates of nitrification in STEs receiving high NH_4^+ groundwater, despite their potential importance for determining speciation and load of groundwater N delivered to coastal waters, remain unconstrained. Given the assumptions and limitation of all methods, combined with potential spatial and temporal variability, rates in the subsurface may best be constrained by applying a multi-technique approach. In this study, we examined the fate of groundwater derived N in the sandy sediment Gloucester Point Beach STE, Virginia, USA. We conducted a method inter-comparison including *in situ* and *ex situ* approaches to estimate nitrification rates in the STE. We hypothesized that nitrification converts NH_4^+ to NO_3^- in the STE, which is then exported to the overlying water via tidal pumping and SGD.

4.3. Methods

4.3.1. Study Site Description and Experimental Set up

This study was conducted at the Gloucester Point Beach STE (GP-STE, 37.248884°N, 76.505324°W), which is located along the York River Estuary, a tributary of the Chesapeake Bay. The GP-STE is a well-studied system where groundwater discharge to overlying water has been observed (Luek and Beck, 2014; Beck *et al.*, 2016; Wilson, Anderson, Song, *et al.*, 2022). It is a sandy sediment beach; approximately 30 m long with a rock jetty on either side and a tidal height of roughly ~0.8 m; a detailed site description can be found in Beck *et al.*, (2016). Groundwater at this site is NH_4^+ rich ($>200 \mu\text{M}$), but in the STE profile where salinity increases, and surface and groundwater appear to be mixing, a NO_3^- ($>50 \mu\text{M}$) peak has been observed. We hypothesize that high concentration NH_4^+ is advected upwards into the oxic portion of the STE and nitrification is responsible for the observed DIN profiles (Wilson *et al.*, 2022a).

In order to estimate nitrification rates in the oxic portion of the STE, three methods were used; conservative mixing models, an *in situ* tracer experiment, and *ex situ* sediment slurry incubations. Conservative mixing models were constructed from *in situ* geochemical characteristics of STE porewater collected seasonally in 2018-2019 from dedicated piezometers (wells) installed at the GP-STE as described by Wilson *et al.*, (2022a). An *in situ* tracer experiment was conducted at the GP-STE in 2019 in two wells, targeting 50 cm depth in the oxic zone. The *ex situ* sediment slurry incubations were conducted in 2020. Sediment cores were collected from the beach adjacent to the existing GP-STE wells, from which porewater (0-50 cm) was collected for addition to the slurries. Each measurement method is described in detail below:

4.3.2. Conservative Mixing Models

Porewater samples were collected in four seasons from dedicated piezometers and analyzed for sample salinity and concentrations of NH_4^+ and NO_3^- as described by Wilson *et al.*, (2022a). Profiles used here included samples taken every ten centimeters from surface water (0 cm) to 110 cm in the subsurface. The vertical salinity distribution was used to construct conservative two endmember derived mixing lines for NH_4^+ and NO_3^- extending from surface water (0 cm) to 110 cm. Conservatively mixed NH_4^+ and NO_3^- concentrations were calculated from fractions of fresh and salt water endmembers and their respective NH_4^+ and NO_3^- concentrations according to:

$$C_i = (f_{sw-i} * C_{sw}) + (f_{gw-i} * C_{gw}) \quad (\text{Equation 1})$$

Where C_i is the calculated concentration for a given depth interval, C_{sw} is the surface water endmember concentration, C_{gw} is the groundwater endmember concentration, f_{sw-i} and f_{gw-i} are the fractions of saline surface water and fresh groundwater, respectively calculated as:

$$f_{sw-i} = (S_i - S_{gw}) / (S_{sw} - S_{gw}) \quad (\text{Equation 2})$$

Where f_{sw-i} is the fraction of saline surface water at a given depth in the STE, S_i is the salinity of porewater at that depth, S_{gw} is the salinity of the groundwater endmember, and S_{sw} is the salinity of the surface water endmember. The fraction of fresh groundwater (f_{gw-i}) at a given depth in the STE was determined as:

$$f_{gw-i} = 1 - f_{sw-i} \quad (\text{Equation 3})$$

As described in Santos et al., (2008), these data were determined to exhibit either linear mixing (conservative), removal, or production. Surface water (0 cm) and porewater samples (110 cm) served as the surface water and freshwater endmembers, respectively, to represent the DIN concentrations in water bodies directly above and below the top 100 cm of the STE, which encompasses the mixing zone of fresh groundwater and overlying saline water. The endmember concentrations were used to calculate the conservative mixing line, which represents the predicted analyte concentrations resulting from mixing of surface water (saline) and groundwater (fresh) alone.

The observed concentrations of NH_4^+ and NO_3^- were compared to the predicted concentrations to determine subsidies or deficits in NH_4^+ and NO_3^- respectively along the STE salinity gradient. The disparity between the predicted, conservative concentrations and the observed concentrations represents the production or consumption of the analyte (Figure 1). The integrated mass of N in the NO_3^- subsidy and NH_4^+ deficit relative to conservative mixing was converted to a net nitrification rate using equation 1:

$$R_1 = \frac{1}{t} \int_{low\ salinity}^{high\ salinity} (C_r - C_s) dS \quad (\text{Equation 4})$$

Where R_1 is the rate ($\mu\text{moles}/\text{L}/\text{day}$), t is the STE residence time, which was 46 days as determined for the GP-STE using radium isotopes by Beck et al. (2016), C_r is the observed concentration ($\mu\text{moles L}^{-1}$), C_s is the predicted concentration due to mixing alone ($\mu\text{moles L}^{-1}$),

and dS is the salinity change. The area between C_s and C_r is integrated, resulting in the amount of NH_4^+ removed or NO_3^- produced along the salinity gradient in $\mu\text{moles L}^{-1} \text{d}^{-1}$. The rate is converted to per m^2 using the following equation:

$$R_2 = R_1 * (\Phi * D_{mix}) \quad (\text{Equation 5})$$

Where R_2 is the per area NH_4^+ loss or NO_3^- production rate along the STE salinity gradient ($\mu\text{moles m}^{-2} \text{d}^{-1}$), R_1 is the loss rate (as determined by equation 1), Φ is the porosity of the GP-STE sediment (0.3) measured by O'Connor *et al.*, (2018), and D_{mix} is the depth of the assumed mixing zone (0-100 cm) that encompasses the STE salinity gradient. This approach yields a per square meter rate averaged over the 100 cm.

4.3.3. In situ experiment with $^{15}\text{NH}_4^+$ tracer injection

The *in situ* $^{15}\text{NH}_4^+$ tracer experiment was conducted in the summer of 2019 in the surficial, oxic sediments of the GP-STE to directly measure nitrification (complete oxidation of NH_4^+ to NO_x) under field conditions. The experiment was conducted as a hybrid single/two well, modified push-pull tracer test similar to that described by Addy *et al.*, (2002), but with $^{15}\text{NH}_4^+$ tracer. Two duplicate clusters of dedicated piezometers were installed, as described by Wilson *et al.*, (2022a), three meters apart along the mid-tide line. Each well cluster included an injection well, installed at 50 cm, and monitoring wells above and below the injection site at 40 and 60 cm. The 50 cm depth was chosen because it represents the top of the STE mixing zone, where anoxic, NH_4^+ rich groundwater is mixing with oxic surface water, forming an interface that may support nitrification. The 50 cm also represents the middle of the depth range over which the conservative mixing estimates were made, and corresponds to the depth of sediment collection used in the *ex situ* tests (next section). One meter in front of the injection well clusters, a tracer well was installed to a depth of 50 cm, with wells above and below at 40 and 60 cm,

respectively. Measurements of dissolved oxygen (DO), salinity, pH, and porewater nutrient concentrations were made prior to the tracer injection to determine background site conditions.

To prepare for injection, five liters of porewater were collected from the duplicate injection wells (50 cm) using an Alexis V3.0 peristaltic pump (Proactive Environmental Products) and gas impermeable tubing (MasterFlex C-Flex Ultra, Cole Parmer) to fill Flex foil bags that had previously been evacuated. Porewater was transported to the lab at *in situ* temperature in 10L FlexFoil Sample Bags (SKC Inc.) where it was amended with $^{15}\text{N-NH}_4^+$ (99 atm%, Cambridge Isotope Laboratories, Inc.) and sulfur hexafluoride (SF_6 , Scott Specialty Gases, Inc.) to final concentrations of $15 \mu\text{M } ^{15}\text{NH}_4^+$ and $15 \mu\text{M SF}_6$. The $^{15}\text{NH}_4^+$ tracer concentration was chosen to match previously measured NH_4^+ concentrations at this depth. The amended injectate was agitated for 12 hours at *in situ* temperature using an orbital shaker to allow for equilibration of the tracer amended porewater. After equilibration, the injectate was pumped back into the injection wells (50 cm) with a peristaltic pump at a rate of $\sim 20 \text{ mL min}^{-1}$ over four hours to minimize dispersion artifacts and to not artificially increase hydraulic head (Figure 2). Porewater samples were collected from the injectate bag and from the injection wells immediately following tracer addition and at regular time intervals over the following days. At each sampling time point, samples of porewater SF_6 and DIN were collected from the injection wells using a peristaltic pump (Proactive Environmental Products) and gas impermeable tubing (MasterFlex C-Flex Ultra, Cole Parmer). Samples for SF_6 were collected in 30 mL serum bottles and crimp-capped. The concentration of SF_6 in porewater was determined with a gas chromatograph fitted with an electron capture detector (GC-ECD, Shimadzu). Samples for determination of DIN concentrations and isotopic composition were filtered with a $0.45 \mu\text{m}$

disposable groundwater filter capsule (Millipore Sigma) into 50 mL falcon tubes that were placed on ice, transported to the lab, and frozen until analysis.

4.3.4. Ex situ sediment slurry incubations with $^{15}\text{NH}_4^+$ tracer addition

Three replicate sediment cores (50 cm in length) were collected from the GP-STE in the summer of 2020. The cores were sectioned into 10 cm increments and homogenized. Porewater was collected at the same time as the cores from surface water (0 cm) and wells at 10 cm, 20 cm, 30 cm, 40 cm as described in Wilson *et al.*, (2022a). Sediment slurries consisting of 10 g homogenized sediment and 40 mL porewater from the same depth section were combined in 100mL HDPE bottles and amended with 5 atom% $15\ \mu\text{M } ^{15}\text{NH}_4^+$ (Cambridge Isotope), similar to that described by Damashek *et al.* (2016) and Santoro *et al.* (2013). Samples were incubated on a shaker table, in the dark, and at *in situ* temperature for 0 (*T0*), 6 (*T1*), and 12 (*T2*) hours. After the incubation period, samples were spun down, porewater was decanted and filtered with a $0.45\ \mu\text{m}$ syringe filter (Whatman GE), and were frozen ($-20\ ^\circ\text{C}$) until analysis.

4.3.5. Analytical methods, Isotopic ^{15}N analysis, and rate calculations

The concentrations of NO_3^- , NO_2^- , and NH_4^+ in all samples were determined with a Lachat autoanalyzer (Lachat Instruments, Lachat QuikChem FIA+ 8000). The isotopic composition of the $^{15}\text{NO}_x$ samples collected during the *in situ* and *ex situ* experiments was determined using a modified version of the bacterial denitrifier method (Sigman *et al.*, 2001) at the UCONN lab. A culture of *Pseudomonas aureofaciens* reduced NO_x in collected samples to N_2O . The isotopic composition of the N_2O was measured with isotope-ratio mass spectrometry (IRMS) (Sigman *et al.*, 2001). Calibrations included laboratory standards (USGS 34 and USGS IAEA-NO-3) with known $^{15}\text{NO}_3^-$ enrichments that were analyzed as samples; reduced using the

P. aureofaciens culture to N₂O and analyzed with IRMS, to confirm method efficiency (Bohlke *et al.*, 1993; Bohlke and Coplen, 1995; Brand *et al.*, 2014).

¹⁵N composition for all data was reported in the delta notation, which was converted to ¹⁵N mole fraction based on:

$$MF_{sample} = \frac{\left(\left(\frac{d^{15}N_{sample}}{1000} + 1 \right) * \frac{^{15}N_{ref}}{^{14}N_{ref}} \right)}{1 + \left(\left(\frac{d^{15}N_{sample}}{1000} + 1 \right) * \frac{^{15}N_{ref}}{^{14}N_{ref}} \right)} \quad (\text{Equation 6})$$

The excess ¹⁵N mole fraction was calculated by subtracting the pre-tracer (background) ¹⁵NO_x mole fraction from the measured ¹⁵NO_x mole fraction in post tracer samples. The excess ¹⁵NO_x mole fraction, multiplied by the measured concentration, yielded the ¹⁵N mass in NO_x attributable to nitrification of the ¹⁵NH₄⁺ as:

$$^{15}N_{mass_{excess}} = MF_{excess} * C_{sample} \quad (\text{Equation 7})$$

Rates of nitrification determined by the *in situ* tracer experiment were calculated as the change in the excess mass of ¹⁵NO_x over time. The ¹⁵NO_x mass was then corrected for the dilution of the ¹⁵NH₄⁺ substrate over time resulting in, what is referred to here as, the nitrified N concentration over time. The evolving mole fraction of ¹⁵NH₄⁺ was calculated based on proportional mixing of the 98 atom% tracer with NH₄⁺ at 0 atom% enrichment. The proportion of each was calculated using the ratio of SF₆ measured in a sample to the SF₆ concentration in the injectate, C/C₀. Only samples from the core of the tracer plume were used for rate calculations; the core of the tracer plume is defined here as samples with a conservative tracer recovery (C/C₀ SF₆) > 0.05%.

Nitrification rates as measured by the *ex situ* sediment slurry incubation were calculated as the change in the excess mass of ¹⁵NO_x over time. Nitrification rates were assumed to be first order and the *ex situ* potential rates were converted to rates at the ambient, background NH₄⁺

concentrations. Rates at ambient concentrations were estimated by dividing the potential rate by the added experimental concentration (15 μM) and multiplying by the *in situ* combined porewater and extractable NH_4^+ sample concentration (1.64 - 6.95 μM).

4.4. Results

4.4.1. Nitrification rates estimated by conservative mixing models

Spatial and temporal variations in GP-STE geochemical profiles were reported in detail in Wilson *et al.*, (2022a). Briefly, NO_3^- concentrations were low ($< 10 \mu\text{M}$) at depths deeper than 90 cm, whereas at the mid-salinity, mid-depth (40-90 cm) concentrations were much higher and, in some instances, exceeded 50 μM (Figure 3A). In contrast, NH_4^+ concentrations were $> 50 \mu\text{M}$ in groundwater deeper than 90 cm, but were $< 10 \mu\text{M}$ in surficial, higher salinity porewater (0-50 cm) (Figure 3B). Groundwater NO_2^- concentrations were always $< 0.5 \mu\text{M}$. The NO_3^- and NH_4^+ mixing curves indicated two endmembers; fresh groundwater and overlying surface water (Figure 3C, D). When observed NO_3^- concentrations were compared to predicted, conservative values along the STE salinity gradient, the observed concentrations were higher than those predicted (Figure 3C). In contrast, observed porewater NH_4^+ concentrations were lower than predicted values determined by conservative mixing (Figure 3D).

The NO_3^- subsidies and NH_4^+ deficits in the GP-STE, as compared to the conservative mixing lines, were observed in all seasons (Figure 4). Nitrification rates in the top 100 cm of the STE were derived from net production and consumption of NO_3^- and NH_4^+ , respectively. NO_3^- production derived from conservative mixing calculations in the top one meter of the STE resulted in nitrification rates that ranged from 39.35 to 181.25 $\mu\text{moles N m}^{-2} \text{d}^{-1}$. Rates of nitrification based on NH_4^+ consumption ranged from 53.50 to 84.70 $\mu\text{moles N m}^{-2} \text{day}^{-1}$ (Table

1). The highest rate of NO_3^- production was observed in summer and the lowest in winter whereas the highest rate of NH_4^+ consumption was observed in fall and the lowest in spring.

4.4.2. Nitrification rates measured by an *in situ* $^{15}\text{NH}_4^+$ tracer injection experiment

In situ $^{15}\text{NH}_4^+$ tracer experiments were conducted to measure nitrification rates and determine the fate of N in the GP-STE. Injection sites had similar biogeochemical conditions of DO, salinity, pH, and DIN concentrations (Table 2) based on background porewater sampling. The 50 cm depth is oxic and brackish and within the groundwater-surface water mixing zone. Injection sites were in the region of the STE where increasing NO_3^- concentrations and decreasing NH_4^+ concentrations were observed (Figure 3A, B).

NH_4^+ concentrations in the injectates were 13.69 and 14.51 μM for injection well #1 and #2, respectively. NH_4^+ concentrations decreased over time and were $< 5 \mu\text{M}$ an hour after injection; ranging from 0.53 to 3.65 μM in all samples (Figure 5C, D). High frequency sampling of STE porewater during the tracer experiment revealed variance in NO_x concentrations overtime, but there was no clear pattern of NO_x production detectable above background concentrations in injection wells (Figure 5A, B). The injection site #1 50 cm tracer well was the only well to exhibit an increase in NO_x overtime (Figure 5A), which could indicate nitrification. The concentrations of NO_x during the *in situ* experiment ranged from 47.4 - 192.3 μM and the NO_x pool was comprised primarily of NO_3^- ; NO_2^- concentrations in all samples were $< 0.22 \mu\text{M}$. Concentrations of the conservative tracer, SF_6 , following tracer injection were initially $> 300 \text{ pM}$, but decreased over time resulting in concentrations of $< 100 \text{ pM}$ SF_6 within 30 hours after injection (Figure 6A, B). Tracer wells consistently exhibited lower SF_6 concentrations as compared to injection wells.

Despite no clear pattern in the concentrations of NO_x in injection wells during the experiment, the enrichment of ^{15}N in NO_x at both injection sites did increase over time, indicating oxidation of the $^{15}\text{NH}_4$ tracer in the STE (Figure 7A, B). The highest $^{15}\text{NO}_x$ enrichments, on the order of ~ 2 atom% ^{15}N . Injection wells in both sites exhibited higher enrichments as compared to the tracer wells (Figure 7A, B). The $^{15}\text{NO}_x$ delta values indicate a decrease in enrichment ~ 40 hours after injection, likely the result of dilution of the $^{15}\text{NH}_4^+$ tracer overtime. When dilution of the $^{15}\text{NH}_4^+$ tracer is accounted for (Section 4.3.4.), the nitrified N produced over time is linear (Figure 8A, B, p-value < 0.05). The *in situ* nitrification rates, based on this increase in $^{15}\text{NO}_x$ overtime, were $7.50 \pm 2.31 \mu\text{moles N L}^{-1} \text{ d}^{-1}$ and $3.14 \pm 0.51 \mu\text{moles N L}^{-1} \text{ d}^{-1}$ in injection sites #1 and #2, respectively. These rates extrapolated to per m^2 become $225.10 \pm 69.23 \mu\text{moles N m}^{-2} \text{ d}^{-1}$ and $94.21 \pm 15.24 \mu\text{moles N m}^{-2} \text{ d}^{-1}$ in injection well #1 and #2, respectively.

4.4.3. Nitrification rates measured ex situ sediment slurry incubations with added $^{15}\text{NH}_4^+$ tracer

Potential nitrification rates were measured in sediment slurries amended with $^{15}\text{NH}_4^+$ tracer. There was no clear pattern in the slurry NH_4^+ concentrations over time, which ranged from 18.39 - 29.09 μM (Figure 9). The NO_x pool was primarily comprised of NO_3^- and NO_2 concentrations were < 0.24 μM in all samples. NO_x concentrations increased over time in all samples (Figure 10A) ranging from 1.86 - 24.42 μM . The concentration of enriched $^{15}\text{NO}_x$ also increased in all incubations, indicating oxidation of the $^{15}\text{NH}_4^+$ tracer to $^{15}\text{NO}_x$ (Figure 10B). Potential nitrification rates ranged from 36.57 ± 3.68 to $109.02 \pm 8.50 \mu\text{moles N m}^{-2} \text{ d}^{-1}$ (Table 3). Rates varied with core depth section; the 10-20 cm core section exhibited the highest production rate, whereas the 30-40 cm core section had the lowest rate.

4.5. Discussion

4.5.1. Mixing model calculations

The observed NH_4^+ and NO_3^- concentrations were compared to predicted concentrations, calculated assuming conservative mixing, along the STE salinity gradient. NH_4^+ consumption and NO_3^- production in the STE, suggesting nitrification, were observed in all seasons.

Nitrification rates determined with mixing model calculations estimated from NO_x production were, when averaged across seasons, higher than those for estimated from NH_4^+ consumption, which may be the result of exchange of NH_4^+ with the sorbed phase.

An integral assumption of conservative mixing calculations is homogeneous mixing, which in this study, would be mixing within the in the top 100 cm of the STE. Vertical profiles of salinity and DO (Wilson *et al.*, 2022a) suggest mixing of groundwater and surface water, but these profiles could represent horizontal features which would mean that fresh groundwater and surficial porewaters are not hydrologically connected. Previous measurements of hydraulic gradients and groundwater seepage indicate vertical groundwater flow in the top 100 cm of the STE and therefore mixing (Beck *et al.*, 2016; Wilson *et al.*, 2022a). However, it is important to recognize that sediments are heterogeneous, so homogeneity of this mixing in the subsurface environment is unlikely. Varying hydraulic conductivities in sediment layers (Ullman *et al.*, 2003), fissures, or bioturbation can complicate subsurface flow paths (Shrivastava *et al.*, 2021). Sediment heterogeneity also influences groundwater residence times, another crucial term in conservative mixing model estimates. Here we used a residence time for the GP-STE estimated with radium isotopes (Beck *et al.*, 2016), but it is likely that the STE residence times vary across different STE reaction zones, with spring-neap tidal cycles, seasons, and hydrologic conditions

(Slomp and Cappellen, 2004), which may be better constrained with long term monitoring of hydraulic gradients.

Endmember concentrations are also important to conservative mixing models as they are integral to calculating the conservative mixing line. At this site, significant variation in the DIN concentrations across space and tidal stage was not observed, but there were significant changes across seasons (Wilson *et al.*, 2022a). This suggests that at this site and in this study, endmembers may be stable over the modeled scale (seasonally); however, STEs are highly variable, and this may not hold true for other sites. Substantial site characterization to verify that the assumptions of conservative mixing are required to ensure reasonable outputs.

4.5.2. In situ tracer experiment

$^{15}\text{NH}_4^+$ was injected into the STE to determine the fate of N under *in situ* conditions. The conservative tracer (SF_6) data indicated that the tracer plume was constrained within the 40-60 cm depth range of the STE and, therefore, our resulting rates can be averaged across this depth interval. Dilution of the tracer plume over time in the experiment was likely driven by tidal pumping, which is known to be an important factor controlling STE biogeochemistry (Slomp and Cappellen, 2004), and groundwater advection. Both tidal pumping and groundwater advection would dilute the SF_6 and $^{15}\text{NH}_4^+$ concentrations in the tracer plume. SF_6 concentrations in overlying water and groundwater outside the plume would have zero SF_6 , so as this water mixes with the tracer plume, the concentrations of SF_6 decrease. This will be similar for $^{15}\text{NH}_4^+$ as there will be essentially no enrichment of organic matter or NH_4^+ in overlying water and groundwater, so as NH_4^+ is produced via remineralization of organic matter or supplied by groundwater advection, the $^{15}\text{NH}_4^+$ in the tracer plume is diluted.

Active nitrification in the STE was revealed by $^{15}\text{N-NO}_x$ enrichment at both injection sites overtime (Figure 7A & B). *In situ* nitrification rates were determined for each injection well. Although both injection sites had similar background geochemical characteristics (Table 2) and wells were placed at the same depth (50 cm), they exhibited different nitrification rates. The variation in the observed rates between wells may be the result of many things, such as a distinctive microbial community structure between well sites, which could include a higher abundance of nitrifiers. Despite being only a few meters apart, it is also possible that there are differences in the physical characteristics of the subsurface environment between the injection sites. Hydraulic gradients and groundwater flow-paths combined with tidal pumping can vary across small spatial scales (Slomp and Cappellen, 2004), influencing the transport of analytes, such as NH_4^+ and dissolved oxygen. The *in situ* experiment, and the subsurface variability it revealed, confirms the complexity of STE systems and the importance of using *in situ* measurements to define a range of possible rates under ambient conditions. Further research, including *in situ* tracer tests, may elucidate the drivers of the observed variation and how this subsurface heterogeneity further influences microbial process rates.

Similar *in situ* tracer approaches have been used to measure denitrification (Addy *et al.*, 2002; Smith *et al.*, 2015) and nitrification (Böhlke *et al.*, 2006; Smith *et al.*, 2006) in groundwater systems. Smith *et al.*, (2006) used *in situ* tracer injections to measure nitrification rates in a Cape Cod, MA, USA aquifer and observed rates ($0.48 - 6.72 \mu\text{moles L}^{-1} \text{d}^{-1}$), which were comparable to those measured in the GP-STE ($3.14 - 7.50 \mu\text{moles L}^{-1} \text{d}^{-1}$). Another aquifer study in Cape Cod used *in situ* tracer measurements to estimate rates of nitrification ($<0.008 \mu\text{moles L}^{-1} \text{d}^{-1}$) which were several orders of magnitude lower than the lowest rates measured in the GP-STE (Böhlke *et al.*, 2006). The GP-STE measurements are higher than those observed in

aquifers likely because the STE represents an interface where biogeochemical dynamics are variable and, therefore, may stimulate higher reaction rates. There are few reported *in situ* tracer measurements of nitrification in STEs; therefore, these rates are a valuable contribution to our understanding of the coastal subsurface N cycle.

4.5.3. Ex situ sediment slurry incubation experiments

Potential nitrification rates were measured in sediment slurry incubations amended with $^{15}\text{NH}_4^+$. Nitrification was evidenced by the increase in the $^{15}\text{NO}_x$ concentrations over time. Rates varied with depth; the highest rates were observed in samples from 10-20 cm and lowest 30-40 cm. Nitrifier abundance or activity and the background NH_4^+ concentrations may drive this variation. Nitrifying prokaryotes have been identified in the GP-STE, revealing genetic potential for nitrification (Wilson *et al.*, 2022b); however, sediment slurry rates did not correlate with reported nitrifier abundance. It should be noted that these studies were not conducted in tandem, so the abundances previously measured may not represent those in the present samples. Also, the presence of nitrifiers, determined by quantification of *amoA* genes in extracted sediment DNA, does not directly relate to nitrifier activity. Nitrification rates did; however, have a positive linear relationship with background porewater NH_4^+ concentrations ($R^2 = 0.33$, Figure 11), suggesting a link between available substrate *in situ* and potential process rates.

Potential nitrification rates determined for the GP-STE were lower than those observed in other coastal sediments. Rates were an order of magnitude lower in the GP-STE ($0.36 - 1.09 \mu\text{moles L}^{-1} \text{d}^{-1}$) than those measured with potential slurry incubations in a sandy beach system on Sapelo Island, GA, USA ($23.52 \pm 3.6 \mu\text{mol L}^{-1} \text{d}^{-1}$) (Schutte *et al.*, 2017). When compared to rates measured in other coastal sediments (Usui *et al.*, 2001; Wankel *et al.*, 2011), potential nitrification rates in the GP-STE were several orders of magnitude lower. It was suggested by

Schutte et al., (2017) that oxygen penetration into the subsurface drove nitrification rates and likely played a role in organic matter remineralization. Nitrification in the surficial 50 cm of the GP-STE is not limited by dissolved oxygen as concentrations are > 3.5 mg/L throughout the year, therefore, observed low rates may be the result of low NH_4^+ supply. The GP-STE sediments have low organic content (Wilson *et al.*, 2022a) and NH_4^+ delivery to the oxic zone by groundwater advection is likely low, but NH_4^+ may also be supplied by remineralization of organic matter in recirculated York River water.

Sediment slurry incubations with $^{15}\text{NH}_4^+$ tracer are considered potential rate measurements as oxic conditions and ample substrate concentrations were maintained throughout the incubation period (Hansen *et al.*, 1981), but rates at ambient concentrations were calculated assuming first order kinetics. Slurry incubations require removal of sediment from the environment, disrupting naturally occurring geochemical gradients and hydrogeological conditions, which may alter process rates. The top 50 cm of the STE, the depth range used in these incubations, is oxic, so oxygenation of these sediments was not a concern, but should be considered when determining process rates in deeper, anoxic sediments. Slurry incubations, once amended with the $^{15}\text{NH}_4^+$ tracer, represent a closed system with no inputs or outputs. These incubations, therefore, do not account for the dynamic *in situ* conditions observed in STEs. Groundwater advection, tidal pumping, and wave action are all excluded from these process rates, which could be important drivers of nitrification and substrate availability. Laboratory incubations are inherently biased by this closed system approach, potential bottle effects, and the assumption that the mesocosm is representative of the larger system. Sample size limitations often make these assumptions a necessity, but it is important to note the loss of spatial and

temporal heterogeneity. This could include variation in the microbial community structure as well as substrate availability and delivery, which control processes such as nitrification.

4.5.4. Comparing nitrification rate measurement with different methods

There are few studies that compare process rates using different approaches of measurement methodologies. In this study, all three methods suggested active nitrification in the GP-STE at varying rates, although the *in situ* tracer experiment showed higher rates than other estimations (Figure 12, p-value < 0.05). In order to compare the conservative mixing model calculations to the direct measurements, loss or production in only the top 50 cm of the STE were used to match the depth range used for sediment slurry and *in situ* tracer experiments (Table S1). Rate estimations by mixing models may be biased by the inherent assumptions associated with conservative mixing calculations, such as homogeneous mixing, a static residence time, and constant endmembers, which may not represent the dynamic STE. There may also be a missing model term, which could degrade the ability of the model to replicate the system. It is possible that with higher frequency sampling of the STE, allowing for higher model resolution, rates may better replicate those observed with direct measurements. Despite these issues with representing the complexity of subsurface systems, conservative mixing models are a useful tool to obtain a preliminary understanding of processes occurring in STEs and determine which tools are needed to directly measure process rates.

Similarly, there are challenges associated with obtaining process rates from sediment slurry incubations. Microcosm incubations, such as slurries, are typically underestimations of true rates (Addy *et al.*, 2002) and require disrupting STE geochemical gradients. The oxygenated conditions of the surficial STE and lack of N removal likely allowed for the similarity between slurry and initial *in situ* tracer rates at this site. However, when sediments are anoxic or sampled

across an oxic-anoxic boundary allowing for coupled nitrification-denitrification, potential slurry rates will not accurately represent the system as aerobic conditions prevent denitrification. Sediment slurries are simple, useful tests to confirm other measurements and geochemical profiles, but because they isolate processes from the complex biogeochemistry and variable physical characteristics of the subsurface environment, their ability to determine the fate of N *in situ* is limited.

The *in situ* tracer experiments revealed spatial variation in nitrification rates measured in this study, which could be due to changing environmental conditions, such as fluctuations in geochemical gradients, tidal pumping, and groundwater advection throughout the experiment and between injection sites. Despite agreement between all measurements, the sediment slurry incubations and conservative mixing model estimations did not elucidate the same variation observed in nitrification rates *in situ*. It is impossible to replicate the complicated and variable conditions of STEs, which are influenced by a range of abiotic and biotic factors (Slomp and Cappellen, 2004; Russoniello *et al.*, 2016). The *in situ* tracer method is complex, but is likely the best available measurement of reactivity, process rates, and fate of groundwater derived constituents. They provide a better understanding of the subsurface environment, the role STEs play in groundwater N concentrations and speciation, and do not isolate processes from other subsurface reactions. If possible, a variety of sampling methods should be used to confirm observations, assess variation in process rates across space and time, and determine the impact of these processes on coastal environments.

The nitrification rates determined in this study were lower than those measured in other coastal sediments such as those in a Monterey Bay estuary, CA, USA (Wankel *et al.*, 2011), the Tama Estuary, Japan (Usui *et al.*, 2001), and at Sapelo Island, GA, USA (Schutte *et al.*, 2017).

The GP-STE rates were more similar to those observed in aquifers such as those reported in Cape Cod, MA, USA (Böhlke *et al.*, 2006; Smith *et al.*, 2006). Lower rates could be the result of the low organic content of the sediments (Wilson *et al.*, 2022a), high humic concentrations (O'Connor *et al.*, 2015) limiting production of NH_4^+ by remineralization, or low groundwater advection rates limiting the supply of NH_4^+ to the oxic zone. Although NO_x is available for N removal the results of the *in situ* tracer experiment and previous work (Wilson *et al.*, 2022a) reveal little potential for microbial N removal at this site. DIN in the surficial 0-50 cm of the STE, therefore, is available for discharge to overlying water and may be exported to the overlying water via SGD or tidal pumping.

4.5.5. Implications for N in STEs

Our data suggest that NH_4^+ is oxidized by nitrification in the sandy GP-STE producing NO_x . STEs and their role in biogeochemical processing are often overlooked when examining groundwater fluxes, so it is typical in SGD studies to assume conservative transport of nutrients (Brooks *et al.*, 2021). This is an oversight as groundwater constituents and those supplied by recirculated seawater are often transformed in STEs and this is critical to defining their importance as nutrient sources to coastal waters. As shown in this study, STE reactions determine speciation, and concentration of N, which determines the impact of that N on our coastal ecosystems after discharge. The form of N can influence mobility, its availability to N removal processes, and its availability to primary producers in surface waters (Taylor *et al.*, 2006). Many coastal ecosystems are at risk of eutrophication due to excess nutrient inputs (Howarth, 2008). To understand how groundwater derived nutrients may contribute to this issue we must consider transformations in STEs, which control nutrient export in SGD.

4.6. References

- Addy, K., Kellogg, D.Q., Gold, A.J., Groffman, P.M., Ferendo, G., and Sawyer, C. (2002) In Situ Push–Pull Method to Determine Ground Water Denitrification in Riparian Zones. *J Environ Qual* **31**: 1017–1024.
- Anschutz, P., Charbonnier, C., Deborde, J., Deirmendjian, L., Poirier, D., Mouret, A., et al. (2016) Terrestrial groundwater and nutrient discharge along the 240-km-long Aquitanian coast. *Mar Chem* **185**: 38–47.
- Beck, A.J., Kellum, A.A., Luek, J.L., and Cochran, M.A. (2016) Chemical Flux Associated with Spatially and Temporally Variable Submarine Groundwater Discharge, and Chemical Modification in the Subterranean Estuary at Gloucester Point, VA (USA). *Estuaries and Coasts* **39**: 1–12.
- Beck, M., Reckhardt, A., Amelsberg, J., Bartholomä, A., Brumsack, H.J., Cypionka, H., et al. (2017) The drivers of biogeochemistry in beach ecosystems: A cross-shore transect from the dunes to the low-water line. *Mar Chem* **190**: 35–50.
- Bohlke, J.K. and Coplen, T.B. (1995) Interlaboratory comparison of reference materials for nitrogen-isotope-ratio measurements, Vienna.
- Bohlke, J.K., Gwinn, C.J., and Coplen, T.B. (1993) New reference materials for nitrogen-isotope-ratio measurements. *Geostand Newsl* **17**: 159–164.
- Böhlke, J.K., Smith, R.L., and Miller, D.N. (2006) Ammonium transport and reaction in contaminated groundwater: Application of isotope tracers and isotope fractionation studies. *Water Resour Res* **42**: 1–19.
- Boyle, E., Collier, R., Dengler, A.T., Edmond, J.M., Ng, A.C., and Stallard, R.F. (1974) On the chemical mass-balance in estuaries. *Geochim Cosmochim Acta* **38**: 1719–1728.
- Brand, W.A., Coplen, T.B., Vogl, J., Rosner, M., and Prohaska, T. (2014) Assessment of international reference materials for isotope-ratio analysis (IUPAC Technical Report). *Pure Appl Chem* **86**: 425–467.
- Brooks, T.W., Kroeger, K.D., Michael, H.A., and York, J.K. (2021) Oxygen-controlled recirculating seepage meter reveals extent of nitrogen transformation in discharging coastal groundwater at the aquifer–estuary interface. *Limnol Oceanogr* **66**: 3055–3069.
- Cho, H.M., Kim, G., Kwon, E.Y., Moosdorf, N., Garcia-Orellana, J., and Santos, I.R. (2018) Radium tracing nutrient inputs through submarine groundwater discharge in the global ocean. *Sci Rep* **8**: 1–7.
- Cole, J.J., Peierls, B.L., Caraco, N.F., and Pace, M.L. (1993) Nitrogen loading of rivers as a human-driven process. In *Humans as components of ecosystems*. Springer, pp. 141–157.
- Cole, M.L., Kroeger, K.D., McClelland, J.W., and Valiela, I. (2006) Effects of watershed land use on nitrogen concentrations and δ^{15} nitrogen in groundwater. *Biogeochemistry* **77**: 199–215.
- Damashek, J., Casciotti, K.L., and Francis, C.A. (2016) Variable Nitrification Rates Across Environmental Gradients in Turbid, Nutrient-Rich Estuary Waters of San Francisco Bay. *Estuaries and Coasts* **39**: 1050–1071.
- Enoksson, V. (1986) Nitrification Rates in the Baltic Sea: Comparison of Three Isotope Techniques. *Appl Environ Microbiol* **51**: 244–250.
- Hansen, J.I., Henriksen, K., and Blackburn, T.H. (1981) Seasonal distribution of nitrifying bacteria and rates of nitrification in coastal marine sediments. *Microb Ecol* **7**: 297–304.
- Hong, Y., Wu, J., Wilson, S., and Song, B. (2019) Vertical Stratification of Sediment Microbial

- Communities Along Geochemical Gradients of a Subterranean Estuary Located at the Gloucester Beach of Virginia, United States. *Front Microbiol* 1–11.
- Howarth, R.W. (2008) Coastal nitrogen pollution: A review of sources and trends globally and regionally. *Harmful Algae* **8**: 14–20.
- Jääntti, H., Leskinen, E., Stange, C.F., and Hietanen, S. (2012) Measuring nitrification in sediments -comparison of two techniques and three $^{15}\text{NO}_3^-$ measurement methods. *Isotopes Environ Health Stud* **48**: 313–326.
- Kroeger, K.D. and Charette, M.A. (2012) Nitrogen biogeochemistry of submarine groundwater discharge. *Limnol Oceanogr* **53**: 1025–1039.
- Lisa, J.A., Song, B., Tobias, C.R., and Hines, D.E. (2015) Genetic and biogeochemical investigation of sedimentary nitrogen cycling communities responding to tidal and seasonal dynamics in Cape Fear River Estuary. *Estuar Coast Shelf Sci* **167**: A313–A323.
- Luek, J.L. and Beck, A.J. (2014) Radium budget of the York River estuary (VA , USA) dominated by submarine groundwater discharge with a seasonally variable groundwater end-member. *Mar Chem* **165**: 55–65.
- Moore, W.S. (1999) The subterranean estuary: A reaction zone of ground water and sea water. *Mar Chem* **65**: 111–125.
- Nixon, S.W. (1995) Coastal marine eutrophication: A definition, social causes, and future concerns. *Ophelia* **41**: 199–219.
- O'Connor, A.E., Luek, J.L., McIntosh, H., and Beck, A.J. (2015) Geochemistry of redox-sensitive trace elements in a shallow subterranean estuary. *Mar Chem* **172**: 70–81.
- Officer, C.B. and Lynch, D.R. (1981) Dynamics of Mixing in Estuaries. *Estuar Coast Shelf Sci* **12**: 525–533.
- Russoniello, C.J., Konikow, L.F., Kroeger, K.D., Fernandez, C., Andres, A.S., and Michael, H.A. (2016) Hydrogeologic controls on groundwater discharge and nitrogen loads in a coastal watershed. *J Hydrol* **538**: 783–793.
- Santoro, A.E. (2010) Microbial nitrogen cycling at the saltwater – freshwater interface. *Hydrogeol J* **18**: 187–202.
- Santoro, A.E., Francis, C.A., De Siewes, N.R., and Boehm, A.B. (2008) Shifts in the relative abundance of ammonia-oxidizing bacteria and archaea across physicochemical gradients in a subterranean estuary. *Environ Microbiol* **10**: 1068–1079.
- Santoro, A.E., Sakamoto, C.M., Smith, J.M., Plant, J.N., Gehman, A.L., Worden, A.Z., et al. (2013) Measurements of nitrite production in and around the primary nitrite maximum in the central California Current. *Biogeosciences* **10**: 7395–7410.
- Santos, I.R., Burnett, W.C., Chanton, J., Mwashote, B., Suryaputra, I.G.N.A., and Dittmar, T. (2008) Nutrient biogeochemistry in a Gulf of Mexico subterranean estuary and groundwater- derived fluxes to the coastal ocean. **53**: 705–718.
- Santos, I.R., Burnett, W.C., Dittmar, T., Suryaputra, I.G.N.A., and Chanton, J. (2009) Tidal pumping drives nutrient and dissolved organic matter dynamics in a Gulf of Mexico subterranean estuary. *Geochim Cosmochim Acta* **73**: 1325–1339.
- Santos, I.R., Chen, X., Lecher, A., Sawyer, A., Moosdorf, N., Rondellas, V., et al. (2021) Submarine groundwater discharge impacts on coastal nutrient biogeochemistry. *Nat Rev Earth Environ* 108–119.
- Schutte, C.A., Wilson, A.M., Evans, T., Moore, W.S., and Joye, S.B. (2017) Deep oxygen penetration drives nitrification in intertidal beach sands. *Limnol Oceanogr* **63**: 1–16.
- Shrivastava, S., Stewardson, M.J., and Arora, M. (2021) Influence of Bioturbation on Hyporheic

- Exchange in Streams: Conceptual Model and Insights From Laboratory Experiments. *Water Resour Res* **57**: 1–18.
- Sigman, D.M., Casciotti, K.L., Andreani, M., Barford, C., Galanter, M., and Bohlke, J.K. (2001) A Bacterial Method for the Nitrogen Isotopic Analysis of Nitrate in Seawater and Freshwater. *Anal Chem* **73**: 4145–4153.
- Slomp, C.P. and Cappellen, P. Van (2004) Nutrient inputs to the coastal ocean through submarine groundwater discharge : controls and potential impact. *J Hydrol* **295**: 64–86.
- Smith, R.L., Baumgartner, L.K., Miller, D.N., Repert, D.A., and Böhlke, J.K. (2006) Assessment of nitrification potential in ground water using short term, single-well injection experiments. *Microb Ecol* **51**: 22–35.
- Smith, R.L., Bohlke, J.K., Song, B., and Tobias, C.R. (2015) Role of Anaerobic Ammonium Oxidation (Anammox) in Nitrogen Removal from a Freshwater Aquifer. *Environ Sci Technol* **49**: 12169–12177.
- Taylor, G.T., Gobler, C.J., and Sañudo-Wilhelmy, S.A. (2006) Speciation and concentrations of dissolved nitrogen as determinants of brown tide *Aureococcus anophagefferens* bloom initiation. *Mar Ecol Prog Ser* **312**: 67–83.
- Ullman, W.J., Chang, B., Miller, D.C., and Madsen, J.A. (2003) Groundwater mixing, nutrient diagenesis, and discharges across a sandy beachface Cape Henlopen, Delaware (USA). *Estuar Coast Shelf Sci* **57**: 539–552.
- Usui, T., Koike, I., and Ogura, N. (2001) N₂O production, nitrification and denitrification in an estuarine sediment. *Estuar Coast Shelf Sci* **52**: 769–781.
- Valiela, I., Collins, G., Kremer, J., Lajtha, K., Geist, M., Seely, B., et al. (1997) Nitrogen loading from coastal watersheds. *Ecol Appl* **7**: 358–380.
- Wankel, S.D., Mosier, A.C., Hansel, C.M., Paytan, A., and Francis, C.A. (2011) Spatial variability in nitrification rates and ammonia-oxidizing microbial communities in the agriculturally impacted Elkhorn Slough estuary, California. *Appl Environ Microbiol* **77**: 269–280.
- Ward, B.B. (2011) Measurement and distribution of nitrification rates in the oceans. In *Methods in Enzymology*. Elsevier Inc., pp. 307–323.
- Ward, B.B. (2013) Nitrification. In *Encyclopedia of Ecology*. pp. 351–358.
- Wilson, S.J., Anderson, I.C., and Song, B. (2022) Geochemical drivers impacting nitrifying communities in sandy sediments. *Environ Microbiol* **Submitted**:
- Wilson, S.J., Anderson, I.C., Song, B., and Tobias, C.R. (2022) Temporal and spatial variation in subterranean estuary geochemical gradients and nutrient cycling rates: impacts on groundwater nutrient export to estuaries. *Limnol Oceanogr* **Submitted**:

4.7. Tables

Table 1. STE mixing model calculations of production of NO_3^- and consumption of NH_4^+ in the top 100 cm of the STE in each season sampled.

	Spring	Summer	Fall	Winter
NO_3^- production ($\mu\text{mol m}^{-2} \text{ day}^{-1}$)	147.30	177.99	106.79	39.67
NH_4^+ consumption ($\mu\text{mol m}^{-2} \text{ day}^{-1}$)	55.00	88.64	183.16	63.44

Table 2. Background geochemical parameters at injection sites (50 cm injection wells) prior to in situ tracer experiment

	Depth (cm)	Salinity	DO (mg/L)	pH	Temp ($^{\circ}\text{C}$)	NO_3^- (μM)	NH_4^+ (μM)
Inj. Site 1	50	13.85	4.64	6.78	26.97	121.67	0.73
Inj. Site 2	50	16.82	5.02	6.91	27.09	127.16	1.17

Table 3. Benchtop sediment slurry incubation rates (\pm Standard error) determined by ^{15}N - NO_x production overtime in incubation samples. Average potential nitrification rate (all measurements) was 62.44 ± 7.23 .

Depth Section (cm)	Potential Rate ($\mu\text{moles m}^{-2} \text{ d}^{-1}$)
0-10	46.44 ± 5.28
10-20	109.02 ± 8.50
20-30	71.50 ± 1.18
30-40	48.68 ± 5.43
40-50	36.57 ± 3.68

4.8. Figures

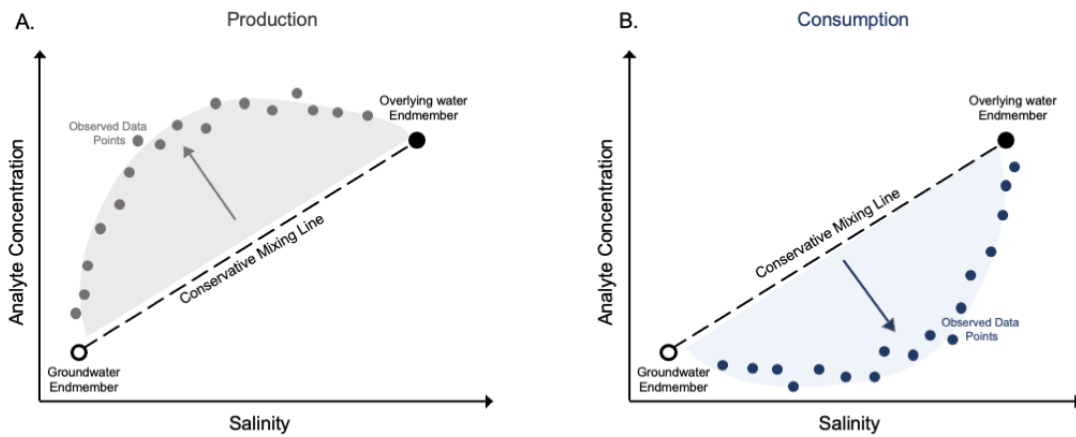


Figure 1. Conceptual diagram depicting observed data compared to conservative mixing lines calculated using endmembers from groundwater and overlying water.

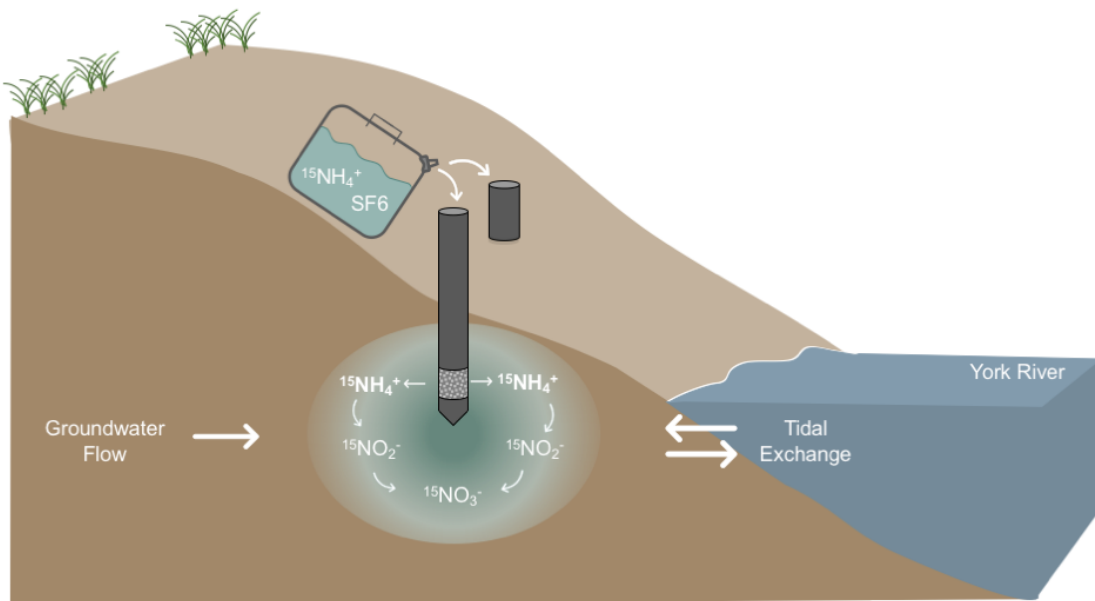


Figure 2. Conceptual diagram of in situ experiment showing tracer plume introduction to the injection well and potential oxidation of the tracer ($^{15}\text{NH}_4^+$) within the STE subsurface to $^{15}\text{NO}_2^-$ and $^{15}\text{NO}_3^-$ by nitrification.

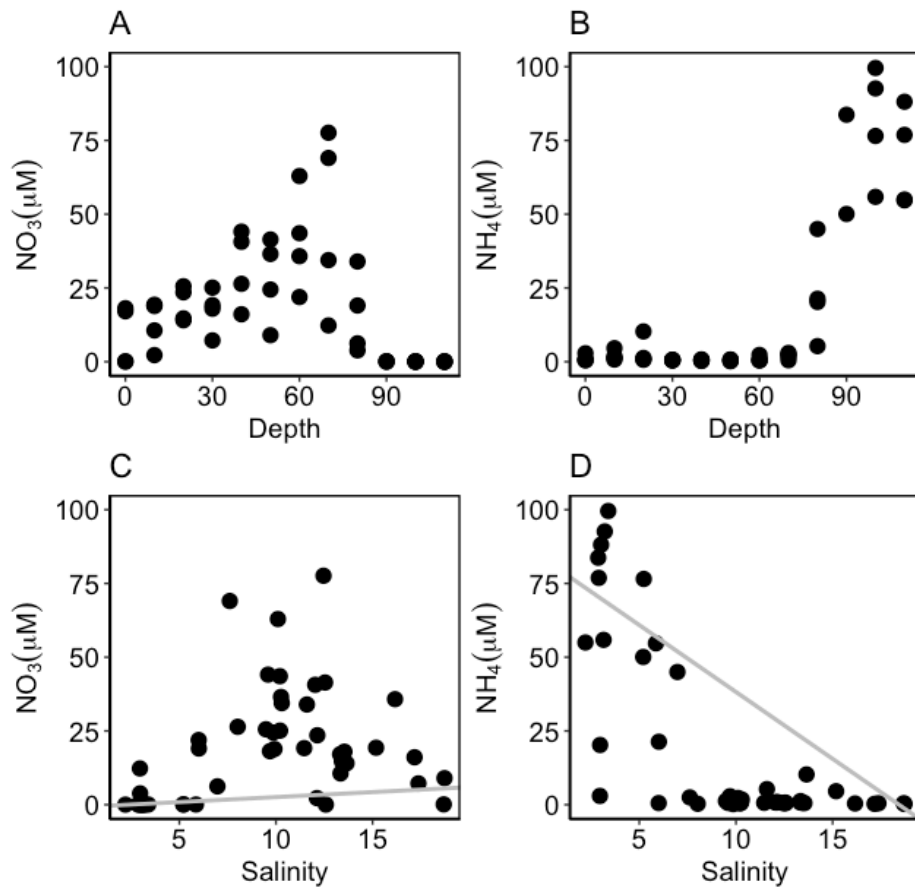


Figure 3. A) Porewater NO_3^- concentrations (μM) in all seasons with porewater depth (cm), B) Porewater NH_4^+ concentrations (μM) in all seasons with porewater depth (cm). C) Porewater NO_3^- concentrations (μM) versus porewater salinity, with conservative mixing line (gray) for reference, D) Porewater NH_4^+ concentrations (μM) in all seasons versus porewater STE salinity, with the conservative mixing line (gray) for reference.

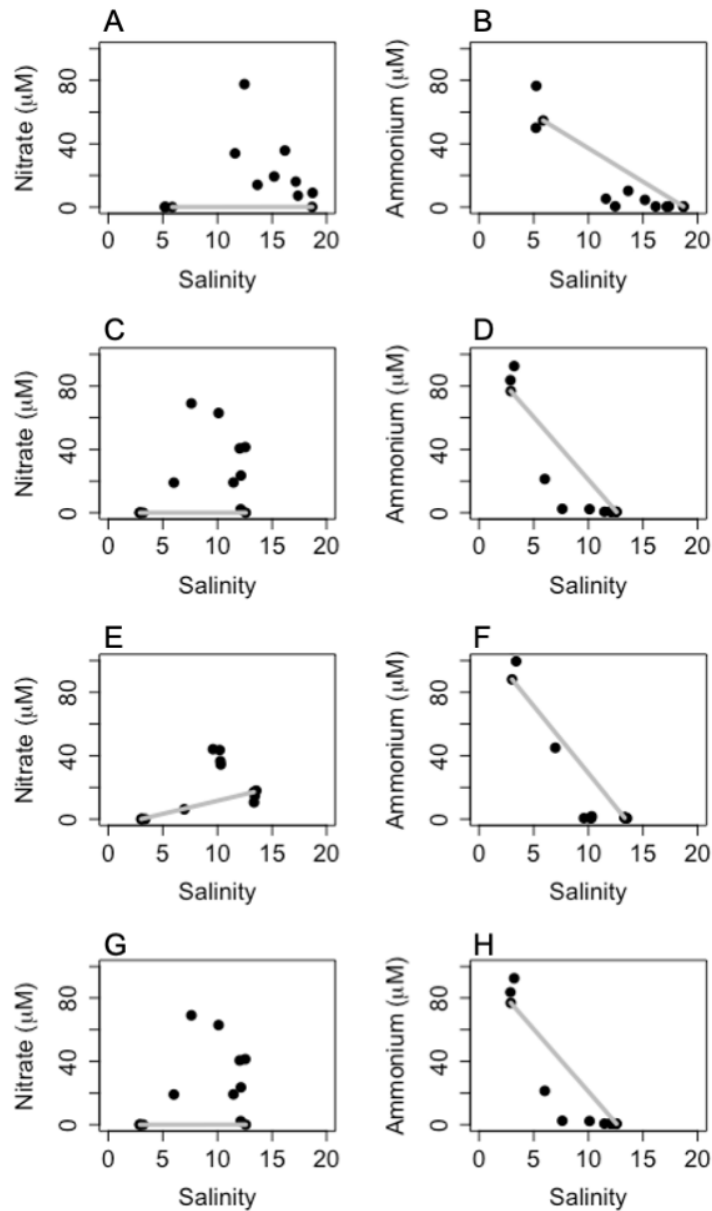


Figure 4. Analytes (μM) vs. salinity used to calculate production or consumption via mixing models for each season A) Spring 2018, Nitrate, B) Spring 2018, Ammonium, C) Summer 2018, Nitrate, D) Summer 2018, Ammonium, E) Fall 2018, Nitrate, F) Fall 2018, Ammonium, G) Winter 2019, Nitrate, H) Winter 2019, Ammonium. Points represent individual observed data points and lines indicate conservative mixing lines resulting from groundwater and surface water endmembers.

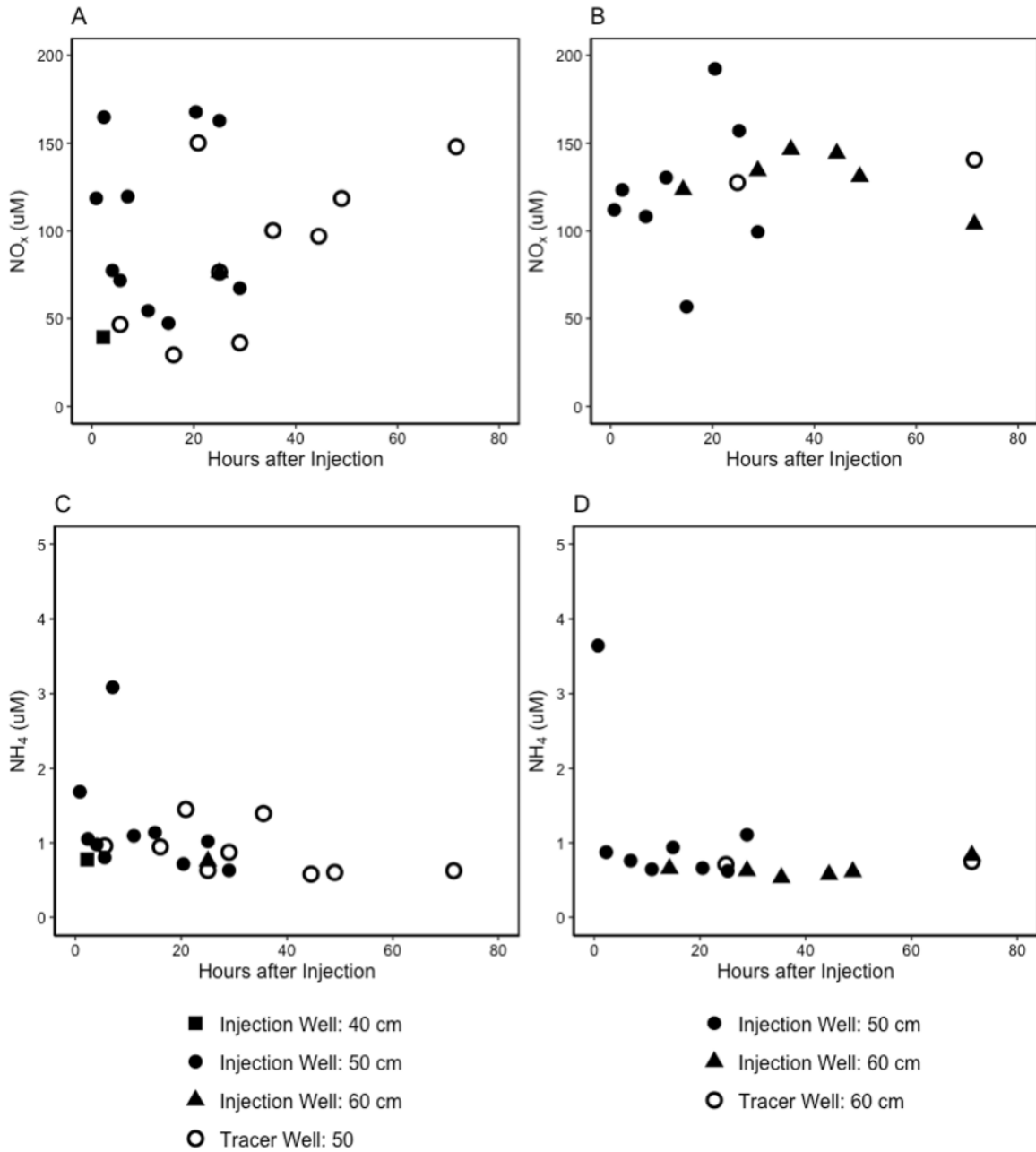


Figure 5. Groundwater NO_x^- concentrations (μM) over time after injection in the *in situ* tracer injections #1 (A) and #2 (B) and NH_4^+ concentrations (μM) in injections #1 (C) and #2 (D); well ID is indicated by point shape.

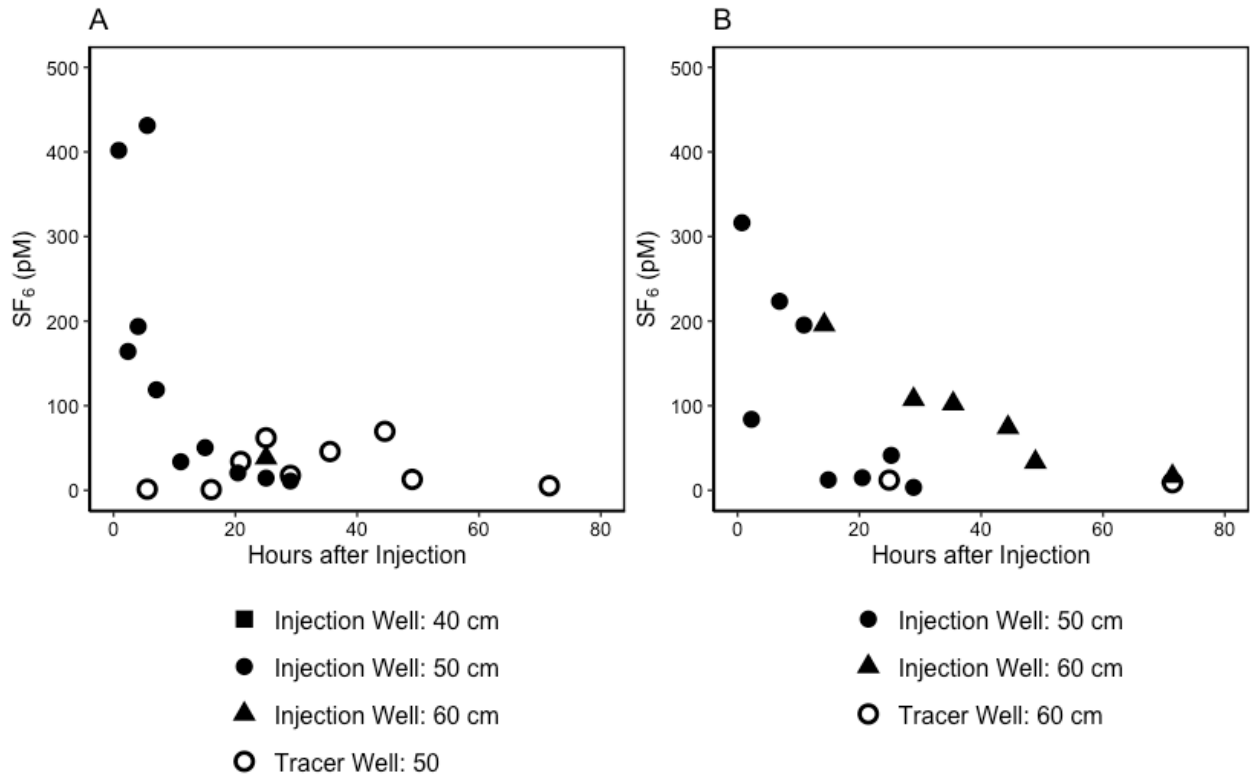


Figure 6. SF₆ concentrations (pM) in groundwater samples over time after the *in situ* tracer injections #1 (A) and #2 (B); sample well DI is indicated by point shape.

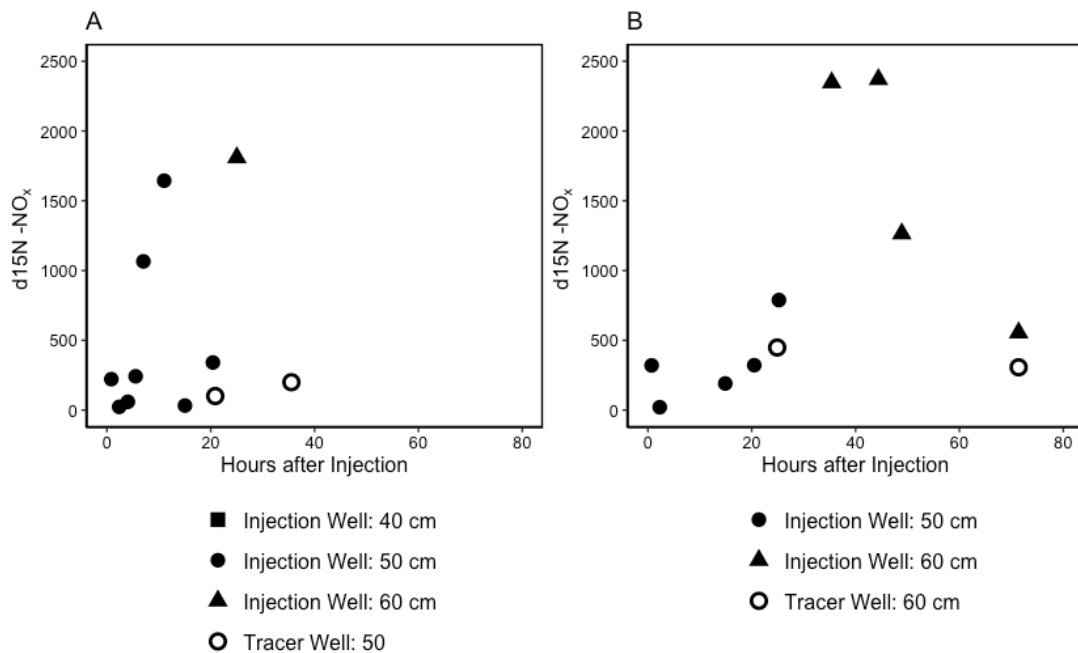


Figure 7. Enrichment of ¹⁵N-NO_x, shown in delta notation, in groundwater samples after the *in situ* tracer injections #1 (A) and #2 (B); sample well ID indicated by point shape.

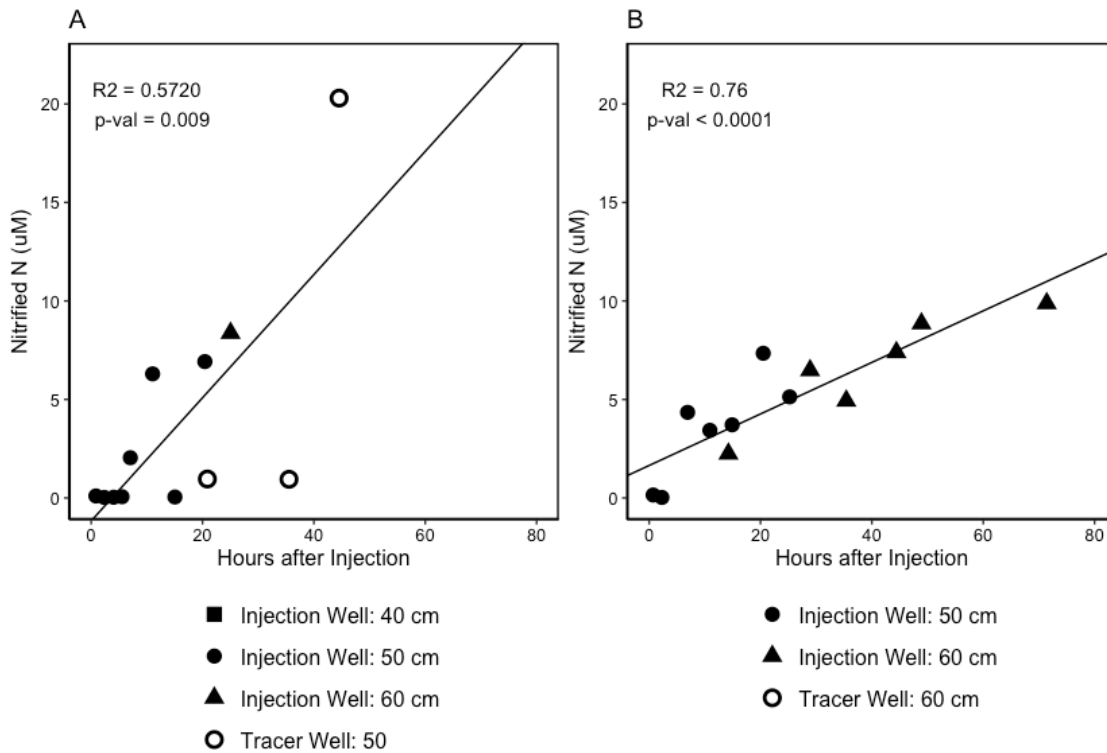


Figure 8. Nitrified N concentrations (μM ; $^{15}\text{NO}_x^-$ corrected for dilution of $^{15}\text{NH}_4^+$ tracer) in groundwater samples after the *in situ* tracer injections #1 (A) and #2 (B). Where sampling well is indicated by shape.

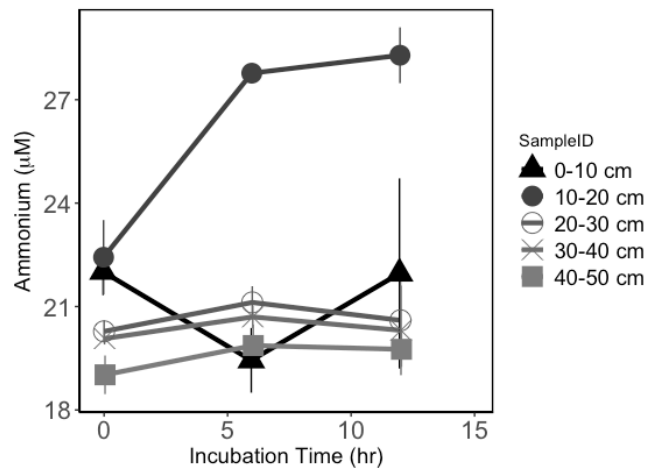


Figure 9. NH_4^+ concentrations (μM) overtime in sediment slurry incubations. Each point represents the mean of triplicate samples and the error bars represent one standard error in each direction.

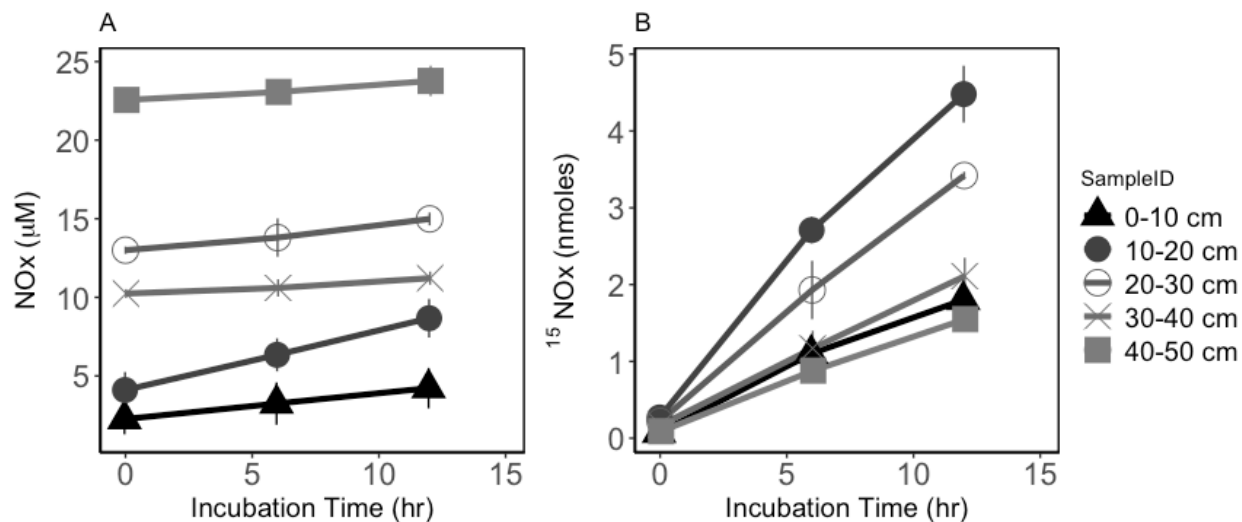


Figure 10. A) NO_x concentrations (µM) overtime and B) ¹⁵NO_x (nmoles) overtime in sediment slurry incubations for each core depth section (indicated by point shape). Each point represents the mean of triplicate cores samples and error bars represent one standard error in each direction.

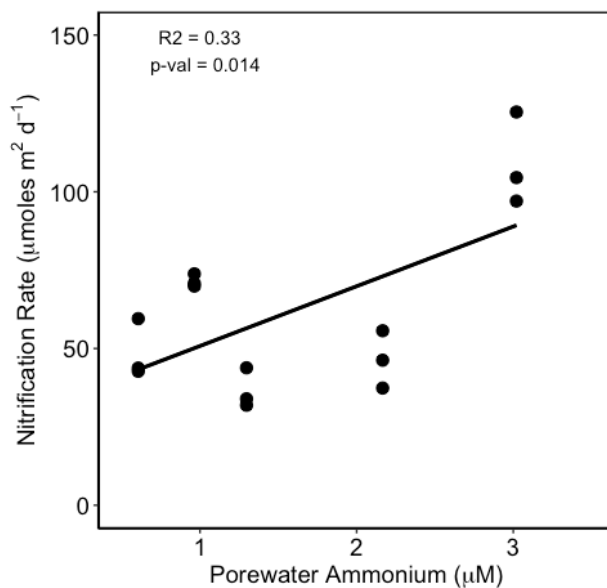


Figure 11. Potential nitrification rates in sediment slurry incubations versus the ambient porewater ammonium concentration (µM) at the associated depth (p-value = 0.014).

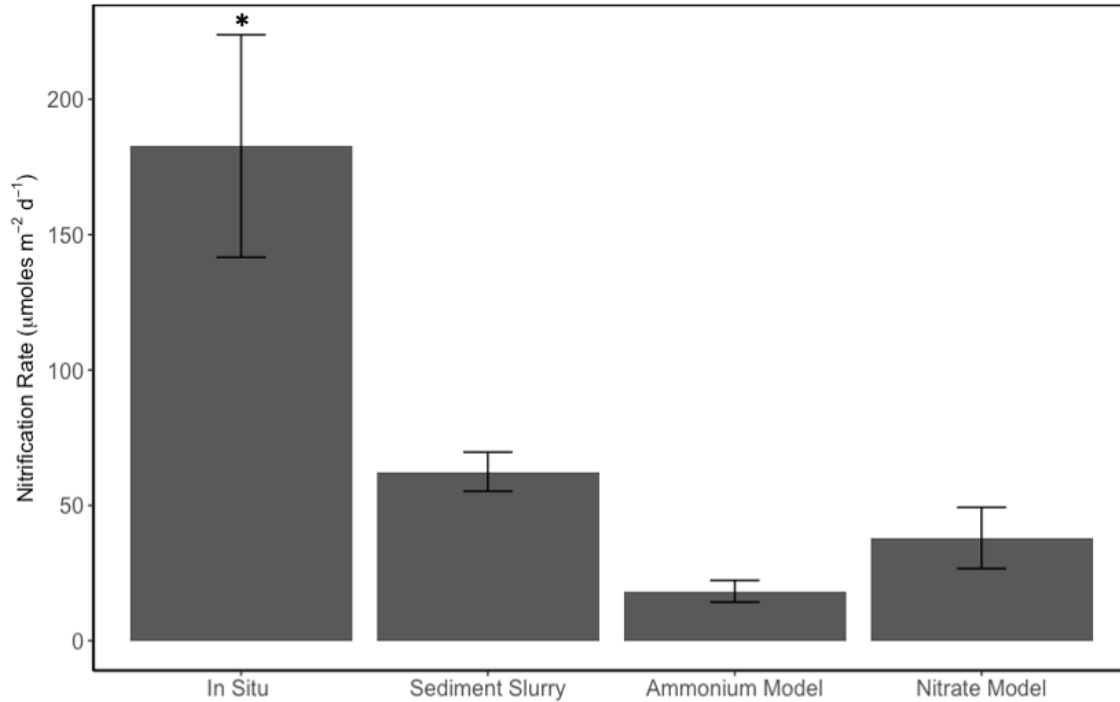


Figure 12. Comparison of average nitrification rates ($\mu\text{moles N m}^{-2} \text{d}^{-1}$) as determined by the *in situ* tracer experiment (average of both injection sites), sediment slurry incubation (averaged over all depth sections), and conservative mixing models of ammonium loss and nitrate production (sum of mass lost from 0-50 cm; averaged across seasons). Error bars represent one standard error in each direction. An analysis of variance (ANOVA) revealed a significant fixed effect of measurement method on nitrification rates for the GP-STE ($p\text{-value} = 0.006$), a post-hoc Tukey test indicated that the *in situ* tracer experiment was statistically different from the sediment slurry and conservative mixing estimation based on ammonium loss, but not nitrate production. The sediment slurry and conservative mixing estimations (both ammonium and nitrate) were not statistically different from one another.

4.9. Appendix E

Table S1. STE mixing model calculations of production of NO_3^- and consumption of NH_4^+ in the top 50 cm of the STE in each season sampled.

	Depth Interval	Spring	Summer	Fall	Winter
NO_3^- production ($\mu\text{mol m}^{-2} \text{day}^{-1}$)	0-50 cm	39.58	69.23	24.03	19.00
NH_4^+ consumption ($\mu\text{mol m}^{-2} \text{day}^{-1}$)	0-50 cm	22.41	12.73	27.41	10.53

4.10. Appendix F

All raw data collected in Chapter 4 has been or is in the process of being made publicly available via the BCO DMO site, the links to this data are shown below:

Seasonal geochemical profile data:

<https://www.bco-dmo.org/dataset/807664/data>

In situ tracer experiment data: BCO DMO submission in progress

Ex situ sediment slurry incubation data: BCO DMO submission in progress

Chapter 5. Subterranean estuaries modify groundwater nutrient fluxes to the global ocean

5.1. Abstract

Groundwater releases nutrients to the ocean that support primary production and increase the risk of eutrophication in coastal ecosystems. Prior to discharge, groundwater flows through the biogeochemically active subterranean estuary where nutrients may be transformed, influencing nutrient concentrations in submarine groundwater discharge (SGD). Here, we used a meta-dataset of >10,000 samples from >200 sites in 42 countries to reveal how nitrogen (N) and phosphorus (P) are transformed within subterranean estuaries, and how this may influence exports by SGD. Salinity, latitude, and land crop cover were the major features explaining groundwater nutrient concentrations. Dissolved organic nitrogen (DON) was identified as an important component of the groundwater nutrient pool, accounting for 30-44% of groundwater N. Subterranean estuaries exhibited non-conservative behavior with respect to nutrients, on average dissolved inorganic N (DIN) and dissolved inorganic P (DIP) were produced while DON concentrations in fresh SGD were reduced at the global scale. Fluxes via total SGD were 2.3 ± 0.6 , 1.6 ± 0.6 , 0.01 ± 0.003 Tmoles yr⁻¹ for DIN, DON, and DIP, respectively. These fluxes were 1.7x, 2.7x, and 0.5x the global riverine DIN, DON, and DIP fluxes to the ocean, respectively, confirming that SGD plays a critical role in coastal biogeochemistry even if most of those fluxes represent a recycled rather than new source.

5.2. Main

Global coastal waters receive large, increasing anthropogenic inputs of nitrogen (N) and phosphorus (P) that create widespread water quality problems (Nixon, 1995; Basu, 2022). Coastal eutrophication triggered mainly by enhanced nutrient inputs modifies biological communities, creates anoxic conditions, and kills fish or other megafauna (Conley *et al.*, 2009; Wurtsbaugh *et al.*, 2019). Nutrient inputs into the coastal ocean originate from watershed runoff via rivers, atmospheric deposition, and submarine groundwater discharge (SGD) (Luijendijk *et al.*, 2020). SGD includes any flow to the coastal ocean through sediments (Moore, 2010; Santos *et al.*, 2021), including both fresh, terrestrial groundwater and seawater that circulates through aquifer systems along the coast on scales greater than meters (Kwon *et al.*, 2014; Cho *et al.*, 2018).

SGD-derived nutrient fluxes may exceed those from rivers and atmospheric deposition (Cho *et al.*, 2018; Santos *et al.*, 2021). However, existing estimates have large unquantified uncertainties, often rely on local-scale observations, and overlook transformations of nutrients within subterranean estuaries. Microbially-mediated processes can either remove (e.g., denitrification) or add (e.g., mineralization) N within subterranean estuaries (Kroeger and Charette, 2008; Santos *et al.*, 2008). Inorganic P can be attenuated by sorption to particles along the groundwater flow-path (Charette and Sholkovitz, 2002; Spiteri *et al.*, 2008). The biogeochemical reactions within subterranean estuaries influence the speciation and concentration of nutrients that are released to the ocean via SGD, making subterranean estuaries important biogeochemical hotspots (Rocha *et al.*, 2021). SGD fluxes rely heavily on defining the nutrient endmember concentrations in both fresh and saline SGD, which is challenging, but required to scale-up small local datasets.

Here, we hypothesize that groundwater nutrient concentrations will be related to site characteristics, subterranean estuaries will act non-conservatively with respect to nutrients, and that SGD is a source of DIN, DON, and DIP to the ocean. We use a global meta-dataset with >10,000 samples from 216 subterranean estuaries (Figure 1) to characterize the coastal groundwater nutrient pool, resolve the key drivers of nutrient endmembers, quantify biogeochemical processing in subterranean estuaries, and finally, reevaluate nutrient inputs into the ocean via SGD at the global scale.

5.2.1. Global distribution of nutrients in subterranean estuaries

A total of 10,636 observations of dissolved inorganic nitrogen (DIN; n=5,660), dissolved organic nitrogen (DON; n=1,890), and dissolved inorganic phosphorus (DIP; n=4,569) from six continents and forty-two countries, both from original and published materials, were included in our analysis. The majority of observations were from Asia, Australia, Europe, and the United States with scarce data from polar coastlines, Africa, and South America (Figure 1). The global averages (\pm standard error), of coastal groundwater DIN, DON, and DIP concentrations were 28.2 ± 8.5 , 18.0 ± 9.5 , and $0.93 \pm 14.7 \mu\text{M}$, respectively. Concentrations of DIN and DON were higher in low salinity (<10) (DIN = $45.9 \pm 7.0 \mu\text{M}$; DON = $25.7 \pm 10.9 \mu\text{M}$) than in high salinity groundwater (>10) groundwater (DIN = $19.8 \pm 9.1 \mu\text{M}$, DON = $12.9 \pm 7.8 \mu\text{M}$). In contrast, DIP concentrations were slightly higher in high salinity (DIP = $1.0 \pm 11.2 \mu\text{M}$) than low salinity groundwater samples (DIP = $0.8 \pm 20.6 \mu\text{M}$). Salinity was the most important feature when estimating groundwater DIN, DON, and DIP concentrations according to random forest analysis (34-52% feature importance) of the data (Figure S3).

Random forest analysis (Methods) also revealed that crop cover had small influences (3.2, 3.4, and 14%), on groundwater DIP, DON, and DIN concentrations (Figure S3). When

these relationships were further assessed, it was revealed that a 1% increase in crop cover in a 1 km radius surrounding a site, results in a ~1% increase in both DIN and DIP concentrations (Figure S8). Inverse relationships between groundwater nitrate (NO_3^-) and ammonium (NH_4^+) concentrations with respect to bare land and tree cover were also observed (Figure S13). As bare land coverage increases, groundwater NO_3^- concentrations increase and NH_4^+ concentrations decrease, whereas when tree cover increases, groundwater NO_3^- concentrations decrease and NH_4^+ increases. These relationships suggest that anthropogenic activities, including agriculture and urbanization, result in higher groundwater nutrient concentrations and influence the speciation of N in groundwater. No relationships with groundwater DON and land cover metrics were observed, which may be the result of the limited number of DON observations or non-linear relationships. No statistically significant linear relationships between rainfall, evaporation, baseflow (Rodell *et al.*, 2004; Zhou *et al.*, 2019), or meteoric, fresh SGD fluxes determined by Zhou *et al.*, (2019) and Luijendijk *et al.*, (2020) were observed with groundwater nutrient concentrations on a global scale and these factors had low relative importance values according to the random forest analysis, although these factors may play an important role at local scales (Figure S6 & S7).

The speciation of N in groundwater is critical for determining its fate and interpreting the impact of SGD on coastal ecosystems (Bowen *et al.*, 2020; Santos *et al.*, 2021). Speciation determines the potential N cycle reactions that may occur in the subterranean estuary. For example, ammonium (NH_4^+), a product of organic matter mineralization, is the substrate for microbially mediated nitrification to nitrite (NO_2^-) or NO_3^- (collectively NO_x), which serve as substrates for N removal by denitrification. Subterranean estuaries with a mixed lithology had low salinity groundwater dominated by DON and NO_3^- , as compared to NH_4^+ (Figure 2). Muddy

sites were dominated by reduced forms of N at all salinities; consistent with the reduced groundwater environment of muddy marshes and mangroves, where nitrification may be inhibited and ammonification is enhanced (Joye and Hollibaugh, 1995). Rocky sites were dominated by DON and NO_x, suggesting minimal time for NH₄⁺ accumulation when residence times are short in karst and volcanic aquifers. N speciation in sandy sites showed no clear patterns.

In all site types, DON represented a substantive portion (32-44%) of the groundwater N pool. DON is often overlooked in SGD and was analyzed in only ~17.5% of all samples compiled in this dataset. However, primary producers in overlying waters can assimilate DON or it may be remineralized by microbial processes in subterranean estuaries and the overlying water column (Bronk *et al.*, 2006). Varying forms of N supplied to coastal systems via SGD may support differential phytoplankton assemblages (Taylor *et al.*, 2006; Cira *et al.*, 2016). To better understand the role SGD plays in coastal eutrophication and nutrient biogeochemistry, future studies should include measurements of DON.

The N to P ratios of SGD can also play a major role in the ecology and biogeochemistry of receiving coastal waters (Downing, 1997; Jickells, 1998). Site types had varying average DIN:DIP (N:P) ratios ranging from 17.2 ± 1.2 in rocky sites to 59.2 ± 1.2 in mixed sites. Higher N:P ratios in groundwater are determined by nutrient sources and redox conditions within subterranean estuaries (Slomp and Van Cappellen, 2004). N accumulation often results from widespread anthropogenic wastewater, septic system failures, fertilizers, and manure leachate (Schlesinger, 2009; Rahman *et al.*, 2021). As aquifers continue to be contaminated with N, groundwater N:P ratios are expected to rise accordingly (Slomp and Van Cappellen, 2004). Since

the coastal ocean is often N-limited, continued excess N from SGD may result in a coastal water regime shift from N to P limitation, enhancing instances of eutrophication (Santos *et al.*, 2021).

5.2.2. Nutrient transformations within subterranean estuaries

We assessed whether biogeochemical transformations within subterranean estuaries modify the concentration of nutrients exported to the ocean via SGD with conservative mixing calculations (Methods). Nutrient behavior was defined as conservative, productive, reductive, or undefined (Figure 3) when compared to predicted concentrations calculated from the mixing of the surface and groundwater endmembers. Conservative mixing models were first developed for surface estuaries (Boyle *et al.*, 1974; Officer and Lynch, 1981; Kaul and Froelich Jr, 1984), but have since been applied to subterranean estuaries (Santos *et al.*, 2009, Wilson *et al.*, in prep.).

Roughly half of the considered sites exhibited either production (an increase in concentrations) or reduction (a decrease in concentrations) of DIP, NO_3^- , NH_4^+ , or DON supplied to the subterranean estuary by fresh groundwater (salinity < 10; Figure 3). DIP exhibited undefined behavior in 53% of the 64 subterranean estuaries assessed. STEs were classified as undefined when there appeared to be more than two endmembers or the data did not present a clear conservative, reductive, or productive behavior preventing classification. With respect to DIP, 14%, 23%, and 9% of sites exhibited production, reductive, and conservative behavior, respectively (Table S1). Remineralization of organic matter or iron-oxides releasing PO_4^- may explain production in subterranean estuaries, but removal is likely a result of sorption to manganese or iron laden particles (Charette and Sholkovitz, 2002; Spiteri *et al.*, 2008).

Of the 72 subterranean estuaries assessed with conservative mixing curves for NO_3^- , 22% exhibited reduction, 22% production, 11% were conservative, and 44% were undefined (Table S1). Production or consumption of NO_3^- indicates active microbially mediated N processes such

as remineralization, nitrification, denitrification, or anaerobic ammonium oxidation (anammox) (Loveless and Oldham, 2010; Robinson *et al.*, 2018). Of the 65 sites assessed for NH_4^+ , 28% were reductive, 26% productive, 11% were conservative, and 34% were undefined. A reduction in NH_4^+ concentrations may result from nitrification, assimilation, or sorption to sediments, whereas production could result from remineralization or dissimilatory nitrate reduction to ammonia (DNRA) along the salinity gradient. Only 28 sites met the criteria for DON behavior analysis, 21% of which exhibited conservative behavior and 46% were undefined. 29% of sites consumed DON, likely due to remineralization of organic matter, and only one site produced DON, suggesting release by microbes. While this analysis cannot resolve the specific pathways of the N and P cycling that control nutrient concentrations at each site, it demonstrates the highly diverse behavior of subterranean estuaries. Accounting for the percentage of subterranean estuaries exhibiting each behavior and the average reduction or production of each analyte (Methods), we reveal that STEs consume DON and produce DIN and DIP in fresh SGD at the global scale.

5.2.3. Nutrient fluxes to the global ocean

Calculating SGD-derived nutrient fluxes to the ocean requires defining a nutrient endmember concentration and the SGD rate. Local scale investigations usually take an overall average of nutrient concentrations in coastal aquifers (Dulaiova *et al.*, 2010; Liu *et al.*, 2018; Sanial *et al.*, 2021), and do not separate fresh from saline SGD fluxes. Here, average global groundwater endmembers were estimated to be, 28.2 ± 8.5 , 18.0 ± 9.5 , and $0.93 \pm 14.7 \mu\text{mol L}^{-1}$ for DIN, DON, and DIP, respectively. Using a well-established total SGD rate derived from a radium mass balance model (Kwon *et al.*, 2014; $12 \pm 3.0 \text{ Tm}^3 \text{ yr}^{-1}$), global nutrient fluxes in total SGD become $2.3 \pm 0.6 \text{ Tmoles yr}^{-1}$, $1.6 \pm 0.6 \text{ Tmoles yr}^{-1}$, and $0.01 \pm 0.003 \text{ Tmoles yr}^{-1}$ for DIN,

DON, and DIP respectively (Methods). Total SGD fluxes were also estimated using several other SGD flux estimations and assumptions to assess potential fluxes from other water fluxes and specific regions (Table S2). Our total SGD DIN export in this study is similar to previous estimates based on averages of 966 groundwater samples (Cho *et al.*, 2018), but the DIP flux was 3x lower than that previously estimated based on 1,001 samples (Cho *et al.*, 2018).

The average global fresh (salinity <10) SGD endmembers for DIN, DON, and DIP were 46.0 ± 7.0 , 25.6 ± 11.0 , and $0.9 \pm 20.6 \mu\text{mol L}^{-1}$, respectively. Using a freshwater SGD rate estimated from hydrogeological models (Luijendijk *et al.*, 2020) ($0.0147 \pm 0.0143 \text{ Tm}^3 \text{ yr}^{-1}$) the calculated fresh SGD nutrient fluxes are $0.01 \pm 0.01 \text{ Tmoles yr}^{-1}$, $0.004 \pm 0.01 \text{ Tmoles yr}^{-1}$, $0.0001 \pm 0.003 \text{ Tmoles yr}^{-1}$ for DIN, DON, and DIP, respectively (Methods). Fresh SGD fluxes were determined using several estimates of global fresh groundwater export (Table S2), but the best estimate was lower than previously reported values (Beusen *et al.*, 2013; Cho *et al.*, 2018).

The fresh portion of SGD passes through the subterranean estuary and is modified before being discharged to the ocean. Assuming our observations represent the diverse global coastlines, we apply the modification term M , resulting in global fresh groundwater endmembers of 99.9 ± 7.0 , 21.8 ± 11.0 , and $1.0 \pm 20.7 \mu\text{mol L}^{-1}$ for DIN, DON, and DIP (Methods). This implies a net production of DIN and DIP, but net removal of DON in subterranean estuaries at the global scale. As a result, biogeochemical transformations increase nutrient fluxes of DIN and DIP from fresh SGD by equivalent amounts, doubling the N flux and increasing the P flux by 12%. In contrast, STE reactions lowered DON fluxes via fresh SGD, resulting in a 15% flux reduction. A global average partially cancels out specific site by site behavior and those that have higher addition and removal of nutrients as compared to the global average, leading to a smaller modification rate on a global scale than would be observed in many local scale investigations.

However, ignoring transformations within subterranean estuaries misrepresents fresh SGD fluxes of DIN, DIP, and DON at local and global scales. Our analysis cannot resolve the complex biogeochemical processing at each site, but it clearly demonstrates the importance of accounting for net transformations when estimating nutrient fluxes.

Both fresh and saline groundwater exhibit nutrient concentrations higher than surface waters (Garcia *et al.*, 2013; Letscher *et al.*, 2013). Fresh SGD endmember concentrations of DIN and DON were higher than saline SGD endmembers by ~63% and ~26%, whereas the DIP concentration was ~3% lower. This is the first report of global DON export via SGD despite its importance as a nutrient in marine systems (Berman and Bronk, 2003). DON represents 30% of the total N export in total SGD globally, yet it is often overlooked in local SGD studies.

5.2.4. Implications

We have compiled the largest coastal groundwater dataset available to quantify SGD export and assess biogeochemical transformations of nutrients in subterranean estuaries at the global scale. Total SGD is an important source of nutrients to the global ocean, and rivals riverine inputs (Figure 4). The fresh portion of SGD is a small volume of water, accounting for only 0.6% of freshwater inputs to the ocean (Luijendijk *et al.*, 2020). After accounting for transformations in the subterranean estuary, the fresh portion of SGD DIN, DON, and DIP fluxes represent ~0.4-0.9% of the riverine nutrient input to the global ocean. Surficial estuaries transport terrigenous materials to the coastal ocean, and they are widely recognized as highly productive systems that cycle and transport both allochthonous and autochthonous organic matter and nutrients. Subterranean estuaries function analogously, cycling terrestrially-derived constituents as they flow to the ocean via SGD. On a global scale, subterranean estuaries act non-conservatively with respect to nutrient concentrations in fresh groundwater. Similar to riverine inputs, fresh SGD is a

source of new nutrients to the coastal ocean. When we account for both fresh and saline SGD, total SGD fluxes were 1.7x and 2.7x higher than riverine fluxes of DIN (Seitzinger *et al.*, 2010) and DON (Harrison *et al.*, 2005), respectively (Figure 4). DIP export from total SGD was half of the global river DIP (Seitzinger *et al.*, 2005) input to the ocean (Figure 4). SGD exporting more N than P may eventually lead to P limitation rather than N limitation in coastal systems (Santos *et al.*, 2021). In contrast to fresh SGD, total SGD delivers a mixture of new nutrients, from meteoric groundwater, and recycled nutrients derived from recirculated seawater, which may be otherwise buried in coastal sediments.

Groundwater derived nutrients drive primary production in systems around the world and influence coastal ocean biogeochemistry (Santos *et al.*, 2021). This analysis revealed that two major factors determining nutrient concentrations in groundwater were salinity and crop cover. Increasing human population and climate change will drive land use changes, increasing temperatures, and groundwater salinization, which will likely enhance nutrient loading from SGD to the coastal ocean. This may exacerbate events of hypoxia, harmful algal blooms, and cause water quality degradation; all of which have large economic and societal consequences. To develop innovative management practices and protect water quality, SGD must be accounted for as a contributor of nutrients at local, regional, and global scales.

5.2.5. Limitations

Meta-analyses require a number of assumptions, but allow for novel global scale investigations (Cadotte *et al.*, 2012; Vetter *et al.*, 2013). This study, as are all meta-analyses, was restricted by the data available and despite limited data from the poles, Africa, and South America, this is the most comprehensive dataset to date. Determining a global groundwater endmember also presents limitations, such as scaling up local datasets, classifying fresh and saline SGD, and taking an

average of global concentrations with high variation. We addressed skewing in our data by calculating the mean from the logged concentrations similar to the method used by Cho *et al.*, 2018. To further address these limitations, Monte Carlo simulations could be employed to estimate a range of possible groundwater fluxes. This analysis would account for the full distribution of values observed for each term in the flux equations and allow better understanding and reporting of the variance associated with potential fluxes.

Applying the theory of conservative mixing to the subterranean estuaries suggests groundwater and seawater mixing, steady state, and constant endmembers (Santos *et al.*, 2009). Despite these assumptions this analysis, which was intentionally simple, allows for application to a variety of sites and comparisons on a global scale. Conservative mixing model analysis cannot resolve specific processes occurring at each site, but our analysis clearly indicated non-conservative behavior with respect to nutrients in many subterranean estuaries around the world. Measurements of process rates within subterranean estuaries would allow for a more accurate interpretation of their role in SGD fluxes, but are not yet widely available at this scale.

When calculating nutrient fluxes in this study, we relied on previously estimated SGD water fluxes as it was beyond the scope of this work to recalculate these values. A variety of sources for both total and fresh SGD water fluxes estimated from radium budgets, hydrogeological models, and seepage meter measurements were used to represent the range of available estimates (Taniguchi, 2002; Moore *et al.*, 2008; Kwon *et al.*, 2014; Cho and Kim, 2016; Cho *et al.*, 2018; Zhou *et al.*, 2019; Luijendijk *et al.*, 2020). These water fluxes vary and, in some cases, have high uncertainties (Table S2). However, the fluxes reported here are the result of the most comprehensive endmember and water flux assessments available. Estimations of SGD nutrient fluxes to the ocean will continue to improve as measurements and models

predicting SGD water fluxes, as well as groundwater endmembers also improve, especially in areas that are currently data poor.

5.3. Methods

5.3.1. Data compilation

Data were compiled from Web of Science searches and collaborators around the world resulting in >10,000 samples with 5,660 observations of DIN, 1,890 of DON, and 4,569 of DIP from 216 subterranean estuaries. The full dataset is available on an interactive website that includes a graphical representation of data for each nutrient at each site (Shiny Interactive Map) as well as the Pangeae repository. Each observation included some or all of the following information; location/site name, latitude, longitude, temperature, salinity, depth, as well as concentrations of nitrate, nitrite, ammonium, total dissolved nitrogen, dissolved organic nitrogen, dissolved inorganic phosphorus (Figure S1). Data were categorized by latitude, continent, ocean basin (Atlantic, Pacific, Indian, Arctic), depth sections including: 0-0.5m, 0.5-1m, 1-5m, >10 m, site type determined by lithology (Muddy, Sandy, Rocky, or Mixed), Dürr Type (Dürr *et al.*, 2011), ECU classification (Sayre *et al.*, 2019), Koeppen Geiger Climate Zone (Kottek *et al.*, 2006), and Copernicus land cover classification (Buchhorn *et al.*, 2020). GLDAS climate data including average rainfall, evaporation, and baseflow as well as fresh SGD fluxes (Zhou *et al.*, 2019; Luijendijk *et al.*, 2020) were determined for each site.

To characterize the groundwater nutrient pool, data were evaluated using random forest analysis to determine important features and potential drivers. Linear regressions were also used to explore relationships between nutrient concentrations and continuous, explanatory variables. To examine N speciation, the percent of NO_x, NH₄⁺, and DON in the total N pool was calculated and visualized based on site type and salinity (Figure 2), salinity (Figure S14), site type (Figure

S15), and depth (Figure S16). DIN and DIP values were used to calculate N:P ratios as DIN:DIP for each sample, these were also averaged to determine an average N:P ratio for each site type (Figure 2).

5.3.2. Statistical Analyses

To resolve the key variables influencing the global distribution of DIN, DON, and DIP concentrations in subterranean estuaries, we assessed both factor and continuous variables, with linear regressions and random forest analysis. When assessing relationships with linear regressions, the data were log transformed to meet the assumption of data normality. All linear regression analysis and data visualization was conducted in R Studio (R Studio, 2020).

A random forest classification was conducted to determine the relative feature importance of site and sample characteristics on groundwater nutrient concentrations (McKenzie *et al.*, 2021). Briefly, the random forest algorithm consists of an ensemble of decisions trees. Feature randomness is used to build individual trees that are uncorrelated to one another to build a forest, the prediction by the ensemble is, therefore, more accurate than any one individual model. This results in a relative feature importance (or percentage contribution) for each input variable with respect to DIN, DIP, and DON (Figure S3). The random forest classification was conducted in Python 3.6 (Van Rossum and Drake, 2009) using the *scikit-learn RandomForestRegressor* package (Pedregosa *et al.*, 2011).

The random forest analysis included latitude as a potentially important factor, indicating that spatial distribution could be important to estimating endmember concentration. Here, we observed no clear trend indicating spatial autocorrelation in our data (Figure S1 & S2). A previous analysis of global DIN and DIP in groundwater including <1000 samples, also found no

difference between estimates made with a gridded approach and those that were not gridded (Cho *et al.*, 2018).

5.3.3. Subterranean estuary transformations

Sites within the meta-dataset were included in conservative mixing model analysis if they met the following criteria: 1) ten or more observations of both the analyte in question (NO_3^- , NH_4^+ , DIP, or DON) and salinity, and 2) data fell across a range of salinities including fresh groundwater samples. Conservative mixing models rely on the conservative behavior of salinity in estuarine systems. Mixing models were initially developed for surface estuaries (Boyle *et al.*, 1974; Officer and Lynch, 1981; Kaul and Froelich Jr, 1984) and later applied to subterranean estuaries (Ullman *et al.*, 2003; Isaac R. Santos *et al.*, 2009). This type of analysis assumes homogeneous mixing of fresh groundwater and saline seawater, only two water masses and, therefore, two endmembers and that these endmembers are constant (Loder and Reichard, 1981; Officer and Lynch, 1981; Isaac R Santos *et al.*, 2009). Despite these assumptions, the analysis results in a coarse-grain view of transformations occurring within subterranean estuaries with respect to non-conservative elements.

Fresh and saline endmember concentrations were determined by taking the 5% and 95% tails of the salinity data and determining the average analyte concentration in those ends. If initially including only one sample, the tails were increased by 5% until at least two values were included. The endmember concentrations were used to calculate predicted conservative mixing lines from the fraction of saline and fresh endmembers at each salinity interval. The observed data were then compared to the predicted mixing line to determine whether the subterranean estuary was producing or consuming NO_3^- , NH_4^+ , DON, or DIP along the subterranean estuary salinity gradient. If data fell along the conservative mixing line, the subterranean estuary was

determined to have “conservative” behavior. If the majority of observations lay above the conservative mixing line, behavior was classified as “productive”. In contrast, observations below the conservative mixing line indicated “reductive” behavior. Sites with no discernable pattern or those that appeared to have more than two endmembers were classified as “undefined”. Subterranean behavior was assessed twice independently then reassessed to reach a final classification qualitatively then the production or consumption along the salinity gradient was quantified by determining the disparity between the observed data points and the predicted concentrations.

5.3.4. Calculating SGD endmembers and nutrient fluxes to the global ocean

The compiled nutrient concentrations were log normally distributed (Figure S4) and, therefore, values were log transformed prior to calculating the mean endmember concentrations to account for skewing by high nutrient concentrations at low salinities (Figure 1) (Cho *et al.*, 2018). These endmembers were used in Equation 1 and 2 to calculate global fluxes of DIN, DON, and DIP in SGD to the ocean. Various known SGD water fluxes of both fresh and total SGD (Taniguchi, 2002; Moore *et al.*, 2008; Kwon *et al.*, 2014; Cho and Kim, 2016; Cho *et al.*, 2018; Zhou *et al.*, 2019; Luijendijk *et al.*, 2020) were used to determine the global nutrient fluxes (Table S2). Error associated with SGD fluxes was propagated from the standard error associated with the endmember and the water flux for each of the calculated potential fluxes.

We calculate export via total SGD as:

$$F_{SGD} = ([C]_{gw} - [C]_{sw}) \times Y_{sgw} \quad (\text{Equation 1})$$

where F_{SGD} is the total SGD nutrient flux to the global ocean, $[C]_{gw}$ is the groundwater endmember nutrient concentration in all samples, $[C]_{sw}$ is the globally averaged seawater

nutrient concentration (Garcia *et al.*, 2013; Letscher *et al.*, 2013) and Y_{sgw} is the total SGD water flux. This approach assumes that saline SGD dominates total SGD, hence the $[C]_{sw}$ term.

Fluxes via fresh SGD were calculated as:

$$F_{fSGD} = [C]_{fgw} M \times Y_{fgw} \quad (\text{Equation 2})$$

where F_{fSGD} is the fresh SGD nutrient flux to the global ocean, $[C]_{fgw}$ is the fresh groundwater (salinity <10) endmember concentration, M is the modification (production or consumption) along the flow-path, and Y is the fresh SGD water flux. The M modification term is the correction term applied to the fresh groundwater endmember concentration (M , Equation 2) to account for transformations within subterranean estuaries based on the conservative mixing analysis. The correction term was determined by estimating the disparity between the observed data and the predicted values, derived from the mixing model analysis, at each data point when that site was determined to be productive or reductive. For each site, the percent change was calculated as the sum of the differences between observed and theoretical values at each point, divided by the sum of the theoretical values. No change along the subterranean salinity gradient was assumed for sites with conservative and undefined behavior. The percent change calculated was averaged across all sites that exhibited productive behavior and reductive behavior, respectfully. Therefore, the M term applied to the fresh groundwater endmember observations becomes:

$$M = (D_{prod} * n_{prod.}) + (D_{consum.} * n_{consum.}) + (n_{conserv.}) + (n_{undef.}) \quad (\text{Equation 3})$$

Where M is the transformation term, D is the average percent change in nutrient concentration due to production ($D_{prod.}$) or consumption ($D_{consum.}$) and n is the percentage of subterranean estuaries exhibiting each behavior. If $M > 1$ indicates net production, $M < 1$ indicates net reduction, and an $M = 1$ represents no change in analyte concentration. The M term was

applied to all nutrient concentrations in the meta-dataset, then average fresh SGD endmembers were recalculated as described above. All nutrient fluxes are reported in Tmoles m^3 and the water fluxes are reported in $\text{m}^3 \text{yr}^{-1}$ resulting in a flux in Tmoles yr^{-1} .

5.4. References

- Basu, N.B. (2022) in. press. *Nat Geosci*.
- Berman, T. and Bronk, D.A. (2003) Dissolved organic nitrogen: A dynamic participant in aquatic ecosystems. *Aquat Microb Ecol* **31**: 279–305.
- Beusen, A. H. W. ; Slomp, C. P.; Bouwman, A.F. (2013) Global land – ocean linkage : direct inputs of nitrogen to coastal waters via submarine groundwater discharge. *Environ Res Lett* **8**.
- Bowen, J.L., Giblin, A.E., Murphy, A.E., Bulseco, A.N., Deegan, L.A., Johnson, D.S., et al. (2020) Not all nitrogen is created equal: Differential effects of nitrate and ammonium enrichment in coastal Wetlands. *Bioscience* **70**: 1108–1119.
- Boyle, E., Collier, R., Dengler, A.T., Edmond, J.M., Ng, A.C., and Stallard, R.F. (1974) On the chemical mass-balance in estuaries. *Geochim Cosmochim Acta* **38**: 1719–1728.
- Bronk, D.A., See, J.H., Bradley, P., and Killberg, L. (2006) DON as a source of bioavailable nitrogen for phytoplankton. *Biogeosciences Discuss* **3**: 1247–1277.
- Buchhorn, M., Smets, B., Bertels, L., De Roo, B., Lesiv, M., Tsendbazar, N.E., et al. (2020) Copernicus Global Land Service: Land Cover 100m: collection 3: epoch 2019: Globe.
- Cadotte, M.W., Mehrkens, L.R., and Menge, D.N.L. (2012) Gauging the impact of meta-analysis on ecology. *Evol Ecol* **26**: 1153–1167.
- Charette, M.A. and Sholkovitz, E.R. (2002) Oxidative precipitation of groundwater-derived ferrous iron in the subterranean estuary of a coastal bay. *Geophys Res Lett* **29**: 85-1-85–4.
- Cho, H. and Kim, G. (2016) Determining groundwater Ra end-member values for the estimation of the magnitude of submarine groundwater discharge using Ra isotope tracers. *Geophys Res Lett* **43**: 3865–3871.
- Cho, H.M., Kim, G., Kwon, E.Y., Moosdorf, N., Garcia-Orellana, J., and Santos, I.R. (2018) Radium tracing nutrient inputs through submarine groundwater discharge in the global ocean. *Sci Rep* **8**: 1–7.
- Cira, E.K., Paerl, H.W., and Wetz, M.S. (2016) Effects of Nitrogen Availability and Form on Phytoplankton Growth in a Eutrophied Estuary (Neuse River Estuary, NC, USA). *PLoS One* **11**: e0160663.
- Conley, D.J., Paerl, H.W., Howarth, R.W., Boesch, D.F., Seitzinger, S.P., Havens, K.E., et al. (2009) Controlling Eutrophication: Nitrogen and Phosphorus. *Science (80-)* **323**: 1014–1015.
- Downing, J.A. (1997) Marine nitrogen: Phosphorus stoichiometry and the global N:P cycle. *Biogeochemistry* **37**: 237–252.
- Dulaiova, H., Camilli, R., Henderson, P.B., and Charette, M.A. (2010) Coupled radon, methane and nitrate sensors for large-scale assessment of groundwater discharge and non-point source pollution to coastal waters. *J Environ Radioact* **101**: 553–563.
- Dürr, H.H., Laruelle, G.G., van Kempen, C.M., Slomp, C.P., Meybeck, M., and Middelkoop, H. (2011) Worldwide typology of nearshore coastal systems: defining the estuarine filter of river inputs to the oceans. *Estuaries and coasts* **34**: 441–458.
- Garcia, H.E., Locarnini, R.A., Boyer, T.P., Antonov, J.I., Baranova, O.K., Zweng, M.M., et al. (2013) Dissolved inorganic nutrients (phosphate, nitrate, silicate). *World Ocean Atlas* **4**: 1–25.
- Harrison, J.A., Caraco, N., and Seitzinger, S.P. (2005) Global patterns and sources of dissolved organic matter export to the coastal zone: Results from a spatially explicit, global model.

Global Biogeochem Cycles **19**:

- Jickells, T.D. (1998) Nutrient Biogeochemistry of the Coastal Zone. *Science* (80-) **281**: 217–222.
- Joye, S.B. and Hollibaugh, J.T. (1995) Influence of Sulfide Inhibition of Nitrification on Nitrogen Regeneration in Sediments. *Science* (80-) **270**: 623–625.
- Kaul, L.W. and Froelich Jr, P.N. (1984) Modeling estuarine nutrient geochemistry in a simple system. *Geochim Cosmochim Acta* **48**: 1417–1433.
- Kottek, M., Grieser, J., Beck, C., Rudolf, B., and Rubel, F. (2006) World map of the Köppen-Geiger climate classification updated. *Meteorol Zeitschrift* **15**: 259–263.
- Kroeger, K.D. and Charette, M.A. (2008) Nitrogen biogeochemistry of submarine groundwater discharge. *Limnol Oceanogr* **53**: 1025–1039.
- Kwon, E.Y., Kim, G., Primeau, F., Moore, W.S., Cho, H.-M., DeVries, T., et al. (2014) Global estimate of submarine groundwater discharge based on an observationally constrained radium isotope model. *Geophys Res Lett* **41**: 8438–8444.
- Letscher, R.T., Hansell, D.A., Carlson, C.A., Lumpkin, R., and Knapp, A.N. (2013) Dissolved organic nitrogen in the global surface ocean: Distribution and fate. *Global Biogeochem Cycles* **27**: 141–153.
- Liu, J., Du, J., Wu, Y., and Liu, S. (2018) Nutrient input through submarine groundwater discharge in two major Chinese estuaries: the Pearl River Estuary and the Changjiang River Estuary. *Estuar Coast Shelf Sci* **203**: 17–28.
- Loder, T.C. and Reichard, R.P. (1981) The dynamics of conservative mixing in estuaries. *Estuaries* **4**: 64–69.
- Loveless, A.M. and Oldham, C.E. (2010) Natural attenuation of nitrogen in groundwater discharging through a sandy beach. *Biogeochemistry* **98**: 75–87.
- Luijendijk, E., Gleeson, T., and Moosdorf, N. (2020) Fresh groundwater discharge insignificant for the world's oceans but important for coastal ecosystems. *Nat Commun* **11**:
- McKenzie, T., Dulai, H., and Fuleky, P. (2021) Traditional and novel time-series approaches reveal submarine groundwater discharge dynamics under baseline and extreme event conditions. *Sci Rep* **11**: 1–14.
- Moore, W.S. (2010) The Effect of Submarine Groundwater Discharge on the Ocean. *Ann Rev Mar Sci* **2**: 59–88.
- Moore, W.S., Sarmiento, J.L., and Key, R.M. (2008) Submarine groundwater discharge revealed by 228 Ra distribution in the upper Atlantic Ocean. *Nat Geosci* **1**: 309–311.
- Nixon, S.W. (1995) Coastal marine eutrophication: A definition, social causes, and future concerns. *Ophelia* **41**: 199–219.
- Officer, C.B. and Lynch, D.R. (1981) Dynamics of Mixing in Estuaries. *Estuar Coast Shelf Sci* **12**: 525–533.
- Pedregosa, F., Varoquaux, G., Gramfort, A., Michel, V., Thirion, B., Grisel, O., et al. (2011) Scikit-learn: Machine learning in Python. *J Mach Learn Res* **12**: 2825–2830.
- Rahman, A., Mondal, N.C., and Tiwari, K.K. (2021) Anthropogenic nitrate in groundwater and its health risks in the view of background concentration in a semi arid area of Rajasthan, India. *Sci Rep* **11**: 1–13.
- Robinson, C.E., Xin, P., Santos, I.R., Charette, M.A., Li, L., and Barry, D.A. (2018) Groundwater dynamics in subterranean estuaries of coastal unconfined aquifers: Controls on submarine groundwater discharge and chemical inputs to the ocean. *Adv Water Resour* **115**: 315–331.

- Rocha, C., Robinson, C.E., Santos, I.R., Waska, H., Michael, H.A., and Bokuniewicz, H.J. (2021) A place for subterranean estuaries in the coastal zone. *Estuar Coast Shelf Sci* **250**.
- Rodell, M., Houser, P.R., Jambor, U., Gottschalck, J., Mitchell, K., Meng, C., et al. (2004) The Global Land Data Assimilation System. *Bull Am Meteorol Soc* **85**: 381–394.
- Van Rossum, G. and Drake, F.L. (2009) Python.
- Sanial, V., Moore, W.S., and Shiller, A.M. (2021) Does a bottom-up mechanism promote hypoxia in the Mississippi Bight? *Mar Chem* **235**.
- Santos, I.R., Burnett, W.C., Chanton, J., Mwashote, B., Suryaputra, I.G.N.A., and Dittmar, T. (2008) Nutrient biogeochemistry in a Gulf of Mexico subterranean estuary and groundwater- derived fluxes to the coastal ocean. *53*: 705–718.
- Santos, Isaac R., Burnett, W.C., Dittmar, T., Suryaputra, I.G.N.A., and Chanton, J. (2009) Tidal pumping drives nutrient and dissolved organic matter dynamics in a Gulf of Mexico subterranean estuary. *Geochim Cosmochim Acta* **73**: 1325–1339.
- Santos, Isaac R, Burnett, W.C., Dittmar, T., Suryaputra, I.G.N.A., and Chanton, J. (2009) Tidal pumping drives nutrient and dissolved organic matter dynamics in a Gulf of Mexico subterranean estuary. *Geochim Cosmochim Acta* **73**: 1325–1339.
- Santos, I.R., Chen, X., Lecher, A., Sawyer, A., Moosdorf, N., Rondellas, V., et al. (2021) Submarine groundwater discharge impacts on coastal nutrient biogeochemistry. *Nat Rev Earth Environ* 108–119.
- Sayre, R., Noble, S., Hamann, S., Smith, R., Wright, D., Breyer, S., et al. (2019) A new 30 meter resolution global shoreline vector and associated global islands database for the development of standardized ecological coastal units. *J Oper Oceanogr* **12**: S47–S56.
- Schlesinger, W.H. (2009) On the fate of anthropogenic nitrogen. *Proc Natl Acad Sci U S A* **106**: 203–208.
- Seitzinger, S.P., Harrison, J.A., Dumont, E., Beusen, A.H.W., and Bouwman, A.F. (2005) Sources and delivery of carbon, nitrogen, and phosphorus to the coastal zone: An overview of Global Nutrient Export from Watersheds (NEWS) models and their application. *Global Biogeochem Cycles* **19**: 1–11.
- Seitzinger, S.P., Mayorga, E., Bouwman, A.F., Kroeze, C., Beusen, A.H.W., Billen, G., et al. (2010) Global river nutrient export: A scenario analysis of past and future trends. *Global Biogeochem Cycles* **24**.
- Slomp, C.P. and Van Cappellen, P. (2004) Nutrient inputs to the coastal ocean through submarine groundwater discharge: Controls and potential impact. *J Hydrol* **295**: 64–86.
- Spiteri, C., Cappellen, P. Van, and Regnier, P. (2008) Surface complexation effects on phosphate adsorption to ferric iron oxyhydroxides along pH and salinity gradients in estuaries and coastal aquifers. *Geochim Cosmochim Acta* **72**: 3431–3445.
- Taniguchi, M. (2002) Tidal effects on submarine groundwater discharge into the ocean. *Geophys Res Lett* **29**: 9–11.
- Taylor, G.T., Gobler, C.J., and Sañudo-Wilhelmy, S.A. (2006) Speciation and concentrations of dissolved nitrogen as determinants of brown tide *Aureococcus anophagefferens* bloom initiation. *Mar Ecol Prog Ser* **312**: 67–83.
- Team, Rs. (2020) RStudio: Integrated Development for R.
- Ullman, W.J., Chang, B., Miller, D.C., and Madsen, J.A. (2003) Groundwater mixing, nutrient diagenesis, and discharges across a sandy beachface Cape Henlopen, Delaware (USA). *Estuar Coast Shelf Sci* **57**: 539–552.
- Vetter, D., Rucker, G., and Storch, I. (2013) Meta-analysis: A need for well-defined usage in

- ecology and conservation biology. *Ecosphere* **4**: 1–24.
- Wurtsbaugh, W.A., Paerl, H.W., and Dodds, W.K. (2019) Nutrients, eutrophication and harmful algal blooms along the freshwater to marine continuum. *WIREs Water* **6**: 1–27.
- Zhou, Y.Q., Sawyer, A.H., David, C.H., and Famiglietti, J.S. (2019) Fresh Submarine Groundwater Discharge to the Near-Global Coast. *Geophys Res Lett* **46**: 5855–5863.

5.5. Figures

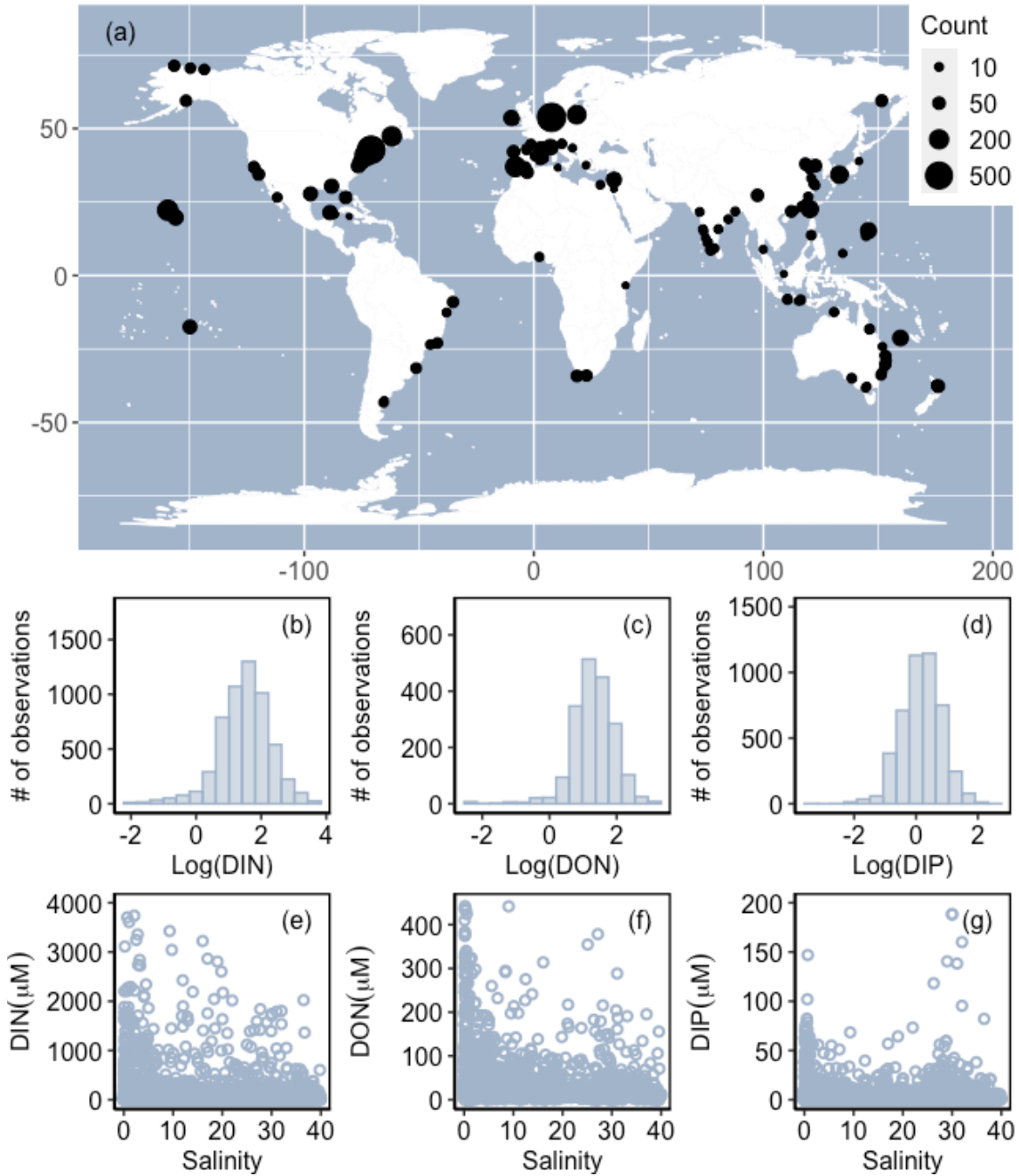


Figure 1. Map indicating sample site locations ($n=216$), including local-scale sample size (count, indicated by dot size). Histograms showing concentrations of b) DIN ($n=5,660$), c) DON ($n=1,890$), and d) DIP ($n=4,569$) on a log scale. Scatter plots of e) DIN, f) DON, and g) DIP concentrations (μM) with sample salinity. The full dataset is available (submitted to Pangaea) and data can be viewed using the Shiny Interactive Map.

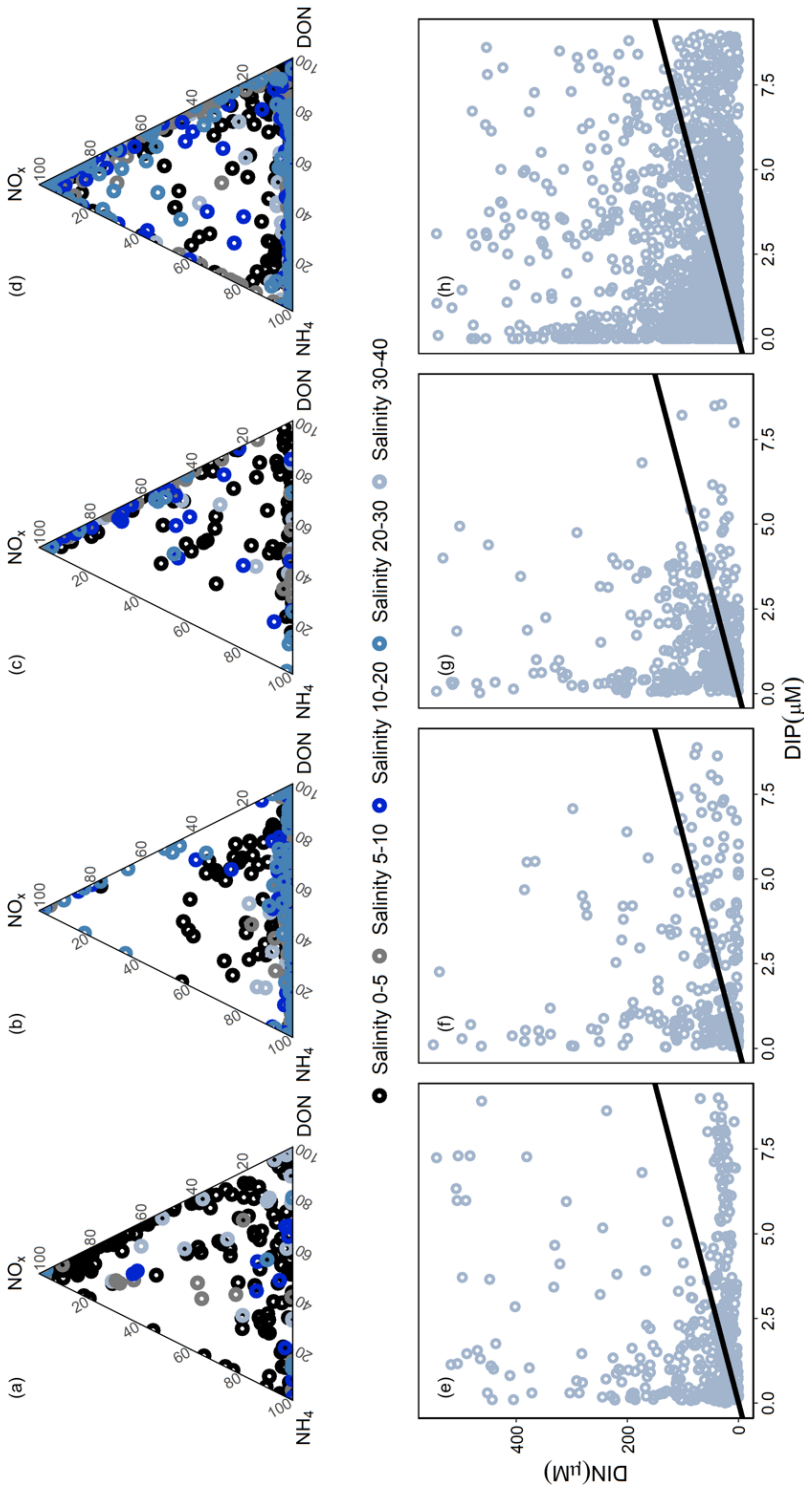


Figure 2. Ternary plots of N speciation in groundwater samples by site lithology and salinity, indicated by color, in a) Mixed, b) Muddy, c) Rocky, and d) Sandy sites. DIN (μM): DIP (μM) ratios for e) Mixed, f) Muddy, g) Rocky, and h) Sandy sites with the Redfield Ratio (16:1) line shown in black.

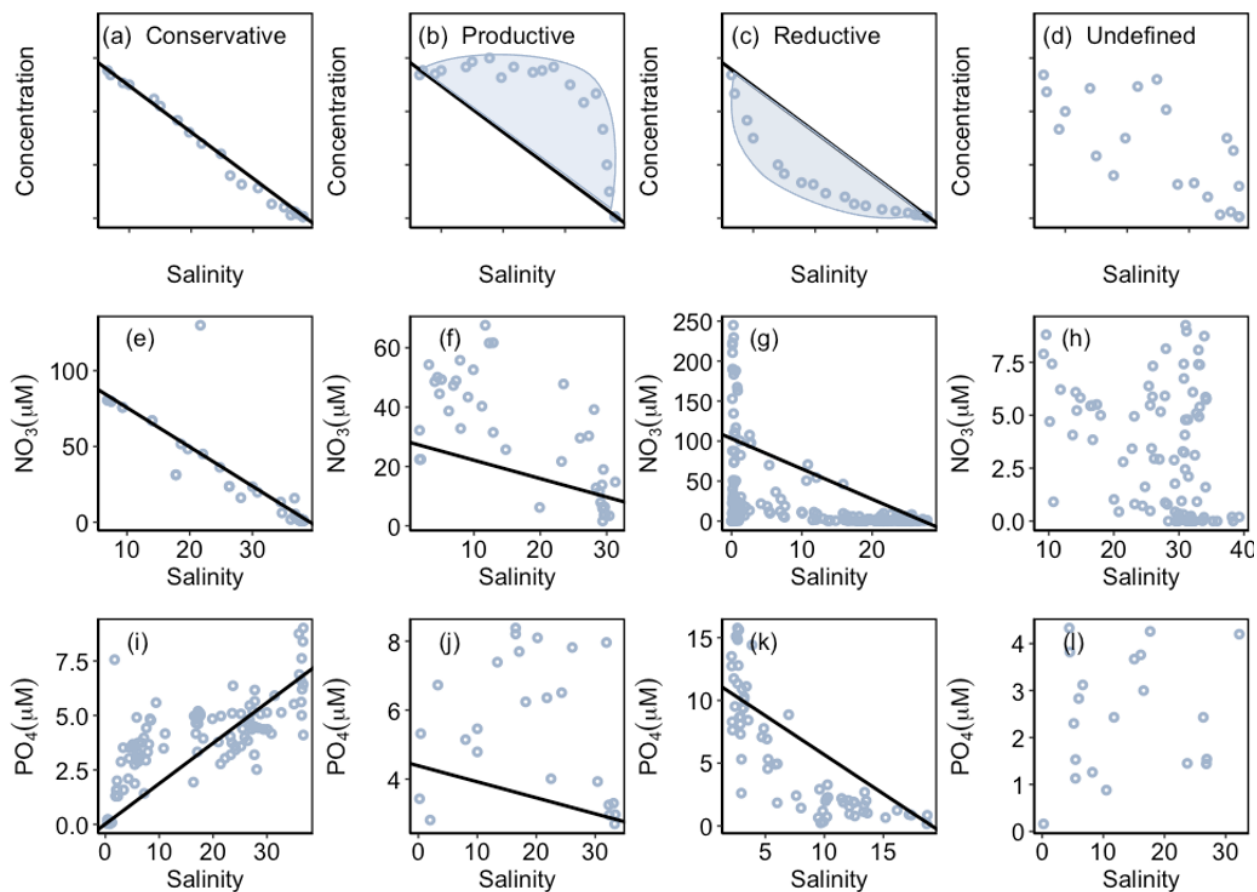


Figure 3. Conceptual diagrams of a) conservative, b) productive, c) consumptive, and d) undefined behavior in subterranean estuaries. Examples of each classification with respect to NO_3^- (μM) and PO_4^{2-} (μM) in subterranean estuaries from the meta-dataset including e) Calanques of Marseille-Cassis, f) Kasitna Bay, g) Waquiot Bay, and h) Killary as well as i) Rarotonga, j) Monterey Bay (Seabright), k) Gloucester Point, and j) Kona Coast.

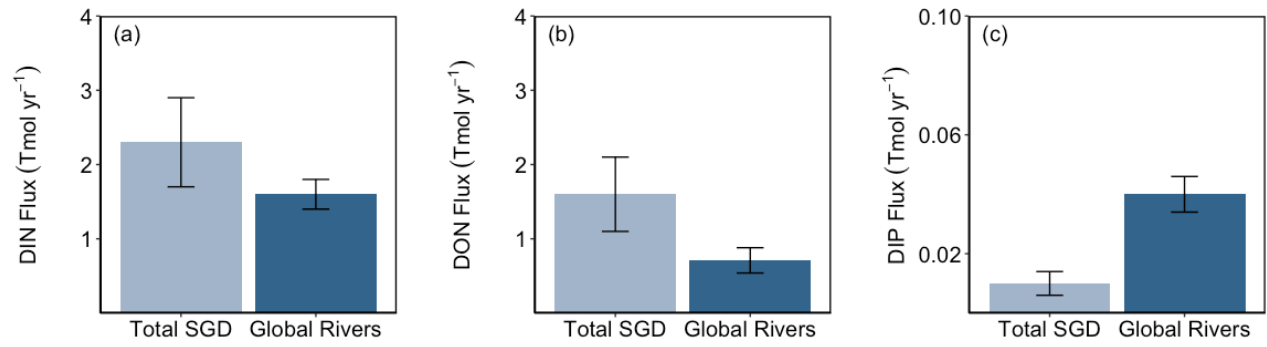


Figure 4. Bar plots comparing fluxes via total SGD and rivers (Seitzinger *et al.*, 2005; Seitzinger *et al.*, 2010; Harrison *et al.*, 2005) of a) DIN, b) DON, and c) DIP to the global ocean.

5.6. Appendix G

Table S1. STE Behavior with respect to NO_3^- , NH_4^+ , DON, and DIP shown as the percentage of sites exhibiting that behavior and the total number of sites assessed for each analyte.

Analyte	Conservative (%)	Productive (%)	Consumptive (%)	Undefined (%)	Sites
NO_3^-	11.1	22.2	22.2	44.4	72
NH_4^+	10.8	26.2	27.7	35.4	65
DON	21.4	3.6	28.6	46.4	28
DIP	9.4	14.1	23.4	53.1	64

Table S2. Fluxes of DON, DIN, and DIP resulting from various endmember and SGD flux assumptions in Tmoles yr⁻¹ (\pm standard error).

Assumption	Water Flux Source	DIN	DON	DIP
Global	Kwon et al., 2014	2.3 (0.6)	1.6 (0.5)	0.01 (0.004)
Global	Cho and Kim, 2016	2.7 (0.8)	1.9 (0.8)	0.02 (0.005)
Global	Taniguchi et al., 2002	0.6 (0.1)	0.4 (0.1)	0.003 (0.001)
Fresh	Elco et al., 2020	0.01 (0.01)	0.004 (0.01)	0.0001 (0.003)
Fresh	Zhou et al., 2019	0.02 (0.02)	0.01 (0.01)	0.0004 (0.001)
Fresh	Cho et al., 2018	0.09 (0.01)	0.05 (0.02)	0.002 (0.04)
Transformed Fresh	Elco et al., 2020	0.01 (0.01)	0.004 (0.01)	0.0001 (0.003)
Transformed Fresh	Zhou et al., 2019	0.02 (0.02)	0.01 (0.01)	0.0004 (0.001)
Transformed Fresh	Cho et al., 2018	0.08 (0.01)	0.04 (0.02)	0.001 (0.04)
Global Sal > 10	Cho and Kim, 2016	0.6 (0.2)	0.5 (0.2)	0.009 (0.003)
Global Sal > 20	Cho and Kim, 2016	0.4 (0.1)	0.4 (0.1)	0.01 (0.003)
Global Sal > 30	Cho and Kim, 2016	0.05 (0.05)	0.09 (0.1)	0.01 (0.01)
Atlantic Ocean	Moore et al., 2008	0.6 (0.003)	0.4 (0.04)	0 (0)

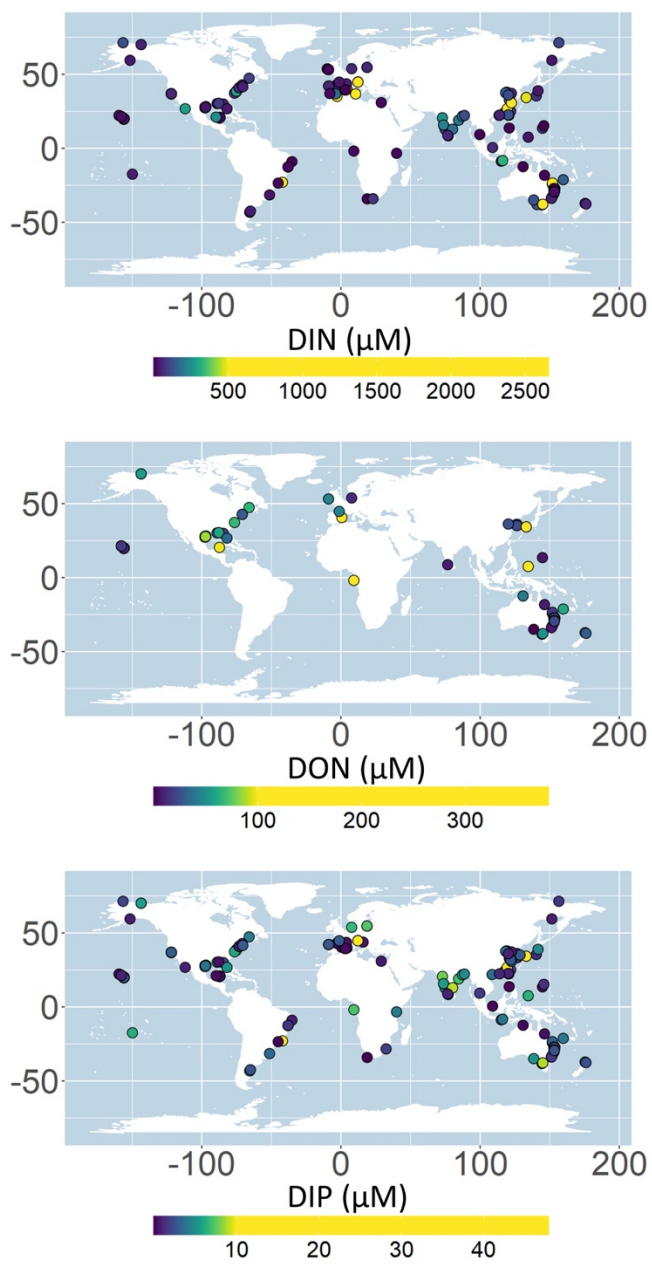


Figure S1. Global maps showing site averaged a) DIP, b) DIN, and c) DON concentrations in $\mu\text{mol L}^{-1}$ where color indicates concentration.

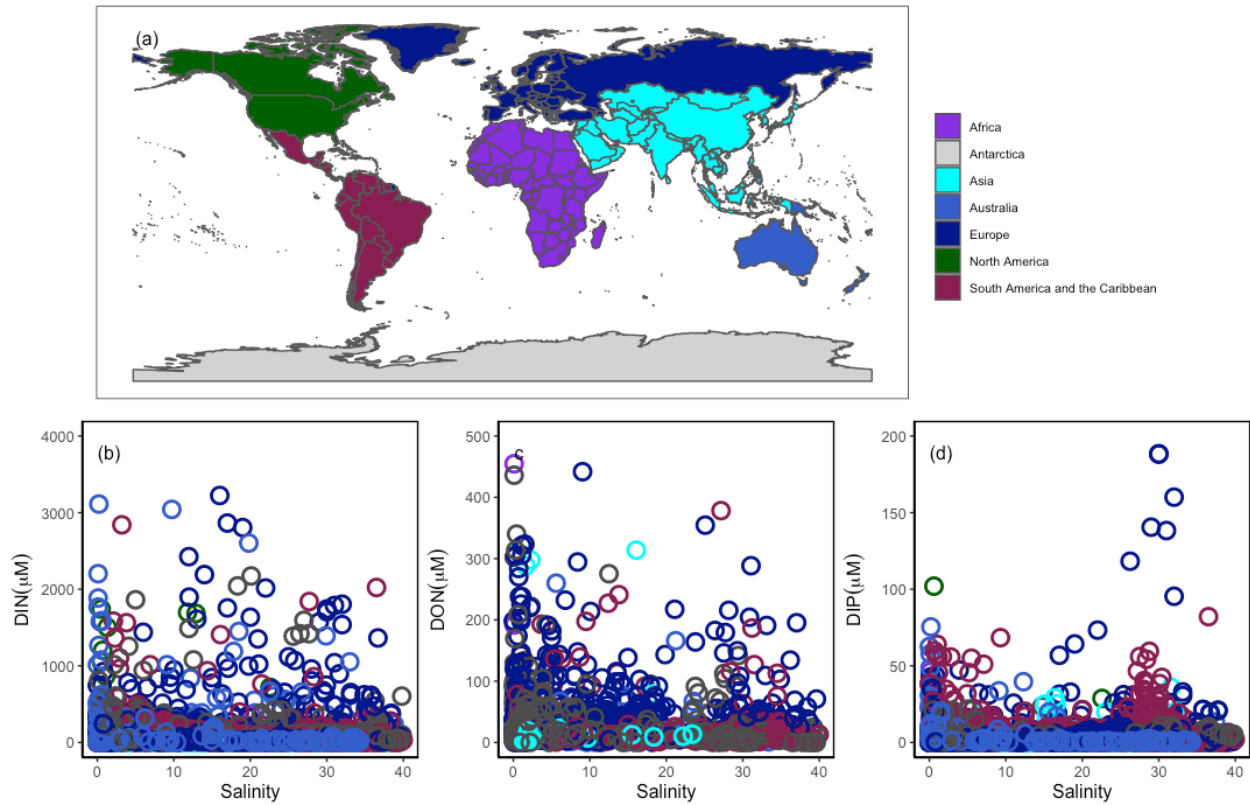


Figure S2. Spatial heterogeneity of global groundwater samples where dot color corresponds to continent a) for b) DIN, c) DON, and d) DIP. No clear spatial trends were determined. Dark grey points are indicative of data from islands.

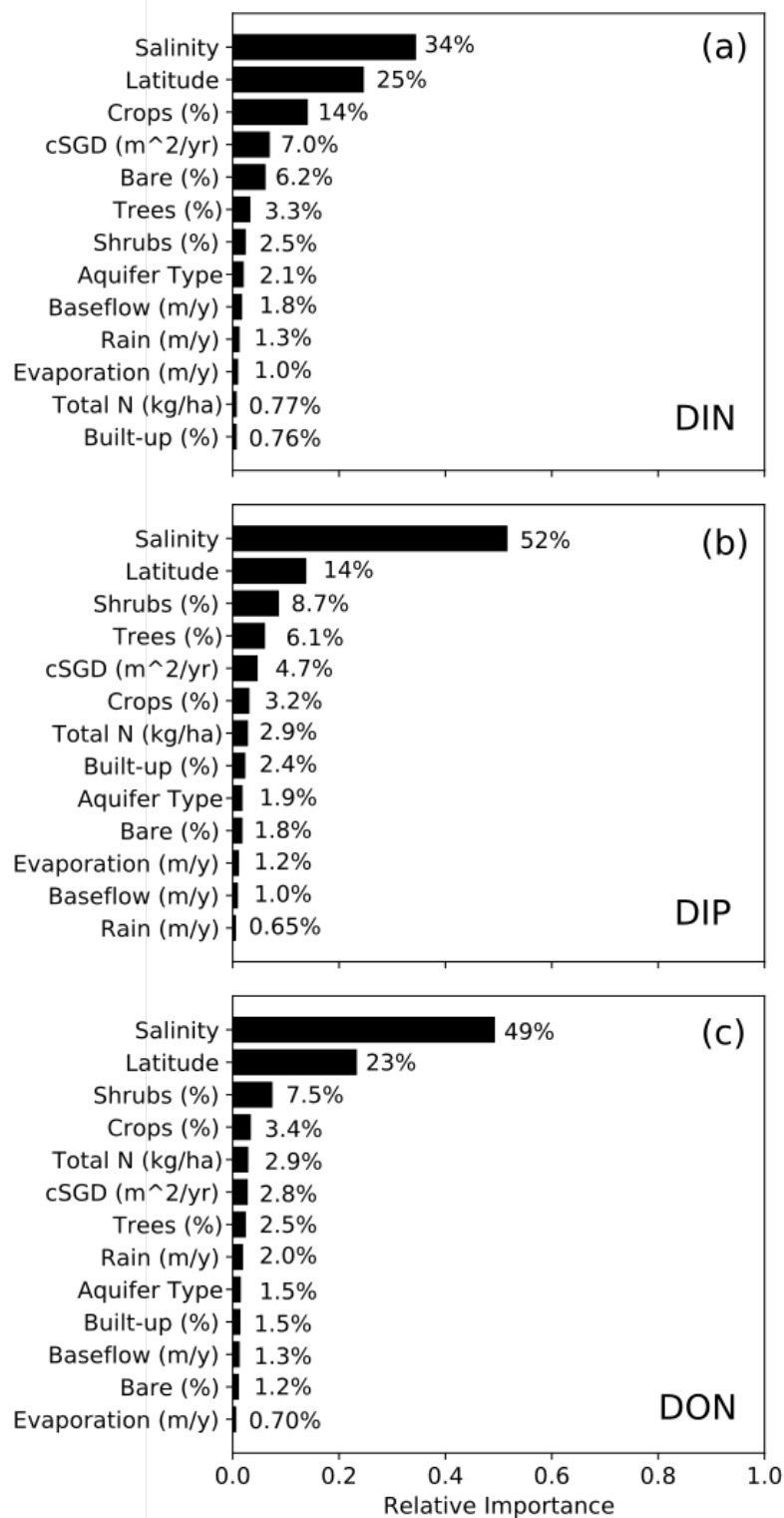


Figure S3. Random forest analysis output: feature importance (%) to groundwater nutrient concentrations of DIN (a), DON (b) and DIP (c).

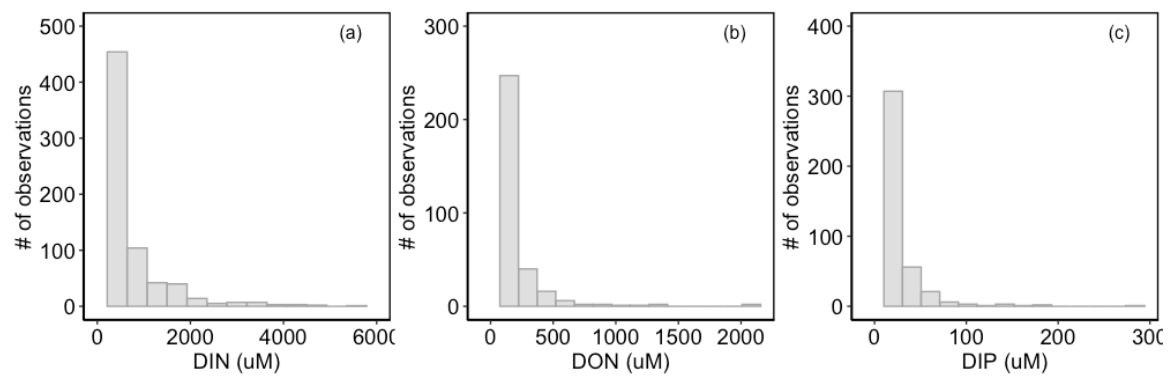


Figure S4. Histogram of untransformed groundwater nutrient concentrations, which clearly shows the log normal distribution of a) DIN, b) DON, and c) DIP concentrations.

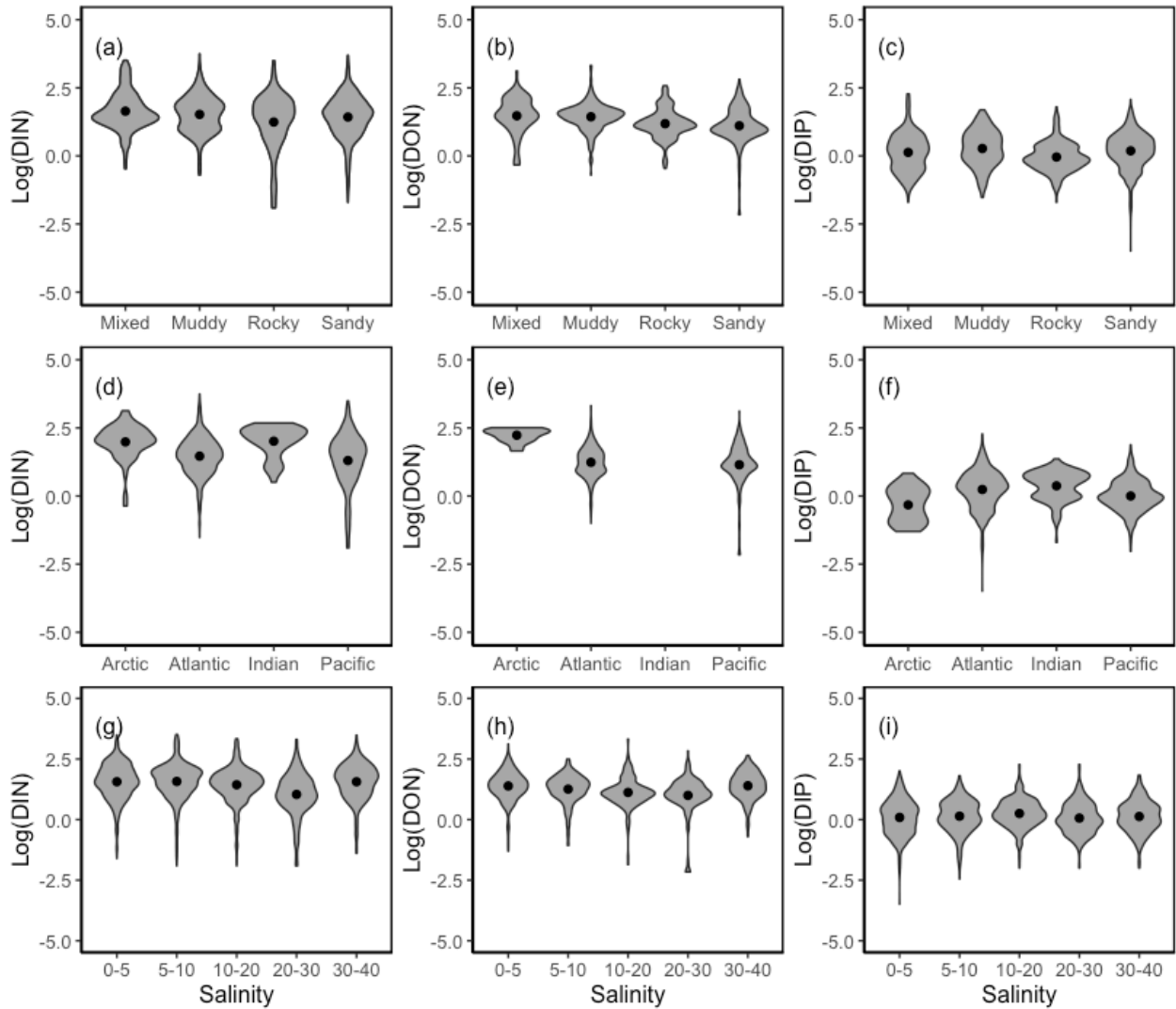


Figure S5. Violin plots showing the distribution of log transformed nutrient concentrations of DIN, DON, and DIP across different factors: Site Type (A-C), Ocean Basin (D-F), and salinity (G-I).

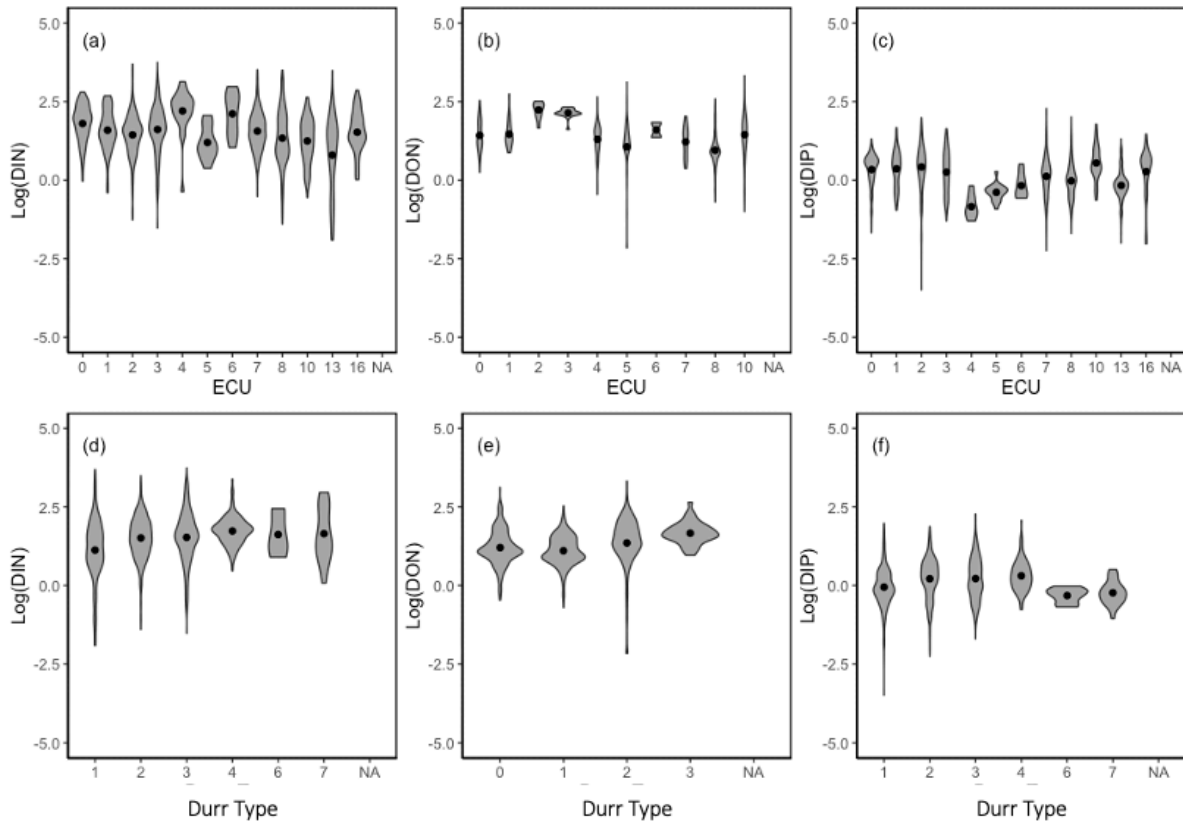


Figure S6. Violin plots showing the distribution of log transformed nutrient concentrations of DIN, DON, and DIP across site specific Ecological Coastal Unit (ECU) Classifications (A-C) and Dürr Type Classifications (D-F).

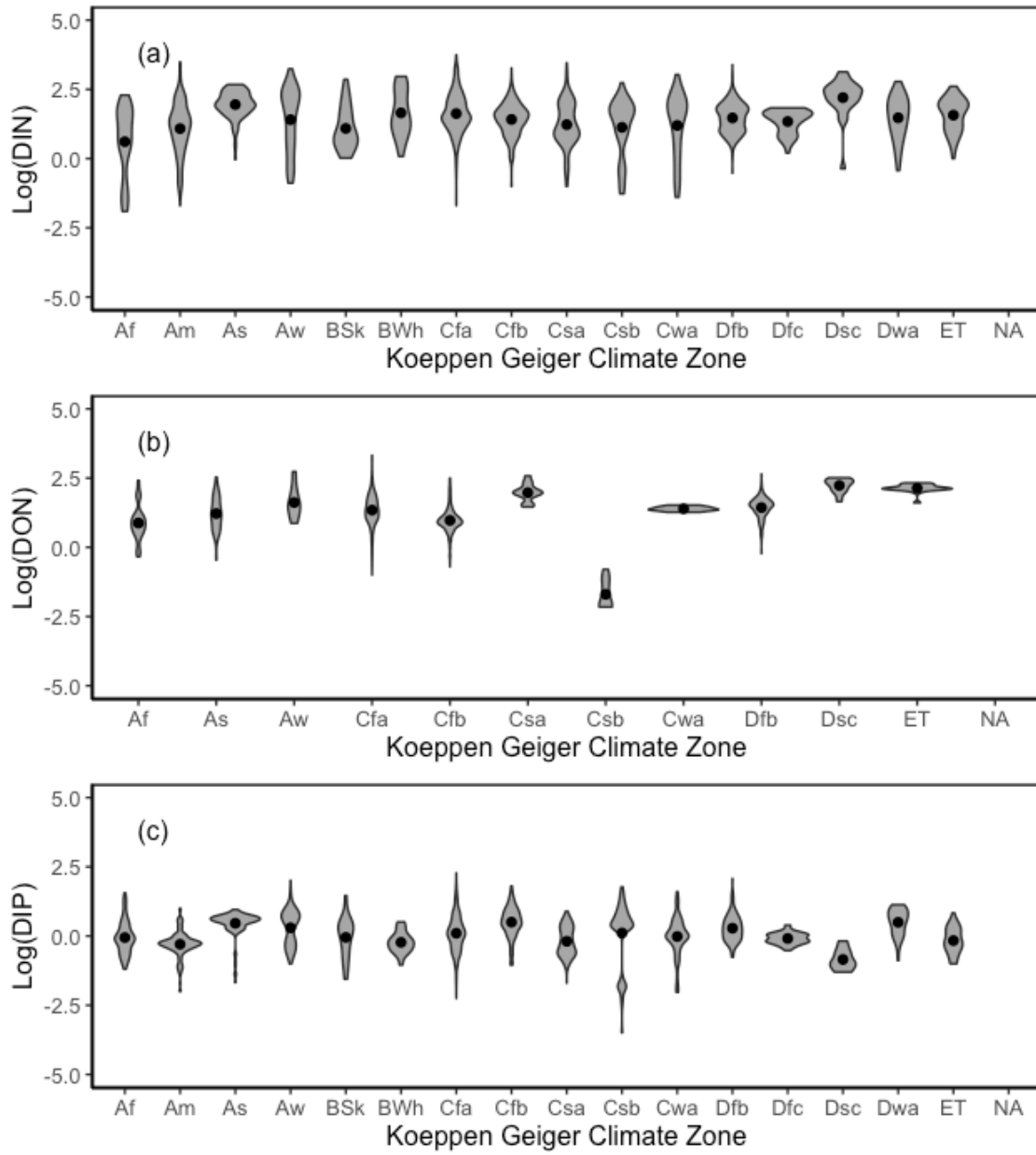


Figure S7. Violin plots showing the distribution of log transformed nutrient concentrations of a) DIN, b) DON, and c) DIP for each Koeppen Geiger Climate classification.

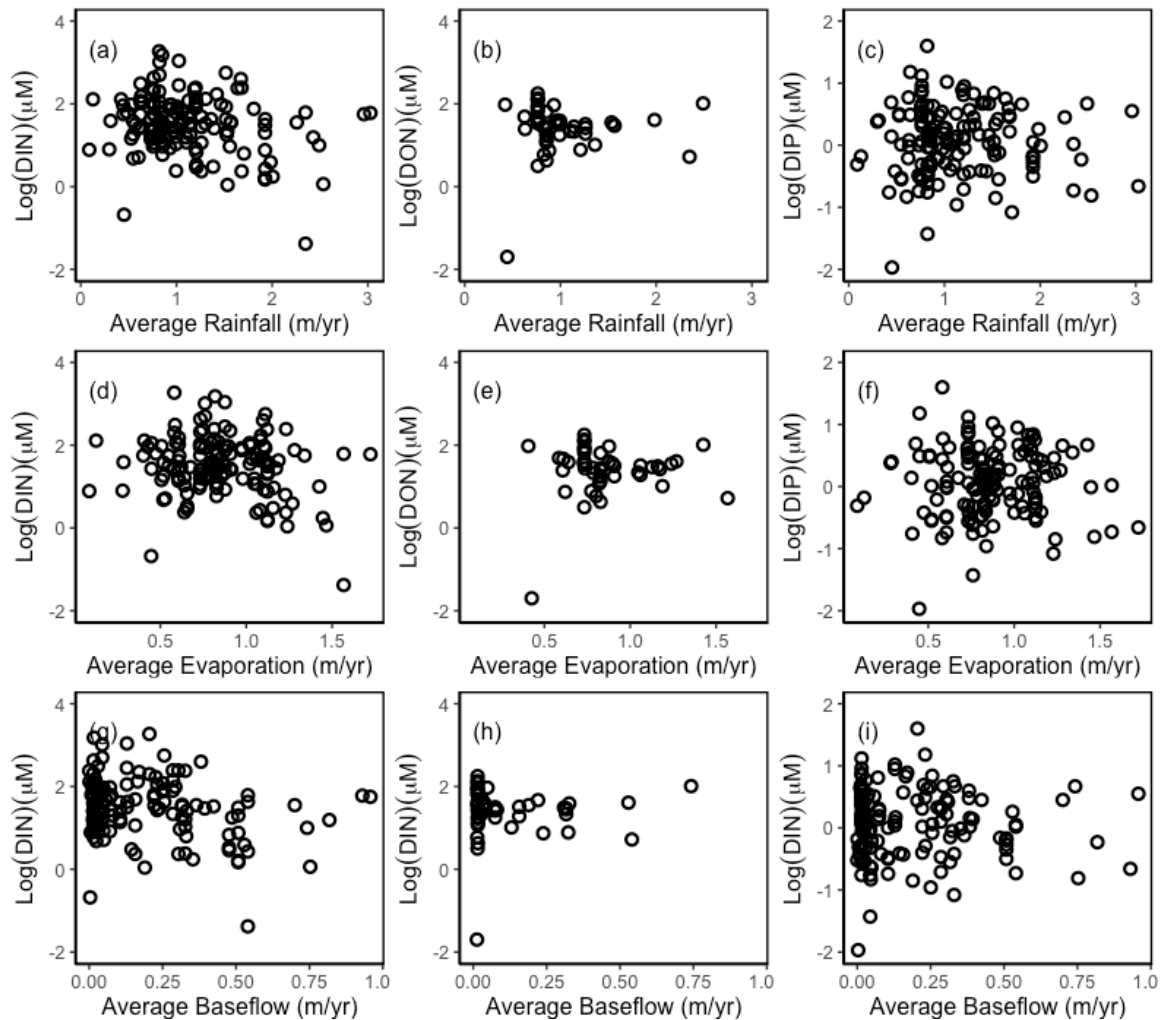


Figure S8. Comparison of log transformed, site averaged groundwater DIN, DON, and DIP concentrations compared to average rainfall (a-c), average evaporation (d-f), and average baseflow (g-i). No statistically significant relationships were identified between site climatological estimates and groundwater nutrient concentrations.

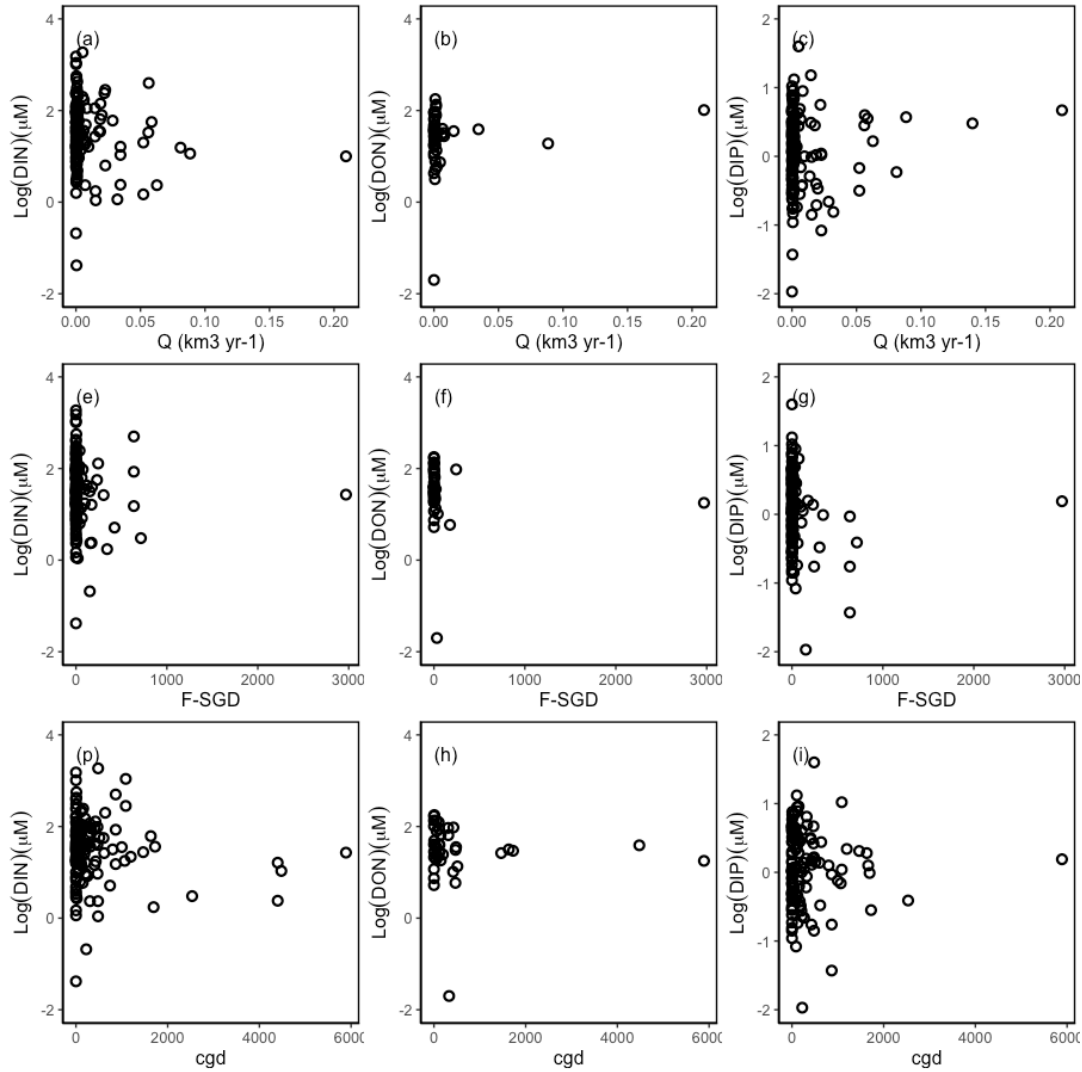


Figure S9. Comparison of log transformed, site averaged groundwater DIN, DON, and DIP concentrations compared to site average annual SGD (Q , km³ yr⁻¹) (a-c), average annual fresh SGD (F-SGD, m² yr⁻¹) (d-f), and average annual coastal groundwater discharge (cgd, m² yr⁻¹) (g-i). No statistically significant relationships were identified between site specific discharge estimates and groundwater nutrient concentrations.

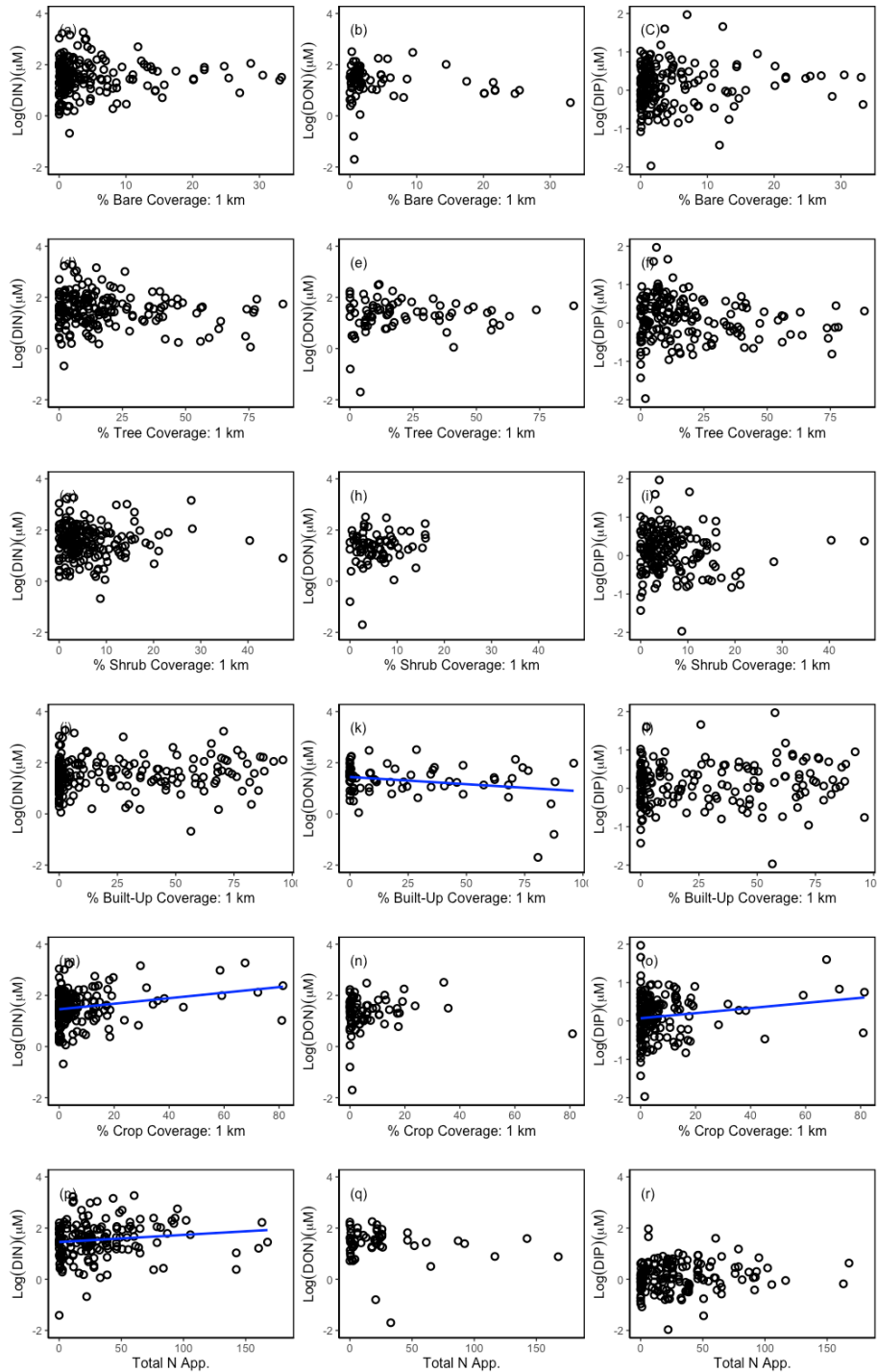


Figure S10. Comparison of log transformed, site averaged groundwater DIN, DON, and DIP concentrations compared to land cover data within a 1 km radius of each site. % of bare land cover (a-c), % built up land cover (d-f), % tree coverage (g-i), % shrub cover (j-l) % crop cover (m-o), and total N application (p-r) (Luijendijk et al., 2020; Potter et al., 2011). Each relationship was assessed with linear regression, plots with significant relationships (p-value < 0.05) include the linear regression line (blue) on the plot.

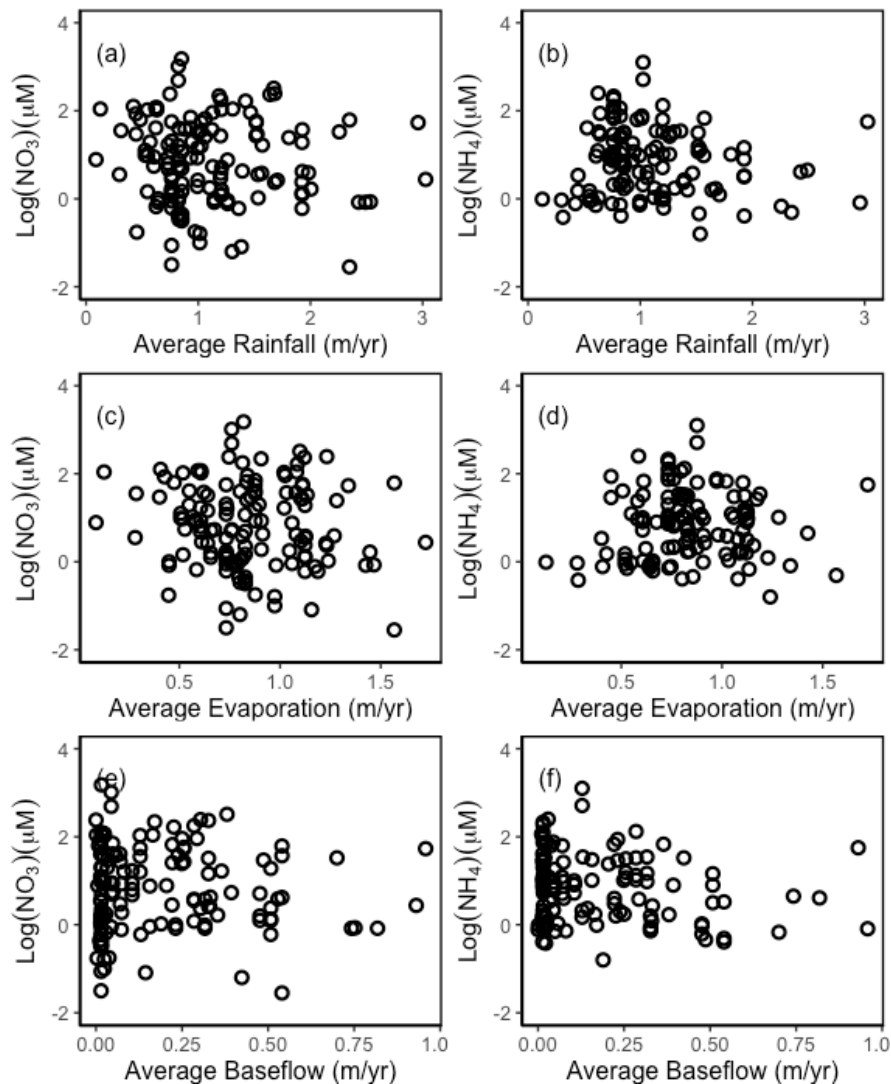


Figure S11. Comparison of log transformed, site averaged groundwater NO₃⁻ and NH₄⁺ concentrations compared to site specific annual average rainfall (a-b), average evaporation (c-d), and average baseflow (e-f). No statistically significant relationships were identified between climatological estimates and groundwater nutrient concentrations.

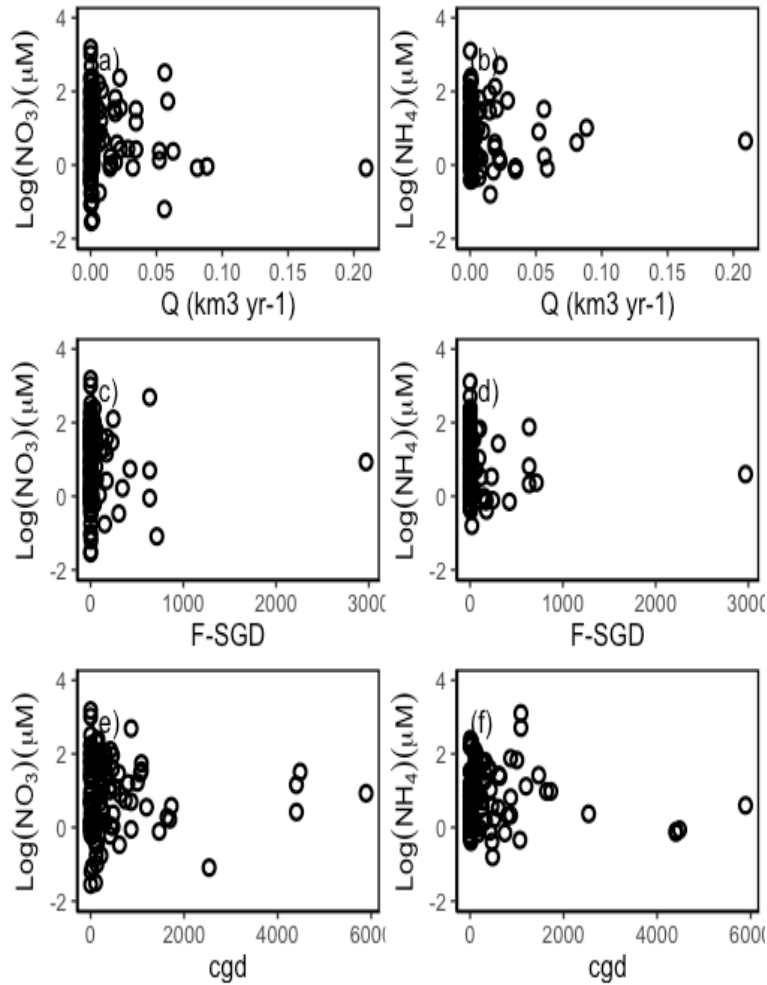


Figure S12. Comparison of log transformed, site averaged groundwater NO_3^- and NH_4^+ concentrations compared to site average annual SGD (Q , $\text{km}^3 \text{ yr}^{-1}$) (a-c), average annual fresh SGD (F-SGD, $\text{m}^2 \text{ yr}^{-1}$) (d-f), and average annual coastal groundwater discharge (cgd, $\text{m}^2 \text{ yr}^{-1}$) (g-i). No statistically significant relationships were identified between site specific discharge estimates and groundwater nutrient concentrations.

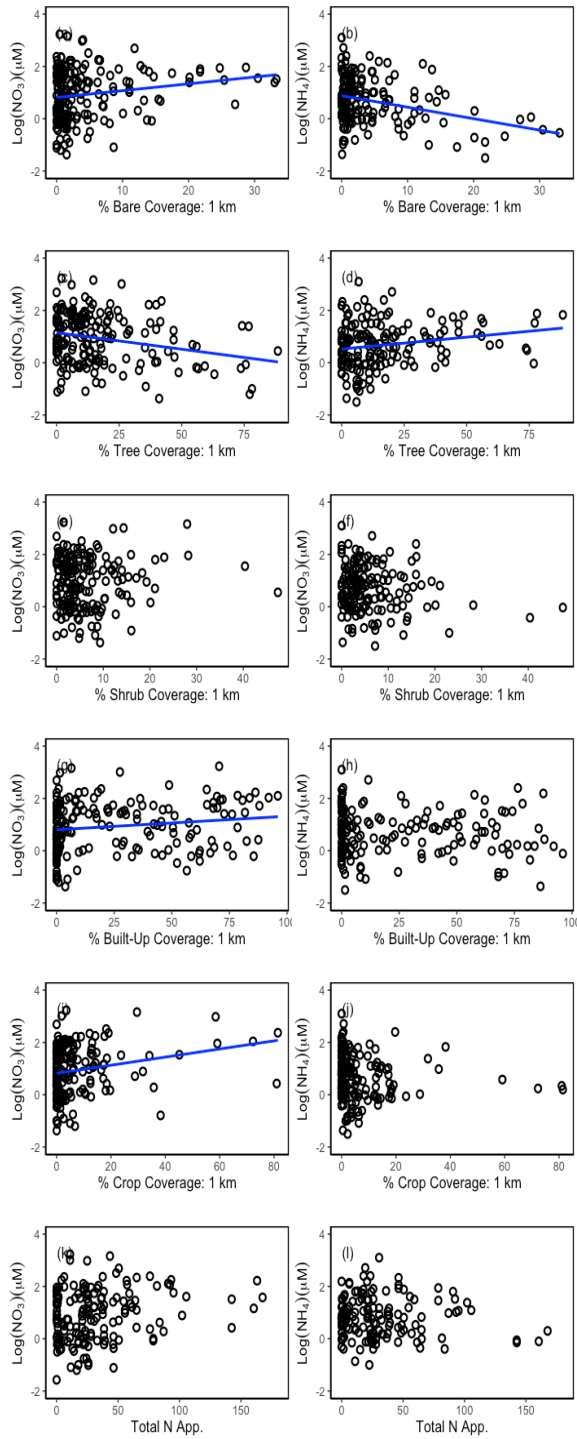


Figure S13. Comparison of log transformed, site averaged groundwater NO_3^- and NH_4^+ concentrations compared to land cover data within a 1 km radius of each site. % of bare land cover (a-c), % built up land cover (d-f), % tree coverage (g-i), % shrub cover (j-l) % crop cover (m-o), and total N application (p-r) (Luijendijk et al., 2020; Potter et al., 2011). Each relationship was assessed with linear regression, plots with significant relationships (p -value < 0.05) include the linear regression line (blue) on the plot.

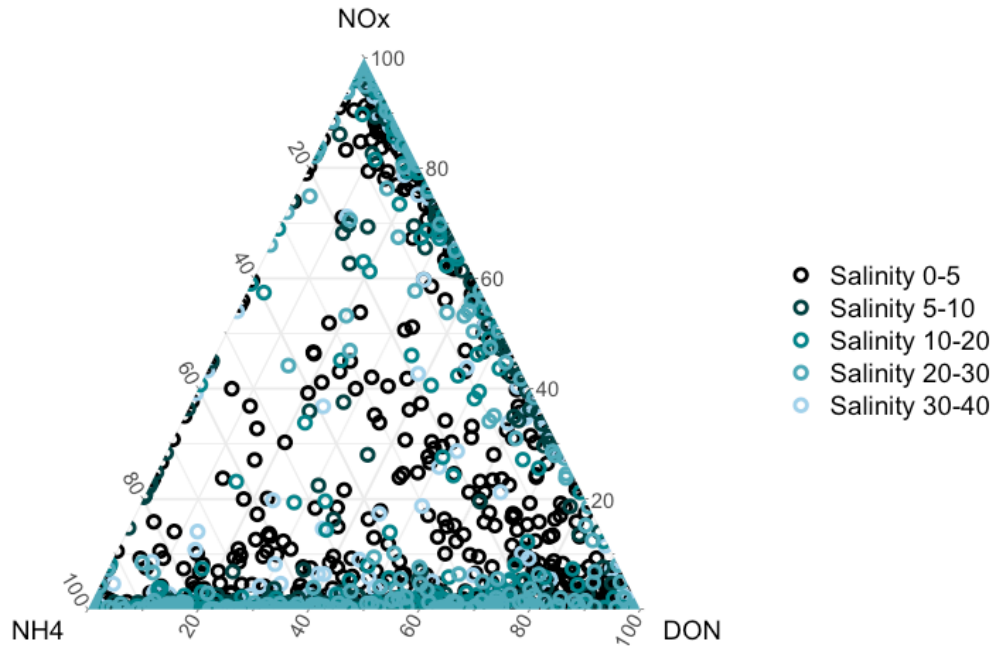


Figure S14. Ternary plot showing groundwater N composition binned by sample salinity (color); no clear trends identified.

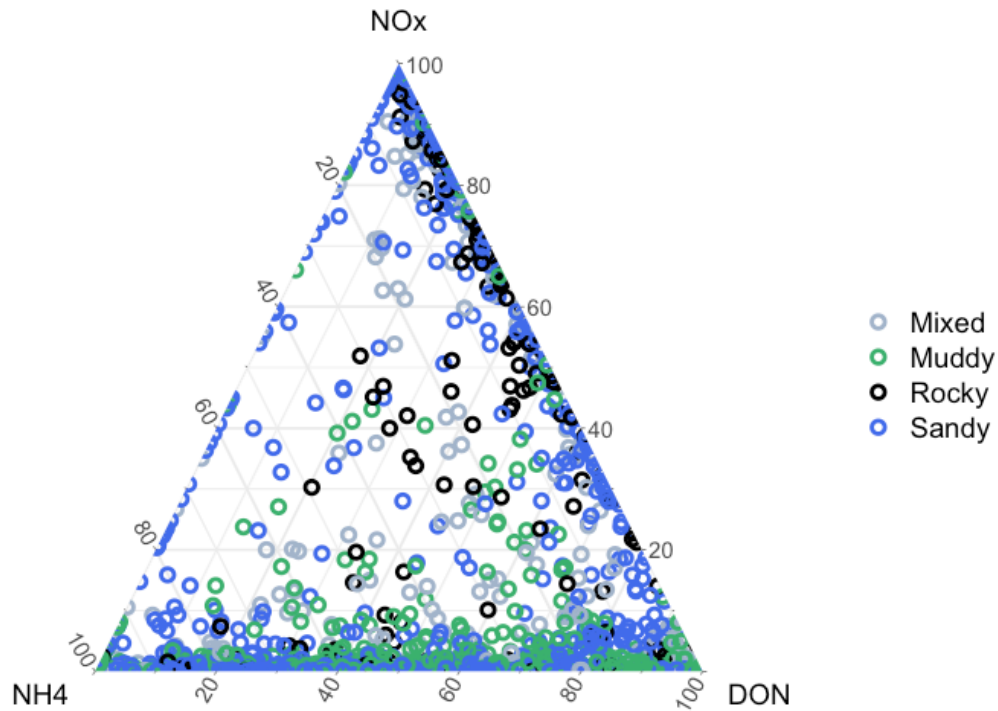


Figure S15. Ternary plot showing N composition when binned by site type (color); no clear trends identified.

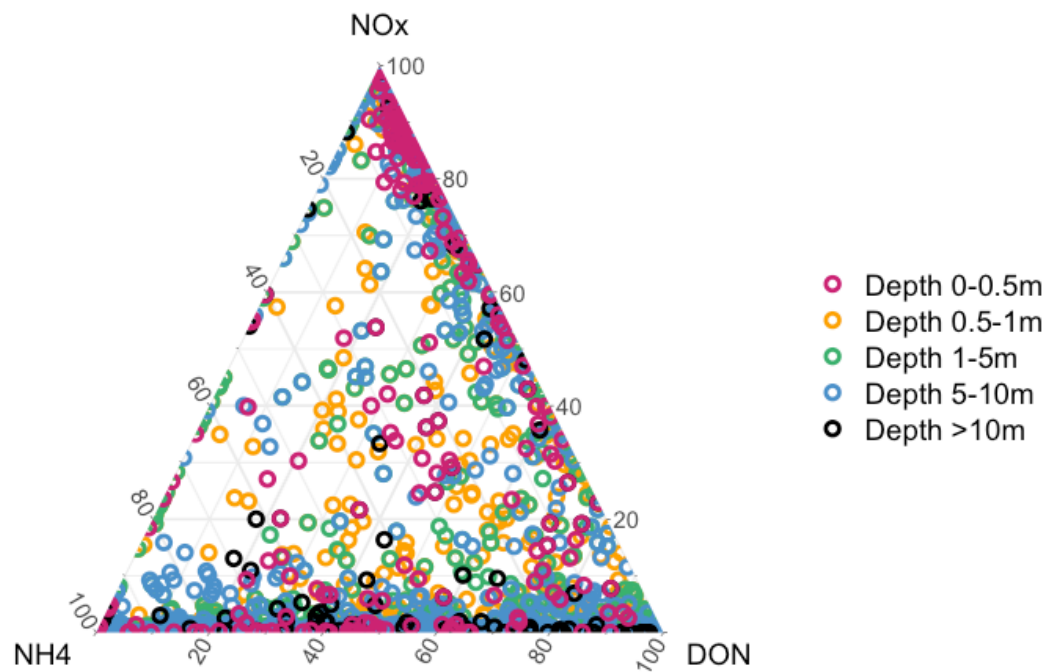


Figure S16. Ternary plot showing N composition binned by sample depth (color); no clear trends identified.

5.7. Appendix H

All data included in the Chapter 5 meta-analysis will be made publicly available via the Pangaea data repository and the public, interactive Shiny Product.

Chapter 6. Conclusions

Subterranean estuaries (STEs) are dynamic, biogeochemically active zones along the land-ocean continuum. This dissertation presents new knowledge regarding how groundwater nutrients, such as nitrogen (N), may be transformed in STEs prior to its export to coastal waters by submarine groundwater discharge (SGD). The approach spanned local and global scales, examining processing and export of nutrients at the Gloucester Point Beach STE (GP-STE) in Virginia USA and determining the role of STEs in SGD fluxes at the global scale with a meta-analysis.

Along the York River Estuary in Virginia, groundwater delivers high concentrations of dissolved inorganic nitrogen (DIN) and phosphorus (DIP) to the GP-STE. The results shown in Chapter 2 revealed that STE geochemical profiles of salinity, dissolved oxygen, DIN, DIP, and other analytes varied with depth and season. At the STE anoxic-oxic transition zone, a shift from ammonium to nitrate-rich groundwater was observed, which may be the result of nitrification. Denitrification was the main pathway of N removal in the STE; potential rates of anaerobic ammonium oxidation (anammox) were low. Groundwater nutrient fluxes in the York River were within the range of fluxes observed along the east coast of the US. Several SGD flux scenarios demonstrated the significant impact of N cycling in STEs on groundwater nutrient export. Denitrification decreased DIN concentrations in SGD and completely attenuated groundwater derived N during winter. Although groundwater inputs were lower than advective riverine fluxes, the results from this study suggest that SGD is a source of nutrients to the York River Estuary. Further research is required to characterize how groundwater discharge and nutrient fluxes vary along the entire York River and to understand the impact of these fluxes on nutrient cycling and primary productivity in the system. STE biogeochemical reactions should be considered when

estimating SGD fluxes, to better characterize the effect of SGD will have on nutrient budgets and water quality in the coastal zone.

Biogeochemical cycling within STEs is mediated by resident microbial communities, which were shown to vary with the steep geochemical gradients observed with depth (Chapter 3). Specifically, salinity, dissolved oxygen, DIN, and dissolved inorganic carbon were important explanatory variables of microbial community structure. Nitrifiers were identified within the microbial community indicating genetic potential for both ammonia oxidation and nitrite oxidation in the STE. The abundance of ammonia oxidizers was related to DIN concentrations, pH, salinity, and dissolved oxygen in the subsurface. STE microbial communities are integral to the fate and transport of groundwater-derived nutrients, future work is needed to understand how function and activity of these communities drive nutrient fluxes to coastal waters.

When measuring transformations within STEs, methodological approaches will vary in their ability to replicate the subsurface environment, resulting in varying process rates (Chapter 4). Nitrification in the GP-STE was evidenced by conservative mixing models informed by *in situ* geochemical profiles estimating ammonium loss and nitrate production, an *in situ* tracer experiment, and *ex situ* sediment slurry incubation experiments. The nitrate produced in surficial porewater by nitrification is likely available for discharge to the overlying water via groundwater discharge and tidal pumping. Despite all methods exhibiting active nitrification, the conservative mixing models and sediment slurry incubations did not resolve the spatial variation observed in nitrification rates during the *in situ* tracer experiment. This is likely due to the challenges associated with modeling the subsurface or attempting to replicate it *ex situ*, therefore, *in situ* tracer tests are likely the best estimate of process rates. When choosing tools to measure

subsurface transformations it is important to consider the inherent assumptions as well as the ability of each method to account for spatiotemporal heterogeneity in STEs.

A meta-analysis of STEs around the world (Chapter 5) demonstrated that groundwater nutrient concentrations and speciation are determined mainly by salinity, latitude, and surrounding land use. At the global scale, STEs produced DIN and dissolved inorganic phosphorus (DIP) and reduced dissolved organic nitrogen (DON) supplied by meteoric groundwater. When STE nutrient transformations are accounted for, fluxes of DIN and DIP increased, while DON fluxes decreased in fresh SGD; however, fresh SGD represents a small portion of the SGD transported to the ocean. Total SGD, a mixture of both fresh and saline groundwater, transports DIN and DON to the ocean at rates 1.7x and 2.7x larger, respectively, than the riverine fluxes of DIN and DON to the global ocean. DIP export via total SGD was half of the riverine flux to the global ocean and was roughly 3x lower than previous estimates. This study shows that groundwater is a source of nutrients to the coastal ocean and supplies more N than P, which can influence coastal water biogeochemistry and primary production. Future work should include understudied regions, such as the poles, Africa, and South America where data is currently limited.

Overall, this dissertation reveals the importance of biogeochemical reactions in STEs to nutrient discharge via SGD at both local and global scales. Many studies overlook these reactions along the groundwater flow path, resulting in inaccurate estimates of nutrient discharge via SGD. As we continue to define the impact groundwater derived nutrients have on coastal ecosystems, the role of STEs as reaction zones must be incorporated. This is of great concern as coastal zones face increasing risk of eutrophication, which groundwater inputs may exacerbate. Future studies should consider monitoring groundwater nutrient discharge to examine its role in

coastal biogeochemistry. This may include continuous monitoring of groundwater tracers such as radon, repeated sampling of groundwater nutrient concentrations over varying time scales, and stable isotope studies to link groundwater nutrients to primary producers in coastal waters. These data may better constrain groundwater fluxes and nutrient loading that can then be included in efforts to model and manage coastal waters.